Acta Oceanologica Sinica

Vol. 37 No. 5 May 2018

CONTENTS

Articles

Acta Oceanol. Sin., 2018, Vol. 37, No. 5, P. 1–7
DOI: 10.1007/s13131-018-1208-2
http://www.hyxb.org.cn
E-mail: hyxbe@263.net

Effects of surface waves and sea spray on air–sea fluxes during the passage of Typhoon Hagupit

HE Hailun[1]*, WU Qiaoyan[1], CHEN Dake[1], SUN Jia[2, 3], LIANG Chujin[1], JIN Weifang[1], XU Yao[4]

[1] State Key Laboratory of Satellite Ocean Environment Dynamics, Second Institute of Oceanography, State Oceanic Administration, Hangzhou 310012, China

[2] The First Institute of Oceanography, State Oceanic Administration, Qingdao 266061, China

[3] Laboratory for Regional Oceanography and Numerical Modeling, Qingdao National Laboratory for Marine Science and Technology, Qingdao 266061, China

[4] School of Geographic and Oceanographic Sciences, Nanjing University, Nanjing 210023, China

Received 15 November 2016; accepted 28 December 2017

Abstract

Air–sea exchange plays a vital role in the development and maintenance of tropical cyclones (TCs). Although studies have suggested the dependence of air–sea fluxes on surface waves and sea spray, how these processes modify those fluxes under TC conditions have not been sufficiently investigated based on *in-situ* observations. Using continuous meteorological and surface wave data from a moored buoy in the northern South China Sea, this study examines the effects of surface waves and sea spray on air–sea fluxes during the passage of Typhoon Hagupit. The mooring was within about 40 km of the center of Hagupit. Surface waves could increase momentum flux to the ocean by about 15%, and sea spray enhanced both sensible and latent heat fluxes to the atmosphere, causing Hagupit to absorb 500 W/m^2 more heat flux from the ocean. These results have powerful implications for understanding TC–ocean interaction and improving TC intensity forecasting.

Key words: air-sea flux, surface wave, sea spray, bulk formula, tropical cyclone

Citation: He Hailun, Wu Qiaoyan, Chen Dake, Sun Jia, Liang Chujin, Jin Weifang, Xu Yao. 2018. Effects of surface waves and sea spray on air–sea fluxes during the passage of Typhoon Hagupit. Acta Oceanologica Sinica, 37(5): 1–7, doi: 10.1007/s13131-018-1208-2

1 Introduction

Momentum and heat exchanges between the atmosphere and ocean are critical in the process of tropical cyclones' (TCs, also known as typhoons) development (Emanuel, 1988). Surface fluxes can be directly observed though turbulence-involved sensors under weak and moderate wind conditions (Gerbi et al., 2008; Li et al., 2013; Wang et al., 2013). The exchange coefficients (characterizing exchange efficiency) for sensible and latent heat fluxes are almost independent of wind (10-m neutral) speed up to 25 m/s, whereas the exchange coefficient for momentum (the drag coefficient) increases quasi-linearly with speeds up to 32 m/s (Smith, 1988). At present, direct *in-situ* measurements of air–sea turbulent fluxes are restricted to wind speeds less than 32 m/s, and these direct measurements are available from towers (Gerbi et al., 2008), buoys (Potter et al., 2015), or aircraft (French et al., 2007; Drennan et al., 2007).

Because there is no directly observed momentum flux for wind speeds greater than 32 m/s, such fluxes under strong wind conditions are generally deduced from environmental parameters that have a much lower frequency than turbulence. Through analyzing the atmospheric wind profile and computing air–sea momentum flux, Powell et al. (2003) discovered the well-known phenomenon that the surface drag coefficient levels off as wind speeds increase above 33 m/s. This phenomenon was supported by indirect estimation via oceanic measurement (Jarosz et al., 2007) and laboratory study (Donelan et al., 2004). The recent work of Potter et al. (2015) presented new evidence of a level-off at wind speeds greater than 22 m/s from direct flux measurements of a moored buoy. This result agrees with Powell et al. (2003)'s discovery, but their level-off was at a lower wind speed. Maximum 30-min sustained wind speeds recorded in Potter et al. (2015) were 26 m/s; however, under most TC conditions, speeds are greater than that. The disagreement in level-off at various wind speeds in different studies calls for further exploration of momentum flux under the strong winds of TCs.

Direct measurements of air–sea turbulent heat fluxes are even more difficult than those of momentum fluxes under strong winds. One possible reason is that the turbulence sensors of temperature and vapor are not as accurate as those of velocity fluctuations (Pedreros et al., 2003). The ONR-sponsored Coupled Boundary Layer Air–Sea Transfer (CBLAST) Hurricane Program made the first ever direct measurements of turbulent heat fluxes within a hurricane boundary layer (French et al., 2007; Drennan et al., 2007; Zhang et al., 2008). The CBLAST field observations gave sensible heat and enthalpy flux for 10-m wind speeds up to 30 m/s, which substantially extended the range of air–sea flux measurements and allowed estimation of the enthalpy exchange coefficients at wind speeds near hurricane force. However, the

Foundation item: Zhejiang Provincial Natural Science Foundation of China under contract No. LR15D060001; the National Program on Global Change and Air-Sea Interactions under contract No. GASI-IPOVAI-04; the National Natural Science Foundation of China under contract Nos 41476021, 41706034 and 41321004.
*Corresponding author, E-mail: hehailun@sio.org.cn

ratio of the exchange coefficient of enthalpy flux to the drag coefficient measured in the CBLAST field was considerably below the threshold for hurricane development suggested by Emanuel (1995) (Zhang et al., 2008).

Because many uncertainties remain in determining the surface flux in strong wind regimes, there is much room for improvement. However, in some practical circumstances, air–sea flux estimation using bulk formulae is still widely used. Surface waves and sea spray can substantially affect the exchange coefficients under TC conditions and contribute to improved air–sea flux estimation. For instance, *in-situ* observations under weak and moderate wind suggest that air–sea flux depends on surface waves (Zhao et al., 2003; Zhao and Xie, 2010). Those waves change surface dynamic roughness and are important in momentum exchange between the atmosphere and ocean (Taylor and Yelland, 2001; Oost et al., 2002; Drennan et al., 2003, 2005; He and Chen, 2011; Song et al., 2015; Zhang et al., 2016; Zhang and Song, 2018). Many scholars have investigated momentum flux under strong winds using theoretical methods. Hara and Belcher (2004) built a coupled wind–wave model by emphasizing the surface wave-induced part of air–sea momentum flux. The model is applicable to all wind conditions from weak to TCs, and the drag coefficient increases with speeds up to 50 m/s (Moon et al., 2004). The model was further improved by including wave breaking stress in the wave boundary layer (Kukulka and Hara, 2008a, b). Surface wave breaking or strong winds on the surface wave crest can generate large amounts of sea spray near the air–sea interface. Recently, from theoretical analysis, the so-called lubrication effect of sea spray explained the level-off phenomenon on the drag coefficient (Rastigejev et al., 2011; Rastigejev and Suslov, 2014). However, the theoretical model requires further validation under strong winds.

The evaporation of sea spray produces strong cooling in the layer of air within a few meters of the ocean surface, and thereby invigorates sensible heat exchange and storm intensity (Bao et al., 2000; Andreas and Emanuel, 2001). Once the 10-m wind speed over the ocean reaches about 11–13 m/s, spray-induced sensible and latent heat fluxes become substantial fractions (Andreas et al., 2008). In fact, the lack of observations under strong winds prohibited correct parameterization of sea spray.

Widely-used estimation of air–sea flux using bulk formulae was established for weak and moderate winds and then roughly extended to the strong wind condition. Major progress in the Coupled Ocean Atmosphere Response Experiment (COARE) flux algorithm included surface wave information (Fairall et al., 2003). To better understand air–sea flux and thereby model TCs, more physical processes in air–sea interaction should been taken into account (Walsh et al., 2010). Ocean-atmosphere coupled models have shown the important role of surface waves in TC development (Bao et al., 2000; Liu et al., 2011, 2012; Li et al., 2016). However, discrepancies in current surface wave models are still large under TC conditions, especially in wave period simulations (Xu et al., 2007; Montoya et al., 2013; Xu et al., 2017). Numerical models for simulating TC intensity are sensitive to the details of sea spray (Bao et al., 2000; Andreas and Emanuel, 2001; Wu et al., 2015), but accurate evaluation of the sea spray effect on air–sea fluxes requires *in-situ* observations.

The South China Sea (SCS) is frequently affected by typhoons. Recently, we deployed a moored buoy in the northern SCS and obtained continuous high-resolution meteorological observations for Typhoon Hagupit. Surface wave data were also provided by the mooring. Using this set of unique *in-situ* observations, the present study evaluates the effects of surface waves and sea spray on air–sea momentum and heat fluxes calculated by bulk formulae.

2 Data

We used best-track data from the Joint Typhoon Warning Center to describe the characteristics of Typhoon Hagupit (0818, Fig. 1). Hagupit first appeared in the western North Pacific at 1 200 UTC on 17 September 2008, and intensified as it passed through the Luzon Strait and entered the SCS. The maximum sustained wind speed of Hagupit reached 64.3 m/s (125 kn), and it eventually became a category-4 tropical cyclone (Xu et al., 2017). The moored buoy (19.5°N, 115.5°E) was on the left side of the Hagupit track. The closest approach to the typhoon track of the mooring was 33 km. Hagupit reached that location at 0513 UTC on 23 September 2008, with a radius of maximum wind of 52 km and translation speed of 8.46 m/s. The inertial period (*IP*) at the mooring site is 1.46 d.

The meteorological data from the buoy include wind speed, air pressure, relative humidity, and air temperature. Table 1 lists details of the instruments installed on the buoy, whose sensors are capable of meteorological measurement under TC conditions. These meteorological data were measured at 3 m above the sea surface. Those data were collected every 10 min and were summed into 1-h averages. Surface wave parameters including

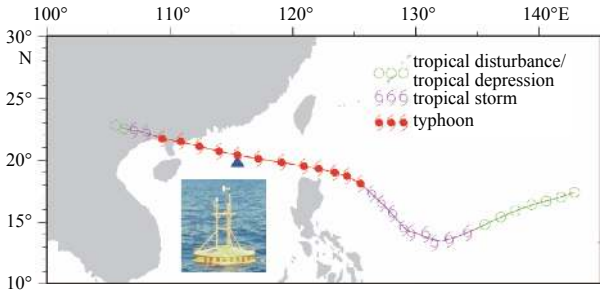

Fig. 1. Track of Typhoon Hagupit (2008) and location of moored buoy (blue triangle). Photo is of deployed buoy in northern SCS.

Table 1. Instruments installed on the buoy

Instruments	Parameter	Range	Accuray
R.M. Young, Wind Monitor 05103	wind speed	0–100 m/s	0.3 m/s
	wind direction	0°–360°	3°
Campbell Scientific, HygroClip S3	air temperature	–40–85°C	0.3°C
	relative humidity	0%–100% RH	1.5%
Vaisala, PTB100 Barometers	air pressure	500–1 100 hPa	0.3hPa@20°C
AXYS, TRIAXYS Wave Sensor	wave height	0–20 m	1%
	wave period	1.5–33 s	1%
	wave direction	0°–360°	1°

significant wave height and peak wave period were recorded once per hour, with measurement interval 20 min. SST data were not available from the buoy and were instead obtained from the AMSR-E satellite (Hilburn and Wentz, 2008). We also used 6-h cloud-cover data from NCEP reanalysis to calculate radiative fluxes.

Figure 2 shows time series of meteorological variables from the buoy. Both atmospheric and oceanic fields exhibited large variations associated with Typhoon Hagupit. The maximum meridional and zonal winds from the buoy were 25 m/s, and the corresponding maximum wind speed was 32 m/s. SST was ~29.8°C at time 2.0 *IP* before Hagupit's arrival, and cooled rapidly to 27.3°C during its passage. There was also cooling of air temperature during the typhoon forcing period. This temperature was cooler than SST before typhoon arrival, indicating that the atmosphere was receiving sensible heat flux at that time. Air pressure dropped from 1 010 to 958 hPa at typhoon arrival. The variance of relative humidity increased as Hagupit approached the mooring. Under the typhoon forcing, wave height reached 11 m, and the corresponding peak wave period was 15 s. Cloud cover increased to 90% during the typhoon forcing period.

3 Bulk formulae for air–sea fluxes

Air–sea turbulent fluxes are usually estimated through bulk formulae that are based on Monin-Obukhov similarity theory (Fairall et al., 1996, 2003; Drennan et al., 2014). These formulae calculate air–sea fluxes through multiplication of air–sea differences and exchange coefficients (Price, 1981). Those coefficients are usually parameterized using other parameters such as roughness length. We used four different algorithms to calculate the air–sea turbulence fluxes (Table 2).

The first algorithm was proposed by Large and Pond (1981, 1982; LP henceforth) based on exchange coefficient parameterizations of momentum, heat and vapor. LP is a very simple and cheap algorithm that provides baseline calculations. It has been applied in previous TC studies (Price, 1981; Moon et al., 2004). The second is the widely used flux algorithm of COARE (henceforth COR; Fairall et al., 2003), with wind-dependent roughness length parameterization. COR is different from LP in its parameterization of velocity and scalar roughness lengths (Charnock, 1955). The third is a COARE (version 3.0) algorithm with surface wave-dependent roughness length parameterization (COR-WAVE henceforth; Taylor and Yelland, 2001). COARE (version

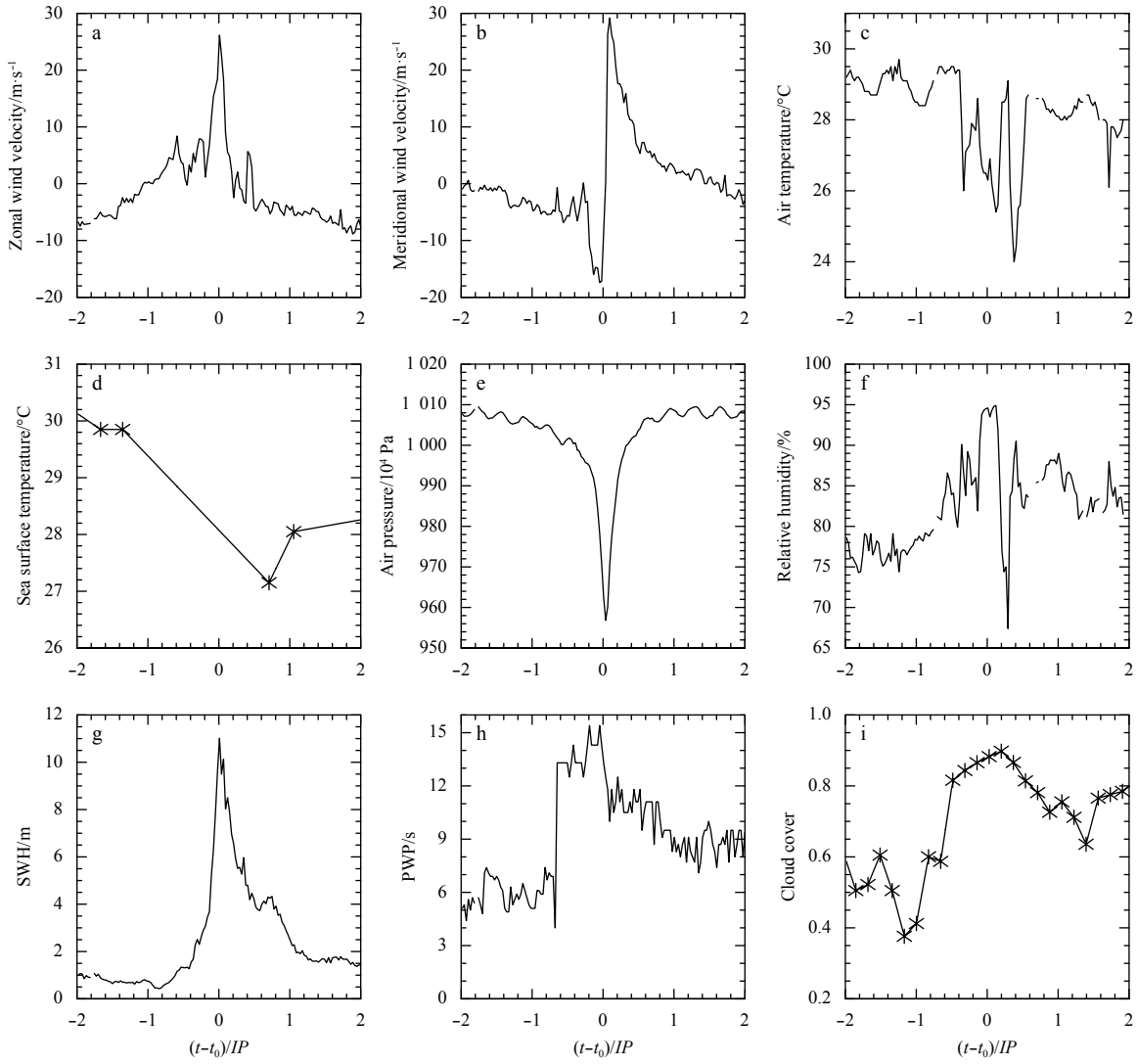

Fig. 2. Time series of meteorological variables from buoy, sea surface temperature from AMSR-E satellite, and cloud cover data from NCEP reanalysis for Typhoon Hagupit (2008). t represents time, t_0 arrival time of the typhoon, and *IP* the inertial period.

Table 2. Bulk formulae for air–sea turbulent fluxes, which include momentum flux (MF), sensible heat flux (SHF) and latent heat flux (LHF)

	MF	SHF	LHF
LP	10^3C_{dn} = 1.2, if U_{10n}<11 m/s; 10^3C_{dn} = 0.49+0.065U_{10n}, else	10^3C_{hn} =1.13	10^3C_{en} = 1.15
COR	$z_0 = 0.011\,u_*^2/g + 0.11\nu/u_*$	$z_{0T}= \nu f_T(R_r)/u_*$	$z_{0q}= \nu f_q(R_r)/u_*$
COR-WAVE	$z_0 = 1\,200h_s(h_s/L_p)^{4.5}+0.11\nu/u_*$	COR	COR
COR-SPRAY	COR	$SHF_{in}+SHF_{sp}$ SHF_{in} = COR $SHF_{sp}=\beta Q_S-(\alpha-\gamma)Q_L$	$LHF_{in}+LHF_{sp}$ LHF_{in} = COR $LHF_{sp}=\alpha Q_L$

Note: Bulk exchange coefficients for momentum, heat, and vapor are denoted by C_{dn}, C_{hn} and C_{en}, respectively, and corresponding roughness lengths are z_0, z_{0T} and z_{0q}. U_{10n} is 10-m neutral wind speed, u_* is friction velocity, ν is kinematic viscosity, g is acceleration of gravity, and R_r is the roughness Reynolds number ($R_r = z_0u_*/\nu$). $f_T(R_r)$ and $f_q(R_r)$ are functions related to SHF and LHF in COR (Fairall et al., 2003). For COR-WAVE MF, surface wave parameters include significant wave height (h_s) and peak wave period (L_p). For COR-SPRAY heat fluxes, new terms are introduced by sea spray as SHF_{sp} and LHF_{sp}, whereas some coefficients (α, β and γ) exist for adjusting physical quantities, such as Q_s (spray sensible heat flux) and Q_L (spray latent heat flux).

3.0) includes two schemes for surface wave-related roughness length. The first is wave steepness dependent (Taylor and Yelland, 2001) and the second wave age dependent (Oost et al., 2002). Under the wave age dependent schemes, when the observed wind speed is greater than 25 m/s, the bulk estimated wind stress exceeds 10 N/m², which appears unrealistic. Hence, we only used the wave steepness dependent scheme in our computation for Typhoon Hagupit. The fourth algorithm adds sea spray-related air–sea fluxes to the COARE parameterization (COR-SPRAY henceforth; Andreas et al., 2008). The Andreas et al. (2008) algorithm is basically the only one available for representing spray transfer. This algorithm uses COARE version 2.6 for interfacial flux estimation. COARE 2.6 is different from COARE 3.0 for scalar roughness lengths of winds greater than 10 m/s (Fairall et al., 1996). In the case of Typhoon Hagupit, the difference in momentum flux between versions 2.6 and 3.0 is very small (<0.05 N/m²), and differences in the maximum sensible heat and latent heat fluxes are 25.0 and 90.0 W/m², respectively.

4 Results

Figure 3a shows drag coefficients estimated from the buoy data during the passage of Hagupit (–1.5 to 1.5 *IP* relative to the arrival time). The drag coefficient from the LP scheme was independent of wind speed for weak winds (<10 m/s) but proportional to that speed for speeds greater than 10 m/s. The COR scheme shows a nearly linear correlation between the drag coefficient and wind speed for all winds. The drag coefficient from the COR-WAVE scheme was less dependent on wind speed, but in general a large drag coefficient corresponded to a strong wind. Under extremely strong winds (>30 m/s), the drag coefficient was larger with wave effects included (COR-WAVE) than without (COR or LP), consistent with Fairall et al. (2003).

Unlike in the COR and COR-WAVE schemes, the exchange coefficients of heat (Fig. 3b) and vapor (Fig. 3c) in the LP scheme were constant for all winds. Those coefficients in COR were nearly constant for wind speeds less than 10 m/s but proportional to speed for speeds greater than 10 m/s. The exchange coefficients of heat and vapor in COR were smaller than those in LP for wind speeds less than 14 m/s, but larger than those in LP for winds greater than 14 m/s. Similar to the drag coefficient, the exchange coefficients of heat and vapor in COR-WAVE were less dependent on wind speed than in the LP and COR schemes. The COR-SPRAY scheme is not included in the comparison shown in Fig. 3, because it has the same exchange coefficient as those in the COR scheme. It did not change the momentum flux but modified sensible and latent heat fluxes because of more flux terms than the exchange coefficients.

Figure 4a shows momentum fluxes calculated by all four algorithms. The evolution of these fluxes was consistent. They started to increase at 0.2 *IP* prior to typhoon arrival. As the typhoon center approached the buoy site, momentum fluxes increased rapidly. The fluxes dropped slightly immediately upon TC arrival and reached a maximum 0.1 *IP* later. Double peaks indicate the typhoon eye passed near the buoy site. The momentum fluxes from LP and COR were very similar, with a maximum of 5.4 N/m². The COR-WAVE scheme gave weaker wind stress in the period between –0.2 and 0 *IP*, but stronger from 0 to 0.2 *IP*. The maximum wind stress from COR-WAVE was 6.2 N/m², ~15%

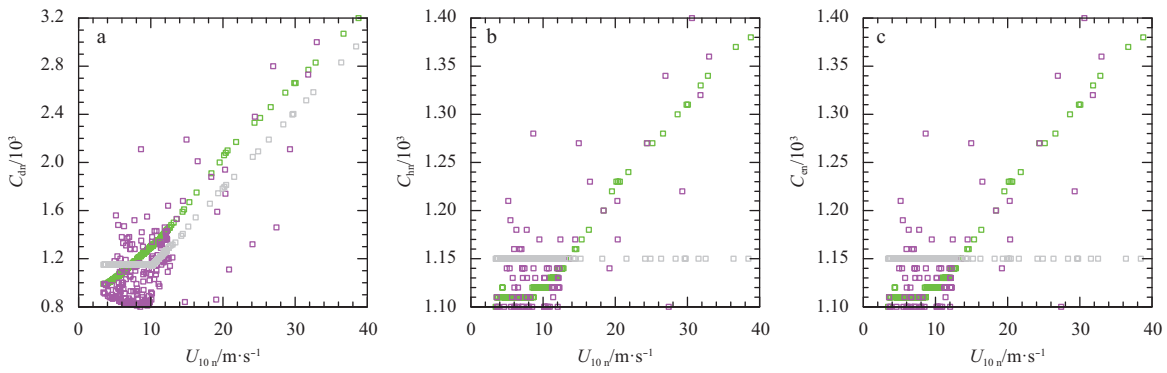

Fig. 3. Neutral exchange coefficients for momentum (C_{dn}) (a), heat (C_{hn}) (b), and vapor (C_{en}) (c) derived from buoy data for Typhoon Hagupit. U_{10n} is 10-m neutral wind speed. Grey, green and magenta squares represent LP, COR, COR-WAVE algorithms, respectively.

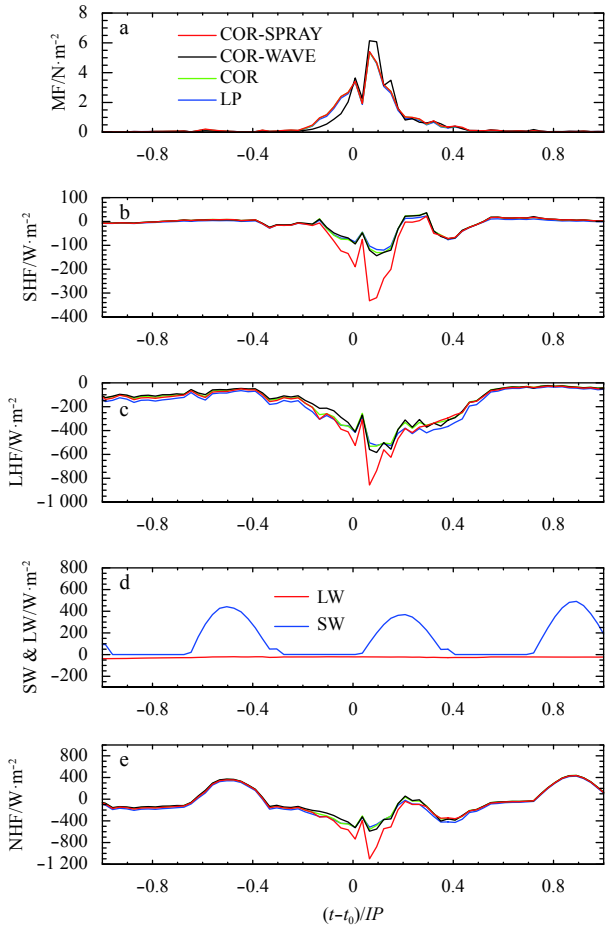

Fig. 4. Time series of air–sea flux at buoy site for Typhoon Hagupit. a. Momentum flux (MF), b. sensible heat flux (SHF), c. latent heat flux (LHF), d. net shortwave (SW) and longwave (LW) radiation, and e. net heat flux (NHF). Negative values of heat flux denote heat loss from ocean to atmosphere.

greater than that from the other three schemes.

Figure 4b shows sensible heat fluxes, in which positive (negative) values represent heat transfer from atmosphere to ocean (ocean to atmosphere). The sensible heat fluxes calculated from four different schemes had a similar evolution, apparently influenced by wind forcing. The variability of sensible heat flux was very small before 0.2 *IP* prior to typhoon arrival, and decreased by 100 W/m^2 in the subsequent 0.2 *IP*. In general, the LP, COR and COR-WAVE schemes gave similar sensible heat fluxes from ocean to atmosphere, with a maximum ~140 W/m^2. The sensible heat flux from the COR-SPRAY scheme, however, reached 340 W/m^2, more than twice that from the other three schemes. This suggests that sea spray can effectively enhance sensible heat exchange under typhoon forcing.

Latent heat fluxes (Fig. 4c) were also strongly influenced by the wind forcing. They were much greater during the typhoon forcing stage (–0.5 to 0.5 *IP*) than before typhoon arrival, and greater than the sensible heat fluxes. Latent heat loss from the ocean increased dramatically from –50 to –500 W/m^2 (LP, COR, and COR-WAVE) or –900 W/m^2 (COR-SPRAY) under the typhoon conditions. Like the sensible heat fluxes, latent heat fluxes from the LP, COR and COR-WAVE schemes were roughly the same, but including sea spray enhanced the maximum latent heat flux by 400 W/m^2.

The net heat flux (Fig. 4e) is the sum of the sensible heat, latent heat, and radiative fluxes. The latter had a distinct diurnal cycle (Fig. 4d). During the period between –0.2 and 0.2 *IP*, Hagupit had a huge heat gain from the ocean through both sensible and latent heat fluxes. Again, net heat fluxes from the LP, COR and COR-WAVE schemes were similar, with a maximum net heat flux ~600 W/m^2. The maximum was ~1 100 W/m^2 in the COR-SPRAY scheme. There was little influence of sea spray on the net heat fluxes in the period without strong winds.

5 Discussion

COARE 3.0 includes intrinsic parameterization of surface waves through wind information (Equation 27 in Fairall et al., 2003). To check the COR-WAVE parameterization in our study, surface wave parameters from the COARE 3.0 intrinsic algorithm were compared with those from *in-situ* observations, as shown in Fig. 5. The COARE 3.0 intrinsic parameterization produces wave heights as high as 40 m (in the period between –0.2 and 0.2 *IP*), which appears unrealistic (Fig. 5a). The peak wave period (Fig. 5b) from the parameterization does not reflect the wave period from observation in the period between 1 *IP* before and 1 *IP* after the typhoon. Because the parameterized wave height and wave period are substantially different from the observations, the dy-

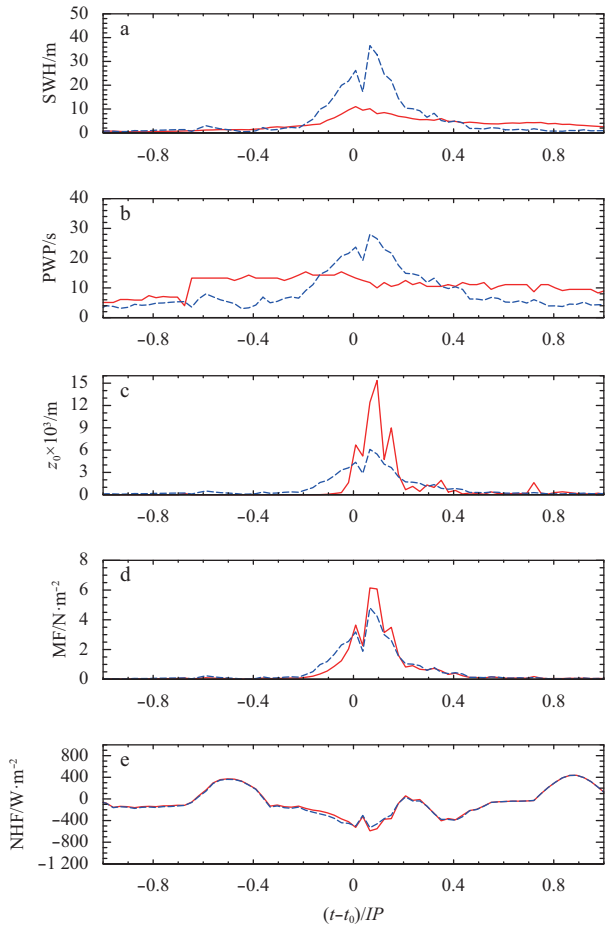

Fig. 5. Time series of wave parameters and air–sea fluxes from COARE 3.0. a. Significant wave height (SWH), b. peak wave period (PWP), c. roughness length (z_0), d. magnitude of momentum flux (MF), and e. net heat flux (NHF). Blue and red lines represent wave information from COARE 3.0 intrinsic wave parameterization and observations, respectively.

namic roughness length (denoted z_0 as shown in Fig. 5c) and corresponding momentum flux (Fig. 5d) are inconsistent with those of realistic waves during the typhoon forcing period. In detail, the dynamic roughness length is parameterized using dominant wave steepness, where that wave steepness is defined by the wave height over wavelength and the wavelength is proportional to the square of the wave period. Therefore, at TC arrival time, although the intrinsic wave parameterization produced a much higher wave height than observation, it gave an even larger wavelength, and the corresponding wave steepness and dynamic roughness length decreased but not increased. As a result, the maximum wind stress estimated from the intrinsic wave parameterization was 22% weaker than that from *in-situ* wave observation. This suggests the necessity of onsite wave observations for bulk momentum flux at typhoon forcing time. Additionally, the interfacial heat flux from the wave parameterization agrees well with that calculated from wave observation (Fig. 5e), indicating that the impact of the observed wave on that flux was relatively weak.

Bulk formulae of spray heat fluxes were parameterized based on field data, which were mostly limited to wind speeds less than 20 m/s. With such winds, the spray contribution to the joint sensible and latent heat fluxes exceeded 100 W/m^2 of the total 400 W/m^2 (Andreas and Emanuel, 2001). However, under most typhoon conditions, wind speeds are stronger than 20 m/s. For wind speeds beyond the range of flux parameterizations that have been tested, Andreas and Emanuel (2001) and Andreas et al. (2008) made extrapolation calculations using idealized analyses in which spray-mediated heat flux increases as a function of the cube of the friction velocity. In those analyses, spray sensible heat flux was ~350 W/m^2 and spray latent heat flux was ~750 W/m^2 for a 10-m wind speed of 40 m/s (Figure 8 in Andreas et al., 2008). In the case of Typhoon Hagupit, for a 10-m wind of 38 m/s (from LP algorithm), spray sensible heat flux was 200 W/m^2 and spray latent heat flux was 400 W/m^2. The underestimation in our study may be attributable to interfacial heat flux from a different version of COARE algorithm and different scenarios of air temperature, sea surface temperature, and air pressure. For instance, in Andreas et al.'s (2008) idealized analysis, air temperature, sea surface temperature, and air pressure were kept constant. These data from our *in-situ* observations varied with time.

The aforementioned level-off phenomenon of drag coefficient was examined further to determine its potential impact (Powell et al., 2003). We used Hwang's (2011) scheme, which emphasizes the concept of saturation (or level-off phenomenon) in the drag coefficient parameterization. The relative difference of momentum flux was as large as 32% when comparing Hwang's (2011) scheme with our LP (results not shown). There is no doubt that saturation effects on the drag coefficient are important and that they dominate strong-wind momentum flux. However, further exploration is beyond the scope of the present work, so we leave it to future study.

6 Concluding remarks

Taking advantage of *in-situ* observations of meteorological variables and ocean surface waves from a moored buoy, we examined the effects of surface waves and sea spray on air–sea fluxes during Typhoon Hagupit. Wind stress estimated from surface waves was 15% greater than that parameterized from wind speed in the case of Hagupit, indicating greater energy loss from typhoon to ocean. Wind stress could also enhance oceanic vertical mixing and thereby sea surface temperature cooling, further weakening the typhoon.

The effects of sea spray on air–sea fluxes were mostly on turbulent heat exchange, including both sensible and latent heat fluxes. In the case of Hagupit, accounting for sea spray increased the maximum sensible heat flux from 140 to 340 W/m^2, and the maximum latent heat flux from 500 to 900 W/m^2. The effect of sea spray resulted in Hagupit gaining 500 W/m^2 of heat flux (sum of sensible and latent heat fluxes) from the ocean. Sea spray was more important in air–sea heat exchanges than surface waves.

The present study evidences the importance of both surface waves and sea spray in typhoon–ocean interaction. The implication is that, in order to reduce uncertainties in estimating air–sea fluxes and thereby improving TC intensity forecasting, the effects of surface waves and sea spay must be properly considered. Finally, it should be noted that our evaluation of these processes was based on existing parameterizations, which need to be further validated by direct flux measurements under TC conditions.

Acknowledgements

The AMSR data are produced by Remote Sensing Systems and sponsored by the NASA Earth Science MEaSUREs DISCOVER Project and the NASA AMSR-E Science Team (www.remss.com). The NCEP Reanalysis data are provided by the NOAA/OAR/ESRL PSD (http://www.esrl.noaa.gov/psd/). The sea spray code is from Dr. E. L. Andreas (http://www.nwra.com/resumes/andreas/).

References

Andreas E L, Emanuel K A. 2001. Effects of sea spray on tropical cyclone intensity. J Atmos Sci, 58(24): 3741–3751

Andreas E L, Persson P O G, Hare J E. 2008. A bulk turbulent airsea flux algorithm for high-wind, spray conditions. J Phys Oceanogr, 38(7): 1581–1596

Bao J W, Wilczak J M, Choi J K, et al. 2000. Numerical simulations of air-sea interaction under high wind conditions using a coupled model: A study of hurricane development. Mon Weather Rev, 128(7): 2190–2210

Charnock H. 1955. Wind stress on a water surface. Q J Roy Meteor Soc, 81(350): 639–640

Drennan W M, Graber H C, Collins III C O, et al. 2014. EASI: An air-sea interaction buoy for high winds. J Atmos Ocean Technol, 31(6): 1397–1409

Drennan W M, Graber H C, Hauser D, et al. 2003. On the wave age dependence of wind stress over pure wind seas. J Geophys Res, 108(C3): 8062

Donelan M A, Haus B K, Reul N, et al. 2004. On the limiting aerodynamic roughness of the ocean in very strong winds. Geophys Res Lett, 31(18): L18306

Drennan W M, Taylor P K, Yelland M J. 2005. Parameterizing the sea surface roughness. J Phys Oceanogr, 35(5): 835–848

Drennan W M, Zhang J A, French J R, et al. 2007. Turbulent fluxes in the hurricane boundary layer: Part II. Latent heat flux. J Atmos Sci, 64(4): 1103–1115

Emanuel K A. 1988. The maximum intensity of hurricanes. J Atmos Sci, 45(7): 1143–1155

Emanuel K A. 1995. Sensitivity of tropical cyclones to surface exchange coefficients and a revised steady-state model incorporating eye dynamics. J Atmos Sci, 52(22): 3969–3976

Fairall C W, Bradley E F, Hare J E, et al. 2003. Bulk parameterization of air-sea fluxes: updates and verification for the COARE algorithm. J Climate, 16(4): 571–591

Fairall C W, Bradley E F, Rogers D P, et al. 1996. Bulk parameterization of air-sea fluxes in TOGA COARE. J Geophys Res, 101(C2): 3747–3764

French J R, Drennan W M, Zhang J A, et al. 2007. Turbulent fluxes in the Hurricane boundary layer: Part I. Momentum flux. J Atmos Sci, 64(4): 1089–1102

Gerbi G P, Trowbridge J H, Edson J B, et al. 2008. Measurements of

momentum and heat transfer across the air-sea interface. J Phys Oceanogr, 38(5): 1054–1072
Hara T, Belcher S E. 2004. Wind profile and drag coefficient over mature ocean surface wave spectra. J Phys Oceanogr, 34(11): 2345–2358
He Hailun, Chen Dake. 2011. Effects of surface wave breaking on the oceanic boundary layer. Geophys Res Lett, 38(7): L07604
Hilburn K A, Wentz F J. 2008. Intercalibrated passive microwave rain products from the unified microwave ocean retrieval algorithm (UMORA). J Appl Meteor Clim, 47(3): 778–794
Hwang P A. 2011. A note on the ocean surface roughness spectrum. J Atmos Oceanic Technol, 28(3): 436–443
Jarosz E, Mitchell D A, Wang D W T, et al. 2007. Bottom-up determination of air-sea momentum exchange under a major tropical cyclone. Science, 315(5819): 1707–1709
Kukulka T, Hara T. 2008a. The effect of breaking waves on a coupled model of wind and ocean surface waves: Part I. Mature seas. J Phys Oceanogr, 38(10): 2145–2163
Kukulka T, Hara T. 2008b. The effect of breaking waves on a coupled model of wind and ocean surface waves: Part II. Growing seas. J Phys Oceanogr, 38(10): 2164–2184
Large W G, Pond S. 1981. Open ocean momentum flux measurements in moderate to strong winds. J Phys Oceanogr, 11(3): 324–336
Large W G, Pond S. 1982. Sensible and latent heat flux measurements over the ocean. J Phys Oceanogr, 12(5): 464–482
Li Shuang, Li Ming, Gerbi G P, et al. 2013. Roles of breaking waves and Langmuir circulation in the surface boundary layer of a coastal ocean. J Geophys Res, 118(10): 5173–5187
Li Funing, Song Jinbao, He Hailun, et al. 2016. Assessment of surface drag coefficient parametrizations based on observations and simulations using the weather research and forecasting model. Atmos Oceanic Sci Lett, 9(4): 327–336
Liu Bin, Guan Changlong, Xie Li'an, et al. 2012. An investigation of the effects of wave state and sea spray on an idealized typhoon using an air-sea coupled modeling system. Adv Atmos Sci, 29(2): 391–406
Liu Bin, Liu Huiqing, Xie Lian, et al. 2011. A coupled atmosphere-wave-ocean modeling system: simulation of the intensity of an idealized tropical cyclone. Mon Weather Rev, 139(1): 132–152
Montoya R D, Arias O A, Royero O J C, et al. 2013. A wave parameters and directional spectrum analysis for extreme winds. Ocean Eng, 67: 100–118
Moon I J, Ginis I, Hara T. 2004. Effect of surface waves on Charnock coefficient under tropical cyclones. Geophys Res Lett, 31(20): L20302
Oost W A, Komen G J, Jacobs C M J, et al. 2002. New evidence for a relation between wind stress and wave age from measurements during ASGAMAGE. Bound-Layer Meteor, 103(3): 409–438
Pedreros R, Dardier G, Dupuis H, et al. 2003. Momentum and heat fluxes via the eddy correlation method on the R/V *L'Atalante* and an ASIS buoy. J Geophys Res, 108(C11): 3339
Potter H, Graber H C, Williams N J, et al. 2015. In situ measurements of momentum fluxes in typhoons. J Atmos Sci, 72(1): 104–118
Powell M D, Vickery P J, Reinhold T A. 2003. Reduced drag coefficient for high wind speeds in tropical cyclones. Nature, 422(6929): 279–283
Price J F. 1981. Upper ocean response to a hurricane. J Phys Oceanogr, 11(2): 153–175
Rastigejev Y, Suslov S A. 2014. E-ε model of spray-laden near-sea atmospheric layer in high wind conditions. J Phys Oceanogr, 44(2): 742–763
Rastigejev Y, Suslov S A, Lin Y L. 2011. Effect of ocean spray on vertical momentum transport under high-wind conditions. Bound-Layer Meteor, 141(1): 1–20
Smith S D. 1988. Coefficients for sea surface wind stress, heat flux, and wind profiles as a function of wind speed and temperature. J Geophys Res, 93(C12): 15467–15472
Song Jinbao, Fan Wei, Li Shuang, et al. 2015. Impact of surface waves on the steady near-surface wind profiles over the ocean. Bound-Layer Meteor, 155(1): 111–127
Taylor P K, Yelland M A. 2001. The dependence of sea surface roughness on the height and steepness of the waves. J Phys Oceanogr, 31(2): 572–590
Walsh K J E, Sandery P, Brassington G B, et al. 2010. Constraints on drag and exchange coefficients at extreme wind speeds. J Geophys Res, 115(C9): C09007
Wang Juanjuan, Song Jinbao, Huang Yansong, et al. 2013. Application of the Hilbert-Huang Transform to the estimation of air-sea turbulent fluxes. Bound-Layer Meteor, 147(3): 553–568
Wu Lichuan, Rutgersson A, Sahlée E, et al. 2015. The impact of waves and sea spray on modelling storm track and development. Tellus A, 67(1): 27967
Xu Yao, He Hailun, Song Jinbao, et al. 2017. Observations and modeling of typhoon waves in the South China Sea. J Phys Oceanogr, 47(6): 1307–1324
Xu Fumin, Perrie W, Toulany B, et al. 2007. Wind-generated waves in hurricane Juan. Ocean Modell, 16(3–4): 188–205
Zhang J A, Black P G, French J R, et al. 2008. First direct measurements of enthalpy flux in the hurricane boundary layer: The CBLAST results. Geophys Res Lett, 35(14): L14813
Zhang Ting, Song Jinbao. 2018. Effects of sea-surface waves and ocean spray on air-sea momentum fluxes. Adv Atmos Sci, 35(4): 469–478, doi: 10.1007/s00376-017-7101-7
Zhang Ting, Song Jinbao, Li Shuang, et al. 2016. The effects of wind-driven waves and ocean spray on the drag coefficient and near-surface wind profiles over the ocean. Acta Oceanol Sin, 35(11): 79–85
Zhao Dongliang, Toba Y, Suzuki Y, et al. 2003. Effect of wind waves on air-sea gas exchange: Proposal of an overall CO_2 transfer velocity formula as a function of breaking-wave parameter. Tellus B, 55(2): 478–487
Zhao Dongliang, Xie Lian. 2010. A practical bi-parameter formula of gas transfer velocity depending on wave states. J Oceanogr, 66(5): 663–671

Acta Oceanol. Sin., 2018, Vol. 37, No. 5, P. 8–12
DOI: 10.1007/s13131-018-1219-z
http://www.hyxb.org.cn
E-mail: hyxbe@263.net

A nowcasting model for the prediction of typhoon tracks based on a long short term memory neural network

GAO Song[1, 2], ZHAO Peng[1, 2], PAN Bin[3], LI Yaru[1, 2*], ZHOU Min[3], XU Jiangling[1, 2], ZHONG Shan[1, 2], SHI Zhenwei[3]

[1] North China Sea Marine Forecasting Center of State Oceanic Administration, State Oceanic Administration, Qingdao 266061, China

[2] Shandong Provincial Key Laboratory of Marine Ecological Environment and Disaster Prevention and Mitigation, Qingdao 266061, China

[3] Image Processing Center, School of Astronautics, Beihang University, Beijing 100191, China

Received 16 July 2016; accepted 16 August 2017

Abstract

It is of vital importance to reduce injuries and economic losses by accurate forecasts of typhoon tracks. A huge amount of typhoon observations have been accumulated by the meteorological department, however, they are yet to be adequately utilized. It is an effective method to employ machine learning to perform forecasts. A long short term memory (LSTM) neural network is trained based on the typhoon observations during 1949–2011 in China's Mainland, combined with big data and data mining technologies, and a forecast model based on machine learning for the prediction of typhoon tracks is developed. The results show that the employed algorithm produces desirable 6–24 h nowcasting of typhoon tracks with an improved precision.

Key words: typhoon tracks, machine learning, LSTM, big data

Citation: Gao Song, Zhao Peng, Pan Bin, Li Yaru, Zhou Min, Xu Jiangling, Zhong Shan, Shi Zhenwei. 2018. A nowcasting model for the prediction of typhoon tracks based on a long short term memory neural network. Acta Oceanologica Sinica, 37(5): 8–12, doi: 10.1007/s13131-018-1219-z

1 Introduction

Typhoons are typical tropical weather systems, which impose severe threats to people's lives, property security and the development of the regional economics in the coastal areas. Timely prediction and warnings of a typhoon can provide effective information support to disaster prevention departments, and reduce injuries and economic losses effectively. Therefore, it is an important research topic to accurately predict typhoon tracks. However, typhoon tracks are influenced by the typhoon background fields, the thermodynamics and kinetics of the typhoon system, etc. (Huang and Jin, 2013). In addition, after the landing of a typhoon, its tracks are influenced by the complex bathymetry and coastline of the coastal region and the topography of the inland, etc. (Yu et al., 2012). It is thus a rather complex and integrated challenge to resolve the typhoon tracks.

The existing forecasting operations mainly rely on the subjective empirical forecasts in the early stage. Chen and Ding (1979) summarized the track types of the typhoon happened in the Northwest Pacific, which provided an empirical reference to the prediction of typhoon tracks. With the development of monitoring methods and computer technology, numerical forecasts of typhoon tracks have been widely developed in recent years. Currently, the forecasting of typhoon tracks has formed a comprehensive system utilizing a wide range of data and methods, which is based on numerical forecasting and combined with human machine interface (Qian et al., 2012). Wang et al. (1996) proposed a scheme for the initial field for the numerical forecasting of typhoon based on artificial data and observations, and applied it to the forecast of typhoon tracks in the South China Sea. Qian et al. (2012) discussed the influence of different initial field and lateral boundary conditions on the accuracy of typhoon numerical forecasts. Li and Chen (2002) reviewed the operating application of the ensemble numerical forecast system in China. Xu et al. (2014) proposed a typhoon forecasting strategy based on GRAPES with an improved convective parameterization. However, although numerical forecasts have been widely applied, the accuracy is still lower than that of empirical forecasting methods (Chen et al., 2015). According to the published data by Shanghai Typhoon Institute of China Meteorological Administration, the current forecasting status of 24 h, 48 h and 72 h typhoon track errors based on subjective empirical methods are 84.2 km, 145.6 km and 205.4 km, respectively, and those based on regional numerical models are 97.4 km, 188.2 km and 302.7 km, respectively (Xu et al., 2010). It is still challenging to further improve the accuracy of the numerical forecasting models.

Currently, a three-dimensional typhoon observation system has been established preliminarily, including meteorological satellites, oceanic observation stations, and ground observation

Foundation item: The National Natural Science Foundation of China under contract Nos 61273245 and 41306028; the Beijing Natural Science Foundation under contract No. 4152031; the National Special Research Fund for Non-Profit Marine Sector under contract Nos 201405022-3 and 2013418026-4; the Ocean Science and Technology Program of North China Sea Branch of State Oceanic Administration under contract No. 2017A01; the Operational Marine Forecasting Program of State Oceanic Administration.
*Corresponding author, E-mail: liyaru@bhfj.gov.cn

posts, which provides numerous data to operating departments and research institutes (Hochreiter and Schmidhuber, 1997). In addition, an enormous number of typhoon observations have been accumulated by typhoon forecasting institutes since 1949. In the era of big data, it is an urgent task to improve the numerical forecasting accuracy by utilizing these data. With the development of machine learning algorithms, especially recurrent neural networks (RNNs), long and short term memory neural networks (LSTM), etc., new ways to solve prediction and regression issues have become available. Inspired by the outstanding performance of LSTM models in image recognition and visual descriptions (Xu et al., 2015), a forecasting model for typhoon tracks is developed based on a deep learning algorithm in this paper, with a large number of observation samples to train the model.

The essence of deep learning algorithms is using a large number of samples to train an end-to-end network and then performing forecasts using test data by this trained network. As there are many parameters involved in the network, sufficient training data are needed to train the model. Research shows that deep learning algorithms can improve the accuracy remarkably with sufficient samples to train the network. A reasonable employment of a deep neural network to deal with the large number of big data can improve the forecast precision of typhoon tracks. RNNs are one of the most widely used regression prediction neural network algorithms. However, the gradient in RNN may disappear, i.e., errors cannot propagate backward to a far-away previous neuron (Donahue et al., 2015). The LSTM is a classic solution to this issue. In LSTM model, the normal neurons containing activation functions are replaced by a memory cell to resolve the disappearance of the gradient. Meanwhile, values of information can be stored in the network within any length of time due to this scheme. Ranzato et al. (2014) proposed a video interpretation algorithm based on the LSTM. Sutskever et al. (2014) employed the LSTM algorithm to predict a time series, and obtained reasonable results. Studies show that deep learning algorithms, especially LSTM, can be employed in weather forecasting and ocean remote sensing areas. Yin et al. (2015) predicted the atmosphere pollution levels using a deep belief network. You et al. (2016) adopted a traditional error back-propagation neural network based on phase space reconstruction to predict storm surges. Shi et al. (2015) proposed a prediction model for precipitation based on a convolutional LSTM algorithm. The aforementioned studies indicate that deep learning algorithms are effective tools to establish models and perform predictions using big data.

A prediction model for typhoon tracks is proposed in this paper based on a deep learning algorithm. The observations of typhoon tracks from 1949 to 2012 provided by the North China Sea Marine Forecasting Center of State Oceanic Administration of China are used to train the LSTM neural network. Six to twenty-four hours typhoon tracks are predicted and compared to observations. The contributions of this paper are threefold.

(1) The typhoon observations during 1949 and 2012 are analyzed comprehensively and a typhoon data set is established.

(2) A deep learning model based on the LSTM is established to predict typhoon tracks using typhoon big data. The applicability of the deep learning algorithm to typhoon tracks prediction is validated.

(3) Six to twenty-four hours typhoon tracks are predicted to provide information support to relevant personnel.

2 Prediction model for typhoon tracks based on LSTM algorithm

The LSTM algorithm is developed based on the RNNs. The recurrent and error back propagation processes are retained in LSTM, with long and short-term memory cells used to replace the hidden neurons in a traditional RNN. An introduction of the RNN is presented firstly in this section, which leads to the introduction to the LSTM algorithm for clarity. Then the LSTM algorithm is applied to establish a prediction model of typhoon tracks.

2.1 *A brief introduction to RNN*

Traditional feedforward neural networks (FNNs) have promising performance in many fields. However, their performance is poor in dealing with time series such as videos. This is mainly due to the following two aspects. First, the input format of an FNN is a vector of a fixed length. Second, samples in an FNN are assumed to be independent, i.e., they are not related to either temporally or spatially. RNNs have fixed this problem and achieved satisfying performance in speech recognition, machine translation, image interpretation, etc., because an RNN can process each element in the input series one by one, and pass the filtered information in a series in the neural network to retain the correlation among elements in a series.

Compared with an FNN, an RNN allows a series format for the input and output, and breaks the limit to only allow data propagate to a forward level one by one. The input and output of an FNN are normally a vector of a fixed length, while those of an RNN can be a time series like $(\boldsymbol{x}^1, \boldsymbol{x}^2, ..., \boldsymbol{x}^t)$ and $(\boldsymbol{y}^1, \boldsymbol{y}^2, ..., \boldsymbol{y}^t)$, the length of which can be finite or infinite, where $\boldsymbol{x}$ and $\boldsymbol{y}$ are vectors, and the superscripts are index number which can be taken as time for a time series. Every sample in an RNN is a couple of an input series and an output series.

The output of a hidden neuron only can be directed to neurons on the next layer in an FNN, while in an RNN, that can be passed on to neurons on the same layer and also itself, therefore, information can be passed without a "time" limit. As shown in Fig. 1, the solid lines denote the information flow in an RNN, and

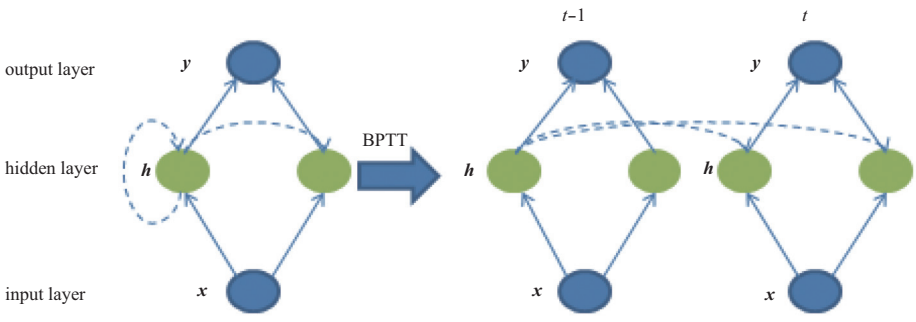

Fig. 1. Unfolding an RNN by the BPTT.

the dashed lines represent the information flow without a "time" limit. With this scheme, it is hard to train an RNN using error back propagation (BP), and thus the back propagation through time (BPTT) method is used to unfold the network by time. The left column in Fig. 1 is an illustration of an RNN and the right column is its unfolded structure by the BPTT. The hidden neurons at time step t can get information of the input at the current time step $\boldsymbol{x}^t$, as well as the information of the hidden layer at the previous time step $\boldsymbol{h}^{t-1}$, i.e., $\boldsymbol{h}^t = \sigma(W_{\boldsymbol{hx}}\boldsymbol{x}^t + W_{\boldsymbol{hh}}\boldsymbol{h}^{t-1} + b_{\boldsymbol{h}})$. Unfolding an RNN by time makes it much easier to train the network as the temporally overlapped parts in an RNN is unfolded as a traditional FNN, which makes the RNN method widely applied.

2.2 *LSTM models*

Although time is introduced in an RNN, and the output of a current time step can be passed to the next time step, the information will be lost unless the value at the next time step is the same as the current one, i.e., the information in a series can only impact the neighboring elements, not any farther. Therefore, the impact is very short in time, the information cannot be stored in the network for a longer time during training, and disappearance or explosion of gradient can happen during error back propagation. Therefore, long and short term memory cells are introduced to store information for any time length to mitigate the disappearance or explosion of gradient remarkably, which is a temporally recurrent neural network called long-short term memory (LSTM).

A special cell structure is used to replace the original hidden neurons in the LSTM. An illustration of the LSTM is shown in Fig. 2, where σ represents the sigmoid function, $\prod$ represents multiplication, the subscript c means that it is a single structure, and all the solid arrows mean that the connection weight is 1. s_c is a memory cell, which is a linear element used to store information to guarantee that information can be stored for a long time to retain the correlation among elements in a sequence. g_c is the input node, which denotes the comprehensive interaction of the input at time step t and the information of previous network status. Its value can be passed on to a memory cell through the control of an input gate i_c. If W is the weight, b is the threshold, then $g_c^t = \sigma\left(W_{hx}\boldsymbol{x}^t + W_{hh}\boldsymbol{h}^{t-1} + b\right)$. i_c is the input gate, which receives the input at time step t and the network status information at previous time steps, and pass the input value of node g_c into a memory cell s_c after the control of the sigmoid function. f_c is the forget gate, which determines whether the value of s_c is stored or not: if the weight is 1, it is stored as it was, and if it is 0, it is cleared.

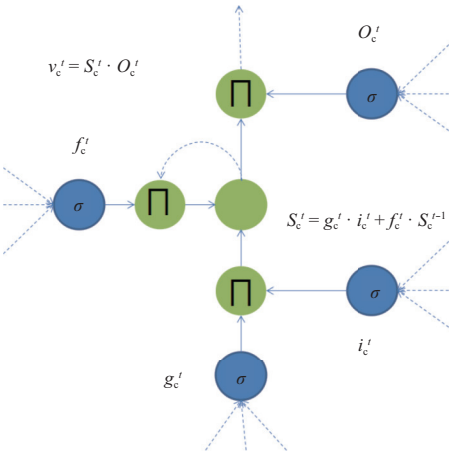

Fig. 2. A memory cell of the LSTM.

O_c is the output gate, which receives the input at the time step t and the network status information at previous time step. It controls the output of s_c after the sigmoid function. v_c is the output value.

Use $\boldsymbol{x}$ and $\boldsymbol{h}$ vectors to denote the values of each layer, then

$$
\begin{aligned}
g^t &= \tanh\left(W_{gx}\boldsymbol{x}^t + W_{gh}\boldsymbol{h}^{t-1} + b_g\right),\\
i^t &= \sigma\left(W_{ix}\boldsymbol{x}^t + W_{ih}\boldsymbol{h}^{t-1} + b_i\right),\\
f^t &= \sigma\left(W_{fx}\boldsymbol{x}^t + \mathrm{W}_{fh}\boldsymbol{h}^{t-1} + b_f\right),\\
o^t &= \sigma\left(W_{ox}\boldsymbol{x}^t + W_{oh}\boldsymbol{h}^{t-1} + b_o\right),\\
s^t &= g^t \odot i^t + s^{t-1}\cdot f^t,\\
\boldsymbol{h}^t &= \tanh(s^t) \odot o^t,
\end{aligned}
$$

where $\odot$ is dot product.

2.3 *Prediction model for typhoon tracks based on LSTM*

Considering a two-dimensional coordinate representation of the typhoon location, for a typhoon which lasts for continuous t time steps (Δt), its track can be represented by a sequence $\left(\left[x_1^1, x_2^1\right]^{\mathrm{T}}, \left[x_1^2, x_2^2\right]^{\mathrm{T}}, \ldots, \left[x_1^t, x_2^t\right]^{\mathrm{T}}\right)$, where $\left[x_1^1, x_2^1\right]^{\mathrm{T}}$ is the coordinates of a two-dimensional vector, the subscript of x_1^1 represents its dimension, the superscript of x_1^1 represents its index in the series, and each two neighboring elements have a time difference of Δt. Considering that when performing predictions of the typhoon position after $m{\cdot}\Delta t$, the typhoon positions at the previous n time steps are necessary to show the typhoon track and subsequently obtain a more accurate prediction, the input series of the LSTM should be $\left[x_1^1, x_2^1, x_1^2, x_2^2, \ldots, x_1^n, x_2^n\right]^{\mathrm{T}}$, $\left[x_1^2, x_2^2, x_1^3, x_2^3, x_1^{n+1}, x_2^{n+1}\right]^{\mathrm{T}}, \ldots, \left[x_1^{t-n-m+1}, x_2^{t-n-m+1}, x_1^{t-n-m+2}, x_2^{t-n-m+2}, \ldots, x_2^{t-m}, x_2^{t-m}\right]^{\mathrm{T}}$ and the corresponding output sequence is $\left[x_1^{n+m}, x_2^{n+m}\right]^{\mathrm{T}}, \left[x_1^{n+m+1}, x_2^{n+m+1}\right]^{\mathrm{T}}, \ldots, \left[x_1^t, x_2^t\right]^{\mathrm{T}}$. One input sequence and the corresponding output series form a sample.

An LSTM neural network for the prediction of typhoon tracks is designed in this way with three layers, i.e., an input layer, a hidden layer, and an output layer. There are $2n$ neurons on the input layer, i.e., the dimension of each element in the input sequence is $2n$. The hidden layer consists of 20 long-short term memory cells. There are 2 neurons on the output layer, i.e., the dimension of each element in the output series is 2.

When training the network, all the network parameters are initialized as random numbers between 0 and 1, and then optimized using the training samples. For each training sample, each element in the series is read one by one by the LSTM neural network. An output vector is derived after the hidden layer and the output layer, which is then compared with labels and the errors are back propagated backward by the BPTT algorithm. The test process follows the same way as the training process.

3 Experiments

Two experiments were designed in this section. The first one was used to verify the feasibility of a typhoon-track-prediction LSTM network. In the second experiment, training data sets with different amount of samples were used to train the LSTM network, so as to discuss the effectiveness of big data. All the experimental data in this section were from CMA-STI optimal tracks data set of tropical cyclones, which recorded the tracks of the tropical cyclones happened in the Northwest Pacific during 1949

and 2011, where the typhoon tracks were recorded using longitude-latitude coordinates with an average precision of 0.1° at every 6 h. The test results were measured by the mean distance errors.

3.1 *Feasibility experiment*

To prove the feasibility of the LSTM neural network to predict typhoon tracks, typhoon positions in 6 h, 12 h, 18 h, 24 h, 48 h, and 72 h were predicted in this experiment, and six data set couples were generated with training set to test set ratio being 8:1. Test results are shown in Fig. 3. The results demonstrate that with the prediction time goes on, the prediction error increases. The prediction results are compared with subjective empirical methods and regional numerical modeling in Table 1. The LSTM network obtained relatively accurate results in 6, 12, and 18 prediction. The prediction error of the LSTM network is comparable to those of the subjective empirical methods and the regional numerical modeling for 24 h predictions, while it soars and becomes much higher than the latter two for 48 h and 72 h predictions. Therefore, it is only meaningful to perform predictions within 24 h using the LSTM network, which also contributes a new method for the prediction of typhoon tracks.

3.2 *Experiment with data sets of various samples*

To examine whether the prediction accuracy can be improved with a larger training dataset, 6 h, 12 h, 18 h, and 24 h predictions were performed with the same dataset correspondingly, yet with the number ratio of samples in the training data set to test the data set being 2:1, 3:1, 4:1, 5:1, 6:1, 7:1 and 8:1, respectively. The experiment results are shown in Fig. 4 and Table 2. It can be seen that the prediction error decreases with a larger training data set, i.e., the prediction accuracy of a LSTM neural network will increase with a larger amount of typhoon tracks observations.

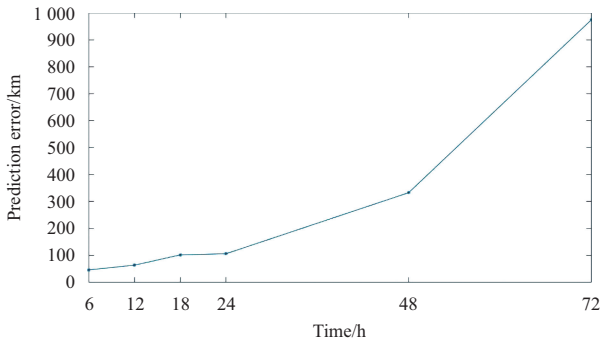

Fig. 3. Prediction errors of the LSTM neural network with time.

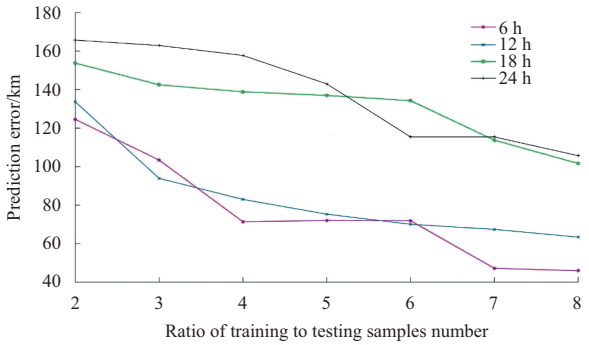

Fig. 4. Results of the experiment with various number of samples in the training data set.

4 Conclusions

A prediction method for typhoon tracks based on a LSTM neural network is proposed in this paper. The CMA-STI optimal tracks data set of tropical cyclones are used for training and testing. The results show that the 24 h prediction errors are reasonable and comparable to those of the traditional subjective empirical method and the regional numerical modeling. Therefore, it provides a new and feasible method for the prediction of typhoon tracks. It also indicates that the typhoon tracks prediction error of the LSTM neural network can be reduced by using a larger training data set. Therefore, with increasingly larger amount of typhoon observations, the prediction accuracy of the LSTM neural network will increase.

In this paper, only the typhoon tracks observations are used as the input for the prediction. More information can be included in future studies, such as the central pressure, topo-

Table 1. Prediction errors (km) of different methods

Prediction time/h	LSTM	Subjective empirical methods	Regional numerical modeling
6	45.954 0	–	–
12	63.367 0	–	–
18	101.624 3	–	–
24	105.676 8	84.2	97.4
48	332.540 7	145.6	188.2
72	974.498 5	205.4	302.7

Table 2. Results of the experiment with various number of samples in the training data set

Ratio of sample numbers in the training data set to the test data set	6 h errors/km	12 h errors/km	18 h errors/km	24 h errors/km
2	124.538 2	133.687 2	153.748 2	165.683 2
3	103.423 8	93.895 5	142.489 5	162.895 3
4	71.380 6	82.986 8	138.851 0	157.741 7
5	72.032 1	75.312 8	136.997 9	142.976 1
6	71.918 1	70.068 3	134.244 2	136.910 6
7	47.212 4	67.421 5	113.758 2	115.425 5
8	45.954 0	63.367 0	101.624 3	105.676 8

graphy, etc., to improve the structure and accuracy of the model.

References

Chen Guomin, Cao Qing, Bai Lina. 2015. Verification on forecasts of tropical cyclones over western north Pacific in 2014. Meteorological Monthly (in Chinese), 41(12): 1554–1561

Donahue J, Anne Hendricks L, Guadarrama S, et al. 2015. Long-term recurrent convolutional networks for visual recognition and description. In: Proceedings of the IEEE Conference on Computer Vision and Pattern Recognition. Boston, MA: IEEE, 2625–2634, doi: 10.1109/CVPR.2015.7298878

Hochreiter S, Schmidhuber J. 1997. Long short-term memory. Neural Computation, 9(8): 1735–1780

Huang Xiaoyan, Jin Long. 2013. An artificial intelligence prediction model for typhoon tracks based on principal component analysis. Chinese Journal of Atmospheric Sciences (in Chinese), 37(5): 1154–1164

Li Zechun, Chen Dehui. 2002. The development and application of the operational ensemble prediction system at national meteorological center. Journal of Applied Meteorological Science (in Chinese), 13(1): 1–15

Qian Chuanhai, Duan Rihong, Ma Suhong, et al. 2012. The current status and future development of China operational typhoon forecasting and its key technologies. Advances in Meteorological Science and Technology (in Chinese), 2(5): 36–43

Ranzato M A, Szlam A, Bruna J, et al. 2014. Video (language) modeling: a baseline for generative models of natural videos. Eprint Arxiv

Shi Xingjian, Chen Z, Wang H, et al. 2015. Convolutional LSTM network: a machine learning approach for precipitation nowcasting. In: Proceedings of the 28th International Conference on Neural Information Processing Systems. Cambridge: MIT Press, 802–810

Sutskever I, Vinyals O, Le Q V. 2014. Sequence to sequence learning with neural networks. In: Proceedings of the 27th International Conference on Neural Information Processing Systems. Montreal, Canada: MIT Press, 3104–3112

Wang Kangling, He Anguo, Xue Jishan. 1996. Preliminary test of typhoon trace numerical prediction for the South China Sea area. Journal of Tropical Meteorology (in Chinese), 12(2): 113–121

Xu Daosheng, Chen Zitong, Dai Guangfeng, et al. 2014. The influence of an improved cumulus parameterization scheme on typhoon forecast from GRAPES model. Journal of Tropical Meteorology (in Chinese), 30(2): 210–218

Xu K, Ba J, Kiros R, et al. 2015. Show, attend and tell: neural image caption generation with visual attention. Computer Science, 2048–2057

Xu Yinglong, Zhang Ling, Gao Shuanzhu. 2010. The advances and discussions on China operational typhoon forecasting. Meteorological Monthly (in Chinese), 36(7): 43–49

Yin Wenjun, Zhang Dawei, Yan Jinghai, et al. 2015. Deep learning based air pollutant forecasting with big data. Chinese Journal of Environmental Management (in Chinese), 7(6): 46–52

You Cheng, Yu Fujiang, Yuan Ye. 2016. Storm surge prediction method of neural network based on phase space reconstruction. Marine Forecasts (in Chinese), 33(1): 59–64

Yu Jinhua, Tang Jiaxiang, Dai Yuhan, et al. 2012. Analyses in errors and their causes of Chinese typhoon track operational forecasts. Meteorological Monthly (in Chinese), 38(6): 695–700

Acta Oceanol. Sin., 2018, Vol. 37, No. 5, P. 13–21
DOI: 10.1007/s13131-018-1210-8
http://www.hyxb.org.cn
E-mail: hyxbe@263.net

The relationships among aerosol optical depth, ice, phytoplankton and dimethylsulfide and the implication for future climate in the Greenland Sea

QU Bo[1]*, GABRIC Albert J.[2], ZHAO Li[1], SUN Wenjing[3], LI Hehe[4], GU Peijuan[5], JIANG Limei[6], ZENG Meifang[7]

[1] School of Science, Nantong University, Nantong 226019, China
[2] School of Environment, Griffith University, Nathan, Qld 4111, Australia
[3] Jurong Country Garden School, Zhenjiang 212400, China
[4] Chinese Sinosoft Company Limited, Beijing 100190, China
[5] Nanjing Kangni New Energy Auto Part Co., Ltd, Nanjing 210000, China
[6] College of Basic Education, Nantong Institute of Technology, Nantong 226002, China
[7] Primary School Department, Kunshan International School, Kunshan 215300, China

Received 19 September 2017; accepted 28 December 2018

Abstract

The sea-to-air flux of dimethylsulphide (DMS) is one of the major sources of marine biogenic aerosol, and can have an important radiative impact on climate, especially in the Arctic Ocean. Satellite-derived aerosol optical depth (AOD) is used as a proxy for aerosol burden which is dominated by biogenic aerosol during summer and autumn. The spring sea ice melt period is a strong source of aerosol precursors in the Arctic. However, high aerosol levels in early spring are likely related to advection of continental pollution from the south (Arctic haze). Higher AOD was generally registered in the southern part of the study region. Sea ice concentration (SIC) and AOD were positively correlated, while cloud cover (CLD) and AOD were negative correlation. The seasonal peaks of SIC and CLD were both one month ahead of the peak in AOD. There is a strong positive correlation between AOD and SIC. Melting ice is positively correlated with chlorophyll *a* (CHL) almost through March to September, but negatively correlated with AOD in spring and early summer. Elevated spring and early summer AOD most likely were influenced by combination of melting ice and higher spring wind in the region. The peak of DMS flux occurred in spring due to the elevated spring wind and more melting ice. DMS concentration and AOD were positively correlated with melting ice from March to May. Elevated AOD in early autumn was likely related to the emission of biogenic aerosols associated with phytoplankton synthesis of DMS. The DMS flux would increase more than triple by 2100 in the Greenland Sea. The significant increase of biogenic aerosols could offset the warming in the Greenland Sea.

Key words: dimethylsulfide flux, sea ice, chlorophyll, aerosol optical depth, Greenland Sea

Citation: Qu Bo, Gabric Albert J., Zhao Li, Sun Wenjing, Li Hehe, Gu Peijuan, Jiang Limei, Zeng Meifang. 2018. The relationships among aerosol optical depth, ice, phytoplankton and dimethylsulfide and the implication for future climate in the Greenland Sea. Acta Oceanologica Sinica, 37(5): 13–21, doi: 10.1007/s13131-018-1210-8

1 Introduction

Atmospheric aerosols are derived from anthropogenic and natural sources. During the Arctic spring, the local aerosol burden maybe influenced by anthropogenic, marine and continental sources (Barrie, 1995). The "Arctic haze" is due to northerly transport of pollution from anthropogenic activities, and has a warming effect on the regional climate (Zhao and Garrett, 2014). Conversely, the emission of biogenic sulfate aerosols during the biologically productive season may offset climate warming. Biogenic sulfate aerosols are produced by oxidation reactions in the atmosphere from gaseous precursors such as dimethylsulfide (DMS) emitted by the marine food web (Charlson et al., 1987). It has been suggested that the greatest perturbation to DMS flux under warming will occur at high latitudes in both hemispheres, with little change simulated in the tropics and sub-tropics (Gabric et al., 2004, 2013).

In remote marine atmospheres, aerosols consist of sea salt particles, organics and sulphate from the oxidation of biogenic DMS (Andreae, 2007). Sea salt is a major component of marine aerosol when wind speeds are high (Meskhidze and Nenes, 2010). Sea ice loss in the Arctic is an indirect source of sea salt aerosols, as the rapid decrease of sea ice cover in recent decades which leads to an increase in the area of open water, resulting in sea salt aerosol emissions increasing, in turn leading to an increase in satellite-derived aerosol optical depth (AOD) in 70°–80°N (Struthers et al., 2011). Osto et al. (2017) (www.nature.com/scientificreports) found that the majority of the ultrafine aerosols were associated with air masses travelling over open water (43%–51%) and sea ice (29%–39%). The area with melt ponds, open leads amidst the pack ice and ice floe, are all the strong

Foundation item: The National Natural Science Foundation of China under contract No. 41276097.
*Corresponding author, E-mail: qubo@ntu.edu.cn

sources of precursor gas of aerosols in summer Arctic. Ice melting is also a significant source of ammonium. Decrease of ice alters marine ecosystems by increasing the rates of phytoplankton by 20%–30%.

The non-sea salt aerosol includes sulfate, particulate organic matter, mineral dust and black carbon. DMS is the main biogenic sulfate aerosol released from the Arctic Ocean (Ferek et al., 1995). As sea ice recedes in the Arctic, phytoplankton growth occurs in open waters, and trapped DMS is released from the ice matrix as well as from blooms in the newly formed open leads. As a consequence, the peak in DMS would occur after the phytoplankton bloom (Gabric et al., 2005).

Aerosol-cloud-climate interactions are closely connected. Curry (1995) has suggested that rising temperatures would lead to a reduction in sea ice and snow extent, hence reduce the polar surface albedo, cause further climate warming. Charlson et al. (1987) suggested there are direct and indirect radiative effects of biogenic aerosols in the troposphere, with both effects possibly offsetting the effects of warming (Leck and Persson, 1996).

Cloud cover in the Arctic has different climate impacts in winter and summer. Cloud reduces surface heating during summer time, and reduces surface cooling during winter time (Curry et al., 1996). About 40% of Arctic cloud cover is made up of thin single-layer clouds with bases below 2 km (Zhao and Garrett, 2014). Arctic haze influences aerosol composition especially during winter and early spring when continental forest fires have a seasonal maxima (Quinn et al., 2007). The changes of winter cloud would alter the AOD signal. There is a negative correlation between winter time cloud fraction and AOD in the Arctic (Struthers et al., 2011). The natural aerosol includes sea salt and biogenic marine sources. In the Arctic Ocean, black carbon and mineral dust aerosols are a smaller component of total AOD. The radiative balance in the Arctic may be largely affected by the changes in surface albedo (decrease) and sea salt aerosol (increase) due to the loss of Arctic sea ice (Struthers et al., 2011). Cloudiness and cloud radiative forcing are strongly coupled to Arctic sea ice cover (Struthers et al., 2011). Clouds are major source of uncertainty in climate model predictions. Cloud cover and albedo may have strong impact on the summer ice melting. Increased cloud cover in Arctic could lead to warming and accelerated sea-ice melting (Osto et al., 2017). Increasing in sea salt particles can affect CDNC (cloud droplet number concentration), but this must be accompany by an increased surface wind speed over the bloom (Meskhidze and Nenes, 2010). Hu et al. (2011) studied the AOD around China's seas during 1980–2001 and found the increase of AOD would result in the decrease of the maximum temperature rather than minimum, with decrease of 0.11/0.08 K for zonal average.

Due to less pollution, remote polar regions are ideal places for examining the effects of marine productivity and biogenic aerosol emissions on clouds. In this work, we examine the relationship between DMS and DMS flux with sea ice concentration (SIC), the relationship among AOD with SIC, cloud cover (CLD), and surface chlorophyll *a* (CHL) in the Greenland Sea (65°–80°N), a region of importance for both the polar and global climate, and describe the key factors influencing the seasonal cycle of these parameters. Furthermore, the DMS flux would be predicted for year 2100 under 4×CO_2 scenario. The implications of future climate in the Greenland Sea would be investigated.

2 Data sources and methods

We focus on the Greenland Sea (65°–80°N, 20°W–10°E) (Fig. 1) for the period 2003–2012. The highlighted study region in Fig. 1 also includes part of the Iceland Sea and Norwegian Sea. Global data on CHL and aerosol optical depth are obtained from the MODIS (Aqua) satellite 8-day, level 3 archive, at a resolution of 4-km (http://oceandata.sci.gsfc.nasa.gov/MODIS-Aqua/Mapped/8Day/4km). SIC is obtained from the NOAA archive at iridl.ldeo.columbia.edu/SOURCES/.NOAA (Reynolds et al., 2002) with resolution of 1°×1°. Surface wind speed and direction are obtained from Remote Sensing Systems (REMSS: www.remss.com/windsat). CLD is calculated from the NASA archive available at http://gdata1.sci.gsfc.nasa.gov/daac-bin/G3/. The SeaDAS 6.4 image analysis package data analysis system is used to subset and analyze the regional AOD and CHL data (seadas.gsfc.nasa.gov/). Mixed layer depth (MLD) is calculated using

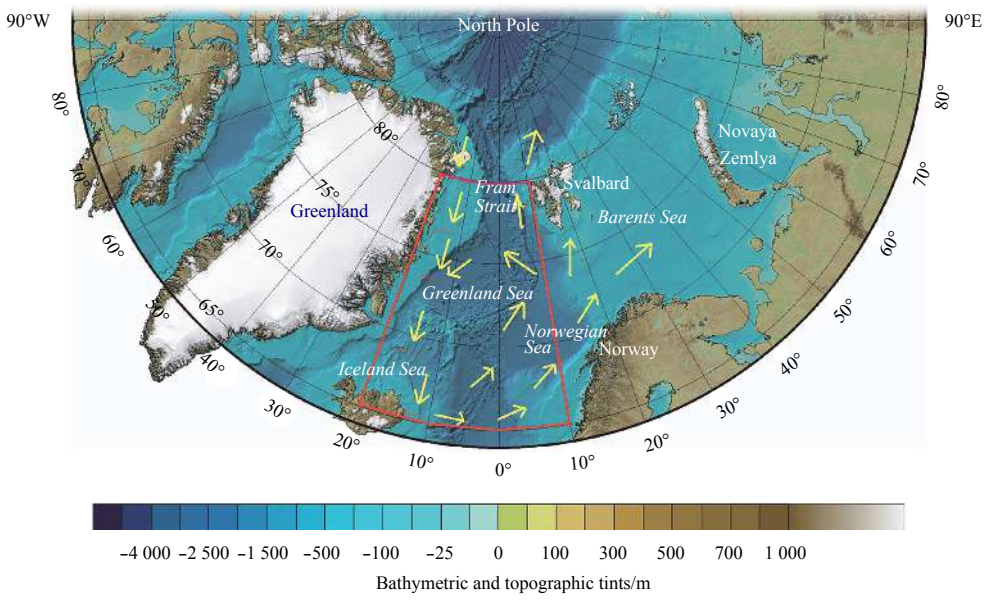

Fig. 1. Map of study region with topography. Red box denotes the study region (65°–80°N, 20°W–10°E) mainly in the Greenland Sea and yellow arrows the surface current directions.

CTD (conductivity, temperature, depth) data available from the Arctic Ocean Measurement Database (http://oregon.iarc.uaf.edu/dbaccess.html). MLD is computed based on constant temperature difference criterion (0.5°C between the surface and bottom). Missing values are replaced by using the five nearest values. Spatial-temporal gridding of MLD of 1°×1° is calculated using *R* statistical software (Qu et al., 2016b). Missing monthly data is inserted by using interpolation of adjacent month data.

The Coupled Model Intercomparison Project Phase 5 archive (CMIP5) (http://pcmdi9.llnl.gov/cmip5/forcing.html) is used to provide forcings under the warming scenarios. Software OpenLDAP (an open source implementation of the Lightweight Directory Access Protocol) is used to retrieve the forcing data in AMIP for SST, CLD, SIC, WIND (wind speed) and MLD for 4×CO_2 conditions.

Correlations and lagged regression analysis for AOD, SIC, CLD and CHL were computed using the statistical software package Eviews and SPSS.

The accuracy of satellite data (especially for the remote Arctic Ocean) would relate directly to the reliability and accuracy of this study. Surface chlorophyll concentration, aerosol optical depth and photosynthetically active radiation (PAR) were obtained from the level-3 MODIS (Aqua) (http://oceandata.sci.gsfc.nasa.gov/MODIS-Aqua/Mapped/8Day/4km) (Moderate Resolution Imaging Spectroradiometer) have unprecedented onboard calibration systems enabling monitoring of its performance and correcting for the errors introduced into the data by system degradation. NASA Goddard Space Flight Center has managed to improve the accuracy of the ocean color products (http://modis.gsfc.nasa.gov/MODIS/CAL/#intro). Spectroradiometric Calibration Assembly (SRCA) is for checking the radiometric, spectral and geometric properties of the MODIS system. Calibrations were done for regional differences between MODIS with SeaWiFS especially for the Arctic Ocean (Bailey and Werdell, 2006). At high latitudes, multiple orbits are considered for a given *in situ* record. However, errors are unavoidable for solar zenith angles more than 70° and view angles more than 45° (Bailey and Werdell, 2006). Generally, the summer time data is more accurate. It is estimated that the satellite-derived CHL underestimates the true concentration by a factor of 1.4 when compared with *in-situ* CHL data (Bailey and Werdell, 2006). The data errors in the Arctic Ocean are well within the range of errors for global data as indicated by an evaluation done for the western Arctic Ocean (Chaves et al., 2015).

The computation of the regional means is another possible source of error due to missing data mainly caused by cloud cover.

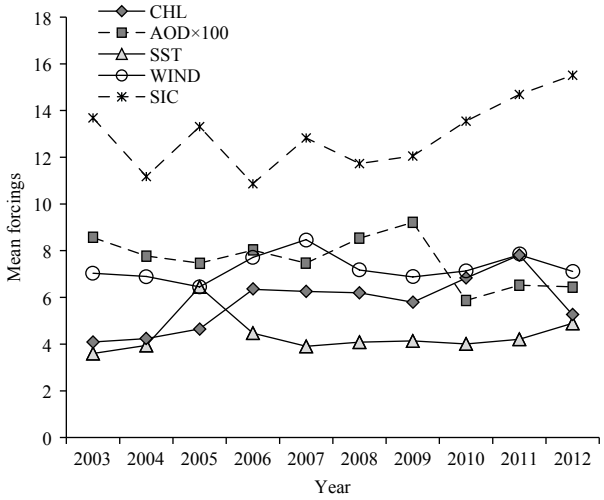

Fig. 2. Regional mean annual forcings (CHL (mg/m^3), AOD×100, SST (°C), WIND (m/s) and SIC (%)) for year 2003–2012.

The missing values occur are mostly north of 80°N. There were very few (less than 5%) missing values during May to August. The missing values were excluded for our estimates of regional means, thus calculated mean values could be slightly higher than reality.

3 Results

3.1 *Regional mean annual forcings*

Regional mean annual forcings are calculated (Fig. 2) for year 2003–2012. SIC had 27% increased rate, AOD had generally 18.8% decreased rate, but increased before year between 2007–2009, and had a big drop in year 2010. WIND had 4% increased rate, CHL had 27% increased rate and SST only 2% increased rate within these 10 years. SIC had an increased trend since year 2009. AOD had the highest peak in year 2009 and had an immediate drop in year 2010. CHL had increased trend from 2009 to 2011 and peaked in year 2011 and dropped in year 2012. Wind speed had peak year in 2007 and second peak in year 2011. SST had peak year in 2005 and decreased since year 2005, had slightly increased trend in year 2012. Generally, with the annual increased SIC, CHL also increased during the ten years,

3.2 *Regional AOD and CLD distributions*

Mean spatial distributions of AOD and CLD are shown in Fig.

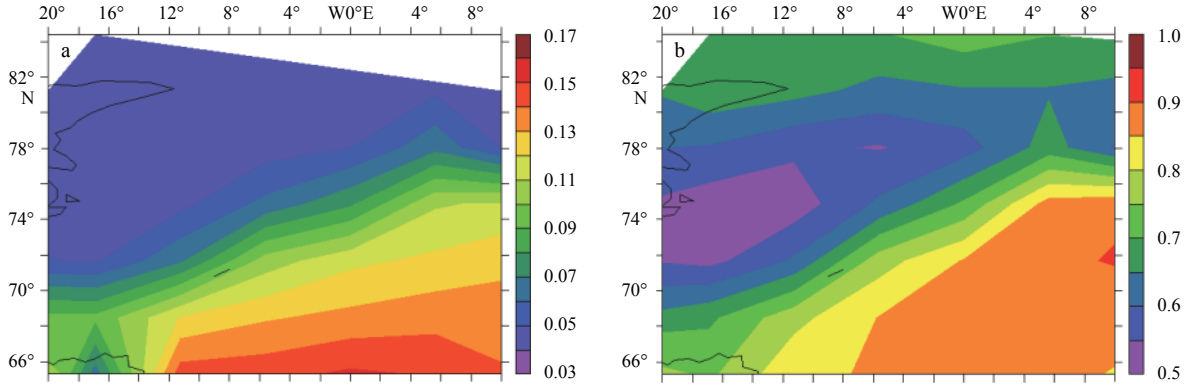

Fig. 3. Mean spatial distributions of AOD (a), and total CLD (0⩽CLD⩽1) (b) in the study region.

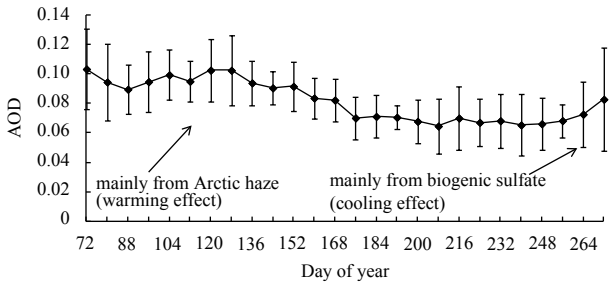

Fig. 4. Mean AOD in the study region (65°–80°N) for 2003–2012. Vertical bars are the standard deviation.

3. There is a clear meridional gradient in AOD with values higher in the south and lower in the north of the study region (Fig. 3a) and a weaker zonal gradient with higher AOD in the east, especially south of 78°N. There was higher CLD in the south (Fig. 3b).

The time series of AOD averaged over the study time period is shown in Fig. 4, with higher AOD in spring and lower in summer followed by an increase during autumn. The elevated springtime AOD is likely due to Arctic haze (Zhao and Garrett, 2014), although high wind speeds at this time could also lead to higher sea salt aerosols. Elevated autumn AOD is likely caused by biogenic aerosol emissions associated with the summer phytoplankton bloom. Arctic haze is thought to come from advection of pollution in Eurasia (Quinn et al., 2007), and is removed in summer by precipitation. The elevated spring aerosols caused by Arctic haze could lead to a warming of the climate (Spracklen et al., 2008), while emission of autumn aerosols due to the biogenic sulfate aerosols could cool the climate (Gabric et al., 2003).

The AOD for selected years is shown in Fig. 5. There is considerable interannual variability, with year 2009 having the highest summer AOD and year 2010 the lowest AOD almost throughout the year (Fig. 4). A negative correlation between AOD and CHL is reported by Qu et al. (2014) for spring and summer time. Lower AOD and higher summer CHL are observed in year 2010 (Qu et al., 2016a). High AOD during the spring of 2003 could be due to the extensive forest fires in Russia at that time (Serreze et al., 2000). Year 2008 had a longer period of higher AOD in spring and much higher AOD in September.

3.3 *Regional CHL and SIC*

Two snapshots of MODIS satellite CHL for 2010 (Day 128 in mid-April and Day 176 in late June) are shown in Figs 6a and b. Unusually high CHL was registered in the northeast of the study region in spring (red shows higher CHL values). By summer, moderate to high CHL was registered throughout the region (Fig.

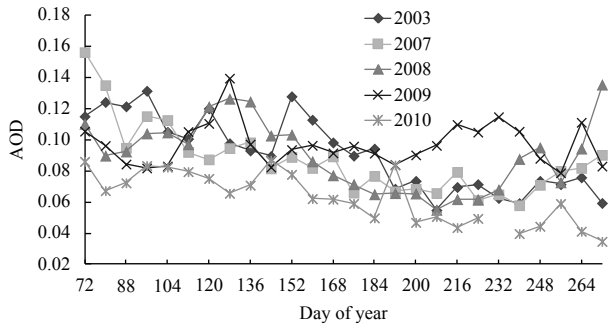

Fig. 5. Mean AOD for years 2003, 2007, 2008, 2009 and 2010 in the study region (65°–80°N, 20°W–10°E).

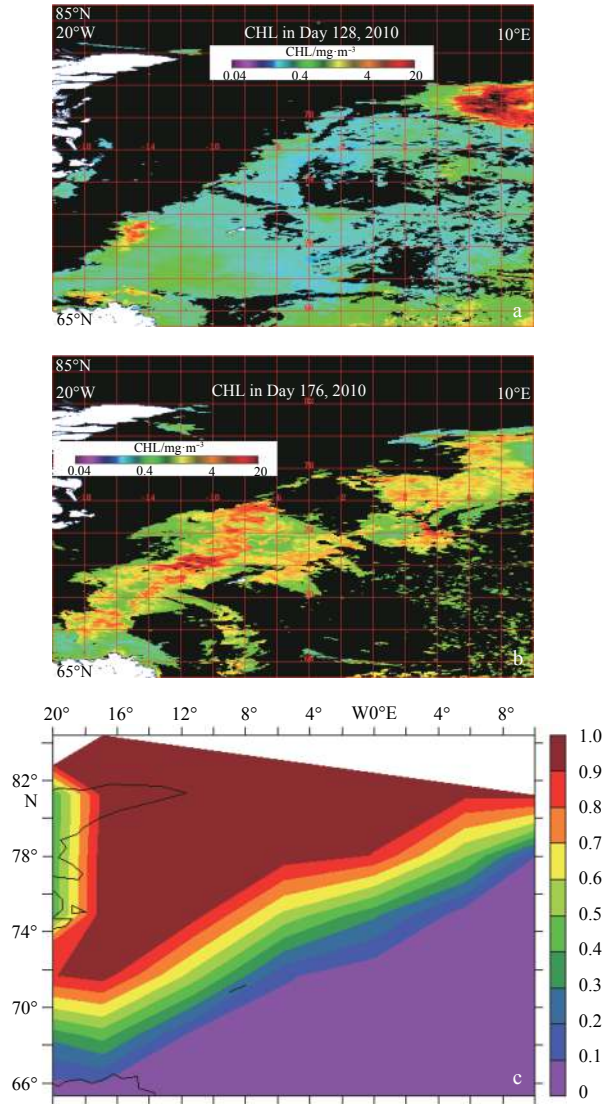

Fig. 6. CHL satellite images in Day 128 (a) and Day 176 (b) in year 2010, and annual mean SIC profile in the study region (0≤ SIC≤1) (c). Black indicates missing data due to sea ice or cloud.

6b). Mean annual SIC in the study region (Fig. 6c) displays a strong zonal gradient, likely due to the effect of the warm North Atlantic Drift in the east of the region (Fig. 1).

Figure 7a highlights the strong inter-annual variability in CHL in the sea ice covered northern part of the study region (75°–80°N). The timing of the seasonal peak in CHL varies from May to July which could be due to numerous factors, including variability in winter SIC and melt water runoff from the Greenland Glacier in eastern Greenland. Glacial melt water increases vertical stability of the water column and possibly delivers iron, a micronutrient which can favor phytoplankton growth (Levasseur, 2013). Figure 7b shows that there is a general north-south gradient in CHL with higher values in the southern part of the study region. However, elevated CHL in the north of the study region was recorded in year 2010 (Qu et al., 2016a).

Profiles of mean SIC over the selected years are shown in Figs 8a and b. The years were selected from the most variable years. Hence, the selection of years is different for south and north regions. Generally, SIC reaches a peak in March and decreases to a minimum in August to September. Both inter-annual and meri-

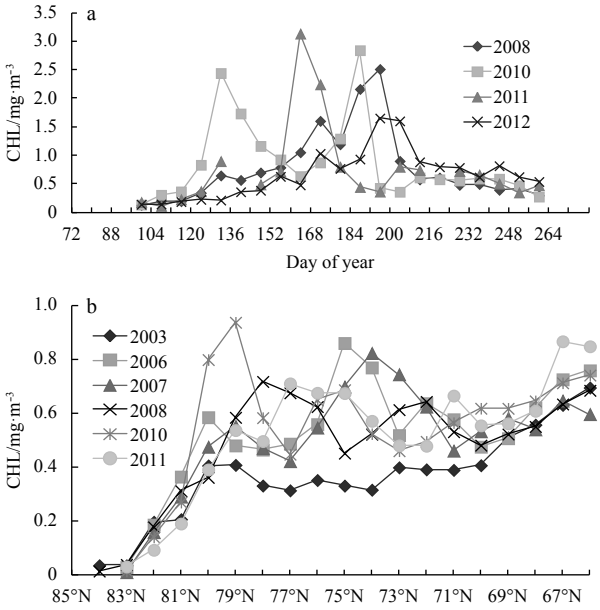

Fig. 7. Mean CHL in northern region (75°–80°N, 20°W–10°E) in years 2008, 2010, 2011 and 2012 (a); and mean CHL along latitude in years 2003, 2006, 2007, 2008, 2010 and 2011 in the study (65°–85°N, 20°W–10°E) (b).

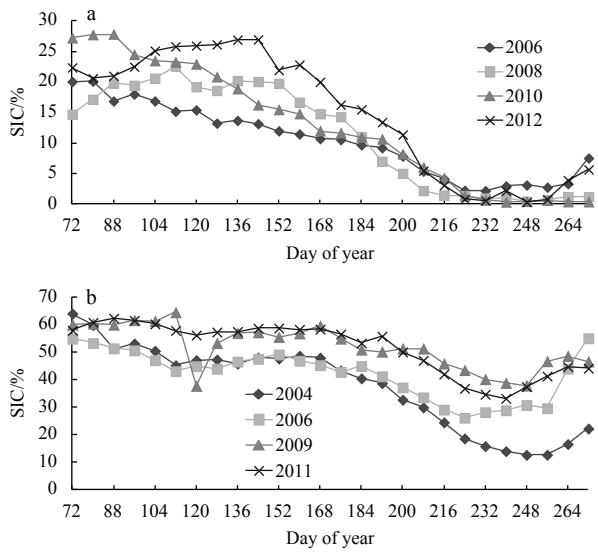

Fig. 8. Monthly mean SIC for year 2006, 2008, 2010 and 2012 in 70°–75°N (a); and monthly mean SIC for year 2004, 2006, 2009 and 2011 in 75°–80°N (b).

dional variability in SIC is evident in these figures.

3.4 *Correlation analyses*

3.4.1 *The effect of high wind speed*

We examine the possible reasons for the elevated spring and autumn AOD. Mean wind speeds and CHL are calculated for the sub-region (70°–80°N) for the ten years (2003–2012). The spring wind speed was high and above 7 m/s (Fig. 8a) with southerly direction (not shown in the figure). The high spring winds would have two effects on the aerosol: advection of pollution from continental sources (North American and East Asian sources), and

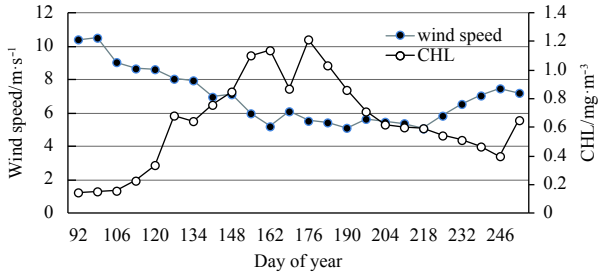

Fig. 9. Decadal mean wind speed and CHL for years 2003–2012 in 70°–80°N.

also an increase in sea salt aerosols from the ocean (Barrie, 1995). It is reported that sea salt aerosols peak mostly in the period of October to May due to stormier conditions in the Arctic Ocean and longer aerosol residence times in the Arctic. The elevated autumn wind speed (after Day 218) would have more effect on the sea salt aerosol (a cooling effect). Huang and Qiao (2009) also confirmed that the effect of wind speed over remote oceans to be significant, reporting a high linear correlation between AOD and wind speed. Figure 9 shows that wind speed is negatively correlated with phytoplankton biomass (CHL) in the spring and early summer (before Day 162). In this period, CHL increases with the decrease of wind speed. Our results show that there is inverse relationship between wind speed and CHL, with the bloom largely suppressed by high wind speed and strong vertical mixing as reported for the Southern Ocean (Fitch and Moore, 2007)

A ten-year climatology of AOD, CLD and SIC at 8-day intervals for the region 75°–80°N is shown in Fig. 10. Clear downward trends in SIC and AOD are evident during spring and summer. In general, CLD is high (around 0.8) with relatively lower CLD in April, higher CLD in summer. AOD and CLD are positively correlated in spring, but not in the autumn.

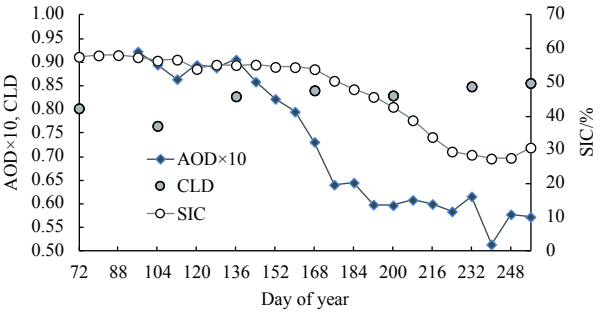

Fig. 10. Mean AOD, SIC and CLD 8-day time series in 75°–80°N for ten years.

3.4.2 *The effect of sea ice*

The rate of ice melt is calculated by computing the weekly change in SIC. Figure 11 shows the time series of ice melt, AOD and CHL for the region 75°–80°N. Ice melt started in April or May (apart from year 2007 and 2012, when melt commenced in March). The rate of ice melt dipped in May for years 2004, 2006, 2009 and 2011. In general, ice melt was positively correlated with CHL, but negatively correlated with AOD during spring and summer, and positively correlated in autumn. The region of 70°–75°N had much lower SIC and ice had little effect on CHL and AOD. The increase in AOD in late summer or autumn after the peak in CHL suggests the influence of biogenic sulfate released by phyto-

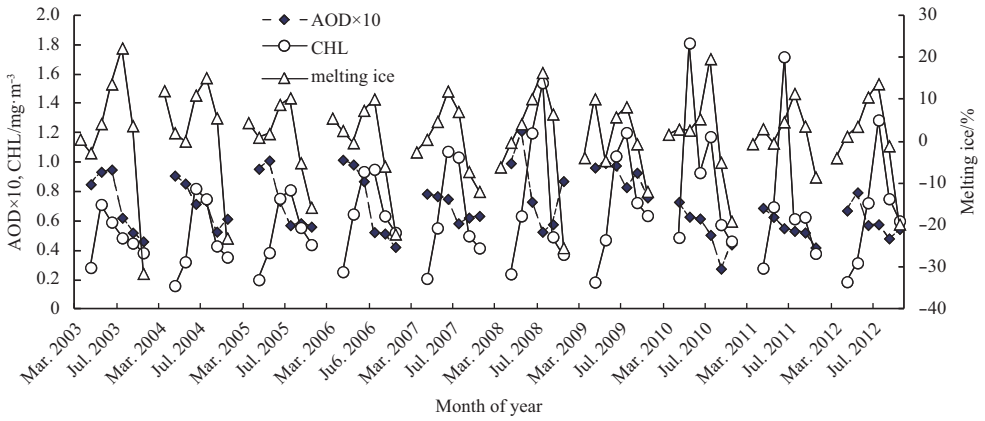

Fig. 11. Monthly mean AOD, CHL and ice melt time series in 75°–80°N.

plankton, although increased autumn wind speed, would also increase sea salt aerosols from the largely open waters.

CHL displayed an increasing trend from year 2003–2010, slightly decreasing after year 2010. The highest rate of ice melt was recorded in year 2003, with year 2010 having the second highest rate of ice melt. A second CHL bloom occurred in year 2010 at the same time as ice melt reached its maximum; AOD increased during spring and early summer in some years (2003, 2005, 2008, 2009, 2012), and then started to drop after May. Elevated AOD was influenced by combination of melting ice and higher spring wind in the region. Summer AOD decreased from June to August due to reduced wind and less ice melting together with increased sea surface temperature. After CHL bloom reached to its peak, AOD would start to increase in early autumn.

3.5 *The multivariable correlations with AOD*

When lagged, the time series of AOD and SIC display a strong correlation. However, AOD and CLD had a weaker correlation. In northern part of study region, spring AOD and SIC all had increased trends (from March to April), decreased thereafter. In the southern region, AOD reached a peak almost one month later (by May) than the southern region. AOD and SIC were negatively correlated in spring and positively correlated after spring (both decreased from May). CHL and SIC had strong negative correlations, with a reduction in SIC leading to an increase in CHL, with ice edge blooms likely contributing to the overall biomass (Levasseur, 2013).

A lagged correlation analysis was done by using the EViews software package (Pang, 2006), as shown in Table 1.

The correlation coefficients for AOD, SIC, CLD and CHL for each year are shown in Table 2. AOD and SIC, are positively correlated in most years apart from year 2009 (also see Fig. 10).

In general, the correlation between AOD and CLD, AOD and CHL were all negative, with decreased AOD accompanied by increased CLD and CHL. CHL had much improved correlations with AOD and SIC after lagging the time series (comparing Table 2 with Table 3). They are all significant. There were quite high positive correlations between AOD and CHL, CHL and SIC after shifting CHL 2 months (or more) ahead. However, the correlations between AOD and SIC, AOD and CLD showed no significant improvement after shifting AOD 1 month ahead.

We have found AOD was negatively correlated with CLD when lagged by one month (Tables 2 and 3). Here *P*-value are all less than 0.005.

The correlation coefficients between AOD and CLD were rather low. After shifting, the three most significant correlations were –0.65, –0.63, –0.93 for year 2003, 2009 and 2012 respectively. Year 2012 had very high negative correlation between CLD and AOD. The results show that AOD and CLD were less correlated compared to AOD and SIC.

3.6 *The relationship between DMS and SIC*

According to Simó's formula (Simó, 2002):

$$DMS = -\ln(MLD) + 5.7, \quad \text{when } CHL/MLD < 0.02; \tag{1a}$$

$$DMS = 55.8\,(CHL/MLD) + 0.6, \quad \text{when } CHL/MLD \geqslant 0.02. \tag{1b}$$

DMS is calculated using the satellite CHL and MLD mean time series within certain time frame and certain regions. There is ±30% uncertainty in the estimate DMS using above formula (Simó and Dachs, 2002). The double formula is not accurate for a different region in different time period influenced by different forcings. The double formula indicated the inverse relationship between DMS and MLD and positive relationship between DMS and CHL under certain conditions.

Due to the complicated MLD calculations from scattered field

Table 1. Correlation analysis for 75°–80°N for the ten years

Variables	Time lag	R^2	Std. error	*t*-statistic	*P*-value
AOD and SIC	1 month (SIC ahead)	0.39	0.000 23	6.56	0.001
AOD and CLD	1 month (CLD ahead)	0.18	0.055 67	–3.23	0.002
AOD and CHL	2 month (AOD ahead)	0.37	0.031 07	2.96	0.004
CHL and SIC	2–3 month (SIC ahead)	0.25	0.003 3	4.4	0.000 1

Note: SIC and CLD were both significantly correlated with AOD at a lag of one month, with AOD more strongly correlated with SIC. There were also significant moderate correlations between AOD and CHL for a lag of two months. The correlations between CHL and SIC were slightly different between 70°–75°N and 75°–80°N, with SIC 2 month ahead of CHL in 70°–75°N region (where CHL blooms earlier) and 3 month ahead of CHL in 75°–80°N.

Table 2. Correlations for the period of March to September

Year	AOD/SIC	AOD/CLD	AOD/CHL	CHL/SIC
2003	0.87	–0.47	–0.27	0.03
2004	0.70	0.25	–0.46	–0.21
2005	0.72	–0.57	0.04	–0.20
2006	0.84	–0.41	–0.31	–0.33
2007	0.78	–0.56	–0.37	0.11
2008	0.58	–0.29	–0.32	0.07
2009	–0.44	–0.01	0.02	–0.53
2010	0.97	–0.36	–0.01	–0.10
2011	0.68	–0.65	0.19	0.05
2012	0.76	–0.53	–0.72	–0.43

data, the time series of DMS were calculated using Eqs (1a, b) only for year 2003–2006. DMS flux then calculated together with profiles of SIC, CHL, AOD (shown in Fig. 12a). Peaks of CHL were 2 month behind SIC. The AOD had positive relationship with SIC for year 2003 and 2005 and negative relationship with SIC for year 2004 and 2006 during spring and early summer. AOD and SIC was decreased during summer period. There was slightly increase of AOD in September. DMS and CHL had similar peak time while DMS flux had its peak time 1–3 month ahead. The DMS flux peaks mostly occurred in spring rather than in summer. The reasons were due to the higher wind speed and more melting ice occurred in spring season in the region. There were increased trends from March to May and reduced trends from May to August for DMS concentration and AOD. Hence, during those two different periods, DMS and AOD were positively correlated. The melting ice accompanied by the increase of CHL and DMS. Generally, with increase of melting ice, DMS would increase accordingly. However, due to the rise of SST and solar radiation, the increasing rate of DMS would reduce or stop by May or June.

The ratio of DMS to SIC is calculated and plotted in Fig. 12b. The highest ratios for each year were different. May or June generally were the two peak months of the ratio, but year 2003 and 2004 had highest ratio towards September. The less SIC in September made the ratio higher. However, the SIC tended to be totally disappeared after year 2004. It is interesting to find that DMS/SIC ratio profile would exhibit the normal distributions after shifting SIC 2 months behind (Fig. 12c).

In Fig. 12a, DMS flux had positive correlations with SIC. They both had the same peak time for years 2005 and 2006, and year 2004 had much early SIC peak and the much later DMS flux peak (two months time lag). Peak of DMS flux was shifted ahead from June (2003) to March (2006). The peak of SIC was almost in March every year (year 2003 was slightly different). CHL and SIC had negative correlations before June and positive correlations after June.

SPSS software is used for correlation analysis for DMS and SIC. DMS and SIC had negative relationship with correlation coefficient of –0.575. The correlation is not significant.

The regression equation is as follows:

$$DMS = -0.981 + 2.003 \times SIC - 0.108 \times SIC^2 + 0.002 \times SIC^3,\ R^2 = 0.606. \quad (2)$$

In 70°–75°N and 75°–80°N two sub-region, DMS and SIC were negatively correlated with correlation coefficient around –0.5, the correlation is significant.

The three order model calculated the regression equation is

$$DMS = 10.434\text{–}0.881 \times SIC\text{–}0.028 \times SIC^2, \text{ for } 70^\circ\text{–}75^\circ\text{N}; \quad (3a)$$

$$DMS = \text{–}4.046 + 1.540 \times SIC\text{–}0.51 \times SIC^2, \text{ for } 75^\circ\text{–}80^\circ\text{N}. \quad (3b)$$

3.7 *Prediction of DMS flux in 4×CO_2*

The CMIP5 model archive is used to retrieve the forcing data for 4×CO_2 conditions. Software OpenLDAP is used to retrieve data for forcings such as SST, CLD, SIC, WIND and MLD. DMS model is used for calculating the regional DMS concentrations (Gabric et al., 1993, 1999; Qu and Gabric, 2010). A genetic algorithm is used for calibrating the key parameters in the DMS model (Qu and Gabric, 2010; Qu et al., 2016b). The satellite CHL mean time series is used for the calibration (to minimize the difference between the model output and the satellite data (CHL)). DMS observed data is also used to calibrate the parameters for DMS related parameters (Qu and Gabric, 2010; Qu et al., 2016b). The DMS model was run again using the newly calibrated parameters and the results of DMS flux for 70°–80°N are shown in Fig. 13 for 4×CO_2 with and without ice.

DMS flux is two times higher for 1×CO_2 (contemporary), and 1.5 times higher for 4×CO_2 when ice is considered. DMS flux increased more than 300% from 1×CO_2 to 4×CO_2. The increasing of melting ice could lead to an increase of CHL and the increase the DMS flux production.

The DMS flux rate under 4×CO_2 with ice considered increased much more than without ice considered. The SIC under 4×CO_2 condition was retrieved from CIMP5 (Coupled Model Intercomparison Project Phase 5). The increased autumn DMS flux is mainly due to the dramatic increase in sea-to-air transfer velocity. The more than 300% increase in DMS flux under 4×CO_2 sug-

Table 3. Lagged correlations for the period of March to September

	AOD and SIC (Shift AOD 1 month ahead)	AOD and CLD (Shift AOD 1 month ahead)	AOD and CHL (Shift CHL 2 month ahead)	CHL and SIC (Shift CHL 2 -3 month ahead)
2003	0.69	–0.65	0.71	0.63 (2 m)
2004	0.71	–0.20	0.88	0.93 (3 m)
2005	0.72	–0.84	0.71	0.99 (3 m)
2006	0.82	–0.46	0.64	0.995 (3 m)
2007	0.49	–0.37	0.52	0.56 (2 m)
2008	0.21	–0.48	0.79	0.74 (2 m)
2009	0.33	–0.63	0.37	0.85 (3 m)
2010	0.79	–0.60	0.83	0.92 (2 m)
2011	0.67	0.06	0.54	0.80 (2 m)
2012	0.67	–0.93	0.02	0.50 (2 m)

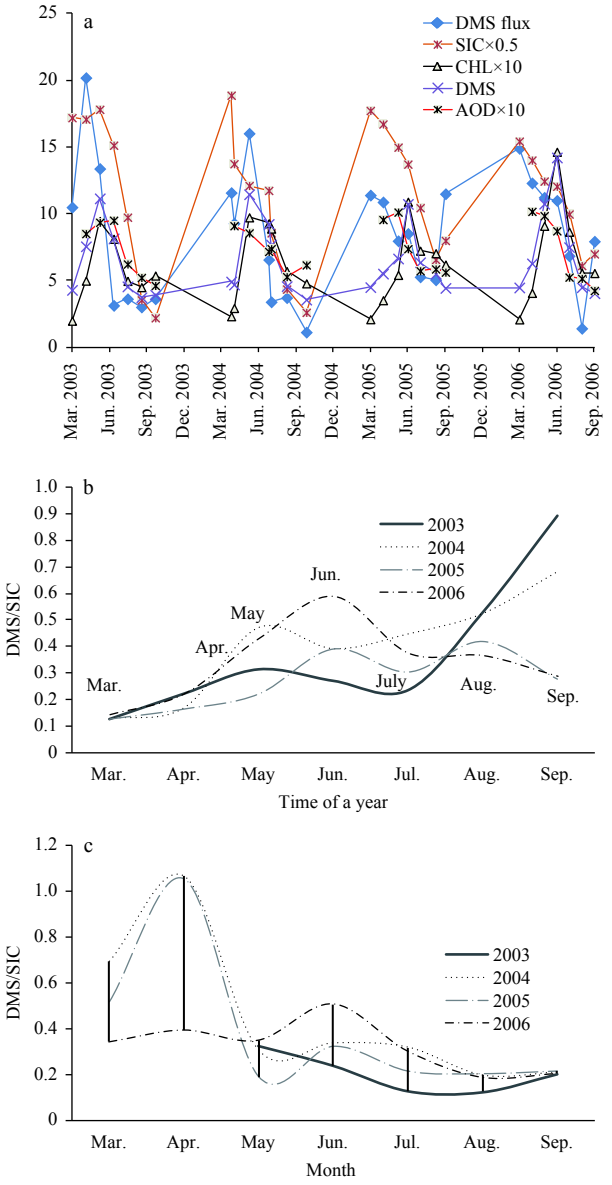

Fig. 12. Comparison among DMS flux (μmol/m^2), DMS (nmol/L), CHL (mg/m^3), SIC (%) and AOD in 70°–80°N (a); the DMS/SIC ratio plot for year 2003–2006 (b); and the DMS/SIC ratio plot after shifting SIC 2 month behind (c).

gests this would increase the indirect sulfate aerosol effect much more (Jones et al., 2001). The significant higher profile of DMS flux under ice condition suggested the melting ice is a major contributor to DMS flux from May to September. The more DMS flux released to atmosphere during summer and early autumn was the main reasons of elevated AOD in autumn.

4 Conclusions

The higher spring aerosols were mostly caused by Arctic haze and sea salt, while emission of autumn aerosols was likely due to biogenic sulfate aerosols (DMS) produced by the marine food web. Wind speed had an influence in the two different periods: spring and autumn. Sea salt aerosols increased with increasing of wind speed. Apart from the effect of Arctic haze caused by anthropogenic sources, sea salt aerosols also had an impact during the spring. It is difficult to distinguish the separate factors influ-

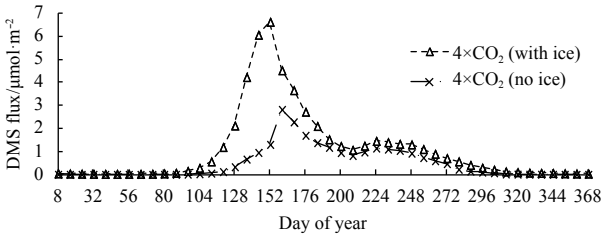

Fig. 13. Comparison of DMS flux with and without ice for 4×CO$_2$ in 70-80°N.

encing the seasonal aerosol cycle. The autumn increase in AOD indicated an increase in emissions of biogenic aerosols. DMS flux played a major role on the autumn elevated aerosols. The increased wind speed in autumn leading to an increased transfer velocity is the major reason of elevated autumn DMS flux. The ice melt in spring and summer also had significant impact DMS flux. This tendency would be magnified by year 2100 if the ice melt occurs earlier in the season.

The time series and correlation between AOD and SIC, AOD and melting ice, AOD and CLD (cloud cover) are examined. In contrast to CHL (which generally peaked in June), AOD was higher in spring and lower in summer. Usually there was a little increase of AOD in autumn due to the emission of biogenic aerosols possibly associated with phytoplankton synthesis of DMS. Interannual variability of AOD was high. Year 2009 had higher AOD and year 2010 had lower AOD. In most years, SIC was positively correlated with AOD in spring and early summer and negatively correlated in late summer and autumn. DMS concentration was calculated by using Simó's formula. The calculations could cause some errors. However, the profiles are the indications. More accurate DMS calculation using different approach is expected to carry out in the future.

Our results for year 2003–2006 show that DMS and CHL had similar peak time and positively correlated. DMS flux had peak in spring due to the high wind speed. DMS concentration, CHL and AOD presented increased trends before May and decreased trends from May to August. Both SIC and CLD were all around one month ahead of AOD and there were good correlations between AOD and SIC and poor correlations between AOD and CLD. Wind speed was generally over 7 m/s and elevated high wind speed from autumn to next spring (not shown) had an effect on AOD concentrations. SIC, surface wind speed and SST were the main physical drivers of sea salt aerosol (Nilsson et al., 2007), while SIC played a significant role in the Arctic (Qu et al., 2016b).

However, DMS may not play a critical role in regulating the cloud formation (Quinn and Bates, 2011). Some other gases may also impact it (such as isoprene (Meskhidze and Nenes, 2010) and sea salt, etc.). Thus, the DMS flux may possibly offset the climate warming but not affirmative. However, in the Greenland Sea, DMS flux is more related to the ice melting and it may have significant impact to the regional climate as we predicted. When SIC dramatic decreasing, more ice free water of Arctic Ocean would make the oceanic input of gaseous aerosol precursors into the atmosphere become more important.

Future changes in anthropogenic aerosol sources cannot be ignored but the impact on the local and global aerosols is difficult to access. Unravelling the relation between CLD and AOD is difficult, as one signal can contaminate the other in satellite data. If greenhouse-gas emissions decrease, the predicted increase of

biogenic sulfate aerosol in the Arctic Ocean may help reduce future warming (Levasseur, 2013; Qu et al., 2016b). However, if emissions of the short life-time sulfate aerosol do not keep pace with the long-lived greenhouse-gases, polar warming will continue to accelerate.

Acknowledgements

The authors are grateful to NASA's Ocean Biology Processing Group for providing MODIS aqua, Level 3 (4-km equi-rectangular projection) 8-day mapped global data for chlorophyll *a* (CHL) and aerosol optical depth (AOD). We thank the NASA Web SeaDAS development group for providing ocean colour SeaDAS Software (SeaWiFS Data Analysis System) for processing regional CHL and AOD data. Thanks to NOAA NCEP EMC CMB GLOBAL Reyn-SmithOIv2 for providing weekly and monthly sea-ice concentration. Thanks to the NASA Earth Science MEaSUREs DISCOVER Project and the NASA Earth Science Physical Oceanography Program for providing Wind Data and Sea Surface Temperature data and NASA for providing cloud cover data (http://gdata1.sci.gsfc.nasa.gov). Thanks to Ren Hongjian from School of Computer Science and Technology in Nantong University for helping with the wind data.

References

Andreae M O. 2007. Aerosols before pollution. Science, 315(5808): 50–51

Bailey S W, Werdell P J. 2006. A multi-sensor approach for the on-orbit validation of ocean color satellite data products. Remote Sensing of Environment, 102(1–2): 12–23

Barrie L A. 1995. Arctic aerosols: Composition, sources and transport. In: Delmas R J, ed. Ice Core Studies of Global Biogeochemical Cycles. Berlin, Heidelberg: Springer, 1–22

Charlson R J, Lovelock J E, Andreae M O, et al. 1987. Oceanic phytoplankton, atmospheric sulphur, cloud albedo and climate. Nature, 326(6114): 655–661

Chaves J E, Werdell P J, Proctor C W, et al. 2015. Assessment of ocean color data records from MODIS-Aqua in the western Arctic Ocean. Deep Sea Research Part II: Topical Studies in Oceanography, 118: 32–43

Curry J A. 1995. Interactions among aerosols, clouds, and climate of the Arctic Ocean. Science of the Total Environment, 160–161: 777–791

Curry J A, Rossow W B, Randall D, et al. 1996. Overview of arctic cloud and radiation characteristics. Journal of Climate, 9(8): 1731–1764

Ferek R J, Hobbs P V, Radke L F, et al. 1995. Dimethyl sulfide in the Arctic atmosphere. Journal of Geophysical Research: Atmospheres, 100(D12): 26093–26104

Fitch D T, Moore J K. 2007. Wind speed influence on phytoplankton bloom dynamics in the Southern Ocean Marginal Ice Zone. Journal of Geophysical Research: Oceans, 112(C8): C08006

Gabric A J, Cropp R, Hirst T, et al. 2003. The sensitivity of dimethyl sulfide production to simulated climate change in the Eastern Antarctic Southern Ocean. Tellus B, 55(5): 966–981

Gabric A J, Matrai P A, Vernet M. 1999. Modelling the production and cycling of dimethylsulphide during the vernal bloom in the Barents Sea. Tellus B, 51(5): 919–937

Gabric A, Murray N, Stone L, et al. 1993. Modelling the production of dimethylsulfide during a phytoplankton bloom. Journal of Geophysical Research: Ocean, 98(C12): 22805–22816

Gabric A J, Qu B, Matrai P A, et al. 2005. The simulated response of dimethylsulfide production in the Arctic Ocean to global warming. Tellus B, 57(5): 391–403

Gabric A J, Qu B, Rotstayn L, et al. 2013. Global simulations of the impact on contemporary climate of a perturbation to the sea-to-air flux of dimethylsulphide. Australian Meteorology and Oceanographic Journal, 63(3): 365–376

Gabric A J, Simó R, Cropp R A, et al. 2004. Modeling estimates of the global emission of dimethylsulfide under enhanced greenhouse conditions. Global Biogeochemical Cycles, 18(3): GB3016

Hu Ting, Sun Zhaobo, Li Zhaoxin. 2011. Features of aerosol optical depth and its relation to extreme temperatures in China during 1980–2001. Acta Oceanologica Sinica, 30(2): 33–45

Huang Chuanjiang, Qiao Fangli. 2009. The relationship between sea surface temperature anomaly and wind energy input in the Pacific Ocean. Progress in Natural Science, 19(10): 1409–1412

Leck C, Persson C. 1996. Seasonal and short-term variability in dimethyl sulfide, sulfur dioxide and biogenic sulfur and sea salt aerosol particles in the arctic marine boundary layer during summer and autumn. Tellus B, 48(2): 272–299

Levasseur M. 2013. Impact of Arctic meltdown on the microbial cycling of sulphur. Nature Geoscience, 6(9): 691–700

Jones A, Roberts D L, Woodage M J, et al. 2001. Indirect sulphate aerosol forcing in a climate model with an interactive sulphur cycle. Journal of Geophysical Research: Atmospheres, 106(D17): 20293–20310

Meskhidze N, Nenes A. 2010. Effects of ocean ecosystem on marine aerosol-cloud interactions. Advances in Meteorology, 2010: 239808

Nilsson E D, Mårtensson E M, Van Ekeren J S, et al. 2007. Primary marine aerosol emissions: size resolved eddy covariance measurements with estimates of the sea salt and organic carbon fractions. Atmospheric Chemistry and Physics Discussions, 7(5): 13345–13400

Osto M D, Beddows D C S, Tunved P, et al. 2017. Arctic sea ice melt leads to atmospheric new particle formation. Scientific Reports, 7: doi: 10.1038/s41598-017-03328-1

Pang Hao. 2006. Econometrics (in Chinese). Beijing: Science Press

Qu Bo, Gabric A J. 2010. Using genetic algorithms to calibrate a dimethylsulfide production model in the Arctic Ocean. Chinese Journal of Oceanology and Limnology, 28(3): 573–582

Qu Bo, Gabric A J, Lu Hailang, et al. 2014. Spike in phytoplankton biomass in Greenland Sea during 2009 and the correlations among chlorophyll-a, aerosol optical depth and ice cover. Chinese Journal of Oceanology and Limnology, 32(2): 241–254

Qu Bo, Gabric A J, Lu Zhiferng, et al. 2016a. Unusual phytoplankton bloom phenology in the northern Greenland Sea during 2010. Journal of Marine Systems, 164: 144–150, doi: 10.1016/j.jmarsys.2016.07.011

Qu Bo, Gabric A J, Zeng Meifang, et al. 2016b. Dimethylsulfide model calibration in the Barents Sea using a genetic algorithm and neural network. Environmental Chemistry, 13(2): 413–424

Quinn P K, Bates T. 2011. The case against climate regulation via oceanic phytoplankton sulphur emissions. Nature, 480(7375): 5–16

Quinn P K, Shaw G, Andrews E, et al. 2007. Arctic haze: current trends and knowledge gaps. Tellus B, 59(1): 99–114

Reynolds R W, Rayner N A, Smith T M, et al. 2002. An improved in situ and satellite SST analysis for climate. Journal of Climate, 15(13): 1609–1625

Serreze M C, Walsh J E, Chapin III F S, et al. 2000. Observational evidence of recent change in the northern high-latitude environment. Climatic Change, 46(1–2): 159–207

Simó R, Dachs J. 2002. Global ocean emission of dimethylsulfide predicted from biogeophysical data. Global Biogeochemical Cycles, 16(4): 1078

Spracklen D V, Bonn B, Carslaw K S. 2008. Boreal forests, aerosols and the impacts on clouds and climate. Philosophical Transactions of the Royal Society A: Mathematical, Physical and Engineering Sciences, 366(1885): 4613–4626

Struthers H, Ekman A M L, Glantz P, et al. 2011. The effect of sea ice loss on sea salt aerosol concentrations and the radiative balance in the Arctic. Atmospheric Chemistry and Physics, 11(7): 3459–3477

Zhao Chuanfeng, Garrett T J. 2014. Effects of Arctic haze on surface cloud radiative forcing. Geophysical Research Letters, 42(2): 557–564

Acta Oceanol. Sin., 2018, Vol. 37, No. 5, P. 22–28
DOI: 10.1007/s13131-018-1189-1
http://www.hyxb.org.cn
E-mail: hyxbe@263.net

Assessment of the Tessier and BCR sequential extraction procedures for elemental partitioning of Ca, Fe, Mn, Al, and Ti and their application to surface sediments from Chinese continental shelf

LIU Yanli[1], ZHANG Jing[1, 2*], HE Huijun[1]

[1] Laboratory of Marine Chemistry Theory and Technology of Ministry of Education, Ocean University of China, Qingdao 266100, China

[2] Earth and Environmental System, Graduate School of Science and Engineering, University of Toyama, Toyama 9308555, Japan

Received 23 September 2017; accepted 30 November 2017

Abstract

Surface sediments can integrate a wide variety of information of seawater in marginal seas, e.g., the Quaternary sedimentary shelf such as the East China Sea (ECS) and Yellow Sea (YS). The Tessier and BCR sequential extraction procedures (SEPs) have been widely applied for extraction of various geochemical phases from sediments. To choose a suitable SEP for phase extraction of sediments from the above Quaternary sedimentary shelf, efficiency and selectivity experiments were conducted on typical individual minerals and the applicability of each SEP was assessed for natural sediments (the natural sediment standard GSD-9 and three surface sediment samples). The geochemical represented elements (Ca, Fe, Mn, Al, and Ti) were measured using both SEPs. Both SEPs have good dissolution efficiency and selectivity for the targeted geochemical phases; the optimized extractant volume for each fraction was determined. The Tessier SEP is particularly recommended for the study of adsorption-desorption process. The application of the Tessier SEP to surface sediments can furnish valuable information, including the productivity conditions (via the reducible fraction Mn) and sedimentary environments (via the carbonate fraction Ca). These results confirm that the Tessier SEP is suitable for elemental fractionation in sediments from the Chinese continental shelf.

Key words: elemental fractionation, surface sediments, Tessier SEP, BCR SEP, efficiency, selectivity

Citation: Liu Yanli, Zhang Jing, He Huijun. 2018. Assessment of the Tessier and BCR sequential extraction procedures for elemental partitioning of Ca, Fe, Mn, Al, and Ti and their application to surface sediments from Chinese continental shelf. Acta Oceanologica Sinica, 37(5): 22–28, doi: 10.1007/s13131-018-1189-1

1 Introduction

Quaternary sedimentary shelves are characterized by complicated ocean circulation (Lie and Cho, 2002), hypoxia (Chen et al., 2007; Rabalais et al., 1991), and large inputs of terrigenous sediment (Walter et al., 2000). The sediments deposited on these shelves are important records of this information (Li et al., 2017; Ding et al., 2017). With regard to rapid variations in seawater hydrology, if the sedimentation rate is sufficiently high, sediments can provide integrated information concerning seawater dynamics over a period of several years in estuaries and on continental shelves. The sedimentary record can reflect sediment provenance, physical processes (adsorption-desorption), chemical processes (oxidation-reduction) and biological processes. To investigate these different types of information and processes, different components in marine sediments must be extracted separately, including carbonates, hydrous metal oxides, organic substances and crystalline minerals (Szefer et al., 1995).

Chemical fractionation is an efficient approach for speciation analysis. The separation and analysis of individual mineral fractions has been used for studying trace element partitions (Chao, 1972; Chester and Hughes, 1967; Choi et al., 2015; Ray et al., 1957; Gutjahr et al., 2007, 2014; Leleyter and Probst, 1999; Poulton and Canfield, 2005; Song and Choi, 2009; Yang et al., 2002; Zhang et al., 2015; Zhu et al., 2006, 2012). Sequential extraction procedures (SEPs) are designed to isolate specific fractions of the sediments. The Tessier and BCR (Bureau Community of Reference) SEPs are most widely applied to metal fractionation in sediments and soil samples (Rauret et al., 1999; Sahuquillo et al., 1999; Tessier et al., 1979; Usero et al., 1998; Lin et al., 2014; Liu et al., 2016; Esmaeilzadeh et al., 2016). The accuracy and validity of SEPs for trace metal speciation have been extensively examined. However, few studies have assessed SEPs for elemental partitioning in sediments from Quaternary sedimentary shelves, such as the East China Sea (ECS) and Yellow Sea (YS). Assuring the selectivity and efficiency of each step and validating SEPs in this environment remains an important challenge.

The purpose of this study was to choose a proper SEP and optimize the extraction conditions with the methodology to be ap-

Foundation item: The National Natural Science Foundation of China under contract Nos 41530965, 41276071 and 41003052; the JSPS KAKENHI Grants under contract Nos JP26241009 and JP15H00973; the Central Universities under contract Nos 201562008 and 201762031.

*Corresponding author, E-mail: jzhang.ouc@ouc.edu.cn

plied to marine sediments on Chinese continental shelf to accurately determine the diverse origins of sediments and interpret various biogeochemical processes. Typical individual minerals (carbonate minerals, Fe-Mn oxides and clay mineral) were extracted to verify the efficiency and selectivity of the extractants. The Changjiang natural sediment standard GBW07309 (GSD-9) was selected and treated using both SEPs to assess their applicability. Finally, further assessment of the Tessier SEP was conducted using marine surface sediments from the Chinese continental shelf in relation to different sedimentary environments and productivity levels.

2 Materials and methods

2.1 *Samples and reagents*

The studied samples include typical individual minerals and natural sediments.

Efficiency and selectivity experiments were conducted on the following typical individual minerals: carbonate minerals (calcite, dolomite, rhodochrosite, and siderite), Fe-Mn oxides (pyrolusite, hematite, magnetite, amorphous $Fe(OH)_3$) and clay mineral (kaolinite). Amorphous $Fe(OH)_3$ was synthesized in laboratory, and the remaining chemicals and minerals were purchased. Calcite and dolomite were obtained from the Wuhan Iron and Steel Research Institute; $MnCO_3$ from the State Bureau of Building Materials Geological Institute; siderite from the Wuhan Iron and Steel Corporation; Fe minerals from the Geophysical and Geochemistry Research Institute; and kaolinite from Tianjin Ruijin Chemical Co. LTD.

The natural sediment standard GSD-9 (from Changjiang) was purchased to determine the optimum volume of extractant for each fraction in both SEPs. Three surface sediment samples collected in July 2013 were used for validity assessment (ME3 from south of the Changjiang Estuary, C05 from the Central Yellow Sea, and MT1 from southwest of Cheju Island).

$MgCl_2$, hexahydrate (>99%, ACS reagent) and $HClO_4$ (70%, ACS reagent) were purchased from Acros Organics. NH_2OH-HCl (Reagent Plus) and HNO_3 ($\geqslant$65%, ISO. Reag. Ph. Eur.) were purchased from Sigma. NaAc (ACS, Reag. Ph. Eur.), NH_4Ac (ACS, Reag. Ph. Eur.), HAc (glacial, 100%, ACS, Reag. Ph. Eur.), H_2O_2 (30%), and HF (70%, ACS reagent) were purchased from Merck.

2.2 *Extraction procedures*

The extraction procedures of BCR (Rauret et al., 1999) and Tessier (Tessier et al., 1979) SEPs used in this study are summarized as follows:

BCR SEPs: (1) carbonate fraction (0.11 mol/L HAc), (2) Fe-Mn oxides fraction (0.5 mol/L NH_2OH-HCl), (3) organic matter fraction (30% H_2O_2), and (4) residual fraction (HNO_3, HF, $HClO_4$).

Tessier SEPs: (1) exchangeable fraction (1 mol/L $MgCl_2$), (2) carbonate fraction (1 mol/L NaAc-HAc), (3) Fe-Mn oxides fraction (0.04 mol/L NH_2OH-HCl), (4) organic matter fraction (30% H_2O_2), and (5) residual fraction (HNO_3, HF, $HClO_4$).

2.2.1 *Efficiency and selectivity experiments on typical individual minerals*

To study the efficiency and selectivity of both SEPs, typical individual minerals were extracted separately with the various extractants; these minerals included natural calcite, dolomite, rhodochrosite, siderite, pyrolusite, hematite, magnetite, synthetic amorphous $Fe(OH)_3$, and clay mineral (kaolinite). For the efficiency experiment, a series of different mass of each mineral was separately treated with a constant extractant volume in each fraction to determine the maximum mass that could be dissolved. For selectivity experiments, the initial mass of all minerals were 0.25 g, the extractant volume was used as determined in the efficiency experiment. After extraction, the percentages of the elements extracted were used to assess the efficiency and selectivity of the SEPs. The percentage of elements in each fraction was calculated based on the total concentration of each element which was determined by total digestion. If the percentage in the extract was close to 100%, the corresponding mass was considered to be the largest mass that could be dissolved completely. If the mineral content in the samples exceed the maximum mass, this demonstrates that a larger extractant volume should be used. For the exchangeable fraction, all minerals were treated to test the efficiency and selectivity. For the carbonate fraction, calcite and dolomite were utilized to evaluate the efficiency, and Fe-Mn oxides and kaolinite were used to assess selectivity. For the Fe-Mn oxides fraction, MnO_2 and amorphous $Fe(OH)_3$ were used to evaluate the efficiency, and hematite, magnetite, and kaolinite were used for selectivity assessment.

2.2.2 *Applicability of both SEPs to the natural sediment standard*

Different elements are associated with specific phases in natural sediment. To differentiate between these phases with minimal impact from other phases, the optimized extractant volume for each fraction was evaluated for the Tessier and BCR SEPs. A 0.25 g sample of GSD-9 was successively treated with different volumes of extractant for each SEP. Each fraction was subjected to leaching after the completion of the last-step extraction. Representative elements (Ca, Fe, Mn, Al, and Ti) were quantified in each fraction: Ca and Mn for exchangeable dissolution, Ca for carbonate dissolution, Fe and Mn for oxide dissolution, Al and Ti for silicates dissolution. Each supernatant solution was separated by centrifugation at 4 000 r/min for 20 min and then transferred to a polytetrafluoroethylene (PTFE) bottle. The residue was washed once with Milli-Q H_2O and decanted into a polyethylene (PE) bottle. The combined supernatant solution was dried to near dryness, 2 mL HNO_3 was added, and the solution was dried again to a HNO_3 matrix. All fractions were brought up to volume in 2% HNO_3 before analysis.

2.2.3 *Applicability of the Tessier SEP to surface sediments on the Chinese continental shelf*

Different from the natural sediment standard, in view of different geographical environments, sedimentary environments, sedimentation rates and productivity levels, three surface sediments from the Chinese continental shelf were extracted using the Tessier SEP to further validate the applicability. These samples were collected from south of the Changjiang Estuary (ME3); the central YS (C05); and southwest of Cheju Island (MT1).

2.3 *Instrumentation*

The Ca, Fe, Mn, Al, and Ti concentrations were determined using an inductively coupled plasma atomic emission spectrometer (ICAP 6300, Thermo Fisher Scientific, USA), and the instrument's reproducibility was less than 3%.

3 Results and discussion

3.1 *Efficiency and selectivity evaluation using typical individual minerals*

The efficiency and selectivity results obtained using the BCR and Tessier SEPs are discussed separately.

3.1.1 *Efficiency*

(1) BCR SEP: 7.5 mL of 0.11 mol/L HAc can completely dissolve 0.04 g calcite and 0.025 g dolomite; 7.5 mL of 5 mol/L NH_2OH-HCl can fully dissolve 0.15 g MnO_2 and 0.025 g amorphous $Fe(OH)_3$.

(2) Tessier SEP: 0.25 g calcite and 0.125 g dolomite could be completely dissolved by 8 mL 1 mol/L NaAc-HAc. Leleyter et al. (1999) also found that sodium acetate (pH=5) was not efficient for dolomite dissolution. 7.5 mL of 0.04 mol/L NH_2OH-HCl could dissolve 0.01 g MnO_2 and 0.04 g amorphous $Fe(OH)_3$.

Compared with the results using 0.5 mol/L NH_2OH-HCl (pH=1.5), a solution of 0.04 mol/L NH_2OH-HCl in 25% HAc more effectively dissolved the amorphous Fe oxide while 0.5 mol/L NH_2OH-HCl (pH=1.5) more efficiently dissolved MnO_2.

Good efficiency usually ensures acceptable selectivity. Selectivity experiments were performed, and the results are listed below.

3.1.2 *Selectivity*

(1) BCR SEP: As presented in Table 1, the low percentages extracted from the Fe-Mn oxides and kaolinite imply that 7.5 mL of 0.11 mol/L HAc does not dissolve oxides and silicates. The high dissolution percentage of carbonate minerals indicates that 0.11 mol/L HAc has good selectivity for distinguishing between carbonates and non-carbonate minerals. 0.5 mol/L NH_2OH-HCl also has poor dissolution efficiency for hematite, magnetite and kaolinite. However, 42% MnO_2 and 11% $Fe(OH)_3$ were dissolved. This finding indicates that 0.5 mol/L NH_2OH-HCl has a greater extraction efficiency for amorphous Fe-Mn oxides than for crystalline oxides.

(2) Tessier SEP: As shown in Table 1, the low dissolution percentage of each mineral indicates that $MgCl_2$ only dissolved the absorbed elements without contamination from other phases (carbonate phase and Fe-Mn oxides). The leachable elements were adsorbed due to the permanent charge (Leleyter and Probst, 1999).

When treated with 8 mL of 1 mol/L NaAc-HAc, carbonate minerals, but not Fe-Mn oxides, were dissolved. Moreover, 100% calcite, 45% dolomite, and 10%–30% $MnCO_3$ were dissolved. Siderite is not the main carbonate mineral in the ECS (Zou et al., 2008), so only a negligible (0.99%) dissolution of siderite here has little effect. Rongemaille et al. (2011) also reported that siderite was not easily dissolved by 2% and 5% HAc.

When 0.25 g individual mineral was leached with 7.5 mL of 0.04 mol/L NH_2OH-HCl, 6.4% MnO_2 and 42% $Fe(OH)_3$ were leached. This liberation did not occur for the exchangeable and carbonate fractions.

In summary, both the BCR and Tessier SEPs have good dissolution efficiency and selectivity for the targeted minerals. When the natural sediment with mixture minerals was studied, the applicability was assessed as follows.

3.2 *Applicability of both SEPs to the natural sediment standard (GSD-9)*

The data are furnished in Fig. 1 and Fig. 2, respectively. The results are discussed below.

3.2.1 *BCR SEP*

(1) Fraction I_B: carbonate fraction

As shown in Fig. 1a, approximately 85% Ca and 35% Mn were

Table 1. The dissolution selectivity of carbonate minerals, Fe-Mn oxides and kaolinite of extractants in the Tessier and BCR SEPs

Mineral	BCR SEP		Tessier SEP		
	Carbonate/%	Fe-Mn oxides/%	Exchangeable/%	Carbonate/%	Fe-Mn oxides/%
Calcite	26.0	–	1.8	100.0	–
Dolomite	18.0	–	1.3	45.0	–
Rhodochrosite	10.0	–	0.1	12.0	–
$MnCO_3$	14.0	–	0.3	31.0	–
Siderite	1.4	–	ND	1.0	–
MnO_2	ND	42.0	0.1	ND	6.4
Hematite	0.2	2.6	ND	0.1	7.8
Magnetite	ND	1.7	ND	0.2	2.3
$Fe(OH)_3$	ND	11.0	0.1	0.5	42.0
Kaolinite	1.2	1.2	0.1	0.3	1.7

Note: % means the percentage of mineral dissolved, ND not detected, and – not extracted. The mass of all mineral was 0.25 g.

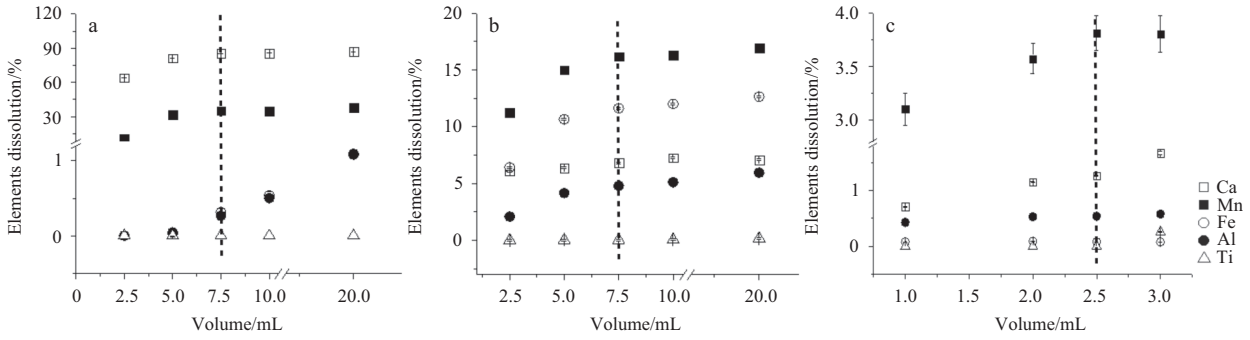

Fig. 1. Effect of extractant volume on the dissolution of Ca, Fe, Mn, Al, and Ti in various fractions of GSD-9 using the BCR SEP. a. Carbonate fraction, b. Fe-Mn oxides fraction, and c. organic matter fraction.

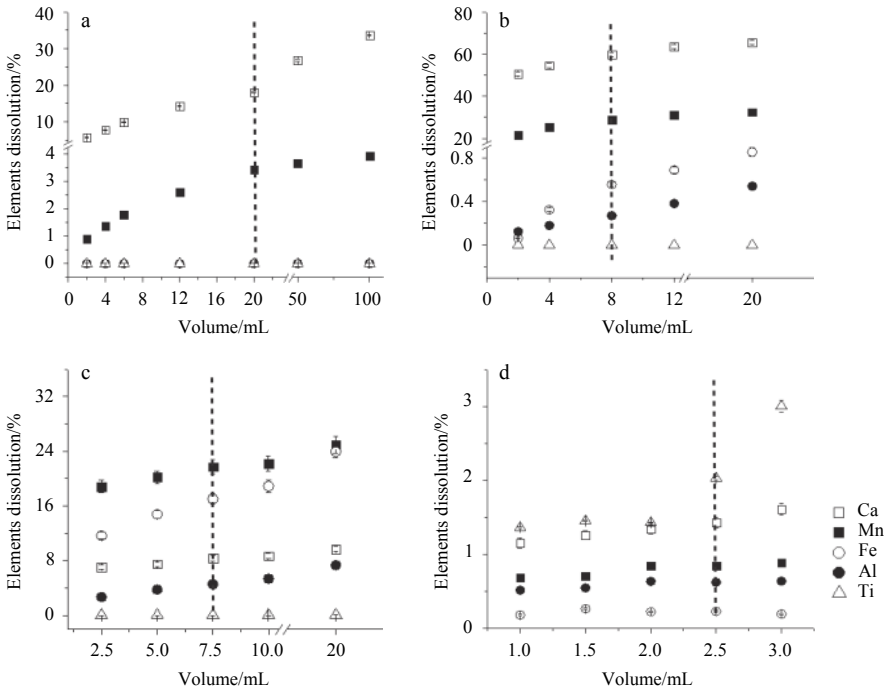

Fig. 2. Effect of extractant volume on the dissolution of Ca, Fe, Mn, Al, and Ti in various fractions of GSD-9 using the Tessier SEP. a. Exchangeable fraction, b. carbonate fraction, c. Fe-Mn oxides fraction, and d. organic matter fraction.

leached when the extractant volume was 7.5 mL, similar amounts of Ca and Mn were dissolved when using a larger volume. Notably, carbonates were sufficiently solubilized. The high percentage of Mn (approximately 35%) in this fraction can be attributed to the dissolution of manganese carbonate, which was demonstrated by the treatment of rhodochrosite and $MnCO_3$ with 0.11 mol/L HAc. The low percentages of Al and Fe indicated that the attack of silicate was minimal. The proportions of Al and Fe increased with the increase of extractant volume (over 7 mL), indicating enhanced contributions from the detrital and oxide phases. Previous results have also indicated that the enhanced extractant volume would lead to the dissolution of non-carbonate minerals (Freslon et al., 2014; He et al., 2015).

Therefore, 7.5 mL of 0.11 mol/L HAc was recommended for the extraction of carbonate phase.

(2) Fraction II_B: Fe-Mn oxides fraction

The results are shown in Fig. 1b. Approximately 13% Fe and 16% Mn were removed and the percentages were nearly constant when the volume exceeded 7.5 mL, indicating the dissolution of the reactive Fe-Mn oxides and poor crystalline hydroxides, such as $Fe(OH)_3$. The low percentage of Al indicated only a slight breakdown of silicates. Thus, 7.5 mL of 0.5 mol/L NH_2OH-HCl was chosen to extract the reactive Fe-Mn oxides and poor crystalline hydroxides.

(3) Fraction III_B: organic matter fraction

The dissolved amounts of Ca, Fe, Mn, Al, and Ti are presented in Fig. 1c. Small portions of each element were extracted, implying these elements rarely existed in the organic matter fraction. The percentages of Ca and Mn did not change when the volume exceeded 2.5 mL, except with an increasing amounts of Al and Ti. Consequently, 2.5 mL H_2O_2 was chosen.

Based on the above experimental work, the optimal volume of each extractant was chosen as follows: 0.25 g GSD-9 was treated progressively with 7.5 mL of 0.11 mol/L HAc at room temperature for 16 h; 7.5 mL of 0.5 mol/L NH_2OH-HCl (pH=1.5) at room temperature for 16 h; 2.5 mL of 30% H_2O_2 (pH=2) at room temperature for 1 h, then at 85°C for 1 h, an additional 2.5 mL of 30% H_2O_2 (pH=2) at 85°C for 1 h and 20 mL of 1 mol/L NH_4Ac (pH=2) at room temperature for 16 h.

3.2.2 *Tessier SEP*

(1) Fraction I_T: exchangeable fraction

According to the concentration plots in Fig. 2a, a logarithmic relationship was observed for Ca and Mn when the volume increased from 2 mL to 20 mL. After an initial rapid increase, the percentage of Mn approached a dynamic balance although there was a slight increasing trend. The low percentages of Al, Fe, and Ti in all extracts implied that $MgCl_2$ treatment did not affect the silicates. The concentration of Ca slowly increased as the volume was larger than 20 mL, indicating minimal attack of the carbonates. Consequently, 20 mL of 1 mol/L $MgCl_2$ (pH=7) was selected.

(2) Fraction II_T: carbonate fraction

The percentages of Ca, Fe, Mn, Al, and Ti are illustrated in Fig. 2b. The Ca and Mn concentration curves show that the carbonates were adequately dissolved at a volume of 8 mL. Previous studies have indicated that carbonates cannot be fully dissolved if the sediment/solvent volume weight ratio is too high (Tessier et al., 1979). The high percentage of Mn (approximately 30%) in this fraction could also be attributed to the dissolution of manganese carbonate, which was proved by the extraction of rhodochrosite and $MnCO_3$. The low levels of Al and Fe indicate that silicate dissolution is minimal. Therefore, 8 mL of 1 mol/L NaAc-HAc was chosen to efficiently extract the carbonate phase.

(3) Fraction III_T: Fe-Mn oxides fraction

Variations in the amounts of Ca, Fe, Mn, Al, and Ti are presented in Fig. 2c. Similar to the BCR extraction, approximately 18% Fe and 20% Mn were removed and the percentages were constant at a volume of 7.5 mL, indicating the dissolution of reactive Fe-Mn oxides. The low percentage of Al indicates only a slight dissolution of silicate occurred. The Fe content was higher

with an increase in volume, indicating partial attack of the crystalline Fe oxides and detrital silicate-rich minerals. Consequently, 7.5 mL of 0.04 mol/L NH_2OH-HCl in 25% HAc was chosen.

(4) Fraction IV_T: organic matter fraction

The amounts of Ca, Fe, Mn, Al, and Ti are shown in Fig. 2d. Small portions of each element extracted in this fraction implied that these elements rarely occurred in the organic matter fraction. The percentages of Mn, Fe, Ca, and Al did not change when the volume exceeded 2.5 mL, except with an increasing percentage of Ti. Hence, 2.5 mL of 30% H_2O_2 was chosen.

Based on the above discussion, the optimal volume of each extractant was presented as follows: 0.25 g GSD-9 was successively extracted with 20 mL of 1 mol/L $MgCl_2$ (pH=7) at room temperature for 1 h; 8 mL of 1 mol/L NaAc-HAc (pH=5) at room temperature for 5 h; 7.5 mL of 0.04 mol/L NH_2OH-HCl in 25% HAc at 96°C for 6 h; 2.5 mL of 30% H_2O_2 at 85°C for 5 h and 5 mL of 3.2 mol/L NH_4Ac (pH=2) at room temperature for 0.5 h.

The sums of the individual fractions for both SEPs agree well with the pseudo-total element analyses, ranging from 94% to 106% for the various elements, and the error is within 2% for most elements as shown in Fig. 3a and Fig. 3b, similar dissolution percentages of Fe, Al, and Ti were extracted from each fraction using both SEPs. The distinct difference between the Tessier and BCR SEPs was the exchangeable fraction in the Tessier SEP. Approximately 18% Ca and 4% Mn existed in the exchangeable fraction, the dissolution of this fraction is usually accompanied by the release of nutrient elements, which is important when studying element cycling in estuaries and on continental shelf areas.

Based on the similarities and differences discussed above between the Tessier and BCR SEPs, we offer several recommendations with regard to the applicability of each SEP to various biogeochemical processes: The Tessier SEP is recommended for the study of the following processes: (1) adsorption-desorption process (exchangeable Ca in estuaries and exchangeable Mn in marine sediments), (2) authigenous origin (carbonate Ca) and carbon cycle, and (3) biogeochemical process of Mn in marine sediments. Both the Tessier and the BCR SEPs can be used for the study of the following processes: (1) oxidation-reduction processes and hypoxia conditions, and (2) clastic rocks and terrigenous sediment provenance.

3.3 *Characterizing the difference of surface sediments from various geographical environments on the Chinese continental shelf*

Based on the application recommendations for each SEP, three surface sediments (ME3, south of the Changjiang Estuary; C05, the central YS; and MT1, southwest of Cheju Island) were extracted using the Tessier SEP. The percentages and concentrations of Ca, Fe, Mn, Al, and Ti are shown in Fig. 4 and Fig. 5, respectively. Ti (>98%) was mainly present in the residual fraction, indicating a terrigenous source. Al (>95%) was in the residual fraction, which agrees with previous results (Yuan et al., 2004). The bulk Al/Ti ratio was likely to be used as a sensitive tracer of particle flux and export production (Kryc et al., 2003; Wei et al., 2003). The Al/Ti ratio was found higher in ME3 (16.8), MT1 (18.4)

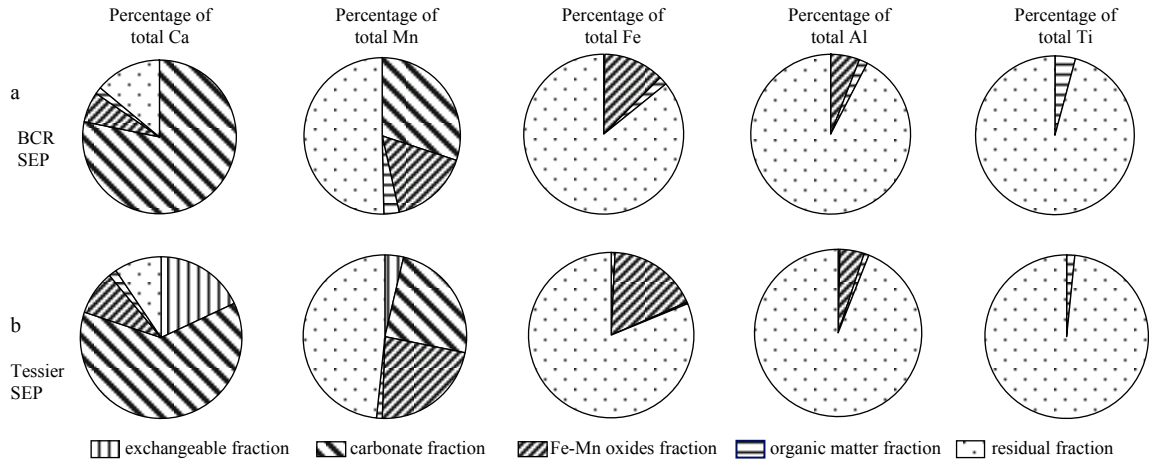

Fig. 3. Ca, Fe, Mn, Al, and Ti distributions for GSD-9 using the BCR (a) and Tessier (b) SEPs.

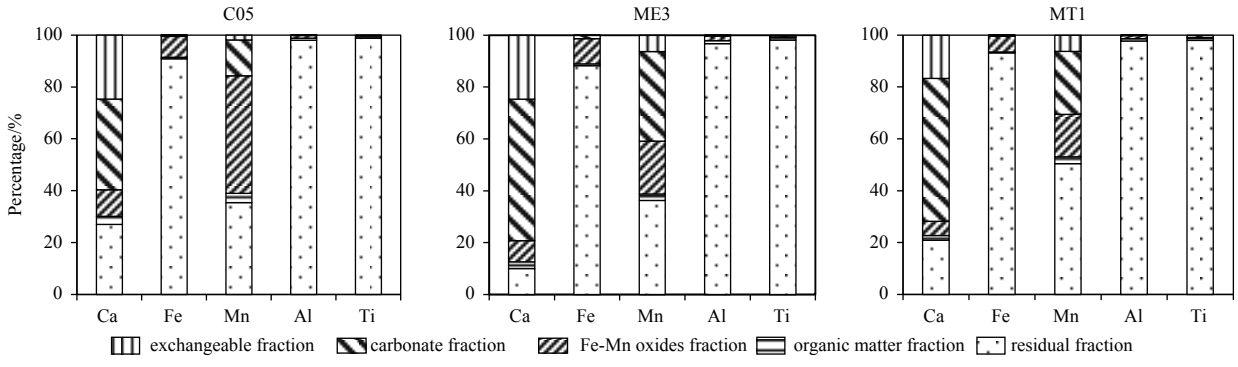

Fig. 4. Ca, Fe, Mn, Al, Ti distributions for C05, ME3, MT1 using the Tessier SEP.

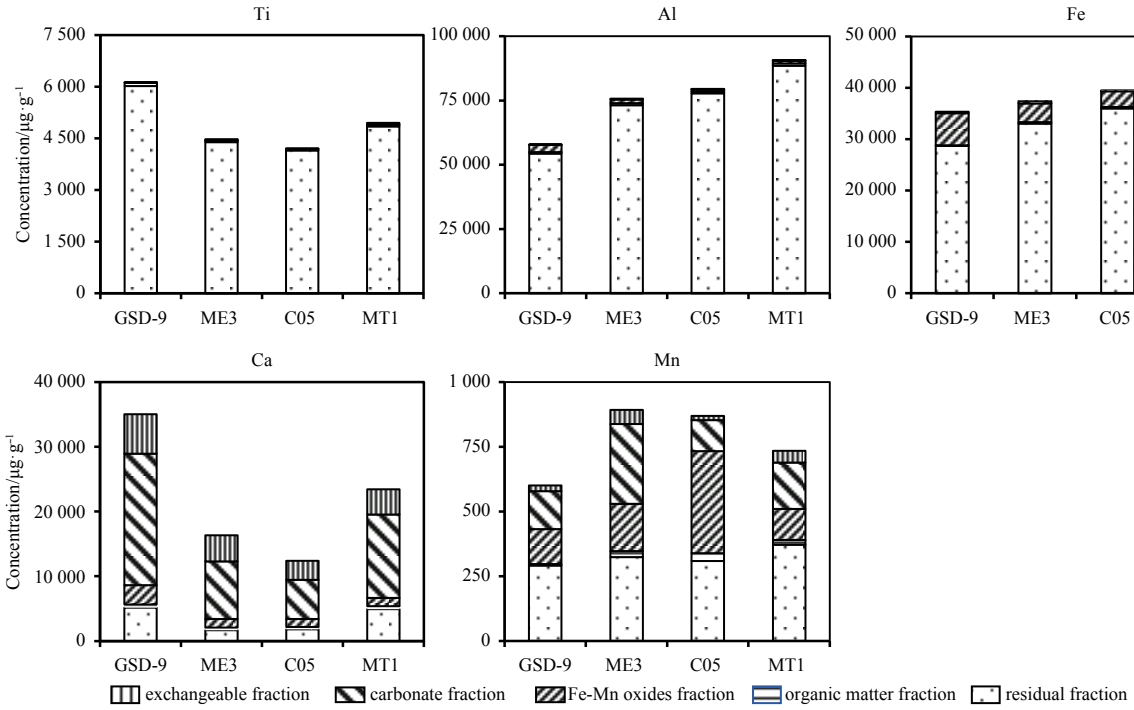

Fig. 5. Ca, Fe, Mn, Al, and Ti concentrations for GSD-9, ME3, C05, and MT1 using the Tessier SEP.

and C05 (18.1) than in the Changjiang (10.5) and Huanghe (16.4) sediments (Zhang et al., 1998), suggesting Al scavenging process by particles. Dou (2007) and Wei et al. (2003) found the excess Al in the ECS and South China Sea (SCS), respectively, suggesting that the excess Al can indicate biogenic matters flux on the shelf area. A total of 80%–90% of Fe was in the residual fraction, followed by 10%–20% Fe in Fe-Mn oxides fraction, agreeing with the results of previous studies (Kryc et al., 2003; Reid et al., 2011). This fraction of Fe arises from oxidation and deposition of Fe in seawater (Huang et al., 1997). About 20%–50%, 20%–40%, 20%–50%, and 2%–5% Mn were in residual, carbonate, reducible, and exchangeable fraction, respectively. The concentration (600 μg/g) and percentage (50%) of Mn in reducible fraction in C05 is higher than that in ME3 and MT1 (100–250 μg/g and 20%–30%, respectively). The excess Mn may result from scavenging of dissolved Mn onto particles settling in high productivity areas near the Yellow Sea Cold Water (Lin et al., 2005). About 30%–60% Ca was associated with carbonates, and 10%–25% was in the exchangeable fraction. This is dissolution of absorbed Ca by electrostatic interaction, poor crystalline Ca and carbonate forms. The concentration of Ca in C05 was lower than that in ME3 and MT1, as a result of the lower concentration of carbonates in the YS (Chen et al., 2000).

4 Conclusions

To choose a suitable SEP for elemental fractionation in Quaternary sediments, the efficiency and selectivity, and application recommendations of the Tessier and BCR SEPs were evaluated.

(1) The extractants used in the BCR and Tessier SEPs have good dissolution efficiency and selectivity for the targeted phases.

(2) The optimal extractant volume for each fraction was determined for each SEP.

(3) To investigate various biogeochemical processes (different elements in specific experimental fraction) the application recommendations for each SEP are given.

(4) The application of the Tessier SEP to the surface sediments on the Chinese continental shelf provides a variety of information including productivity conditions (via higher Al/Ti ratio and the reducible fraction Mn) and sedimentary environments (via carbonate fraction Ca), which further demonstrates the suitability of the Tessier SEP.

References

Chao T T. 1972. Selective dissolution of manganese oxides from soils and sediments with acidified hydroxylamine hydrochloride. Soil Science Society of America Journal, 36(5): 764–768

Chen Chungchi, Gong Gwoching, Shiah F K. 2007. Hypoxia in the East China Sea: one of the largest coastal low-oxygen areas in the world. Marine Environmental Research, 64(4): 399–408

Chen Zhihua, Shi Xuefa, Wang Xiangqin. 2000. Distribution characteristics of carbonate as well as Ca, Sr and Ba in the surface sediments in the South Yellow Sea. Marine Geology & Quaternary Geology (in Chinese), 20(4): 9–16

Chester R, Hughes M J. 1967. A chemical technique for the separation of ferro-manganese minerals, carbonate minerals and adsorbed trace elements from pelagic sediments. Chemical Geology, 2: 249–262

Choi M, Park J, Cho D, et al. 2015. Tracing metal sources in core sediments of the artificial lake An-Dong, Korea: Concentration and metal association. Science of the Total Environment, 527–528: 384–392

Ding Ling, Zhao Meixun, Yu Meng, et al. 2017. Biomarker assessments of sources and environmental implications of organic matter in sediments from potential cold seep areas of the northeastern South China Sea. Acta Oceanologica Sinica, 36(10): 8–19

Dou Weiwei. 2007. Biogeochemical characteristics of metal elements and speciation of aluminum and titanium in sediments in the Yellow Sea and East China Sea (in Chinese) [dissertation]. Qingdao: Ocean University of China

Esmaeilzadeh M, Karbassi A, Moattar F. 2016. Assessment of metal pollution in the Anzali Wetland sediments using chemical partitioning method and pollution indices. Acta Oceanologica Sin-

ica, 35(10): 28–36
Freslon N, Bayon G, Toucanne S, et al. 2014. Rare earth elements and neodymium isotopes in sedimentary organic matter. Geochimica et Cosmochimica Acta, 140: 177–198
Gutjahr M, Frank M, Lippold J, et al. 2014. Peak last glacial weathering intensity on the North American continent recorded by the authigenic Hf isotope composition of North Atlantic deep-sea sediments. Quaternary Science Reviews, 99: 97–111
Gutjahr M, Frank M, Stirling C H, et al. 2007. Reliable extraction of a deepwater trace metal isotope signal from Fe-Mn oxyhydroxide coatings of marine sediments. Chemical Geology, 242(3-4): 351–370
He Jun, Liu Guanglong, Zhu DuanWei, et al. 2015. Sequential extraction of calcium in lake sediments for investigating the cycle of phosphorus in water environment. International Journal of Environmental Science and Technology, 12(3): 1123–1136
Huang Yongyang, Yang Huining. 1997. Controlling of the formation and distribution for polymetallic nodules by the seafloor sediment type and its geochemical environment (in Chinese). Wuhan: China University of Geosciences Press
Kryc K A, Murray R W, Murray D W. 2003a. Elemental fractionation of Si, Al, Ti, Fe, Ca, Mn, P, and Ba in five marine sedimentary reference materials: results from sequential extractions. Analytica Chimica Acta, 487(1): 117–128
Kryc K A, Murray R W, Murray D W. 2003b. Al-to-oxide and Ti-to-organic linkages in biogenic sediment: relationships to paleo-export production and bulk Al/Ti. Earth and Planetary Science Letters, 211(1–2): 125–141
Leleyter L, Probst J L. 1999. A new sequential extraction procedure for the speciation of particulate trace elements in river sediments. International Journal of Environmental Analytical Chemistry, 73(2): 109–128
Li Yanping, Jiang Shaoyong, Yang Tao. 2017. Br/Cl, I/Cl and chlorine isotopic compositions of pore water in shallow sediments: implications for the fluid sources in the Dongsha area, northern South China Sea. Acta Oceanologica Sinica, 36(4): 31–36
Lie H J, Cho C H. 2002. Recent advances in understanding the circulation and hydrography of the East China Sea. Fisheries Oceanography, 11(6): 318–328
Lin Cai, Liu Yang, Li Wenquan, et al. 2014. Speciation, distribution, and potential ecological risk assessment of heavy metals in Xiamen Bay surface sediment. Acta Oceanologica Sinica, 33(4): 13–21
Lin Chen, Ning Xiuren, Su Jilan, et al. 2005. Environmental changes and the responses of the ecosystems of the Yellow Sea during 1976–2000. Journal of Marine Systems, 55(3–4): 223–234
Liu Ming, Fan Dejiang, Liao Yongjie, et al. 2016. Heavy metals in surficial sediments of the central Bohai Sea: their distribution, speciation and sources. Acta Oceanologica Sinica, 35(9): 98–110
Poulton S W, Canfield D E. 2005. Development of a sequential extraction procedure for iron: implications for iron partitioning in continentally derived particulates. Chemical Geology, 214(3–4): 209–221
Rabalais N N, Turner R E, Wiseman W J, et al. 1991. A brief summary of hypoxia on the northern Gulf of Mexico continental shelf: 1985–1988. Geological Society, London, Special Publications, 58(1): 35–47
Rauret G, López-Sánchez J F, Sahuquillo A, et al. 1999. Improvement of the BCR three step sequential extraction procedure prior to the certification of new sediment and soil reference materials. Journal of Environmental Monitoring, 1(1): 57–61
Ray S, Gault H R, Dodd C G. 1957. The separation of clay minerals from carbonate rocks. American Mineralogist, 42: 681–686
Reid M K, Spencer K, Shotbolt L. 2011. An appraisal of microwave-assisted Tessier and BCR sequential extraction methods for the analysis of metals in sediments and soils. Journal of Soils and Sediments, 11(3): 518–528
Rongemaille E, Bayon G, Pierre C, et al. 2011. Rare earth elements in cold seep carbonates from the Niger delta. Chemical Geology, 286(3–4): 196–206
Sahuquillo A, López-Sánchez J F, Rubio R, et al. 1999. Use of a certified reference material for extractable trace metals to assess sources of uncertainty in the BCR three-stage sequential extraction procedure. Analytica Chimica Acta, 382(3): 317–327
Song Y H, Choi M S. 2009. REE geochemistry of fine-grained sediments from major rivers around the Yellow Sea. Chemical Geology, 266(3–4): 328–342
Szefer P, Glasby G P, Pempkowiak J, et al. 1995. Extraction studies of heavy-metal pollutants in surficial sediments from the southern Baltic Sea off Poland. Chemical Geology, 120(1–2): 111–126
Tessier A, Campbell P G C, Bisson M. 1979. Sequential extraction procedure for the speciation of particulate trace metals. Analytical Chemistry, 51(7): 844–851
Usero J, Gamero M, Morillo J, et al. 1998. Comparative study of three sequential extraction procedures for metals in marine sediments. Environment International, 24(4): 487–496
Walter H J, Hegner E, Diekmann B, et al. 2000. Provenance and transport of terrigenous sediment in the South Atlantic Ocean and their relations to glacial and interglacial cycles: Nd and Sr isotopic evidence. Geochimica et Cosmochimica Acta, 64(22): 3813–3827
Wei Gangjian, Liu Ying, Li Xianhua, et al. 2003. Excess Al in the sediments from South China Sea. Bulletin of Mineralogy, Petrology and Geochemistry (in Chinese), 22(1): 23–25
Yang Shouye, Jung H S, Choi M S, et al. 2002. The rare earth element compositions of the Changjiang (Yangtze) and Huanghe (Yellow) river sediments. Earth and Planetary Science Letters, 201(2): 407–419
Yuan Chungang, Shi Jianbo, He Bin, et al. 2004. Speciation of heavy metals in marine sediments from the East China Sea by ICP-MS with sequential extraction. Environment International, 30(6): 769–783
Zhang Chaosheng, Zhang Shen, Wang Lijun, et al. 1998. Geochemistry of metals in sediments from Changjiang River and Huanghe River and their comparison. Acta Geographica Sinica (in Chinese), 53(4): 314–322
Zhang Kan, Zhu Xiangkun, Yan Bin. 2015. A refined dissolution method for rare earth element studies of bulk carbonate rocks. Chemical Geology, 412: 82–91
Zhu Zhaozhou, Liu Congqiang, Wang Zhongliang, et al. 2006. Rare earth element for tracing the source of suspended particulate matter of Lake Chaohu. Journal of Lake Sciences (in Chinese), 18(3): 267–272
Zhu Zhaozhou, Wang Zhongliang, Li Jun, et al. 2012. Distribution of rare earth elements in sewage-irrigated soil profiles in Tianjin, China. Journal of Rare Earths, 30(6): 609–613
Zou Mingliang, Huang Sijing, Hu Zuowei, et al. 2008. The origin of carbonate cements and the influence on reservoir quality of Pinghu Formation in Xihu Sag, East China Sea. Lithologic Reservoirs (in Chinese), 20(1): 47–52

Acta Oceanol. Sin., 2018, Vol. 37, No. 5, P. 29–38
DOI: 10.1007/s13131-018-1220-6
http://www.hyxb.org.cn
E-mail: hyxbe@263.net

Clay minerals in Arctic Kongsfjorden surface sediments and their implications on provenance and paleoenvironmental change

SHI Fengdeng[1, 2], SHI Xuefa[2, 3*], SU Xin[1], FANG Xisheng[2, 3], WU Yonghua[2, 3], CHENG Zhenbo[2, 3], YAO Zhengquan[2, 3]

[1] School of Ocean Sciences, China University of Geosciences (Beijing), Beijing 100083, China

[2] Key Laboratory of State Oceanic Administration for Marine Sedimentology and Environmental Geology, The First Institute of Oceanography, State Oceanic Administration, Qingdao 266061, China

[3] Laboratory for Marine Geology, Qingdao National Laboratory for Marine Science and Technology, Qingdao 266061, China

Received 1 September 2017; accepted 7 December 2017

Abstract

Kongsfjorden is a typical fjord on the edge of the ice cap of the Arctic Svalbard-Barents Sea. Its inner bay is connected with a modern glacier front along the direction of the fjord axis with a significant gradient change in the parameters of hydrology, sedimentation, and biology. In summer, ice and snow melt-water and floating ice collapse continuously and thus transport the weathering products on the surrounding land into the sea. Thus Kongsfjorden is regards as a natural laboratory for the study of unique sedimentation in polar fjords under modern glacial-sea water conditions. In this study, fifty-two surface sediments were collected in Kongsfjorden for clay mineral analysis to study the sediment source and sediment-transport process. Our results indicate that clay minerals in the surface sediments from Kongsfjorden are mainly composed of illite, chlorite, and kaolinite, and no smectite is found. Rocks from different periods exposed extensively in the surrounding areas of Kongsfjorden provide an important material basis for clay minerals in the Kongsfjorden. Kaolinite may be mainly derived from the fluvial deposits, weathered from reddish sandstones and conglomerates during the Carboniferous Period. Illite is mainly derived from Proterozoic low-grade and medium-grade metamorphic phyllite, mica schist, and gneiss. While chlorite is mainly from Proterozoic low-grade metamorphic phyllite and mica schist. In the direction from the fluvio-glacial estuary to the sea of the glacier front of Kongsfjorden, illite increase gradually, and the content of kaolinite declines gradually. However, the change pattern of chlorite is insignificant, which may be related to the provenance. Kongsfjorden detritus is mainly transported by the fluvio-glacial streams and icebergs into the sea and deposited in the inner bay. Coarse sediments are rapidly deposited in the glacier front, estuary, and near-shore areas. Clay fraction begins to deposit significantly by 200–400 m after flowing into the sea, which due to the crystal behavior of clay minerals, hydrodynamic condition and flocculation. Kaolinite and chlorite on the south of the bay near the Blomstrandhalvøya Island is mainly affected by ice-rafted detritus and thus can reveal the trajectory of transportation by the floating ice while entering the sea.

Key words: Arctic Pole, Kongsfjorden, clay mineral, provenance, sedimentation

Citation: Shi Fengdeng, Shi Xuefa, Su Xin, Fang Xisheng, Wu Yonghua, Cheng Zhenbo, Yao Zhengquan. 2018. Clay minerals in Arctic Kongsfjorden surface sediments and their implications on provenance and paleoenvironmental change. Acta Oceanologica Sinica, 37(5): 29–38, doi: 10.1007/s13131-018-1220-6

1 Introduction

Kongsfjorden is a typical fjord developed on the edge of the ice cap of the Arctic Svalbard-Barents Sea. It is located at 78° 40′–79°00′N, 11°20′–12°30′E in Ny-Ålesund on the northwest shore of the Svalbard Archipelago. The Svalbard Archipelago was totally covered by the ice cap of Svalbard-Barents Sea during the ice age of the Late Weichselian period (Landvik et al., 1992). The ice cap front of the Svalbard-Barents Sea gradually receded to the west shore of the archipelago (Landvik et al., 1998; Lehman and Forman, 1992) and formed a series of extremely deep fjords at the entrance to the sea given the increase in temperature since the last deglacial period. Thus, Kongsfjorden was formed during this period. Given that it is in the alternate zone of the ocean and the mainland ice cap, the hydrological, sedimentary, and biological gradient changes along the fjord axis are significant and provide a long-term sequence, high-resolution record for the study of changes in climate and environment (Syvitski and Shaw, 1995; Gilbert, 2000). Kongsfjorden has become a natural laboratory for the study of global climate change in the Arctic region.

Scientists' research has focused on the response of the hydrological and biological environment to global climate change (Halldal and Halldal, 1973; Lydersen and Gjertz, 1986; Ito and

Foundation item: The National Natural Science Foundation of China under contract Nos 41606223 and U1606401; the Basic Scientific Fund for National Public Research Institutes of China under contract No. 2011G27; the Polar Strategic Research Foundation of China under contract No. 20140305; the Taishan Scholar Program of Shandong Province.
*Corresponding author, E-mail: xfshi@fio.org.cn

Kudoh, 1997; Ingvaldsen et al., 2001; Hop et al., 2002; Svendsen et al., 2002; Kwasniewski et al., 2003; Basedow et al., 2004; Cottier et al., 2005; Jiang et al., 2005; Lefauconnier et al., 1999; Ji et al., 2014), and less attention has been paid to the process of sedimentary environment changes (Zajączkowski, 2002, 2008; Shi et al., 2011). The sedimentary environment of the Arctic region is extremely sensitive to global climate changes. Particularly in the past 100 years, a large area of the Svalbard Archipelago glacier has receded because of continuous global warming (Nordli et al., 1996; Ziaja, 2001). With increased glacier activity, the amount of freshwater and terrestrial detritus transported to the fjord increases accordingly (Elverhøi et al., 1995; Svendsen et al., 2002; Zajączkowski et al., 2004; Wlodarska-Kowalczuk et al., 2007), which results in high turbidity of water bodies near glaciers or estuaries (Syvitski, 2002). The existence of high turbidity of water bodies has resulted in the suppression of biological primary productivity in the bay (Keck, 1999), and much plankton has been killed by osmotic impulsive forces (Zajączkowski and Legeżyńska, 2001). The high deposition rate of terrestrial detritus affects the composition and diversity of benthic fauna (Wlodarska-Kowalczuk and Pearson, 2004). The changes in the sedimentary environment in modern fjords, such as the widespread occurrence of high turbidity in water bodies, seriously affect the near-shore ecosystem and hydrological (halocline) situation in the fjords. Therefore, understanding the modern sedimentation process in the Arctic fjord areas at high latitudes is important to global research on climate change.

Kongsfjorden is an ideal place for the study of the modern sedimentation process in the Arctic region. Its inner bay remains connected to the front of modern glaciers at present. In summer, ice and snow meltwater and floating ice collapsed continuously to transport the products of weathering and denudation on the surrounding land into the sea (Shi et al., 2011). Howerer, the questions such as the provenance, transportation and distribution of the sediments after entering the sea need to be answered to understand the modern sedimentation process in the Arctic Kongsfjorden region. Clay minerals, as the main component of marine sediments, are relatively stable. Most of them are from the weathering products of land rocks (Ehrmann et al., 1992). The climate is extremely cold in the Arctic high-latitude areas. In the mostly frozen natural environment, the physical weathering effect on the rocks is strong, but the chemical weathering effect is weak, which is conducive to the preservation of clay minerals. Moreover, clay minerals are highly sensitive to the hydrodynamic force condition because of their unique fine-grain flaky texture. The condition simplifies the identification of the source of the detritus materials and their transportation route from the clay minerals in the marine sediments rather than from other components, which reflects the characteristics of the rocks and climate in the source area. Thus, researchers can understand the sedimentation process and the rules on the movement of detritus materials after entering the sea (Naidu et al., 1971, 1982, 1995; Naidu and Mowatt, 1983; Chamley, 1989; Nürnberg et al., 1994; Stein, 1994; Petschick et al., 1996; Gingele and Leipe, 1997; Viscosi-Shirley et al., 2003; Stein et al., 2004; Chen et al., 2004; Zhang et al., 2008; Li et al., 2012a; Dong et al., 2014).

The establishment of the Arctic Yellow River Station in July 2004 in Ny-Ålesund region of the Svalbard Archipelago provided an effective scientific research platform for Arctic geological research in China. This study selected fifty-two surface sediments collected in Kongsfjorden for clay mineral analysis and research during the summer investigation of the Arctic Yellow River Station in 2007 and 2008. Combined with the geological data of the region, the source, formation cause, and transportation process of clay minerals in the sediments was identified, and sediments distribution rules and the main influencing factors of the clay minerals in Kongsfjorden were revealed, thereby enriching the understanding of the sedimentation effect in the polar region.

2 Regional geological background

Owing to the poor vegetation coverage and the lack of soil layer in the study area, numerous rock strata was exposed with extensive strata developed in each period from the Proterozoic to the Quaternary period (Dallmann et al., 1999; Hjelle, 1993). Figure 1 (Hjelle, 1993) shows that the commonly exposed bedrock in the north shore of Kongsfjorden comprises gneiss and granites with remnants of schist and limestone beds, in which limestone is susceptible to severe metamorphism into marble. The degree of metamorphism of the schist and gneiss is gradually increasing to the north, and the schist produced in the south contains much chlorite and white mica. Moreover, the schist produced in the north is mainly composed of biotite, hornblende, and garnet. In the Blomstrandhalvøya Island, Lovénøyane archipelago, and north of the Blomstrandbreen, some red conglomerates and sandstones of Devonian without metamorphism are visible and distributed in a north-south banding zone. In Brøggerhalvøya at the south shore of Kongsfjorden, the exposed bedrock in the southeast contains garnet, hornblende, and micacite of layered marble from the early and middle Proterozoic, and the exposed bedrock in the north contains phyllite of lamellar quartzite from the late Proterozoic. The exposed bedrock in the west and north contains sedimentary rock from the middle and late Permo-carboniferous periods. A set of fluvial sedimentary facies dominated by reddish sandstone and conglomerate developed in the middle Carboniferous, and the uniquely developed lamellar limestone, dolomite with more fossils and gypsum and anhydrite interlayer were found in the late Permo-carboniferous period. Lower Carboniferous strata can be seen only in the northwest of Kulmodden. Approximately 200–250 m thick sandstone overlies were found on the eroded surface of bedrock, and a set of 3 m thick shale deposits were found in the lower part of the bedrock, mixed with impure coal seams. During the transition from the Cretaceous period to Palaeocene epoch, affected by the oblique extrusion of Greenland, a series of thrust evidence from SSW to NNE appears in this region, and old strata are often pushed over by new strata (Hjelle and Lauritzen, 1982). Paleogene strata are exposed in the west and the small areas south of Ny-Ålesund (4.5 km^2), surrounded by lower Permo-Carboniferous rocks. The exposed bedrock in the Ossian Sarsfjellet area at the east of Kongsfjorden is dominated by schist. The metamorphic grade increases, with limestone transforming into marble, because of its closeness to the east of the fjord. The exposed bedrock further to the east is dominated by gneiss with a small amount of gray granite because of the strong metamorphic effect in Stemmeknausane. Gneiss is also exposed in two small mountains towards the south. Middle and upper Permo-carboniferous strata in other moutains in the east and north of Kongsvegen glacier are mainly exposed. The rock stratum is essentially horizontal because of the intense tertiary folding and faulting effect in the western belt. The mountains are of Pyramid type. The Kroner is typical. Horizontally distributed Permo-Carboniferous strata cover the Devonian strata that are subjected to minor folds lower than 1 000 m. Black Jurassic rocks intruded prevalently and formed cliffs on mountain ranges (Hjelle, 1993).

Many glaciers developed on both sides of Kongsfjorden and the leading edge of basin. Brøggerbreen, Midtre Lovénbreen,

Austre Lovénbreen, Pedersenbreen, and Uversbreen belong to Valley glacier. Blomstranbreen, Conwaybreen, Kongsbreen, Kronebreen and Kongsvegen belong to tidewater glacier. A large number of tillites are found near these glaciers. The study area is covered with ice most of the year. The warming on the surface in summer leads to the partial melting of ice and snow and forms a series of small seasonal glacial-meltwater rivers on both side of Kongsfjorden.

3 Material and methods

Fifty-two surface sediment samples analyzed in this study were acquired by boat and comprised the Chinese 4th and 5th Arctic Summer Expedition of the Yellow River Station in 2007 and 2008 (Fig. 1). The sample collection method was clamshell grab. Surface sediment samples were sampled in 0–2 cm layers.

X-ray diffraction method (XRD) for oriented thin section of clay grade mineral (<2 μm) was used for clay mineral analysis (Li et al., 2012b). Samples were prepared as follows. Roughly 1 cm^3 of the sample was taken to remove organic matter with 30% of H_2O_2. Approximately 0.5% HCl was used to remove carbonate, and the sample was washed repeatedly with deionized water until deflocculation occurred. Particles less than 2 μm were sucked with a needle tubing for centrifugation based on the settling time determined by the Stokes sedimentation principle. The scraping method was used to prepare sample-oriented slices to dry naturally. AD/max-2500 type rotating target X-ray diffraction instrument (Japan) was used to for XRD inspection. The preparation and testing of samples were conducted in a test center at the Key Laboratory of State Oceanic Administration for Marine Sedimentology and Environmental Geology.

4 Results and discussion

4.1 *Content and distribution characteristics of clay minerals*

The evaluation of clay minerals only considers four types: kaolinite, illite, chlorite and smectite. The evaluation and calculation are in accordance with the literature (Li et al., 2012b). Table 1 presents based on comprehensive identification and semi quantitative calculation of various maps and curves. Clay minerals in surface sediment mainly consist of illite, chlorite and kaolinite, and no smectite was observed.

Illite is a type of clay mineral with the highest content in the study area. The changing range is 69%–78% with a mean value of 74.4%. Its distribution follows a certain rule, as shown in Fig. 2a. Illite is gradually increasing from the south shore of Kongsfjorden to the north. The content of illite is also increasing gradually from the leading edge of glacier at the east of Kongsfjorden to the ocean. The content of illite shows decreasing and then increasing trends in a small area near the south of Blomstrandhalvøya Island.

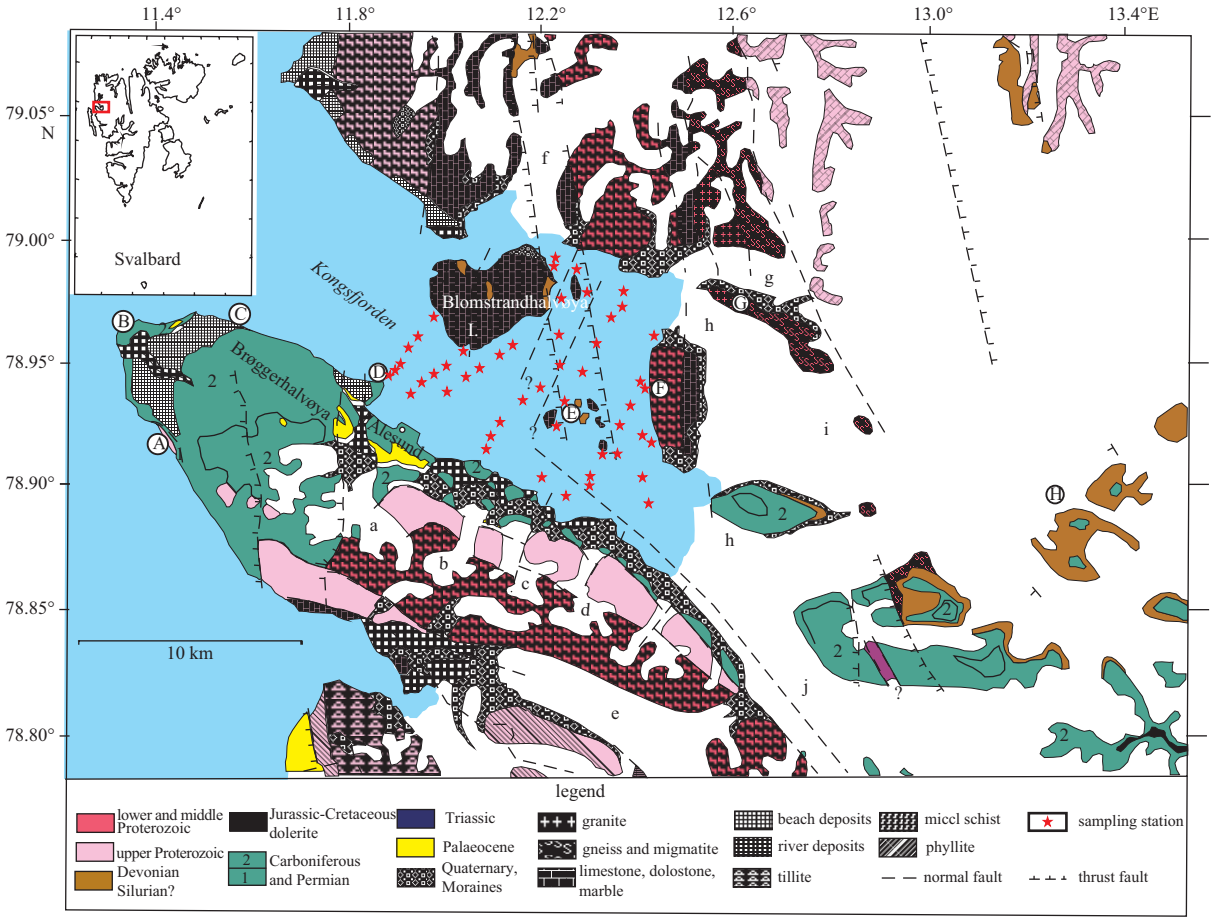

Fig. 1. The geological map of Ny-Ålesund area (modified from Hjelle, 1993). The name of place: A. Kulmodden, B. Kvadehuken, C. Kongsfjordneset, D. Brandalpynten, E. Lovénøyane, F. Ossian Sarsfjellet, G. Stemmeknausane, and H. Tre Kroner. The name of glacier: a. Brøggerbreen, b. Midtre Lovénbreen, c. Austre Lovénbreen, d. Pedersenbreen, e. Uversbreen, f. Blomstranbreen, g. Conwaybreen, h. Kongsbreen, i. Kronebreen, and j. Kongsvegen.

Table 1. Statistics of clay mineral contents in the surface sediments, Kongsfjorden

Content	Illite	Kaolinite	Chlorite	Smectite
Sample number	52	52	52	52
Max/%	78	17	21	0
Min/%	69	9	11	0
Average/%	74.4	12.7	12.9	0

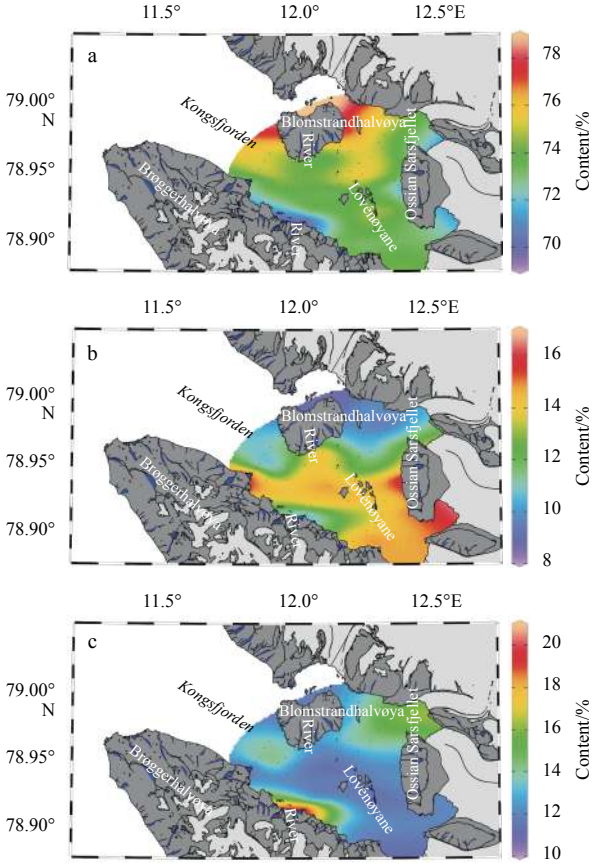

Fig. 2. The distributions of clay mineral content in the surface sediments. a. Illite, b. kaolinite and c. chlorite. This figure was generated with "Ocean Data View" (Schlitzer, 2015).

The content of kaolinite in the surface sediment in the study area is 9%–17%, with a mean value of 12.7%. Figure 2b shows that two high-value areas are found in Kongsfjorden for the content of kaolinite. The content of kaolinite is gradually decreasing in the entrance of glacier rivers and tide water glacier slightly to the south Ossian Sarsfjellet mountain. The content of kaolinite is also decreasing gradually from the estuary of glacial-melt water formed by Midtre Lovénbreen, Austre Lovénbreen, and Pedersenbreen at the south shore of Kongsfjorden to the ocean. The content of kaolinite shows increasing and then decreasing trends in a small area near the south of Blomstrandhalvøya Island.

The chlorite content in the surface sediment in the study area is within 11%–21%, with a mean value of 12.9%. Figure 2c shows that the chlorite content gradually decreasing from the estuary of glacial-melt water formed by the Midtre Lovénbreen, Austre Lovénbreen, and Pedersenbreen at the south shore of Kongsfjorden, and the west and east of Ny-Ålesund to the ocean. The chlorite content also decreases from the Conwaybreen on the north of Kongsfjorden and the leading edge near Kongsbreen to the ocean. However, the change in the chlorite content is not obvious in other areas.

4.2 *Provenance and environmental significance indicated by clay minerals*

4.2.1 *Illite*

Illite generally emerges from feldspar, mica, and other aluminosilicate minerals under the condition of weathering and K^+ removal at low temperatures and weak alkaline environment. Its major cations are composed of Si, Al, and K. The crystallinity of illite is determined by half band width at 10 Å diffraction peak (Li et al., 2012b). The previous division standard of the degree of crystallization is adopted (Diekmann et al., 1996): the degree of crystallization is divided into four types: very good, good, moderate and bad. The ranges of crystallinity values are <0.4, 0.4–0.6, 0.6–0.8 and >0.8. Low crystallinity value of illite indicates a high degree of crystallinity. Such a result indicates that the land provenance area is weak in hydrolysis and shows dry and cold weather conditions. The parameter is consistently used to trace provenance areas and transport paths (Krumm and Buggisch, 2010). The chemical index of illite is determined by using 5 Å/10 Å peak area ratio. A ratio of more than 0.5 indicates that illite with rich Al is characterized by strong hydrolysis. A ratio of less than 0.5 indicates that illite with rich Fe-Mg, which is the product of physical weathering (Esquevin, 1969). Figure 3 shows that via calculation, the crystallinity value of illite in surface sediments in Kongsfjorden is 0.30–0.43, with a mean value of 0.39. Based on the previous division standard, the crystallinity of illite can be judged as very good–good. The chemical index is within

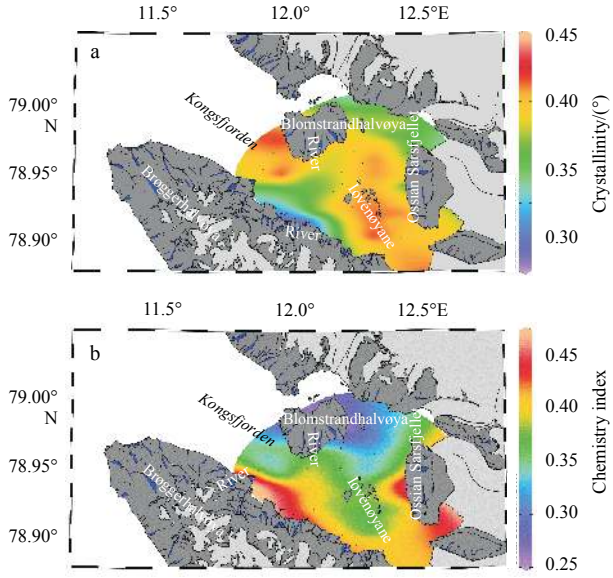

Fig. 3. The distributions of illite crystallinity and chemistry index in the surface sediments of Kongsfjorden. a. Illite crystallinity ($\Delta 2\theta$, °) and b. illite chemistry index. This figure was generated with "Ocean Data View" (Schlitzer, 2015).

0.26–0.46, with a mean value of 0.37, which can be determined as illite with rich Fe-Mg. This result indicates that the provenance area has dry and cold weather conditions, which is consistent with the modern environment. Thus, illite in the study area is the product of the strong physical weathering of rocks.

Illite in the ocean is mainly from land (Shi, 1995). Low and intermediate metamorphic rocks from the Proterozoic era are widely exposed around Kongsfjorden and mainly include phyllite, mica schist, and gneiss, which contain rich feldspar, mica and other aluminosilicate minerals. The rocks provide an important physical basis for the formation of illite. Moreover, the natural environment characteristics of dry and cold climate and weak leaching action in the provenance area are conducive to the formation and conservation of illite. Thus, illite is a clay mineral with the highest content in the study area. Svalbard is also considered the main source area of the Arctic Ocean illite (Stein et al., 1994).

4.2.2 *Kaolinite*

Previous studies have mentioned that kaolinite is generally recognized to be formed by two pathways: hydrothermal alteration and surface weathering (Zhu, 1987; Yang, 1988). Warm and humid climatic conditions and dense vegetation cover on the surface are necessary to produce weathering. The soil medium is acidic, and leaching is powerful. Thus, K, Na, Ca, Mg can be separated from aluminosilicate minerals. Feldspar and mica minerals are weathered into kaolinite. No signs of hydrothermal activity are found on the seafloor. Measured pH values in surface sediments in Kongsfjorden that are more than 8 (Zhu et al., 2014), indicating a marine alkaline environment. Thus, the basic conditions for forming kaolinite minerals are not available in the modern submarine environment. Moreover, the source of its material is transported from the land to the sea by geological agents such as glaciers and rivers. Based on the current surface environment in the study area, the annual average temperature is roughly –5.8°C and the average annual precipitation is up to 400 mm (Hisdal, 1998). The plant species are relatively rare and dominated by polar tundra plants. No natural condition for the formation of kaolinite appears possible. Determining whether strong chemical weathering is needed to produce kaolinite is necessary. Xia and Xie (2007) analyzed 16 elements in lake sediments (49.5 cm long, drilling to the bedrock) from L1 drilling hole in the Blomstrandhalvøya Island in Arctic Ny-Ålesund and the calculated component variance index. The researchers found that component variance index in sediments was significantly higher than the indices of feldspar and clay minerals and close to the component variance index of primary rock (Xia and Xie, 2007). This result indicates that the content of clay minerals produced after the weathering effect in the study area is far less than the content of the primary mineral. Thus, in the study, the chemical weathering is weaker in the primary stage. These results show that kaolinite is not produced by weathering. Moreover, kaolinite can be converted from other clay minerals. Generally, illite can be converted into smectite under the condition of continuous weathering and K^+ removal (Tang et al., 2002). In hot and humid climates, chemical weathering is thorough and can be further decomposed into kaolinite (Tang et al., 2002). No smectite is found in sediments in the study area. These results indicate a lack of smectite materials in the provenance area. Moreover, the results indicate that the weak chemical weathering in the modern environment in this area is insufficient to make Na, K and other strongly active alkali metals well leached. The metals only stay in the formatting stage of illite. Therefore, the kaolinite minerals in the study area are unlikely to be formed under modern environmental conditions. Given frequent glacial events during the historical period in the area, the erosion and transport of glaciers cause fewer sediments older than 700 years to be conserved in the study area (Jones and Birks, 2004). Moreover, kaolinite minerals are easy to be destroyed during metamorphism or deep burial. A correlation analysis revealed a significant negative correlation with illite and chlorite content, which indicates that the sources were different (Fig. 4). Kaolinite in this area is inferred to be the product of sedimentary rocks that have been kaolinized or contain kaolinite that was formed before the Quaternary after physical weathering, similar to the origin of kaolinite in the Arctic and Antarctic continents (Zhang et al., 2008; Blakemore and Swindala, 1958). Based on the study conducted by regional geology (Hjelle, 1993), the kaolinite present in this area likely originated from the fluvial facies that were dominated by reddish sandstone and conglomerate in the middle Carboniferous. The reason is that the Svalbard archipelago at that time is at the same latitude as the North African desert today. The climate is hot and the area is near the ocean. Moreover, strong leaching property helps the formation of kaolinite. Rock stratum from this era is widely exposed in the coast of the cape between Brandalpynten and Kongsfjordneset, the east of Kvadehuken, near Brøggerbreen, and around Kongsvegen. Given extremely strong etching from Brøggerbreen, Kongsvegen, and Kronebreen and other

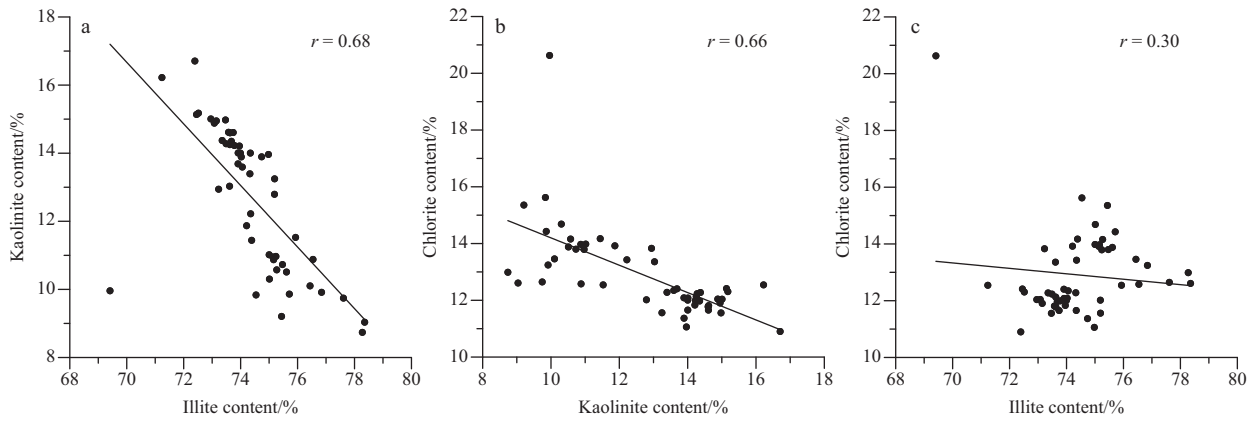

Fig. 4. Correlation diagrams between clay minerals in the surface sediments of Kongsfjorden. a. Kaolinite versus illite, b. chlorite versus kaolinite and c. chlorite versus illite.

modern glaciers, sedimentary rocks from this period are often broken into the muddy matter, which brings a red color to many rivers and streams near Ny-Ålesund and the rivers south of Ossian Sarsfjellet. The particles are then transported into the fjord. Kaolinite minerals are deposited in these estuaries with relatively high content (Fig. 2b).

4.2.3 *Chlorite*

Chlorite is usually formed in alkaline and less leaching environments. Under weathering effect, Fe^{2+} in water magnesium layer is easily oxidized. Thus, it can only be preserved when the chemical weathering is inhibited (Rateev et al., 2010). Chlorite can be used to indicate cold climatic conditions (Griffin et al., 1968). The chlorite content is the highest in the Antarctic Ocean, land, and Arctic and subarctic seas. Chlorite is generally formed from metamorphic rock in terrigenous areas by intense physical weathering and weak chemical weathering under cold and dry climatic conditions. Previous studies have shown that the origin of chlorite is complicated. Its formation is related to low-temperature hydrothermal action, epimetamorphism and sedimentation (Pan et al., 1993). Several studies have reported that chlorite can be transformed from gibbsite when volcanic material is subjected to intense chemical weathering (Shi, 1995). Volcanic material must be present in the study area if it is transformed from gibbsite. Moreover, volcanic material can easily form smectite under the weathering effect. However, no smectite is found in this area. A significant negative correlation was found between chlorite and kaolinite content, and a weak negative correlation was observed between chlorite and illite content, which indicate that the sources were different (Fig. 4). Moreover, no volcanic material is found in regional rock formations. Therefore, chlorite is unlikely to be changed from gibbsite. The schist produced in the south of the north shore of Kongsfjorden contains many chlorite minerals due to the low degree of metamorphism. The typical mineral combination in the phyllite exposed in the south shore of Kongsfjorden contains chlorite. Therefore, combined with cold and dry environments in the study area, the chlorite in this area mainly comes from low-grade metamorphic phyllite and mica schist in the Proterozoic era that surrounds Kongsfjorden. Chlorite formed under physical weathering can be preserved in the glacier environment after these rock formations are subjected to glacial erosion. Finally, it is carried into the sea by glaciers or glacial meltwater rivers. Figure 2c shows that high chlorite content area that emerges in the south and north of Kongsfjorden is closely related to the provenance.

4.3 *Transportation and deposition process of clastic (clay) materials*

Glacier volume shows an obvious decline after the end of the little ice age in the Svalbard archipelago. The ice layer becomes thin constantly in front of the ablation zone and then shrinks backward at the end of the glacier tongue (Hagen et al., 2003; Ai et al., 2013). Further studies have shown that glaciers with persistent recession are usually small in size (<10 km^2) and low in altitude (<500 m) (Xu et al., 2007). Many clastic materials in the glacier recession are transported and deposited by glaciers and rivers. Two different types of glaciers are found in Kongsfjorden: valley glacier and tidal water glacier. Differences are observed in the abilities and means of the clastic material transportation between them.

Valley glaciers were developed in Brøggerhalvøya on the south shore of Kongsfjorden. The flow rate of such glaciers is extremely low because of the effects of low temperatures. For example, the flow rates of Austre Brøggerbreen, Midre Lovénbreen, and Austre Lovénbreen are only 2 m, 4.5 m and 7 m, respectively (Svendsen et al., 2002). Pro-talus ramparts or rock glaciers are formed from some broken glacier materials generally found near the glaciers, which are distributed in the area in which Quaternary moraine is deposited in Fig. 1. The moving rate of these rock glaciers is extremely low, at roughly 3–4 cm or less per year (Sollid and Sørbel, 1992). Regardless of valley glaciers or rock glaciers previously formed, the ability of this type of glacier in the study area to directly transport fragmentary materials is weak because of the very low flow rate. The clastic materials are mainly transported and deposited via rivers on land. The study area is covered by glacier and snow for most of the year. The transportation mainly happens in summer.

A large amount of firn and meltwater in a small area of valley glacier at the low altitude flow out from the sides or bottom of the glacier. Moreover, after passing through the leading edge of the glacier or cutting terminal moraine dam and rock glacier, the terrain becomes wide and slow, and a series of small braid-shape rivers exists at the coast of Kongsfjorden. These glacial-melt water rivers show seasonal activity. No permanent deep-incised valley is found, except for the Bayelva River. A wide glacial-melt water deposition plain can be formed (Fig. 5). Coarse fluvial deposits are prevalent and vegetation development is rarely found. Many clastic materials are deposited after glacial-meltwater enters the ocean. The analysis on the grain size of surface sediment in Kongsfjorden shows that sediments in Kongsfjorden contain gravel, sand, silt, and clay components, and is dominated by silt and clay components. The distribution of gravel, sand, and clay has highly significant characteristics. From the south shore of Kongsfjorden to the north, the contents of gravel and sand fragments gradually decreased, and that of clay increases. It is closely related to onshore glacial-melt water river input (Shi et al., 2011).

Four tidal glaciers, namely Kronebreen, Kongsvegen, Blomstranbreen, and Conwaybreen developed on the north shore of Kongsfjorden and the leading edge of the basin. Polythermal Kongsbreen formed by Kronebreen and Kongsvegenr in the front of glaciers is the largest and most active in this area (Lefauconnier et al., 1994). The maximum amount of glacial meltwater occurs in July, and the flow rate is up to 138 m^3/s (Zajączkowski and Legeżyńska, 2001). Statistics indicate that roughly 1.4 km^3 of fresh water is discharged into Kongsfjorden annually (Svendsen et al., 2002). The amount of meltwater discharged into glaciers is roughly 0.33 km^3 (Beszczyńska-Möller et al., 1997). The glacier meltwater flows out from inside the glacier and directly into the fjord along the glacier cliff (Zajączkowski, 2008). In the area around Kongsvegen glacier, many rocks are broken and transported to the fjords because of highly intense glacier erosion. Roughly 2 million tons of sand, mud and gravel are transported annually by glacial meltwater rivers to the inland basin near the front of the glacier. This amount is equivalent to 2 000 tons of materials per square kilometer of glacier (Hjelle, 1993). However, Blomstranbreen and Conwaybreen are inactive. Only a small amount of turbid water is discharged yearly (Svendsen et al., 2002). Two types of sediment are generated in the fjord given different transportation modes and sedimentary differentiation abilities. First, ice-edge fan deposits dominated by lamellar sand and gravels occur in the front of glacier. Second, massive argillaceous deposits dominated by silt and clay occur in the leading edge of the glacier (Shi et al., 2011). Icebergs formed after disintegration are another major geological agent for transport and deposition of sediment in the leading edge of the tidal glacier in

Fig. 5. Sandur and braided drainage systems in the Ny-Ålesund.

Fig. 6. Small iceberg strand in the Kongsfjorden.

summer. Kronebreen only releases small-scale icebergs to the fjord and they transport from the basin under the effect of the southeast wind (120°) prevailed in Ny-Ålesund (Svendsen et al., 2002). Large icebergs consistently strand in the east area of Lovénøyane island or on the boundary line between the basin and central fjord and the north between Lovénøyane and Blomstrandhalvøya island. These icebergs consistently carry much clastic matter (Fig. 6). A particular type of sediment that contains more fine gravels may occur in the transportation process.

Fine clay component is mainly composed of clay minerals compared with gravel, sand, and silt components.Therefore, the clay minerals are easily transported and difficult to deposit after carried by rivers or glaciers into the sea. They are the main component that constitutes suspended matter in water. The sediment trap placed in the fjord show that the concentration of the total suspended matter begins to increase in April and reaches the maximum in July. The deposition process ends in the middle of September. Suspended particles remain for approximately 30 days in the fjord (Svendsen et al., 2002). The basin of Kongsfjorden is covered by sea ice in winter. Sea ice begins to subside by April of each year as the weather becomes warmer. Sea ice is completely melted in July. Glaciers and rivers enter an active phase at this time. The seasonal variation in freshwater input creates a stable stratification in summer and weak stratification in winter. The upper layer circulation in summer is confined to a shallow surface layer (Svendsen et al., 2002). A large number of terrigenous clastic materials are transported to the sea. In mid-September, the weather turns cold and the handling process ends. The concentration of suspended particles is increased to the maximum, and terminal time of deposition process is consistent with the beginning and ending times of the transport of terrigenous material into the sea by glaciers and rivers. The concentration of suspended particles has a significant peak in the spatial distribution at the leading edge of the glacier. The deposition is extremely fast. The deposition rate is up to the maximum in a place 200–400 m distant to the leading edge of glacier (Svendsen et al., 2002). During the Chinese 6th Arctic Yellow River Summer Expedition in August 2009, a LISST-100B field laser particle size analyzer was used to make cross-section measurements on the concentration of suspended matter in the water of Kongsfjorden from the leading edge of the glacier, basin, and middle fjords to outside fjords. The concentration of the total suspended matter decreased regularly from the basin, and middle fjord to outside fjord, and the subsurface showed the maximum in the vertical direction (unpublished data). Generally, the transport process of clay minerals in waters can be indicated by the change in the concentration of the total suspended matter. However, the deposition process of clay minerals from water bodies is highly complicated and restricted by many factors. First, clay minerals with fine particles are highly sensitive to hydrodynamic forces. Thus, clay minerals are not easy to deposit. Second, the sedimentation of clay minerals mainly depends on flocculation. In the position of Kongsfjorden roughly 10 m close to the glacier, brackish water is mixed with more saline water to produce flocculation. The flocculation in the middle and outside fjord is mainly produced in 20 m position (Syvitski, 1980). Moreover, clay minerals differ in their crystal behavior. Thus, debris, flakes, granules and plates occur. The deposition rate also varies with different crystal forms. The hydrodynamic force is relatively strong in the leading edge of the glacier and the estuary of glacial meltwater. A strong surface current meandered along the glacier front with a maximum speed exceeding 1 m/s (Svendsen et al., 2002). Affected by diluted water, the surface salinity is lower and the flocculation is weaker. The flocculation at the position roughly 10 m below the surface is produced by mixing brackish water with more saline water. The sedimentation of kaolinite minerals in even-grained or thick plate is relatively fast, which form a high-value region of kaolinite distribution. The hydrodynamic condition is relatively weak in the area far from the estuary and the leading edge of the glacier. The speed of the brackish current, measured in July 1999 in the constriction between the inner and middle basin, ranges from 10 to 30 cm/s (Svendsen et al., 2002). Given that the influence of diluted water is relatively small, the salinity of the surface is increased and the flocculation is significantly enhanced. Patch or flaky illite deposits gradually form a high-value region of illite distribution. Chlorite is easier to deposit than illite and can easily form a high-value area on the leading edge of the glacier and the estuary of glacial meltwater with abundant provenance given a larger grain size than illite. ^{210}Pb dating technique is used to measure the deposition rate of a series of columnar sediments from the leading edge of the glacier to the outside (Svendsen et al., 2002). The result shows that deposition rate is significantly reduced from the basin (20 000 g/(m^2·a)) and middle fjord (1 800–3 800 g/(m^2·a)) to the outside fjord (200 g/(m^2·a)). ^{137}Cs test result, which is closely related to clay minerals, provides good verification. ^{137}Cs in the basin is maximum, namely, >60 cm; 10 cm in middle fjord and <5 cm in the outside fjord (Papucci et al., 1998). The most intensive turbulent eddies with diameters of a few meters were commonly found in close proximity to direct outflows from the front of Kongsbreen. Sharp fronts that separate waters with different concentra-

tions of suspended matter were clearly visible at the surface. Patches of strong turbulent mixing were distinguishable (Svendsen et al., 2002). These results indicate that, not only gravel, sand, silt, but also other fine-grained components can be identified in the inner bay. Fine clay component are mainly deposited in this place. A small area on the south side of Blomstrandhalvøya Island in Kongsfjorden (Ω-shape area in Fig. 2c) is the place in which small icebergs produced from the disintegration of Conwaybreen and Kongsbreen tidal glaciers pass through into the sea in summer. Moreover, some large icebergs are stranded in this area (Fig. 6). The icebergs gradually melt under the action of warm seawater. A type of mixture that contains fine gravel appears in its surface sediments (Shi et al., 2011), which is considered fragmentary matters in different sizes that fall from icebergs, and are formed when deposition rate of the unloading materials is extremely high. The distribution of illite and kaolinite here is highly regular in this area. The content of kaolinite in the outside fjord is increased and then decreased. However, the change in the content of illite is the opposite. This behavior is related to the unloading of a large quantity of fragmentary matter that is carried by icebergs in entering the sea or stranding. With the difference in crystallization behavior, the sedimentation of kaolinite is fast and that of illite is relatively slow. Thus, the changes in their contents are different in spatial distribution. The abnormal changes in the contents of two types of clay minerals in the middle of the fjord can reveal the melting place of icebergs and the trajectory of the transportation by the floating ice when entering the sea, which provides a new means of thinking for studying the route of the glacier to enter the sea in historical periods.

5 Conclusions

Through systematical analysis of the characteristics of clay mineral components in surface sediment samples from Arctic Kongsfjorden, and a combination of rock types and weathering conditions in the surrounding area of Kongsfjorden, the cause of clay mineral formation and sediment-transport process have been discussed in this paper. The following conclusions are presented:

(1) The combination of clay minerals in the surface sediments from Kongsfjorden is dominated by illite, which is followed by chlorite and kaolinite. No smectite is observed.

(2) Rock strata widely exposed in the area surrounding Kongsfjorden in each period provide an important material basis for the formation of various clay minerals in the surface sediment of Kongsfjorden. Among the strata, kaolinite is from fluvial facies with micro-red sandstone and conglomerate mainly from the middle Carboniferous period. Illite is mainly from low and intermediate metamorphic phyllite, mica schist, and gneiss in the Proterozoic era. Chlorite is mainly from low-grade metamorphic phyllite and mica schist in the Proterozoic era.

(3) Clastic materials are mainly transported into the sea through two geological agents: glaciers and rivers. The gravel, sand, and silt components in the sediments are deposited successively under mechanical sedimentary differentiation. A clay component is mainly composed of clay minerals with fine particles (<2 μm). The component can be easily moved and is difficult to deposit after entering the sea. Its distribution in surface sediments of Kongsfjorden is regular. The content of illite is gradually increased in the leading edge of the glacier in Kongsfjorden, the estuary of glacial-melt water to the sea. Moreover, the content of kaolinite is gradually decreased, and the change in the content of chlorite is not obvious. The content in the process of deposition is restricted by hydrodynamic conditions, flocculation, crystal behavior and provenance. The abnormal changes in the contents of kaolinite and illite in a small scope in the south of Blomstrandhalvøya Island in Kongsfjorden reveal the trajectory of the transportation by the floating ice while entering the sea, which provides a new approach for studying the route of the glacier in entering the sea during historical periods.

Acknowledgements

The authors thank Chinese Arctic and Antarctic Administration and the members of the 4th and 5th Chinese Arctic Research Expedition for their support and assistant. Two anonymous reviewers are greatly thanked because of their kindly comments to this article.

References

Ai Songtao, Wang Zemin, Tan Zhi, et al. 2013. Mass change study on Arctic glacier Pedersenbreen, during 1936-1990-2009. Chinese Science Bulletin, 58(25): 3148–3154, doi: 10.1007/s11434-013-5772-8

Basedow S L, Eiane K, Tverberg V, et al. 2004. Advection of zooplankton in an Arctic fjord (Kongsfjorden, Svalbard). Estuarine, Coastal & Shelf Science, 60(1): 113–124

Beszczyńska-Möller A, Weslawski J M, Węsławski W, et al. 1997. Estimation of glacial meltwater discharge into Svalbard coastal waters. Oceanologia, 39(3): 289–299

Blakemore L C, Swindale L D. 1958. Chemistry and clay mineralogy of a soil sample from Antarctica. Nature, 182(4627): 47–48

Chamley H. 1989. Clay Sedimentology. Berlin: Springer, 1–623

Chen Zhihua, Shi Xuefa, Han Yibing, et al. 2004. Clay mineral distributions in surface sediments from the western arctic ocean and their implications for sediment environments. Advances in Marine Science (in Chinese), 22(4): 446–454

Cottier F, Tverberg V, Inall M, et al. 2005. Water mass modification in an Arctic fjord through cross-shelf exchange: the seasonal hydrography of Kongsfjorden, Svalbard. Journal of Geophysical Research: Oceans, 110(C12): C12005

Dallmann W K, Dypvik H, Gjelberg J G, et al. 1999. Lithostratigraphic lexicon of Svalbard. Oslo: Norsk Polarinstitutt, 1–31

Diekmann B, Petsehick R, Gingele F X, et al. 1996. Clay mineral fluctuations in late quaternary sediments of the southeastern South Atlantic: implications for past changes of deep water advection. In: Wefer G, Berger W H, Siedler G, et al., eds. The South Atlantic. Berlin: Springer, 1–621

Dong Linsen, Liu Yanguang, Shi Xuefa, et al. 2014. Distributions and sources of clay minerals in the surface sediments of the western Arctic Ocean. Haiyang Xuebao (in Chinese), 36(4): 22–32

Ehrmann W U, Melles M, Kuhn G, et al. 1992. Significance of clay mineral assemblages in the Antarctic Ocean. Marine Geology, 107(4): 249–273

Elverhøi A, Svendsen J I, Solheim A, et al. 1995. Late Quaternary sediment yield from the high Arctic Svalbard area. The Journal of Geology, 103: 1–17

Esquevin J. 1969. Influence de la composition chimique des illites surcristallinite. Bull Centre Rech Rau-SNPA, 3(1): 147–153

Gilbert R. 2000. Environmental assessment from the sedimentary record of high-latitude fiords. Geomorphology, 32(3-4): 295–314

Gingele F X, Leipe T. 1997. Clay mineral assemblages in the western Baltic Sea: recent distribution and relation to sedimentary units. Marine Geology, 140(1–2): 97–115

Griffin J J, Windom H, Goldberg E D. 1968. The distribution of clay minerals in the World Ocean. Deep Sea Research and Oceanographic Abstracts, 15(4): 433–459

Hagen J O, Kohler J, Melvold K, et al. 2003. Glaciers in Svalbard: mass balance, runoff and freshwater flux. Polar Research, 22(2): 145–159

Halldal P, Halldal K. 1973. Phytoplankton, chlorophyll and submarine light conditions in Kings Bay, Spitsbergen, July 1971. Norwegian Journal of Botany, 20: 99–108

Hisdal V. 1998. Svalbard Nature and History. Oslo: Norsk Polarinstitutt, 1–12
Hjelle A. 1993. Geology of Svalbard. Oslo: Norsk Polarinstitutt, 1–165
Hjelle A, Lauritzen Ø. 1982. Geological Map of Svalbard 1:500 000. Sheet 3G, Spitsbergen Northern Part. Oslo: Norsk Polarinstitutt Skrifter, 154 C
Hop H, Pearson T, Hegseth E N, et al. 2002. The marine ecosystem of Kongsfjorden, Svalbard. Polar Research, 21(1): 167–208
Ingvaldsen R, Reitan M B, Svendsen H, et al. 2001. The upper layer circulation in Kongsfjorden and Krossfjorden-a complex fjord system on the west coast of Spitsbergen (scientific paper). Memoirs of National Institute of Polar Research. Special Issue, 54: 393–407
Ito H, Kudoh S. 1997. Characteristics of water in Kongsfjorden, Svalbard. Proceedings of the NIPR Symposium on Polar Meteorology and Glaciology, 11: 211–232
Ji Zhongqiang, Gao Shengquan, Jin Haiyan, et al. 2014. Nutrient distribution and the influencing factors of seawater in Arctic Kongsfjorden, summer 2010. Haiyang Xuebao (in Chinese), 36(10): 80–89
Jiang Xiaodong, He Jianfeng, Cai Minghong. 2005. Abundance and biomass of heterotrophic microbes in the Kongsfjorden, Svalbard. Acta Oceanologica Sinica, 24(6): 143–152
Jones V J, Birks H J B. 2004. Lake-sediment records of recent environmental change on Svalbard: results of diatom analysis. Journal of Paleolimnology, 31(4): 445–466
Keck A. 1999. West Spitsbergen fjords (Svalbard, Norwegian Arctic): physical setting and sedimentation. In: Heiskanen A S, Lundsgaard M, Reigstad K, et al., eds. Sedimentation and Recycling in Aquatic Ecosystems-the Impact of Pelagic Processes and Planktonic Food Web Structure. Helsinki: The Finnish Environment Institute, 263: 58–68
Krumm S, Buggisch W. 2010. Sample preparation effects on illite crystallinity measurement: grain-size gradation and particle orientation. Journal of Metamorphic Geology, 9(6): 671–677
Kwasniewski S, Hop H, Falk-Petersen S, et al. 2003. Distribution of *Calanus* species in Kongsfjorden, a glacial fjord in Svalbard. Journal of Plankton Research, 25(1): 1–20
Landvik J Y, Bolstad M, Lycke A K, et al. 1992. Weichselian stratigraphy and palaeoenvironments at Bellsund, western Svalbard. Boreas, 21(4): 335–338
Landvik J Y, Bondevik S, Elverhøi A, et al. 1998. The last glacial maximum of Svalbard and the Barents sea area: ice sheet extent and configuration. Quaternary Science Reviews, 17(1–3): 43–75
Lefauconnier B, Hagen J O, Ørbæk J B, et al. 1999. Glacier balance trends in the Kongsfjorden area, western Spitsbergen, Svalbard, in relation to the climate. Polar Research, 18(2): 307–313
Lefauconnier B, Hagen J O, Rudant J P. 1994. Flow speed and calving rate of Kongsbreen glacier, Svalbard, using SPOT images. Polar Research, 13(1): 59–65
Lehman S J, Forman S L. 1992. Late weichselian glacier retreat in kongsfjorden, west Spitsbergen, Svalbard. Quaternary Research, 37(2): 139–154
Li Jun, Gao Jianhua, Wang Yaping, et al. 2012a. Distribution and dispersal pattern of clay minerals in surface sediments, eastern Beibu Gulf, South China Sea. Acta Oceanologica Sinica, 31(2): 78–87
Li Chuanshun, Shi Xuefa, Kao Shuji, et al. 2012b. Clay mineral composition and their sources for the fluvial sediments of Taiwanese rivers. Chinese Science Bulletin, 57(6): 673–681
Lydersen C, Gjertz I. 1986. Studies of the ringed seal (Phoca hispida Schreber 1775) in its breeding habitat in Kongsfjorden, Svalbard. Polar Research, 4(1): 57–63
Naidu A S, Burrell D C, Hood D W. 1971. Clay mineral composition and geologic significance of some Beaufort Sea sediments. Journal of Sedimentary Research, 41(3): 691–694
Naidu A S, Creager J S, Mowatt T C. 1982. Clay mineral dispersal patterns in the north Bering and Chukchi Seas. Marine Geology, 47(1–2): 1–15
Naidu A S, Han M W, Mowatt T C, et al. 1995. Clay minerals as indicators of sources of terrigenous sediments, their transportation and deposition: Bering Basin, Russian-Alaskan Arctic. Marine Geology, 127(1–4): 87–104
Naidu A S, Mowatt T C. 1983. Sources and dispersal patterns of clay minerals in surface sediments from the continental-shelf areas off Alaska. Geological Society of America Bulletin, 94(7): 841–854
Nordli P Ø, Hanssen-Bauer I, Forland E J. 1996. Homogeneity analyses of temperature and precipitation series from Svalbard and Jan Mayen. Klima 16/96. Oslo: Norwegian Meteorological Institute
Nürnberg D, Wollenburg I, Dethleff D, et al. 1994. Sediments in Arctic sea ice: implications for entrainment, transport and release. Marine Geology, 119(3–4): 185–214
Pan Zhaolu, Zhao Aixing, Pan Tiehong. 1993. Crystallography and Mineralogy (in Chinese). 3rd ed. Beijing: Geological Press, 178–179
Papucci C, Delfanti R, Mordeglia B. 1998. Radionuclides as tracers of particle dynamics in the W-Svalbard marine environment. In: Casacchia R, eds. The Arctic and Global Change. Multidisciplinary and International Efforts at Ny-Ålesund: Proceedings from the Fourth Ny-Ålesund Seminar. v 7. Ravello, Italy: Ny-Ålesund Science Managers Committee Public, 185–192
Petschick R, Kuhn G, Gingele F. 1996. Clay mineral distribution in surface sediments of the South Atlantic: sources, transport, and relation to oceanography. Marine Geology, 130(3–4): 203–229
Rateev M A, Gorbunova Z N, Lisitzyn A P, et al. 2010. The distribution of clay minerals in the oceans. Sedimentology, 13(1–2): 21–43
Schlitzer R. 2015. Ocean data view. http://odv.awi.de [2015-05-15/2017-02-07]
Shi Xuefa. 1995. Progress and trends in marine clay minerals research. Marine Geology Letters (in Chinese), (1): 1–3
Shi Fengdeng, Cheng Zhenbo, Wu Yonghua, et al. 2011. The research on glacial-marine deposit types and sedimentary processes in the arctic Kongsfjorden. Haiyang Xuebao (in Chinese), 33(2): 115–123
Sollid J L, Sørbel L. 1992. Rock glaciers in Svalbard and Norway. Permafrost and Periglacial Processes, 3(3): 215–220
Stein R, Dittmers K, Fahl K, et al. 2004. Arctic (palaeo) river discharge and environmental change: evidence from the Holocene Kara Sea sedimentary record. Quaternary Science Reviews, 23(11–13): 1485–1511
Stein R, Grobe H, Wahsner M. 1994. Organic carbon, carbonate, and clay mineral distributions in eastern central Arctic Ocean surface sediments. Marine Geology, 119(3–4): 269–285
Svendsen H, Beszczynska-Møller A, Hagen J O, et al. 2002. The physical environment of Kongsfjorden-Krossfjorden, an Arctic fjord system in Svalbard. Polar Research, 21(1): 133–166
Syvitski J P M. 1980. Flocculation, agglomeration, and zooplankton pelletization of suspended sediment in a fjord receiving glacial meltwater. In: Freeland H J, Farmer D M, Levings C D, eds. Fjord Oceanography. Boston, MA: Springer US, 615–623
Syvitski J P M. 2002. Sediment discharge variability in Arctic rivers: implications for a warmer future. Polar Research, 21(2): 323–330
Syvitski J P M, Shaw J. 1995. Sedimentology and geomorphology of fjords. Developments in Sedimentology, 53: 113–178
Tang Yanjie, Jia Jianye, Xie Xiande. 2002. Environment significance of clay minerals. Earth Science Frontiers (in Chinese), 9(2): 337–344
Viscosi-Shirley C, Mammone K, Pisias N, et al. 2003. Clay mineralogy and multi-element chemistry of surface sediments on the Siberian-Arctic shelf: implications for sediment provenance and grain size sorting. Continental Shelf Research, 23(11-13): 1175–1200
Wlodarska-Kowalczuk M, Pearson T H. 2004. Soft-bottom macrobenthic faunal associations and factors affecting species distributions in an Arctic glacial fjord (Kongsfjord, Spitsbergen). Polar Biology, 27(3): 155–167
Wlodarska-Kowalczuk M, Szymelfenig M, Zajiczkowski M. 2007. Dynamic sedimentary environments of an Arctic glacier-fed river estuary (Adventfjorden, Svalbard): II. Meio- and macrobenthic

fauna. Estuarine, Coastal & Shelf Science, 74(1–2): 274–284

Xia Chonghuan, Xie Zhouqing. 2007. Environmental change in Ny-Ålesund, Arctic as recorded in lake sediments. Journal of University of Science and Technology of China (in Chinese), 37(8): 1003–1008

Xu Mingxing, Yan Ming, Kang Jiancheng, et al. 2007. Progress in studies on mass balance of glaciers, Svalbard, arctic. Journal of Glaciology and Geocryology (in Chinese), 29(5): 730–737

Yang Hefu. 1988. The infrared spectral analysis of Kaolinite in the clay minerals of surface sediment from Prydz Bay and adjacent sea area. Antarctica. Marine Sciences (in Chinese), 12(3): 25–30

Zajączkowski M. 2002. On the use of sediment traps in sedimentation measurements in glaciated fjords. Polish Polar Research, 23(2): 161–174

Zajączkowski M. 2008. Sediment supply and fluxes in glacial and outwash fjords, Kongsfjorden and Adventfjorden, Svalbard. Polish Polar Research, 29(1): 59–72

Zajączkowski M, Legeżyńska J. 2001. Estimation of zooplankton mortality caused by an Arctic glacier outflow. Oceanologia, 43(3): 341–351

Zajączkowski M, Szczuciński W, Bojanowski R. 2004. Recent changes in sediment accumulation rates in Adventfjorden, Svalbard. Oceanologia, 46(2): 217–231

Zhang Deyu, Gao Aiguo, Zhang Daojian. 2008. Clay minerals in surface sediments from the Chukchi Sea and Canadian Basin. Advances in Marine Science (in Chinese), 26(2): 171–183

Zhu Fengguan. 1987. Origin of Kaolinite from sediments in Prydz Bay and adjacent sea area in the Antarctic. Marine Geology & Quaternary Geology (in Chinese), 7(3): 37–46

Zhu Renbin, Ding Wei, Hou Lijun, et al. 2014. Matrix-bound phosphine and phosphorus fractions in surface sediments of Arctic Kongsfjorden, Svalbard: effects of glacial activity and environmental variables. Chemosphere, 103: 240–249

Ziaja W. 2001. Glacial recession in sørkappland and central nordenskiöldland, Spitsbergen, Svalbard, during the 20th century. Arctic, Antarctic, and Alpine Research, 33(1): 36–41

Acta Oceanol. Sin., 2018, Vol. 37, No. 5, P. 39–46
DOI: 10.1007/s13131-018-1209-1
http://www.hyxb.org.cn
E-mail: hyxbe@263.net

Time correction of the ocean bottom seismometers deployed at the southwest Indian ridge using ambient noise cross-correlation

LIU Yunlong[1, 2], LIU Cai[1], TAO Chunhui[1, 2]*, YAO Huajian[3], QIU Lei[2], WANG Ao[2, 4], RUAN Aiguo[2], WANG Hanchuang[2], ZHOU Jianping[2], LI Huaiming[2], DONG Chuanwan[2, 5]

[1] College of Geoexploration Science and Technology, Jilin University, Changchun 130026, China

[2] Key Laboratory of Submarine Geosciences, Second Institute of Oceanography, State Oceanic Administration, Hangzhou 310012, China

[3] Laboratory of Seismology and Physics of Earth's Interior, School of Earth and Space Sciences, University of Science and Technology of China, Hefei 230026, China

[4] Institute of Geophysics and Geomatics, China University of Geosciences, Wuhan 430074, China

[5] School of Earth Sciences, Zhejiang University, Hangzhou 310027, China

Received 7 September 2017; accepted 3 January 2018

Abstract

Seismic monitoring using ocean bottom seismometers (OBS) is an efficient method for investigating earthquakes in mid-ocean ridge far away from land. Clock synchronization among the OBSs is difficult without direct communication because electromagnetic signals cannot propagate efficiently in water. Time correction can be estimated through global positioning system (GPS) synchronization if clock drift is linear before and after the deployment. However, some OBSs in the experiments at the southwest Indian ridge (SWIR) on the Chinese DY125-34 cruise had not been re-synchronized from GPS after recovery. So we attempted to estimate clock drift between each station pairs using time symmetry analysis (TSA) based on ambient noise cross-correlation. We tested the feasibility of the TSA method by analyzing daily noise cross-correlation functions (NCFs) that extract from the data of another OBS experiment on the Chinese DY125-40 cruise with known clock drift and the same deployment site. The results suggest that the NCFs' travel time of surface wave between any two stations are symmetrical and have an opposite growing direction with the date. The influence of different band-pass filters, different components and different normalized methods was discussed. The TSA method appeared to be optimal for the hydrophone data within the period band of 2–5 s in dozens of km-scale interstation distances. A significant clock drift of ~2 s was estimated between OBSs sets through linear regression during a 108-d deployment on the Chinese cruise DY125-34. Time correction of the OBS by the ambient noise cross-correlation was demonstrated as a practical approach with the appropriate parameters in case of no GPS re-synchronization.

Key words: clock drift, cross-correlation, ambient noise, OBS

Citation: Liu Yunlong, Liu Cai, Tao Chunhui, Yao Huajian, Qiu Lei, Wang Ao, Ruan Aiguo, Wang Hanchuang, Zhou Jianping, Li Huaiming, Dong Chuanwan. 2018. Time correction of the ocean bottom seismometers deployed at the southwest Indian ridge using ambient noise cross-correlation. Acta Oceanologica Sinica, 37(5): 39–46, doi: 10.1007/s13131-018-1209-1

1 Introduction

Hydrothermal fields at mid-ocean ridges are active areas of magma and tectonics with frequent induced seismic activity. Most of this activity is low magnitude earthquakes that cannot be detected by seismic stations on land. Our study area, the Dragon Horn field (e.g., Tao et al., 2012, 2014) is located at 49.6°E on the Southwest Indian Ridge, which is more than 2 000 km far from the adjacent African continent to the north and Antarctica to the south. Ocean bottom seismometer (OBS) monitoring systems are thus necessary to explore the microearthquakes related to magmatism in the hydrothermal environment. Previously, a single OBS developed near the Longqi hydrothermal vents recorded thousands of earthquakes with a small magnitude (M_L<3) (Liu et al., 2018). In order to improve the accuracy of the epicenter measurements, our group conducted experiments with OBS arrays during the cruises CDC 34th and 40th (hereinafter referred to as CDC 34th and 40th of Chinese DY125-34 and DY125-40 cruises).

Time synchronization must be considered when processing seismic data. Clock drift between OBS arrays is common because OBSs do not have real-time synchronization with GPS, which is in contrast to onshore monitoring stations. Generally, an internal clock with a crystal oscillator reckons an OBS recording. The frequency of the crystal oscillator can be changed depending on its environments with regards to temperature and pressure (Gardner and Collins, 2012). Moreover, such clock drift can accumulate up to several seconds for a long observation. Application of the double-difference technique to the relocation of microearthquakes near the Longqi hydrothermal vents requires accuracy of tens of meters in order to study the hydrothermal circula-

Foundation item: China Ocean Mineral Resources R & D Association Major Project under contract No. DY135-S1-01; the National Natural Science Foundation of China under contract Nos 41506078, 41706042 and 41522404; the Basic Research Foundation of Second Institute of Oceanography, SOA under contract No. JG0608.
*Corresponding author, E-mail: taochunhuimail@163.com

tion and detachment faults where microearthquakes are concentrated (e.g., Stroup et al., 2009; Pontbriand and Sohn, 2014; Schlindwein and Schmid, 2016). Therefore, suitable correction of clock drift is necessary for the location of earthquakes with high-precision and tomographic inversion of velocity structure (Gouedard et al., 2014). The instrument clock can be synchronized to a GPS time prior to a typical OBS deployment, and the offset from GPS time is measured immediately after recovery, which allows a linear drift to be removed from the dataset. However, in the processing of recycled OBS in CDC 34th, GPS resynchronization was unsound, and clock drift could not be corrected. Hence, we use noise cross-correlation to synchronize the clocks between station pairs among an array of OBSs based on the continuous recording of ambient noise (e.g., Sabra et al., 2005; Stehly et al., 2007; Sens-Schönfelder, 2008; Gouedard et al., 2014).

The technique of retrieving surface wave Green functions by ambient noise cross-correlation is used to obtain group or phase velocity for ambient noise tomography (e.g., Shapiro et al., 2005; Yao et al., 2006, 2011), as well as to correct the time error of the stations and measure the time variation of clock drift with the date (e.g., Stehly et al., 2007; Sens-Schönfelder, 2008; Gouedard et al., 2014). The possibility of using the oceanic ambient noise cross-correlation function to estimate the time offset between two hydrophone arrays with a large value of 35 s was confirmed by Sabra et al. (2005). Stehly et al. (2007) separated time shifts associated with instrumental clock drift from the Green's function by observing the evolution of surface-wave travel times over approximately 11 years of continuous recordings. The accuracy of this method was proposed by Sens-Schönfelder (2008) to exceed the precision of the internal station clocks after only a single day of uncorrected drift. It was later applied by Hannemannn et al. (2014) to synchronize clocks of a deep water OBS arrays with a 75 km aperture, which showed that the linear drift was visible in the correlation results of the vertical components and the hydrophone. Gouedard et al. (2014) presented two techniques to retrieve clock drift between OBSs that is the time symmetry analysis (TSA) method and the virtual doublet analysis method, and discussed their advantages and drawbacks. For a fully isotropic noise source, TSA has a superior resolution over a long time scale.

In our experiments, two OBS arrays were developed in the Dragon Horn area at different cruises (CDC 34th and CDC 40th). We tested the feasibility of TSA for ambient noise cross-correlation using CDC 40th dataset with known clock drift. Here we used 37-d continuous records to extract the surface wave part of the Green's function. Time variation of symmetry of the noise cross-correlation functions (NCFs) using different components, time window duration and period bands were discussed in order to select the best parameter for achieving the recovery of the Green's function from ambient noise (Campillo, 2006). Furthermore, we applied these parameters to measure relative clock drift between the OBSs of CDC 34th by the same method. Finally, the relative clock drifts with time between station pair were calculated using the linear form $y=kx+b$.

2 Data and methods

2.1 *Data acquisition*

In 2015, we conducted an OBS experiment during CDC 34th to better interpret the geological processes of hydrothermal circulation in the Longqi field (37.7°S, 49.6°E). Four OBSs with three-component seismometers and a hydrophone were deployed in the 2.5–3.5 km deep water near the Longqi vents from December 2014 to April 2015. As shown in Fig. 1, there were two kinds of OBS: (1) Geopro Sedis IV (60 s–50 Hz) made in Germany; and (2) 1-4C long-period OBS (30 s–50 Hz) developed independently by the Institute of Geology and Geophysics, Chinese Academy of Sciences (Ruan et al., 2010). The longest interval in the OBS array was approximately 20 km. The OBSs recorded seismic data over approximately four month with a sampling rate of 100 Hz for the German devices and 50 Hz for the Chinese ones. During recovery, OBS did not resynchronize from GPS after rising from the water because of instrument malfunction. Therefore the clock drift could not be calibrated by linear regression after resynchronization.

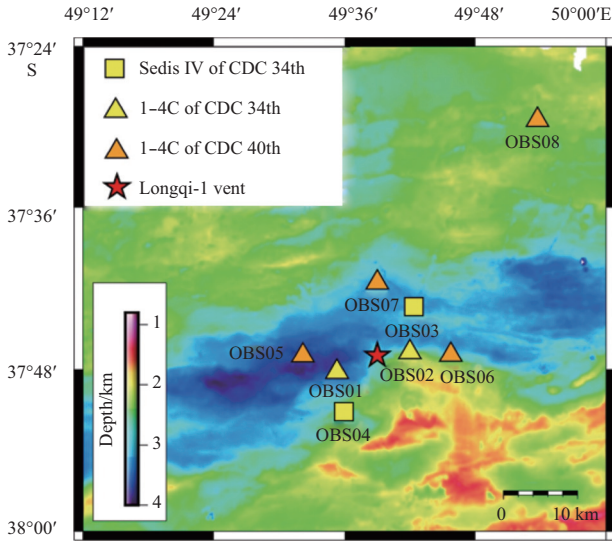

Fig. 1. Bathymetric maps of the Dragon Horn area showing the location of OBSs. Yellow symbols denote the OBSs of CDC 34th (the rectangles are the Sedis IV made in Germany and the triangles the 1-4C made in China), orange triangles the 1-4C OBSs of CDC 40th, and the red star the Longqi-1 hydrothermal vent.

A series of OBS arrays with a larger scale of ~30 km were deployed in the same field in 2016 for a period of 37 days during the CDC 40th. Four of them were used to calculate the clock drift by ambient noise cross-correlation due to the known time shift in clock drift (Fig. 1). The time shift rate of these OBSs was determined by a computed crystal oscillator difference with a range of 2–20 s per year. These large clock drifts cannot be ignored for recording over a long period. The OBSs recording of CDC 40th is used to test the feasibility of the TSA method and the appropriation of different parameters such as the surface wave period band, the instrument component and the duration of the time window.

2.2 *Time symmetry analysis method*

When noise sources are distributed homogeneously, the Green's function of the medium is reconstructed flawlessly, for a pair of stations the surface wave travel time should be symmetrical and not vary with time. In a practice however, the recorded wave-field is not isotropic and the travel time of the NCF is asymmetrical. Three main factors can lead to the asymmetry of NCFs: (1) physical property changes in the medium; (2) temporal variations in the spatial distribution of noise sources; and (3) clock drift of the stations. In our OBS deployment, firstly, variations in crustal velocities are usually negligibly small; secondly, in the

seabed environment, the main noise is the secondary ocean microseisms with a period of ~4 s (Aster et al., 2008) in deep water. We selected the secondary ocean microseisms that are distributed nearly equally in a diffuse field by filtering in a convenient band (Webb et al., 1991; Dolenc et al., 2005), as discussed in the following section. In this way, we assumed the asymmetry of NCF travel time to result from the clock drift among the OBSs.

Based on the above assumptions, we used the TSA method to determine the clock drift of each station pairs. Normally, the clock drift can be decomposed into static clock drift (stationary) and dynamic clock drift (changing in time). A synthetic test to demonstrate how clock drift influences the correlation results in 30 s time windows and how to measure the static and dynamic clock drift respectively is displayed in Fig. 2 (Hannemann et al., 2014). Several wavelets occurring every 30 s starting at 10 s at Trace 1 and 5 s at Trace 2 were used instead of consecutive ambient noise. A time variation clock drift of 1 s per 100 s at Trace 1 was then added (red dashed line in Fig. 2). The cross-correlation method was applied to Trace 1 and Trace 2 in the fixed time window (blue box in Fig. 2). The static clock drift (dt^{stat}) and dynamic clock drift (dt^{dyn}) were measured from zeros-shift of lag time marked in the cross-correlation results. We could then estimate the static clock drift and dynamic clock drift as a sample workflow extract following the method of Gouedard et al. (2014):

(1) For each pair of OBSs, we calculated a daily NCF $s(t)$ consisting of the causal parts from one side and the anti-causal parts coming from the opposite side, denoted as $s^{+}(t)$ and $s^{-}(t)$ and written as

$$\left.\begin{aligned} s\left(t\right) &= s^{-}\left(t\right) + s^{+}\left(t\right). \\ s^{+}\left(t\right) &= 0, t < 0;\ s^{-}\left(t\right) = 0, t > 0. \end{aligned}\right\} \tag{1}$$

(2) The first daily NCF was used as our reference trace $r(t)$ which is decomposed into $r^{+}(t)$ and $r^{-}(t)$, akin to what was described in Eq. (1). The reference trace was correlated with the correlation results of the station pairs at all other dates. The time shift dt^{+} and dt^{-} for the positive and negative sides were measured by selecting the lag time for the maximum cross-correlations $r^{+}\left(t\right) \otimes s^{+}\left(t\right)$ and $r^{-}\left(t\right) \otimes s^{-}\left(t\right)$, respectively. Then the dynamic clock drift was obtained by the difference $dt^{+} - dt^{-}$ as follows:

$$dt^{\mathrm{dyn}} = \frac{dt^{+} - dt^{-}}{2}. \tag{2}$$

(3) Likewise, the static clock drift dt^{stat} was obtained from the cross-correlation $r^{+}\left(t\right) \otimes r^{-}\left(t\right)$ as described in the dynamic clock drift, and finally the absolute clock drift was obtained as

$$dt^{\mathrm{rel}} = dt^{\mathrm{dyn}} + dt^{\mathrm{stat}}. \tag{3}$$

(4) For any three stations A, B and C, the relative clock drifts $dt^{\mathrm{rel}}_{\mathrm{AB}}$, $d^{\mathrm{rel}}_{\mathrm{BC}}$ and $dt^{\mathrm{rel}}_{\mathrm{AC}}$ between each pair must satisfy the closure relation:

$$dt^{\mathrm{rel}}_{\mathrm{AB}} + dt^{\mathrm{rel}}_{\mathrm{BC}} - dt^{\mathrm{rel}}_{\mathrm{AC}} = 0. \tag{4}$$

To help reduce the error in the clock drift, the closure relations between all combinations of the three stations as an additional constraint were considered. Hence, we determined the optimal clock drift of each station pairs at all dates by conjugate gradient methods to find the optimal solution of the linear Eq. (4).

The feasibility of the TSA approach was firstly verified by estimating the clock drift of the OBSs during the survey of CDC 34th with the known clock drift. Secondly, the signal to noise ratio (SNR) of NCFs in the four recording components was estimated and the superior one was selected and cross-correlated. We also analyzed the symmetry of the NCFs in different bands to test which frequency band was appropriate for recovering the Green's function from ambient noise. Furthermore, through observing the time variation of NCFs, the clock drift with date was computed by linear regression and the measurement error was estimated by comparing the estimated drift with the expected one. Finally, we confirmed that the clock drift estimated by ambient noise cross-correlation was good, and applied it to compute

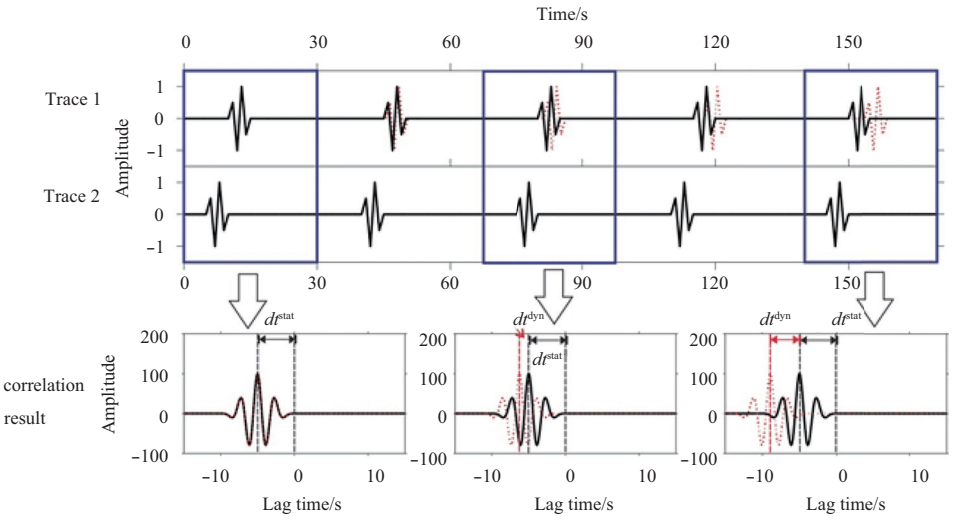

Fig. 2. Schematic plots of generating the clock drifts by a wavelet. The black solid line represents waveforms and their correlation results without time-shift, and the red dashed line waveform with time-shift; dt^{stat} is the static drift, dt^{dyn} the dynamic time-shift, and the total clock drift $dt^{\mathrm{rel}} = dt^{\mathrm{dyn}} + dt^{\mathrm{stat}}$; correlation results between Trace 1 and Trace 2 are given for un-shifted time windows (blue boxes). This figure is modified from Figure 3 in Hannemann et al. (2014).

the clock drift of OBSs on CDC 34th using the appropriate parameters discussed in the next section.

3 Results and discussion

3.1 *Time symmetry of NCFs on CDC 40th*

In this study, we used the TSA method for experiments on CDC 40th. Prior to computing the cross-correlations, several data processing methods were considered for recovering the Green's function of ambient noise and improving the SNR of NCFs.

3.1.1 *Influence of component selection*

The seismic data were cross-correlated between each station pairs in 1-d records to form the daily NCFs following preprocessing of down-sampling, spectrum whitening, amplitude normalization and low frequency band-pass filtering. Figure 3 shows an example of daily NCFs for four components filtered in the period band of 2–5 s at the available pair of OBS05 and OBS07. The hydrophone and vertical seismometer share the symmetry of the daily NCFs. However, by selecting the maximum NCFs (marked by the red dots in Fig. 3), the measured lag time of the horizontal component infrequently shows the level of symmetry expected due to low SNR of the horizontal recordings. To measure the quality of the NCFs results in different components, we calculated the SNR according to the following method: (1) a signal window was selected around the arrival time of the surface wave and the maximum of the absolute value in this time window was found; (2) the mean square deviation of noise signal in the selected window was then computed based on the actual situation; and (3), finally the SNR of the NCFs was defined as

$$SNR = \frac{\max(|S_i|)}{\sqrt{\frac{\sum_{j=1}^{n}(N_j-\bar{N})^2}{n-1}}}, \tag{5}$$

where S_i is the signal sequence of the m length, N_j is the noise sequence of the n length, $\bar{N}$ is the mean of noise sequence, $i = 1, 2, \ldots, m; j = 1, 2, \ldots, n$.

Using the Eq. (5) the SNR of NCFs was calculated for each day and then stacked them to a total of 37 d. We selected 5 s around the surface wave arrival time for signal and 60–80 s of the lag time for noise. The result indicates that the SNR of the stacked NCFs in the hydrophone component is highest at 7.6 and the second highest is the vertical component of 6.0. However, they are relatively low in the other two horizontal components (west-east component and north-south component) at 5.3 and 2.4 respectively. Hannemann et al. (2014) found good agreement in the clock drift behavior between the vertical seismometer and the hydrophone by comparing their correlation results. Furthermore, the hydrophone usually works well and the vertical component is occasionally clamped. Combined with our study results, we used the hydrophone component signal for cross-correlation in the following processing.

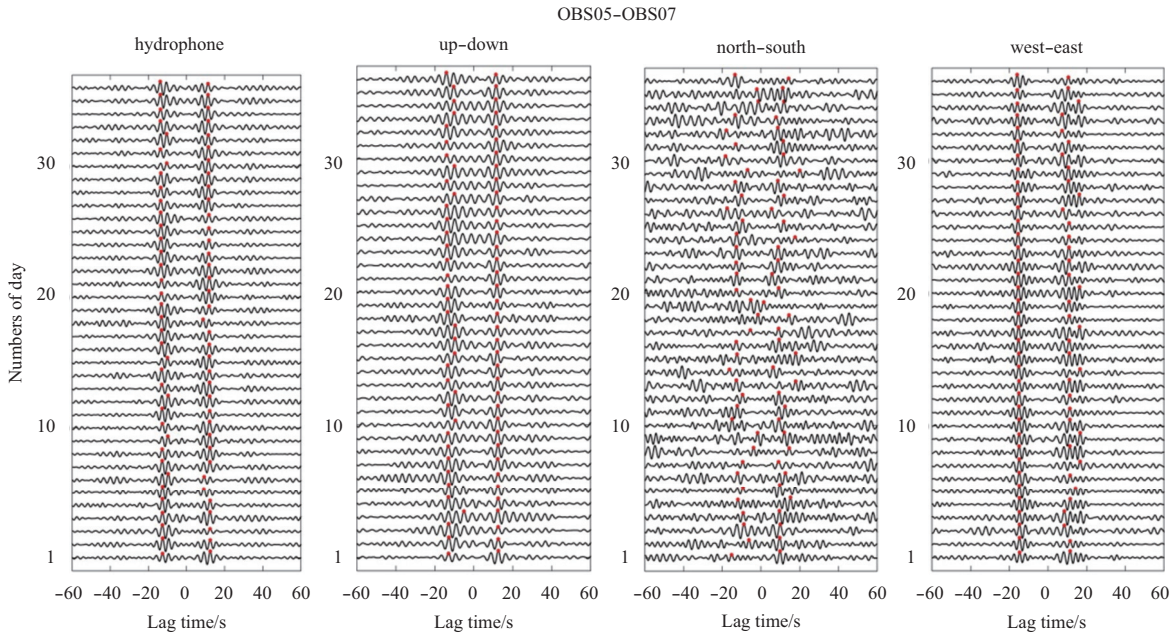

Fig. 3. Daily NCFs at the pair of OBS05-OBS07 in the 2–5 s period band in four components: hydrophone component, up-down component, north-south component and west-east component. Both positive and negative times were selected by the maximum of each daily NCF marked by the red dots.

3.1.2 *Influence of band-pass in different period bands*

The NCFs in several narrow bands (1–2 s, 2–5 s, 5–10 s and 10–20 s) was investigated to determine what part of the period band is usable, as shown in Fig. 4. The daily NCFs of the hydrophone recording between the station pairs in each band were computed. In order to evaluate the SNR of the NCFs in these bands, Eq. (5) was also used to find an appropriate band. The results show that the signal filtered in the 2–5 s band has a higher SNR of 7.2 than those in the other bands (SNR=2.8, 1–2 s; SNR=5.9, 5–10 s; SNR=2.1, 10–20 s) and the symmetry of the NCFs in the band of 2–5 s is superior to the others (Fig. 4).

On the other hand, Bensen et al. (2007) summarized the empirical relation Eq. (6) based on many tests on the recovery of Green's function:

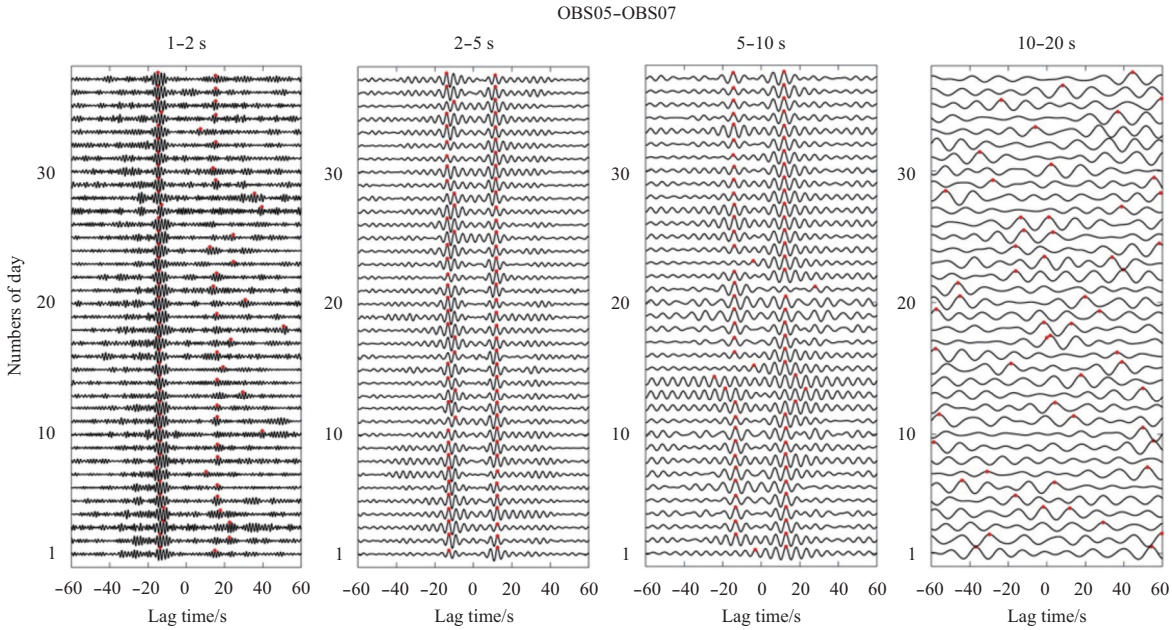

Fig. 4. Daily NCFs for the pair OBS05-OBS07 on the hydrophone components in different period bands: 1–2 s, 2–5 s, 5–10 s, and 10–20 s. Both positive and negative travel times are selected by the maximum of each day NCF marked by the red dots.

$$r \geqslant 3\lambda = 3cT \rightarrow T \leqslant \frac{r}{3c}, \tag{6}$$

where r is the interstation distances, λ is the wavelength, c is the surface wave phase velocity, and T is the selected period. This means that the longest period of the recovered Green's function from ambient noise recorded by the two stations should be less than one third of the ratio of station spacing to phase speed. The longest period adopted was 5 s because of the greatest interstation distance of 30 km and a surface wave velocity of 2 km/s. Additionally, the SNR of cross-correlation results of the signal filtered in 2–5 s is the highest, thus we used this period band as an appropriate parameter in the processing of NCFs.

3.1.3 *Time variation of NCFs*

The fluctuation of the NCFs following the time variation using 37-d records on the hydrophone component filtered in the period band of 2–5 s was analyzed. We also computed clock drift, based on the time delay measurements. Before obtaining NCFs between every two station pairs, preprocessing was necessary as described in details by Bensen et al. (2007). These include removal of instrument response, resampling, removal of mean and trend, band-pass filter, temporal normalization and spectrum whiting. Specifically, amplitude normalization in the time domain was necessary because the surface wave travel time of NCFs is influenced by large earthquakes and any unstable noise sources near the station. The two normalization methods are one-bit and running-average. The latter is widely used to remove the earthquakes effect and air gun signals during the experiments to improve the SNR (Larose et al., 2004). We compared the two methods by computing the SNR of NCFs as Eq. (5). The SNR results using a running average were a little higher than for the one-bit method. Hence, we used the normalization method of the running average in our study. Additionally, we assume the instrument response is the same for the same kind of OBS and so the influence from the removal of instrument response is limited.

Six pairs of daily NCFs among the four OBSs are shown in Fig. 5. We observed a clear linear trend for the NCFs with date, which indicates the influence of dynamic clock drift between OBSs. For example, amplitude in the positive and the negative parts between the OBS05 and OBS06 is different, which may be due to inhomogeneous illumination of noise sources (Stehly et al., 2006), but the positive and negative times are symmetrical and change with time. Stehly et al. (2007) proposed that the clock drift between the two stations would produce a time-shift of NCFs resulting in a longer travel time in the positive time and a shorter travel time in the negative time or vice versa and their differences would remain the same by observing evolution of cross-correlation results with date.

To confirm that the linear variation in the positive and negative time is almost exclusively affected by clock drift, we tested cross-correlation results of different length for one day, two day and five day (Fig. 6). The time shifts satisfied the linear regression between the start and the end of the experiment and the dynamic clock drift can be obtained by the slope of the date. Table 1 shows variation rate of the dynamic clock drift per day measured by the time shift of NCFs of one day, two days and five days using linear regression. The theoretical dynamic clock drifts in Table 1 were obtained by the computed crystal oscillator difference of the instrument. Compared with the standard frequency of a crystal oscillator (12 288 000 Hz), the instruments began with a variance recorded in the log file because of the temperature and pressure influence of the surrounding environment. We used a simple relationship in Eq. (7) to compute the theoretical dynamic drift per day:

$$dt_{ij}^{\text{the}} = \frac{PClk_i - PClk_j}{12\ 288\ 000} \times 24 \times 3\ 600, \tag{7}$$

where $PClk_i$ and $PClk_j$ are the vibration frequency of crystal oscillator of the ith and jth OBS respectively; i, j=1, 2, 3, 4 represent the number of the OBS.

The clock drift rates of different day lengths were almost identical (Table 1). The largest error was 0.003 4 s per day. Therefore the NCF time shifts that changed linearly with date in Fig. 5

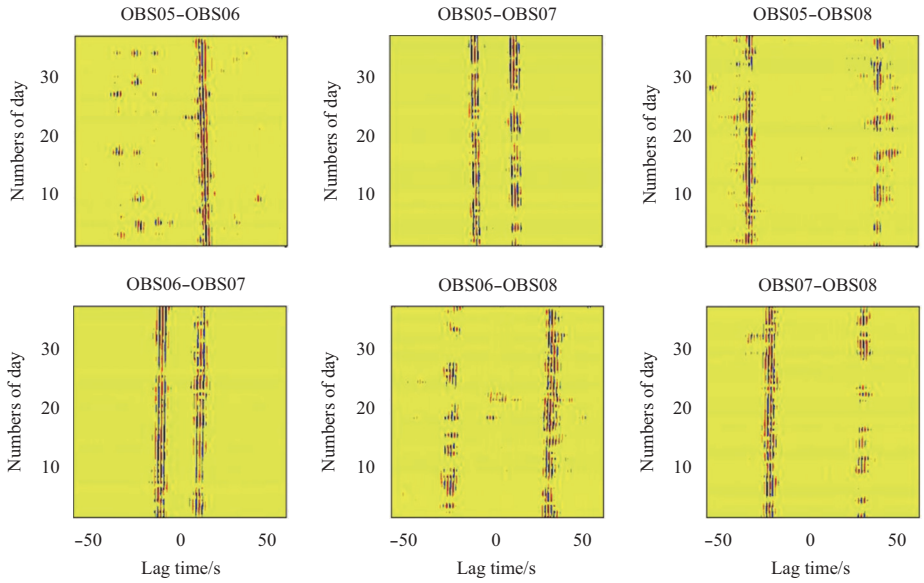

Fig. 5. Daily NCFs on the hydrophone component in the band of 2–5 s between each pair of the four stations. The window of lag time ranges from –60 s to 60 s, which is enough for the surface-wave arrival time in this case.

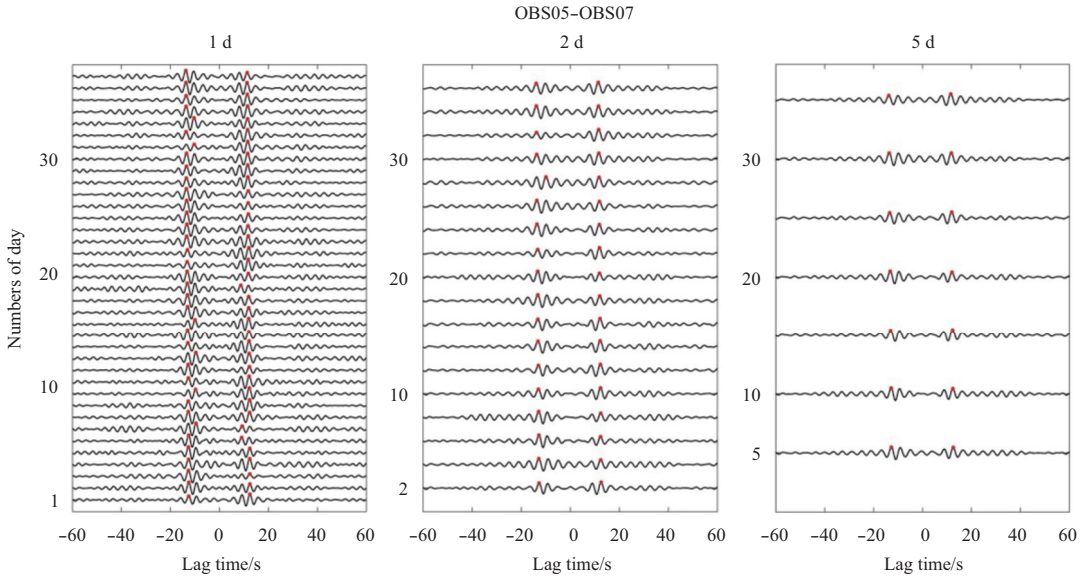

Fig. 6. NCFs of one day, two days and five days at the pair of OBS05-OBS07 on the hydrophone components filtered in the band of 2–5 s. Both positive and negative times are indicated by the maximum of NCFs marked by the red dots.

results from the influence of the dynamic clock drift between stations. Meanwhile, the dynamic shift due to a change in the spatial distribution of the noise source was expected to decrease when increasing the length of the correlated time-series. This was because of the improved spatial homogenization of the noise for a longer time. Concurrently, the time resolutions of the longer time become lower. In our cross-correlation results, symmetry of the NCFs was good and only slightly affected by the temporal variations in source distribution. Therefore we utilized the time series of one day for the time window of cross-correlation in this paper.

3.1.4 *Estimation of time error between the estimated and theoretical values*

In this experiment, a reference trace is defined as the first day of the deployment and the start time of all stations is synchronized through GPS so there is no static clock error between the stations and the dynamic clock drift represents the whole clock drift. We found small errors in the dynamic clock drift per day of our estimates and good agreement with that of the theoretical values for the majority of the stations (Table 1). The standard deviation of the difference between the estimated relative clock drift and the theoretical value of the OBS pair was computed using the following equation:

$$\sigma = \sqrt{\frac{1}{N}\sum_{n=1}^{N}\left(dt^{\mathrm{dyn}} - dt^{\mathrm{the}}\right)^2}, \tag{8}$$

where dt^{dyn} is the dynamic relative clock drift and dt^{the} is the the-

Table 1. The dynamic clock drift estimated using the different length data

Station pairs	Dynamic clock drift rate per day/s·d^{-1}			
	Theoretical	NCFs of one day	NCFs of two days	NCFs of five days
OBS05-OBS06	0.073 8	0.066 9	0.066 1	0.067 0
OBS05-OBS07	0.032 3	0.032 9	0.032 8	0.033 0
OBS05-OBS08	–0.007 1	–0.002 1	–0.000 8	–0.001 1
OBS06-OBS07	–0.041 5	–0.038 2	–0.038 5	–0.038 4
OBS06-OBS08	–0.080 9	–0.080 5	–0.079 9	–0.080 0
OBS07-OBS08	–0.039 4	–0.040 7	–0.043 5	–0.044 1

oretical relative clock drift measured by the frequency of the crystal oscillator. N is the day length of deployment.

Figure 7 illustrates the measurement of the dynamic clock drift for OBSs related to the reference station OBS05. The standard deviation errors between the estimated clock drift and the expected value for each pairs are 0.128 s for OBS06, 0.070 5 s for OBS07 and 0.150 1 s for OBS08 respectively.

3.2 *Application of TSA on the CDC 40th*

As discussed above, the TSA method of ambient noise with suitable parameters was applied successfully to the measurement of clock drift on the CDC 40th. The results confirm that the difference between the estimated value and the theoretical value is small enough to correct our clock drift using this method. The same process was applied to the clock drift of OBSs on CDC 34th with the relatively greater time drift because of a longer observation. The preprocessing for the NCF computing was as above, and the hydrophone time series of one day with the period band 2–5 s was selected in this experiment.

For each pairs of stations, the positive time dt^+ and negative time dt^- of the NCFs were evaluated to the same direction symmetrically. The dynamic relative drift with respect to the reference trace was obtained by Eq. (2) on the assumption of linear regression. Static drift was a large difference of every two OBSs because several instruments began with a static clock offset from GPS and a different deployment time. Thus the total clock drifts were estimated by the following linear fitting equation:

$$dt_n^{\mathrm{rel}} = K\,(n-1) + B\,, \tag{9}$$

where K is the slope of the dynamic clock drift, B is the static clock drift that is constant over time, and n=1, 2, 3, ..., 108 is the number of day.

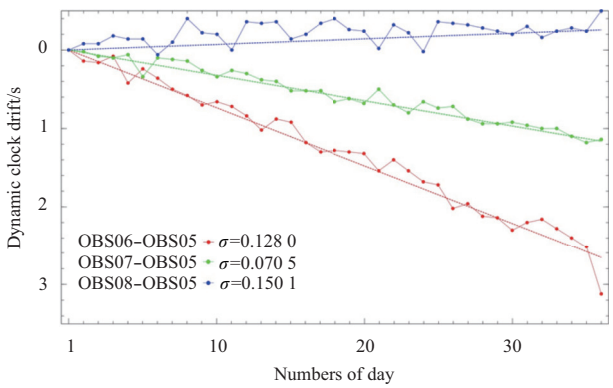

Fig. 7. Time variation of clock drifts using TSA for three OBSs relative to OBS05 with date. The dashed lines represent the expected value of time drift for comparison with the estimated one.

Additionally, compared with estimation of the dynamic clock drift the static clock drift is inaccurate because the positive and negative parts of the NCF for the first day as the reference trace are not constantly similar. To determine the static offset to a high precision we used the cross-correlation of $r^+(t) \otimes r^-(t)$, where the reference trace is rebuilt by the stack of all NCFs over the period of the experiments after dynamic clock drift. Figure 8 illustrates that the symmetry of the stacked NCFs is perfectly related to the daily NCF. This is due to sufficient averaging and, possibly, an increased influence of an isotropic source exemplified by a reference trace stacked by all the NCFs of OBS01 and OBS03.

Finally, the total clock drift consisting of the static and dynamic drift is present as in Eq. (9) for each station pair. In order to reduce the estimated error and improve OBS precision, we utilized a conjugate gradient algorithm to determine the optimal results of all stations based on the relation of interstation clock drifts described by Eq. (4). Figure 9 shows that the final clock drift results of the OBSs related to OBS01 as a reference station, as well as linear fitting of the clock drift with the root mean square errors calculated by Eq. (8) where the dt^{exp} is the linear expected result. The standard deviation estimated using TSA are 0.062 5 s, 0.080 6 s and 0.094 5 s for the OBS02-OBS01, OBS03-OBS01, and OBS04-

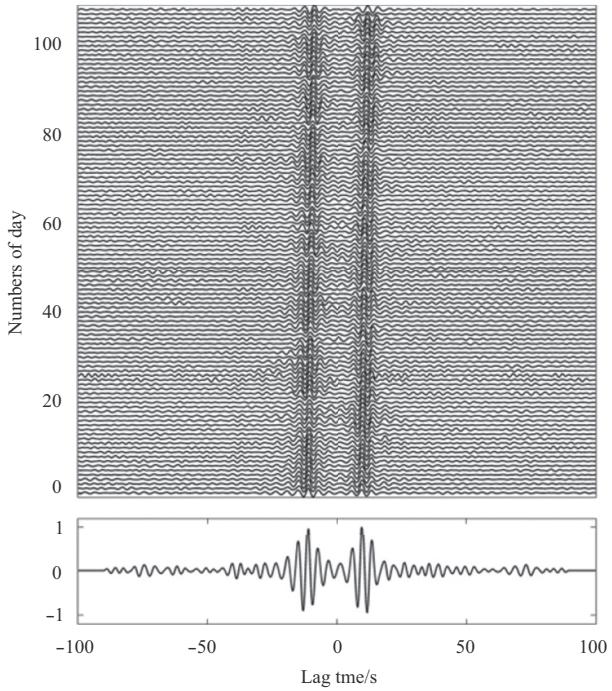

Fig. 8. An example of reference trace of a stack of 108 d NCFs over lag time ranging from –100 s to 100 s using the hydrophone component of OBS01 and OBS03 in the 2–5 s period band on CDC 34th.

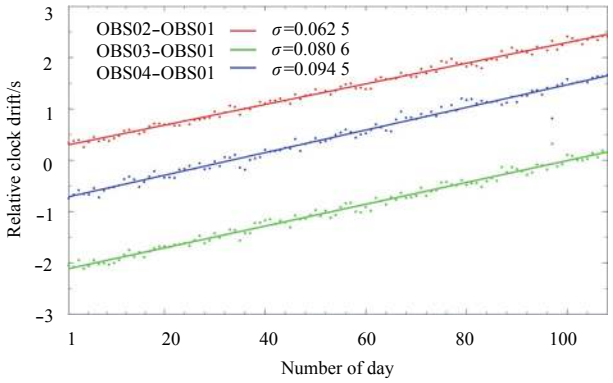

Fig. 9. The relative clock drifts of the OBSs related to OBS01 as a reference station using TSA. The oblique line is the line of best fit; the standard deviation (s) of each pair is shown on the top left.

OBS01, respectively. Although the estimated clock drift is the related value of all stations, it is adequate for correcting time consistently in the same OBS array. The largest relative clock drift accumulated between two OBSs was approximately 2.2 s. This means that research on earthquake location and tomography using the arrival time of the data will improve in accuracy by an order of magnitude.

4 Summary and conclusions

A visible linear clock drift with date was found for the NCFs in the experiments of the OBSs deployed on both CDC 34th and 40th. Using a 1-d series recorded by the hydrophone component filtered to the 2–5 s period bands, we verified that the symmetry of NCFs is nearly perfect with a high SNR. The influence of amplitude normalization using the one-bit and running average methods was almost identical. We evaluated the feasibility of these parameters on the CDC 40th because the clock drift of the OBSs was known. We then applied the same parameters successfully to the OBSs on the CDC 34th. Additionally, the precision of the static drift was improved using the stacked reference trace of all dates. We further optimized the clock drift of all the stations based on the interstation relationship. In the end, the clock drift between every two OBSs was estimated by linear regressions with small deviations. After the 108 d accumulation, the largest relative clock drift exceed non-negligible level of 2 s. Thus time correction is necessary for a long term seismic observation.

In this paper, we confirmed that OBS clock drift, including the static and dynamic offsets could be estimated using TSA techniques with appropriate parameters based on ambient noise cross-correlation. In the deep-sea environment the low frequency secondary ocean microseism are taken as nearly homogeneous noise sources and the time shift of the NCFs results solely from the clock drift between each OBS pair. Hence, using the low frequent noise cross-correction technique can be particularly useful for the OBS data, especially in cases where OBSs malfunction or there is non-linear drift.

Acknowledgements

The authors thank the captain and the crew of CDC 34th and 40th for their efforts to complete the development of the OBSs.

References

Aster R C, McNamara D E, Bromirski P D. 2008. Multidecadal climate-induced variability in microseisms. Seismol Res Lett, 79(2): 194–202

Bensen G D, Ritzwoller M H, Barmin M P, et al. 2007. Processing seismic ambient noise data to obtain reliable broad-band surface wave dispersion measurements. Geophys J Int, 169(3): 1239–1260

Campillo M. 2006. Phase and correlation in 'random' seismic fields and the reconstruction of the Green function. Pure Appl Geophys, 163(2–3): 475–502

Dolenc D, Romanowicz B, Stakes D, et al. 2005. Observations of infragravity waves at the Monterey ocean bottom broadband station (MOBB). Geochem Geophys Geosyst, 6(9): Q09002

Gardner A T, Collins J A. 2012. Advancements in high-performance timing for long term underwater experiments: A comparison of chip scale atomic clocks to traditional microprocessor-compensated crystal oscillators. In: IEEE Oceans. Hampton Roads, VA, USA: IEEE, doi: 10.1109/OCEANS.2012.6404847

Gouedard P, Seher T, McGuire J J, et al. 2014. Correction of ocean-bottom seismometer instrumental clock errors using ambient seismic noise. Bull Seismol Soc Am, 104(3): 1276–1288

Hannemann K, Kruger F, Dahm T. 2014. Measuring of clock drift rates and static time offsets of ocean bottom stations by means of ambient noise. Geophys J Int, 196(2): 1034–1042

Larose E, Derode A, Campillo M, et al. 2004. Imaging from one-bit correlations of wideband diffuse wave fields. J Appl Phys, 95(12): 8393–8399

Liu Yunlong, Tao Chunhui, Liu Cai, et al. 2018. Seismic activity recorded by a single OBS/H near the active Longqi hydrothermal vent at the ultraslow spreading Southwest Indian Ridge (49°39′E). Mar Geores Geotechnol: doi: 10.1080/1064119X.2017.1420114

Pontbriand C W, Sohn R A. 2014. Microearthquake evidence for reaction-driven cracking within the Trans-Atlantic Geotraverse active hydrothermal deposit. J Geophys Res: Solid Earth, 119(2): 822–839

Ruan Aiguo, Li Jiabiao, Chen Yongshun, et al. 2010. The experiment of broad band 1–4C type OBS in the Southwest Indian Ridge. Chin J Geophys (in Chinese), 53(4): 1015–1018

Sabra K G, Roux P, Thode A M, et al. 2005. Using ocean ambient noise for array self-localization and self-synchronization. IEEE J Ocean Eng, 30(2): 338–347

Schlindwein V, Schmid F. 2016. Mid-ocean-ridge seismicity reveals extreme types of ocean lithosphere. Nature, 535(7611): 276–279

Sens-Schönfelder C. 2008. Synchronizing seismic networks with ambient noise. Geophys J Int, 174(3): 966–970

Shapiro N M, Campillo M, Stehly L, et al. 2005. High-resolution surface-wave tomography from ambient seismic noise. Science, 307(5715): 1615–1618

Stehly L, Campillo M, Shapiro N M, et al. 2006. A study of the seismic noise from its long-range correlation properties. J Geophys Res: Solid Earth, 111(B10): B10306

Stehly L, Campillo M, Shapiro N M. 2007. Traveltime measurements from noise correlation: stability and detection of instrumental time-shifts. Geophys J Int, 171(1): 223–230

Stroup D F, Tolstoy M, Crone T J, et al. 2009. Systematic along-axis tidal triggering of microearthquakes observed at 9°50′N East Pacific Rise. Geophys Res Lett, 36(18): L18302

Tao Chunhui, Li Huaiming, Jin Xiaobing, et al. 2014. Seafloor hydrothermal activity and polymetallic sulfide exploration on the southwest Indian ridge. Chin Sci Bull, 59(19): 2266–2276

Tao Chunhui, Lin Jian, Guo Shiqin, et al. 2012. First active hydrothermal vents on an ultraslow-spreading center: Southwest Indian Ridge. Geology, 40(1): 47–50

Webb S C, Zhang Xin, Crawford W. 1991. Infragravity waves in the deep ocean. J Geophys Res, 96(C2): 2723–2736

Yao Huajian, Van Der Hilst R D, De Hoop M V. 2006. Surface-wave array tomography in SE Tibet from ambient seismic noise and two-station analysis: I. Phase velocity maps. Geophys J Int, 166(2): 732–744

Yao Huajian, Gouédard P, Collins J A, et al. 2011. Structure of young East Pacific Rise lithosphere from ambient noise correlation analysis of fundamental- and higher-mode Scholte-Rayleigh waves. Comptes Rendus Geosci, 343(8–9): 571–583

Acta Oceanol. Sin., 2018, Vol. 37, No. 5, P. 47–53
DOI: 10.1007/s13131-018-1211-7
http://www.hyxb.org.cn
E-mail: hyxbe@263.net

Heavy metal stress induced hyperglycemia in blue swimmer crab, *Portunus pelagicus*

SARAVANAN R.[1], SUGUMAR V.[1]*, BEEMA MAHIN M. I.[1]

[1] Department of Oceanography and Coastal Area Studies, Alagappa University, Thondi Campus, Thondi 623409, Tamilnadu, India

Received 11 January 2017; accepted 1 August 2017

Abstract

The study was to find out the effect of cadmium and mercury on levels of hemolymph glucose, crustacean hyperglycemic hormone (CHH) and hepatopancreas glycogen in the blue swimmer crab *Portunus pelagicus*. The experiments were performed in both intact and eyestalk ablated crabs. Quantification of CHH was done by the indirect ELISA with the aid of primary anti-*Carcinus maenas*-CHH antibody. Higher glucose concentration was observed on exposure to 8×10^{-6} of cadmium ((825.6±5.42) μg/mL) and 6×10^{-6} of mercury ((90.5±6.25) μg/mL) after 48 h and 24 h respectively. Higher level of hemolymph glucose was observed in eyestalk intact crabs on exposure to cadmium and mercury than eyestalk ablated crabs. Decrease in the levels of CHH was observed in both eyestalk intact and ablated crabs on heavy metal exposure. Decline of the hepatopancreas glycogen level was also witnessed with the exposure to heavy metal, which validated its utilization in the production of glucose. Thus this study brings to light, the variations in hemolymph glucose, CHH and hepatopancreas glycogen on heavy metal stress. These carbohydrate metabolites can be used as biomarkers in assessing heavy metal contamination in water bodies.

Key words: crustacean hyperglycemic hormone, cadmium, mercury, decapod crustaceans, blue swimmer crab

Citation: Saravanan R., Sugumar V., Beema mahin M. I.. 2018. Heavy metal stress induced hyperglycemia in blue swimmer crab, *Portunus pelagicus*. Acta Oceanologica Sinica, 37(5): 47–53, doi: 10.1007/s13131-018-1211-7

1 Introduction

Heavy metals from farming as well as industrial activities cause environmental pollution of the marine ecosystem and can easily enter the food chain through the process of bioaccumulation, which causes extreme health complications towards human beings. It has been well documented that crustaceans have greater sensitivity towards heavy metals (Ahsanullah et al., 1981; Migliore and De Nicola Giudici, 1990). Heavy metals have major impact on the life cycle, reproduction, moulting stages and nutrition values of the crustaceans (Vernberg et al., 1974; Madsen and Shine, 1992; McGee et al., 1998). Heavy metals are not only harmful but also have some beneficial role in crustaceans. Copper is important for the functioning of hemocyanin and zinc is important component of many enzymes (Bryan, 1984; Rainbow, 1988). Trace amounts of heavy metals are absorbed by animals and stored as metabolically active forms, and are actively involved in the essential biochemical processes. Sometimes the heavy metals are detoxified into chemically inert forms and stored permanently or temporarily. The accumulation process of heavy metals may differ depending on the metals and species (Rainbow, 1988, 1997). Cadmium and mercury attracted increased awareness after the outbreak of Minimata and Itai-Itai diseases due to consumption of fish and other seafood contaminated with those heavy metals (Ui, 1972). These heavy metals are more harmful to the aquatic organism even at lower concentration because of their bioaccumulation, immutable and non-degradable properties (Reddy et al., 2011).

Mercury and cadmium have the ability to inhibit ovarian maturation in *Procambarus clarkii* (Reddy et al., 1997); additionally, cadmium can reduce the fecundity and hatching success in *P. clarkii* (Naqvi and Howell, 1993), and inhibits the molting process in the crab *Chasmagnathus granulate* (Moreno et al., 2003). Excess amount of copper can stop the growth of *Penaeus merguiensis* and *Penaeus monodon* (Ahsanullah and Ying, 1995). Mercury, cadmium and zinc are found to inhibit limb regeneration and molting in *Uca pugilator* and other fiddler crabs (Weis, 1978, 1980).

Cadmium distribution has been studied in different subcellular fractions of gill and hepatopancreas tissues of eastern oysters *Crassostrea virginica*. In both the tissue types, there was a significant accumulation of cadmium. Among the organelles, mitochondria were the main target for cadmium bioaccumulation in gills, whereas in hepatopancreas tissues, it was in lysosomes (Júdová, 2006). Chronic metal exposure (Zn, Cu, Cd) has been demonstrated to inhibit growth of sea cucumber with increased metal concentration (Li et al., 2016). Accumulation of heavy metals especially cadmium has been found to be 12 times higher in crustaceans in the Gulf of Khumbat than that of European community, three times higher than that of England standards and one time higher than that of FAO/WHO prescribed limits (Prakash Jebakumar et al., 2015).

Hormones play an important role in the different physiologic-

Foundation item: The grant from the Department of Science and Technology, New Delhi under contract No. SR/FT/LS-137/2009 dt. 17.01.2012.
*Corresponding author, E-mail: crustacealab@gmail.com

al process of crustaceans. The production and release of hormones may differ before and after exposure to the pollutants. In crustaceans, the most important response is hyperglycemia after exposure to the pollutants (Fingerman et al., 1996, 1998). Research findings suggest that this stress hyperglycemia is instigated by the release of crustacean hyperglycemic hormone (CHH) to the circulatory system (Reddy et al., 2011). Numerous studies on endocrine regulation in stalk-eyed decapod crustaceans have established the neurosecretory structures in the eyestalk as the most important component of neuroendocrine system of these animals (Dean and Vernberg, 1965). The hemolymph glucose concentration is controlled by CHH (Abramowitz et al., 1944) that is synthesized in and released from the X-organ sinus gland complex. Reddy et al. (1994) reported that cadmium induced hyperglycemia in the red swamp crayfish, *P. clarkii*. Cadmium and naphthalene induced hyperglycemia in the fiddler crab, *U. pugilator* as reported by Reddy et al. (1996). Lorenzon et al. (2000) showed evidence that sublethal heavy metal concentration cause a variation of blood glucose level mediated by eyestalk hormone in *P. elegans* within a 24 h exposure period.

The blue swimmer crab, *Portunus pelagicus* represents a valuable component of small-scale coastal fisheries in many countries in the tropics (Batoy et al., 1980; Joel et al., 1987; Kyomo, 1999; Mgaya et al., 1999). Its distribution outspreads from the southern Mediterranean Sea, the east coast of Africa and across the Indian Ocean to Japan and the western Pacific Ocean (Smith, 1982; Potter et al., 1983). In India, it distributes extensively throughout West Bengal, Andhra Pradesh, Tamil Nadu, Kerala, Karnataka and Maharashtra, and contributes about 30% of the total annual marine crab landings (Samuel et al., 2004). Blue swimmer crabs are found mainly within estuaries and inshore coastal waters. In estuaries, they live in mud, sand and seagrass habitats, and often buried in the sediment.

Palanichamy and Rajendran (2000) have studied heavy metal concentration in seawater and sediments of the Gulf of Mannar and Palk Bay, southeast coast of India. Levels of cadmium were in order of Arumuganeri > Tuticorin > Thondi > Mandapam. Govindasamy et al. (2011) have observed high accumulation of heavy metals in Thondi. The increase in urbanisation and industrialisation leading to an increase of marine discharges and therefore the total load of pollutants being delivered to the sea, has been postulated as the reason for increased heavy metal incidence at Thondi. The culturable bacterial diversity of marine sediments from the Palk Bay (Thondi coast) has been evaluated using biochemical analysis, 16S rRNA gene sequencing, and their potential for antibiotic production has been assessed. Members of Firmicutes, Actinobacteria, Alphaproteobacteria, Gammaproteobacteria and *Bacillus* species have been identified in the Thondi coast (Nithya and Karutha Pandian, 2010). The blue swimmer crab, *P. pelagicus* inhabiting in Thondi coast, is often exposed to varying environmental stresses and hence its metabolism and physiological activities are affected. These crabs are observed to accumulate cadmium in the hepatopancreas after being presented elevated levels of the metals Cd, Cu, Zn, As, Fe and Al via a food source, the mussel *Trychomya hirsuta*. Over 8 weeks, crabs were fed a controlled diet to determine the accumulation of metals and accumulation was detected after 4 weeks of feeding (McPherson and Brown, 2001). Hence, the present study was conducted, to determine the effect of cadmium and mercury on hemolymph glucose and CHH in the intact and eyestalk ablated crabs after 24 h and 48 h exposure to metals in the blue swimmer crab, *P. pelagicus*.

2 Materials and methods

2.1 *Collection and maintenance of crabs*

Healthy adult blue swimmer crabs, *P. pelagicus*, were caught from the Thondi coast, Thondi (9°45′N, 79°04′E) with the carapace length of (10±1) cm and (80±5) g wet weight. The crabs were cautiously transported to the laboratory in aerated plastic troughs and introduced into the tank containing pre-aerated filtered sea water and acclimatized for a week at about 34±2 salinity and room temperature ((30±2)°C). During the period, the crabs were fed with oyster (*Crassostrea madrasensis*) meat twice a day. The unconsumed meat and other debris particles were removed by siphoning. The water was removed and fresh sea water was introduced daily.

2.2 *Heavy metal stress*

Crabs were gathered and segregated into groups for different heavy metals treatment. Each group contains ten crabs for heavy metal stress. Heavy metals like mercury (Hg) and cadmium (Cd) are actively involved in bioaccumulation and transferable through the food chain process.

Heavy metal stock solution:

Mercury and cadmium stock solutions ($1\ 000\times10^{-6}$) were prepared by dissolving their respective salts namely, mercury chloride and cadmium chloride.

Experimental setup:

Experimental group 1: the intact crabs exposed to mercury (8×10^{-6});

Experimental group 2: the eyestalk ablated crabs exposed to mercury (8×10^{-6});

Experimental group 3: the intact crabs exposed to cadmium (8×10^{-6});

Experimental group 4: the eyestalk crabs exposed to cadmium (8×10^{-6});

Experimental group 5: this group served as control.

2.3 *Collection of hemolymph and hepatopancreas*

Hemolymph and hepatopancreas were sampled from Groups 1 and 2 crabs at 0th, 12th, 24th, 36th and 48th h, samples from Groups 3 and 4 were collected at 0th, 12th and 24th h. Before sample collection, crabs were anaesthetised on ice for 5 min and the hemolymph (~2 mL/crab) was collected from the arthrodial membrane of swimmeret and stored at –20°C. The hemolymph collected from the experimental crabs during different hours of exposure was centrifuged at 5 000 r/min for 5 min to get cell free hemolymph (CFH) and was used to estimate hemolymph glucose and CHH levels.

Determination of glucose was done by glucose oxidase method (Tietz et al., 1976) in a multiwall format. Estimation of total glycogen in hepatopancreas was done according to the methodology of Carroll et al. (1956).

2.4 *Quantification of hemolymph CHH by indirect ELISA*

Quantification of CHH in the hemolymph was carried out as per the methodology of Levenson et al. (1999). The CFH were mixed 1:1 (v/v) with coating buffer (0.2 mol/L sodium carbonate-bi carbonate buffer, pH 9.4) and 100 μL was loaded in each well. The plate was incubated at 4°C overnight. After washing with washing buffer (10 mmol/L PBS, pH 7.4 and 0.1% Tween 20) the plate was blocked with 100 μL of blocking buffer (10 mmol/L PBS, 0.1% Tween 20, 2% BSA) for 2 h at room temperature. After washing, the plate was incubated with anti-*Carcinus maenas*-CHH (dilution 1:10 000 in blocking buffer) for 2 h at room tem-

perature. Plate was then washed and incubated with the secondary antibody, anti-rabbit IgG peroxidase (Sigma, A4914) (dilution 1:500 in blocking buffer) for 2 h at room temperature. Again, the plate was washed and 100 μL of TMB substrate was added into each well to initiate the enzymatic reaction. The plate was incubated in dark for 10–30 min at 37°C. The reaction was stopped by adding 2 mol/L H_2SO_4. Finally, multiwell plates were read at 450 nm on ELISA-reader (Cyberlab Inc., USA).

3 Results

3.1 *Effect of cadmium*

Preliminary experiments revealed higher hemolymph glucose level ((824.9±40) μg/mL) in the crabs when exposed to 8×10^{-6} of cadmium chloride after 48 h than other concentrations (Fig. 1). This concentration was chosen as the test concentration for hemolymph glucose, hepatopancreas glycogen and hemolymph CHH studies over increasing time periods.

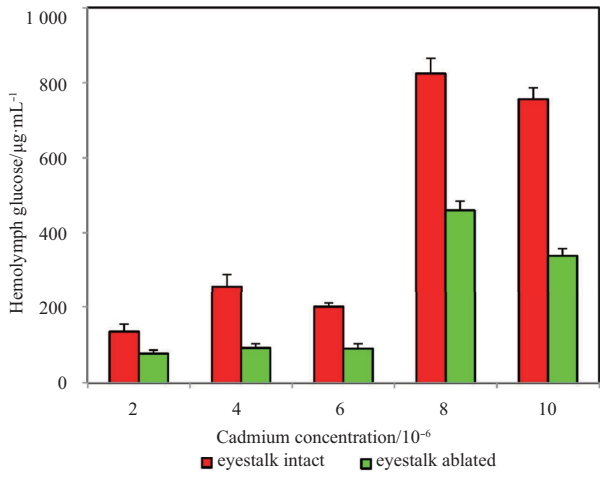

Fig. 1. Effect of varying cadmium concentrations on hemolymph glucose level in *P. pelagicus*.

3.2 *Effect of cadmium on hemolymph glucose*

Fluctuating variations in the hemolymph glucose level was observed on exposure to 8×10^{-6} cadmium chloride over the 48 h time period (Fig. 1). A significant increase in the hemolymph glucose level was observed at 24 h ((440±7.20) μg/mL) and 48 h ((825.6±5.42) μg/mL) of cadmium exposure in eyestalk intact crabs when compared to the 0 h of exposure ((373±5.23) μg/mL) (t<0.001). A sharp decline was observed between the two hours, i.e., during 12 h and 36 h.

The first peak in glucose level of (320±7.21) μg/mL was observed after 24 h of cadmium exposure compared with (86.6±5.24) μg/mL at 0 h of exposure in eyestalk ablated crabs. A decline in its level was observed thereafter at 36 h ((226.6±8.32) μg/mL) and then increased to its maximum around 48 h ((459.2±4.88) μg/mL) (t<0.01). Comparison between the two experimental groups of crabs showed higher level of hemolymph glucose in eyestalk intact crabs at 24 h period of exposure (P<0.01) (Fig. 2).

3.3 *Effect of cadmium on hepatopancreas glycogen*

Insignificant variations in the hepatopancreas glycogen level were observed between eyestalk intact and ablated crabs during the period of exposure (P>0.05) (Fig. 3). Variations did not follow

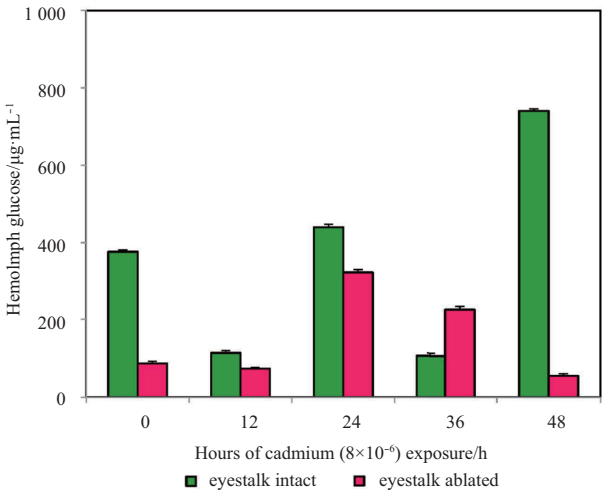

Fig. 2. Variations in the level of hemolymph glucose on cadmium exposure in *P. pelagicus*.

a definite trend of increase or decrease. The hepatopancreas glycogen level was (1.55±0.2) μg/mg at 0 h of exposure, without drastic changes during the later hours of cadmium exposure till 48 h ((1.425±0.11) μg/mg) (t>0.05). Though a notable decrease in the glycogen level of (1.433±0.11) μg/mg and (1.325±0.23) μg/mg were observed during 12 h and 36 h of cadmium exposure in eyestalk ablated crabs, the levels were set back to those of 0 h of exposure ((1.725±0.23) μg/mg) at 48 h (t<0.05).

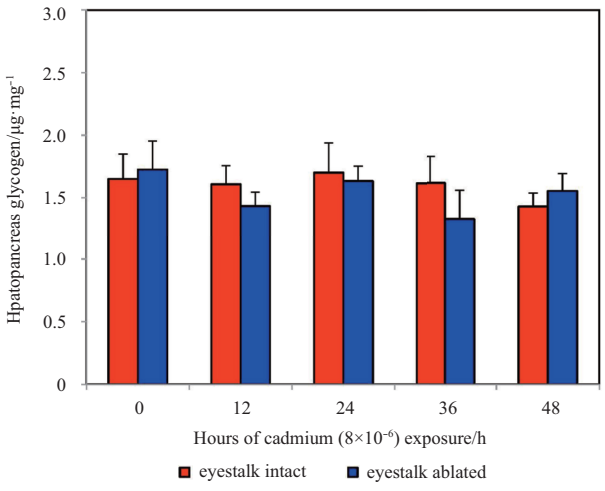

Fig. 3. Variations in the level of hepatopancreas glycogen on cadmium exposure in *P. pelagicus*.

3.4 *Effect of cadmium on hemolymph CHH*

Significant variations were observed in the hemolymph level of CHH in both eyestalk intact and ablated crabs (Fig. 4). Higher level of hemolymph CHH was observed in the eyestalk intact crabs after 36 h of cadmium exposure ((33.02±1.44) fmol/mL) when compared to eyestalk ablated crabs ((15.84±1.27) fmol/mL). Decrease in the level of hemolymph CHH was observed from 0 h ((25.63±2.32) fmol/mL) to 48 h ((16.83±2.14) fmol/mL) of cadmium exposure in eyestalk ablated crabs (P<0.001). Variations noted in the hemolymph CHH levels of eyestalk intact crabs were vague and did not follow a steady pattern of increase or decrease. Increase in the CHH levels to (32.78±2.85) fmol/mL

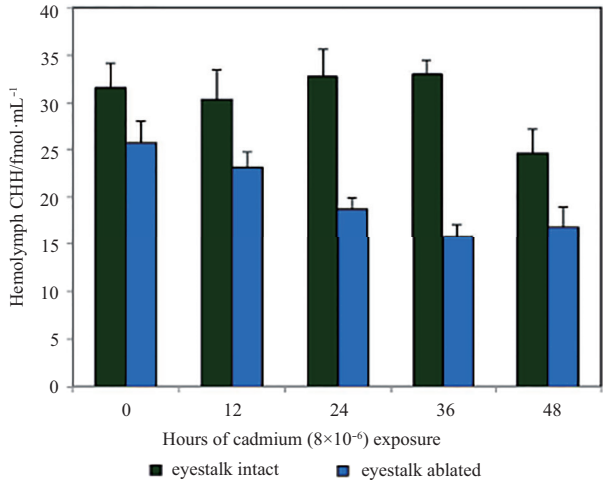

Fig. 4. Variations in the level of hemolymph CHH on cadmium exposure in *P. pelagicus*.

was observed after 24 h of cadmium exposure and further increased after 36 h of exposure (P<0.05).

3.5 *Effect of mercury*

Crabs were pushed to heavy stress on 36 h and 48 h of mercury exposure and mortality was recorded after 24 h of exposure (Fig. 5). An elevated glucose level of (817.7±40) μg/mL was observed after 24 h of exposure in the crabs when exposed to 6×10^{-6} of mercuric chloride than other concentrations. Hence, 6×10^{-6} was tested over increasing time periods in terms of hemolymph glucose, hepatopancreas glycogen and hemolymph CHH.

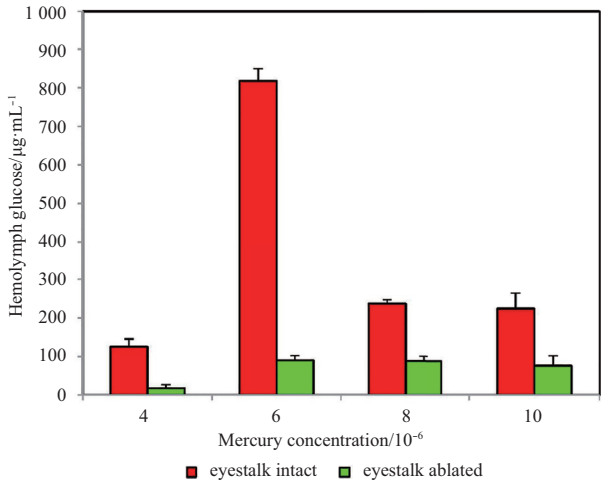

Fig. 5. Effect of varying mercury concentrations on hemolymph glucose level in *P. pelagicus*.

3.6 *Effect of mercury on hemolymph glucose*

Highly significant increase in hemolymph glucose level to (817±11.78) μg/mL was observed on 24 h of mercury exposure when compared to 0 h of exposure ((182.21±9.14) μg/mL) in eyestalk intact crabs (t<0.000 1) (Fig. 6). Eyestalk ablated crabs showed less significant variations in the hemolymph glucose level on mercury exposure. The hemolymph glucose level of (26.21±8.24) μg/mL observed at 0 h of exposure and increased insignificantly to (45.13±5.23) μg/mL during 12 h of exposure and reached (90.5±6.25) μg/mL at 24 h of mercury exposure (t<0.05).

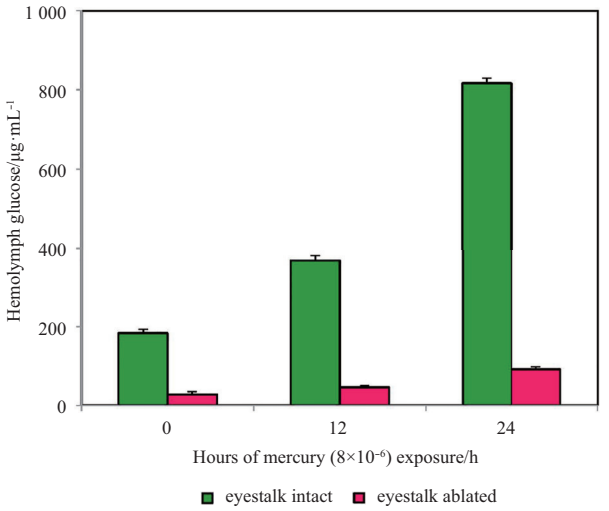

Fig. 6. Variations in the level of hemolymph glucose on mercury exposure in *P. pelagicus*.

3.7 *Effect of mercury on hepatopancreas glycogen*

Insignificant variations were observed in the level of hepatopancreas glycogen between eyestalk intact and eyestalk ablated crabs (P>0.05) (Fig. 7). The hepatopancreas glycogen reserves were observed to decrease gradually from 0 h ((1.24±0.12) μg/mg), through 12 h ((0.683±0.11) μg/mg) to 24 h ((0.437±0.08) μg/mg) of mercury exposure in eyestalk intact crabs (t<0.05). A similar trend was observed in eyestalk ablated crabs with the level of glycogen being comparatively lower. Higher level of hepatopancreas glycogen of (0.78±0.13) μg/mg was observed at 0 h of exposure which declined to (0.371±0.10) μg/mg at 24 h of exposure (t>0.05).

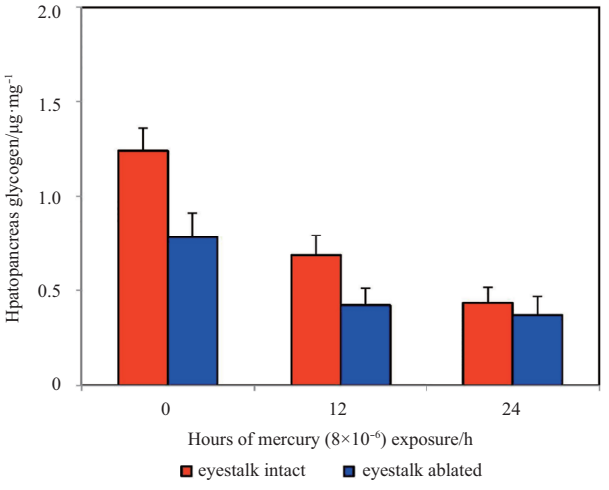

Fig. 7. Variations in the level of hepatopancreas glycogen on mercury exposure in *P. pelagicus*.

3.8 *Effect of mercury on hemolymph CHH*

Mercury exposure decreased the hemolymph CHH levels and proved its effect on the hormone in the eyestalk intact and ablated crabs, with the eyestalk intact crabs showing higher levels of CHH (t<0.05). In eyestalk intact crabs, the CHH level was (33.18±0.99) fmol/mL at 0 h of exposure and decreased significantly to (14.21±1.12) fmol/mL around 12 h of exposure. This level

increased to (21.57±1.54) fmol/mL at 24 h of exposure after which mortality of the crab was observed. The hemolymph CHH levels decreased during the early hours of exposure from 0 h ((27.11±1.28) fmol/mL) till 12 h ((10.21±1.94) fmol/mL) and increased slightly to (14.79±2.01) fmol/mL at 24 h of exposure in eyestalk ablated crabs (Fig. 8).

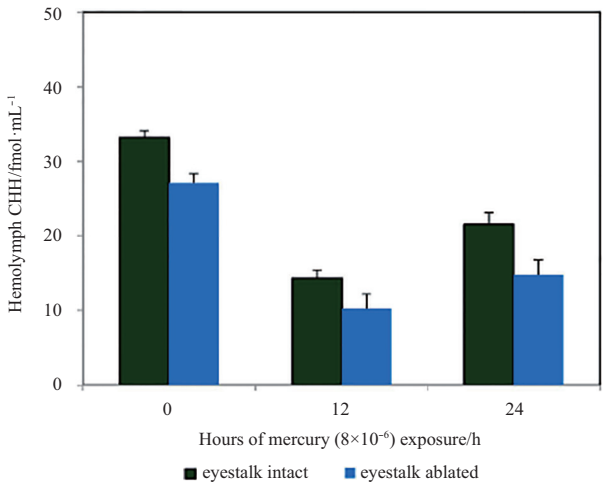

Fig. 8. Variations in the level of hemolymph CHH on mercury exposure in *P. pelagicus*.

4 Discussion

This paper aims to investigate the relationship between heavy metal stress and the release of crustacean hyperglycemic hormone from the x-organ sinus gland into the hemolymph, and thereby glycemic response in the blue swimmer crab *P. pelagicus*. Furthermore, the present study validates the use of a cross reactivity of the antibody, anti-*Carcinus maenas*-CHH to access the CHH in the hemolymph of *P. pelagicus*, with the focuses on quantification of the variation in glucose, glycogen and CHH after exposure with different heavy metals.

An elevation in the glucose concentration was observed in the hemolymph of *P. pelagicus* following exposure to cadmium chloride and mercury chloride. Higher glucose concentration was observed on exposure to 8×10^{-6} of cadmium and 6×10^{-6} of mercury after 48 h and 24 h respectively. Insignificant increase in glucose level was observed in the eyestalk ablated individuals. Cadmium exposed eyestalk ablated crabs showed gradual increase in glucose until 36 h and sudden decrease till 48 h. Mercury exposed eyestalk ablated crabs also showed the pattern of gradual increase in glucose level until the end of the experiment. Cadmium exposed intact crabs showed higher glucose during different exposure time. Lorenzon et al. (2000) showed that the higher concentrations of mercury, cadmium and lead elicited no hyperglycemia in 24 h, while the intermediate sub lethal concentration of these metals produced a significant hyperglycemic response in the shrimp *Palaemon elegans*. Studies demonstrate that heavy metals induce hyperglycemic response in the fresh water crab *Barytelphusa cunicularis* (Machale et al., 1989), *Oziotelphusa senex senex*, the crayfish *P. clarkii*, the fiddler crab *U. pugilator* (Reddy et al., 1994, 1996, 2011) and in the shrimp *P. elegans* (Lorenzon et al., 2000). Variations in the glucose level of intact and eyestalk-ablated individuals have been reported in *U. pugilator* and in *O. senex senex* (Reddy et al., 1996, 2011) on exposure to cadmium and mercury.

Hyperglycaemia results from the mobilization of glycogen in target tissues (e.g., midgut glands and abdominal muscles), due to the activation of phosphorylase and the inhibition of glycogen synthase via the CHH (Sedlmeier, 1982). Stentiford et al. (2001) found significantly lower levels of hepatopancreatic glycogen in lobsters *Nephrops norvegicus* after infected with dinoflagellate parasite (*Hematodinium* sp.). CHH-injected crayfish (*Cherax quadricarinatus*) showed increased hemolymphatic levels of glucose, in accordance with a significant utilization of glycogen reserves from the hepatopancreas (Prymaczok et al., 2016). It has been reported that the CHH levels increased instantly after exposure to stressful conditions such as emersion, hypoxia, salinity and thermal stress (Chang et al., 1998; Chung and Zmora, 2008; Webster, 1996), which leads to the modulation of glucose levels in hemolymph through utilization of glycogen stored in hepatopancreas and muscle (Santos and Keller, 1993; Santos et al., 2001; Sedlmeier, 1985).

In our study, variations of glycogen did not follow a definite trend of increase or decrease after exposure to cadmium. The hepatopancreas glycogen level was higher at 0 h of exposure, did not experience drastic changes during the later hours of cadmium exposure till 48 h. Though a notable decrease in the glycogen level was observed at 12 h and 36 h of cadmium exposure in eyestalk ablated crabs, the levels at 48 h were back to those of 0 h of exposure. Whereas, mercury exposed crabs showed insignificant differences in glycogen levels between eyestalk intact and eyestalk ablated crabs. Significant decrease of glycogen levels was observed during the exposure period from 0 h to 24 h.

In the present study, more substantial hyperglycemic response in *P. pelagicus* was observed at LC_{50} levels of cadmium and mercury exposure than higher concentrations in 24 h. Lorenzon (2005) also reported that intermediate sublethal concentration of cadmium, mercury and lead showed significant hyperglycemic response than higher concentrations during 24 h incubation period. Heavy metals like cadmium, mercury and lead have been reported to cause hyperglycemia in the freshwater prawn, *Macrobrachium kistenensis*, the crab, *Barytelphusa canicularis* (Nagabhushanam and Kulkarni, 1981; Machale et al., 1989) and *Scylla serrata* (Reddy and Bhagyalakshmi, 1994). Lorenzon et al. (2004) found that massive release of CHH from the eyestalk into hemolymph of *P. elegans* after exposure to copper. Moreover, cadmium chloride has been observed to induce hyperglycemia in intact crayfish *P. clarkii*, but not in eyestalk ablated crabs (*U. pugilator*), suggesting a CHH mediated response (Reddy et al., 1996). The two heavy metals did not elicit significant hyperglycemic response in eyestalk ablated crabs which clearly indicates the involvement of optic ganglia. The relationship between toxicant exposure and release of the CHH was confirmed by variation in hemolymph glucose (Lorenzon et al., 2005).

In conclusion, the present study demonstrated different stress effect of heavy metals on glycemic control system in blue swimmer crab and the regulation of glycemic response. Base evidence of heavy metals interference on control of this mechanism and analysis of these metabolites could lead to better understanding and assessment of the environment quality.

Acknowledgements

The authors thank H. Dircksen Stockholm University for kindly providing the CHH antiserum.

References

Abramowitz A, Hisaw F, Papandrea D. 1944. The occurrence of a diabetogenic factor in the eyestalks of crustaceans. The Biological Bulletin, 86: 1–4

Ahsanullah M, Negilski D S, Mobley M C. 1981. Toxicity of zinc, cadmium and copper to the shrimp *Callianassa australiensis*: I. Effects of individual metals. Marine Biology, 64(S3): 299–304

Ahsanullah M, Ying W. 1995. Toxic effects of dissolved copper on *Penaeus merguiensis* and *Penaeus monodon*. Bulletin of Environmental Contamination and Toxicology, 55(1): 81–88

Bryan G W. 1984. Pollution due to heavy metals and their compounds. In: Kinne O, ed. Marine Ecology: A Comprehensive, Integrated Treatise on Life in Oceans and Coastal Waters. London: John Wiley & Sons Ltd, 1290–1430

Carroll N V, Longley A, Roe J H. 1956. The determination of glycogen in liver and muscle by use of anthrone reagent. The Journal of Biological Chemistry, 220(2): 583–593

Chang E S, Keller R, Chang S A. 1998. Quantification of crustacean hyperglycemic hormone by ELISA in hemolymph of the lobster, *Homarus americanus*, following various stresses. General and Comparative Endocrinology, 111(3): 359–366

Chung J S, Zmora N. 2008. Functional studies of crustacean hyperglycemic hormones (CHHs) of the blue crab, *Callinectes sapidus*—the expression and release of CHH in eyestalk and pericardial organ in response to environmental stress. The FEBS Journal, 275(4): 693–704

Batoy C B, Sarmago J F, Pilapil B C. 1980. Breeding season, sexual maturity and fecundity of blue crab, *Portunus pelagicus* (L.) in selected coastal waters in Leyte and Vicinity, Philippines. Annals of Tropical Research, 9: 157–177

Dean J M, Vernberg F J. 1965. Effects of temperature acclimation on some aspects of carbohydrate metabolism in decapod crustaceans. The Biological Bulletin, 129: 87–94

Fingerman M, Devi M, Reddy P S, et al. 1996. Impact of heavy metal exposure on the nervous system and endocrine-mediated processes in crustaceans. Zoological Studies, 35(1): 1–8

Fingerman M, Jackson N C, Nagabhushanam R. 1998. Hormonally-regulated functions in crustaceans as biomarkers of environmental pollution. Comparative Biochemistry and Physiology Part C: Pharmacology, Toxicology and Endocrinology, 120(3): 343–350

Govindasamy C, Arulpriya M, Ruban P, et al. 2011. Concentration of heavy metals in seagrasses tissue of the Palk strait, Bay of Bengal. International Journal of Environmental Sciences, 2(1): 145–153

Joel D R, Raj P S S. 1987. Marine crab fisheries around Pulcat. Seafood Expo, 19: 16–24

Júdová J. 2006. Crustacea and heavy metal accumulation. Oecologia Montana, 15: 29–37

Kyomo J. 1999. Distribution and abundance of crustaceans of commercial importance in Tanzania Mainland coastal waters. Bulletin of Marine Science, 65: 321–335

Levenson J, Byrne J H, Eskin A. 1999. Levels of serotonin in the hemolymph of *Aplysia* are modulated by light/dark cycles and sensitization training. The Journal of Neuroscience: the Official Journal of the Society for Neuroscience, 19(18): 8094–8103

Li Li, Tian Xiangli, Yu Xiao, et al. 2016. Effects of acute and chronic heavy metal (Cu, Cd, and Zn) exposure on sea cucumbers (*Apostichopus japonicus*). BioMed Research International, 20167: 453269

Lorenzon S, Edomi P, Giulianini P G, et al. 2004. Variation of crustacean hyperglycemic hormone (cHH) level in the eyestalk and haemolymph of the shrimp *Palaemon elegans* following stress. The Journal of Experimental Biology, 207(Pt 24): 4205–4213

Lorenzon S, Edomi P, Giulianini P G, et al. 2005. Role of biogenic amines and cHH in the crustacean hyperglycemic stress response. The Journal of Experimental Biology, 208(Pt 17): 3341–3347

Lorenzon S, Francese M, Ferrero E A. 2000. Heavy metal toxicity and differential effects on the hyperglycemic stress response in the shrimp, *Palaemon elegans*. Archives of Environmental Contamination and Toxicology, 39(2): 167–176

Machale P R, Khan A K, Sarojini R, et al. 1989. Copper and cadmium induced changes in blood sugar level of the crab *Barytelphusa cunicularis*. Uttar Pradesh Journal of Zoology, 9(1): 113–115

Madsen T, Shine R. 1992. Determinants of reproductive success in female adders, *Vipera berus*. Oecologia, 92(1): 40–47

McGee E A, Hsu S Y, Kaipia A, et al. 1998. Cell death and survival during ovarian follicle development. Molecular and Cellular Endocrinology, 140(1–2): 15–18

McPherson R, Brown K. 2001. The bioaccumulation of cadmium by the blue swimmer crab *Portunus pelagicus* L.. Science of the Total Environment, 279(1–3): 223–230

Mgaya Y D, Muruke M H S, Chande A I, et al. 1999. Evaluation of crustacean resources in Bagamoyo District. In: Howell K M, Semesi A K, eds. Coastal Resources of Bagamoyo District Tanzania. Proceedings of a workshop on coastal resources of Bagamoyo, 18–19 December 1997, Bagamoyo. Faculty of Science, University of Dar es Salaam, 55–63

Migliore L, De Nicola Giudici M. 1990. Toxicity of heavy metals to *Asellus aquaticus* (L.) (Crustacea, Isopoda). Hydrobiologia, 203(3): 155–164

Moreno P A R, Medesani D A, Rodrıguez E M. 2003. Inhibition of molting by cadmium in the crab *Chasmagnathus granulata* (Decapoda Brachyura). Aquatic Toxicology, 64(2): 155–164

Nagabhushanam R, Kulkarni G K. 1981. Freshwater palaemonid prawn, *Macrobrachium kistnensis* (Tiwari)—Effect of heavy metal pollutants. Proceedings of the Indian National Science Academy. Part B. Biological Sciences, 47B: 380–386

Naqvi S M, Howell R D. 1993. Toxicity of cadmium and lead to juvenile red swamp crayfish, *Procambarus clarkii*, and effects on fecundity of adults. Bulletin of Environmental Contamination and Toxicology, 51(2): 303–308

Nithya C, Karutha Pandian S. 2010. Isolation of heterotrophic bacteria from Palk Bay sediments showing heavy metal tolerance and antibiotic production. Microbiological Research, 165(7): 578–593

Palanichamy S, Rajendran A. 2000. Heavy metal concentrations in seawater and sediments of Gulf of Mannar and Palk Bay, Southeast coast of India. Indian Journal of Geo-Marine Sciences, 29(2): 116–119

Potter I C, Chrystal P J, Loneragan N R. 1983. The biology of the blue manna crab *Portunus pelagicus* in an Australian estuary. Marine Biology, 78: 75–85

Prakash Jebakumar J P, Nandhagopal G, Sundradarajan S, et al. 2015. Eminence of heavy metal accumulation in fishes and crustaceans from the Gulf of Khambhat, India. Current Science, 109(3): 409–412

Prymaczok N C, Pasqualino V M, Viau V E, et al. 2016. Involvement of the crustacean hyperglycemic hormone (CHH) in the physiological compensation of the freshwater crayfish *Cherax quadricarinatus* to low temperature and high salinity stress. Journal of Comparative Physiology B, 186(2): 181–191

Rainbow P S. 1988. The significance of trace metal concentrations in decapods. Symposia of the Zoological Society of London, 59: 291–313

Rainbow P S. 1997. Ecophysiology of trace metal uptake in crustaceans. Estuarine, Coastal and Shelf Science, 44(2): 169–176

Reddy P S, Bhagyalakshmi A. 1994. Changes in oxidative metabolism in selected tissues of the crab (*Scylla serrata*) in response to cadmium toxicity. Ecotoxicology and Environmental Safety, 29(3): 255–264

Reddy P S, Devi M, Sarojini R, et al. 1994. Cadmium chloride induced hyperglycemia in the red swamp crayfish, *Procambarus clarkii*: Possible role of crustacean hyperglycemic hormone. Comparative Biochemistry and Physiology Part C: Pharmacology, Toxicology and Endocrinology, 107(1): 57–61

Reddy P S, Katyayani R V, Fingerman M. 1996. Cadmium and naphthalene-induced hyperglycemia in the fiddler crab, *Uca pugilator*: differential modes of action on the neuroendocrine system. Bulletin of Environmental Contamination and Toxicology, 56(3): 425–431

Reddy P S, Reddy P R, Sainath S B. 2011. Cadmium and mercury-induced hyperglycemia in the fresh water crab, *Oziotelphusa senex senex*: involvement of neuroendocrine system. Ecotoxicology and Environmental Safety, 74(3): 279–283

Reddy P S, Tuberty S R, Fingerman M. 1997. Effects of cadmium and mercury on ovarian maturation in the red swamp crayfish, *Procambarus clarkii*. Ecotoxicology and Environmental Safety, 37(1): 62–65

Santos E A, Keller R. 1993. Regulation of circulating levels of the crustacean hyperglycemic hormone: evidence for a dual feedback control system. Journal of Comparative Physiology B, 163(5): 374–379

Santos E A, Keller R, Rodriguez E, et al. 2001. Effects of serotonin and fluoxetine on blood glucose regulation in two decapod species. Brazilian Journal of Medical and Biological Research, 34(1): 75–80

Sedlmeier D. 1982. The mode of action of the crustacean neurosecretory hyperglycemic hormone (CHH): II. Involvement of glycogen synthase. General and Comparative Endocrinology, 47(4): 426–432

Sedlmeier D. 1985. Mode of action of the crustacean hyperglycemic hormone. American Zoologist, 25(1): 223–232

Stentiford G D, Chang E S, Chang S A, et al. 2001. Carbohydrate dynamics and the crustacean Hyperglycemic hormone (CHH): effects of parasitic infection in Norway lobsters (*Nephrops norvegicus*). General and Comparative Endocrinology, 121(1): 13–22

Samuel N J, Thirunavukkarasu N, Soundarapandian P, et al. 2004. Fishery potential of commercially important portunid crabs along Parangipettai coast. In: Proceedings of Ocean Life Food and Medicine Expo, 165–173

Smith H. 1982. Blue crabs in South Australia: their status, potential and biology. South Australian Fishing Industry Council, 6: 6–9

Tietz N W. 1976. Clinical Guide to Laboratory Tests. London: W B Saunders Company Ltd, 238

Ui J. 1972. A few coastal pollution problems in Japan. In: Dyrssen D, Jagner D, eds. The Changing Chemistry of the Oceans. Stockholm: Almqvist and Wiksell, 364

Vernberg W B, DeCoursey P J, Padgett W J. 1974. Synergistic effects of environmental variables on larvae of *Uca pugilator*. Marine Biology, 22(4): 307–312

Webster S G. 1996. Measurement of crustacean hyperglycaemic hormone levels in the edible crab *Cancer pagurus* during emersion stress. The Journal of Experimental Biology, 199(7): 1579–1585

Weis J S. 1978. Interactions of methylmercury, cadmium, and salinity on regeneration in the fiddler crabs *Uca pugilator, U. pugnax* and *U. minax*. Marine Biology, 49(2): 119–124

Weis J S. 1980. Effect of zinc on regeneration in the fiddler crab *Uca pugilator* and its interactions with methylmercury and cadmium. Marine Environmental Research, 3(4): 249–255

Acta Oceanol. Sin., 2018, Vol. 37, No. 5, P. 54–66
DOI: 10.1007/s13131-017-1101-4
http://www.hyxb.org.cn
E-mail: hyxbe@263.net

Differential gene expression in the body wall of the sea cucumber (*Apostichopus japonicus*) under strong lighting and dark conditions

ZHANG Libin[1, 2], FENG Qiming[1, 3], SUN Lina[1, 2], FANG Yan[4], XU Dongxue[5], ZHANG Tao[1, 2], YANG Hongsheng[1, 2*]

[1] CAS Key laboratory of Marine Ecology and Environmental Sciences, Institute of Oceanology, Chinese Academy of Sciences, Qingdao 266071, China

[2] Laboratory for Marine Ecology and Environmental Science, Qingdao National Laboratory for Marine Science and Technology, Qingdao 266071, China

[3] University of Chinese Academy of Sciences, Beijing 100049, China

[4] School of Agriculture, Ludong University, Yantai 264025, China

[5] College of Marine Science and Engineering, Qingdao Agricultural University, Qingdao 266109, China

Received 25 January 2017; accepted 9 March 2017

Abstract

Sea cucumber, *Apostichopus japonicus* is very sensitive to light changes. It is important to study the influence of light on the molecular response of *A. japonicus*. In this study, RNA-seq provided a general overview of the gene expression profiles of the body walls of *A. japonicus* exposed to strong light ("light"), normal light ("control") and fully dark ("dark") environment. In the comparisons of "control" vs. "dark", "control" vs. "light" and "dark" vs. "light", 1 161, 113 and 1 705 differentially expressed genes (DEGs) were identified following the criteria of $|\log_2 \text{ratio}| \geqslant 1$ and FDR$\leqslant$0.001, respectively. Gene ontology analysis showed that "cellular process" and "binding" enriched the most DEGs in the category of "biological process" and "molecular function", while "cell" and "cell part" enriched the most DEGs in the category of "cellular component". And the DEGs were mapped to 214, 41 and 229 pathways in the Kyoto Encyclopedia of Genes and Genomes database, and 51, 2 and 57 pathways were significantly enriched, respectively. Light-specific DEGs identified in this study will be important targets for further investigation to establish the biochemical mechanisms involved in the adaption of this sea cucumber to changes in the level of environmental light.

Key words: sea cucumber, *Apostichopus japonicus*, gene expression, dark, light, body wall

Citation: Zhang Libin, Feng Qiming, Sun Lina, Fang Yan, Xu Dongxue, Zhang Tao, Yang Hongsheng. 2018. Differential gene expression in the body wall of the sea cucumber (*Apostichopus japonicus*) under strong lighting and dark conditions. Acta Oceanologica Sinica, 37(5): 54–66, doi: 10.1007/s13131-017-1101-4

1 Introduction

Light is an important ecological factor. The photoperiod, light intensity and light color can influence the distribution (Thorson, 1964), movement (Ringelberg, 1995), behavior (Naylor, 1999), physiology (Lambert and Brandt, 1967), feeding (Volpato et al., 2013), reproduction (Lambert and Brandt, 1967; West and Lambert, 1976), and growth of aquatic animals (Zhou et al., 2000).

Apostichopus japonicus, a common temperate species of sea cucumber, is distributed in the northwest Pacific (Liao, 1980; Sloan, 1984). *Apostichopus japonicus* is a very important mariculture species and is considered to be one of the most flavorful species in markets in East and Southeast Asian countries (Zhou et al., 2014). In 2015, the area occupied by *A. japonicus* culture was 216 508 hm^2 for a total output that reached 205 791 t in China (Fisheries Bureau of Ministry of Agriculture, 2016). It generates the highest single-species output value and profit of mariculture in northern China (Zhang et al., 2015b).

Light is a very important factor in the culture of *A. japonicus*, especially during the stages of brood stock and larval culture and juvenile rearing. A dark environment is usually maintained in the hatchery (Zhang et al., 2015b). To optimize the light conditions is a key technique in *A. japonicus* culture. Therefore it is important to study the influence of light on the behavior and physiology of *A. japonicus*.

Recently, the effects of light intensity on the daily activity rhythm of juvenile *A. japonicus* (Dong et al., 2010a), and on the daily feeding rhythm and movement, and the behavior and physiology of the species (Sun et al., 2015; Pan et al., 2015) have been investigated and quantified. The influence of light on the growth (Xue et al., 2007; Lin et al., 2013), respiration and excretion (Sui et al., 2010), and energy budget (Bao et al., 2014) of *A. japonicus* have also been investigated. In addition, some of the molecular responses of differentially expressed genes in *A. japonicus* have been studied during the aestivation stage (Zhao et

Foundation item: The National Natural Science Foundation of China under contract No. 41676136; the Strategic Priority Research Program of the Chinese Academy of Sciences under contract No. XDA11020703; the Science and Technology Major Project of Shandong Province (Industry Transformation and Upgrading) under contract No. 2015ZDZX05002.
*Corresponding author, E-mail: hshyang@qdio.ac.cn

al., 2014a; Chen and Storey, 2014), the intestine regeneration stage (Sun et al., 2013) and between different growth stages (embryo and larva) (Yang et al., 2010), under thermal (Shao et al., 2015) and osmotic stress (Dong et al., 2008), and even suffered from pathogen challenge (Zhang et al., 2013; Shao et al., 2013; Zhang et al., 2014). However, the molecular responses of differentially expressed genes in *A. japonicus* exposed to strong light and darkness, and the molecular basis of these adaptations, is poorly understood.

Generally speaking, *A. japonicus* is more like a nocturnal animal, and the feeding and activity peak mostly occurs late at night (Sun et al., 2015). Therefore, these organisms may be sensitive when exposed to different intensities of light. Some species of echinoderms have photosensory organs related to illumination, such as the brittle star *Ophiocoma wendtii* on the backs of the arms (Aizenberg et al., 2001) and the purple sea urchin *Strongylocentrotus purpuratus* on the tube feet (Raible et al., 2006). Some photosensory cells are composed of specialized structures of the ossicles (Aizenberg et al., 2001).

The body wall of *A. japonicus*, containing undeveloped bones with tiny scattered ossicles, which is in contact with the light directly by day and night, may be a sensitive photosensory tissue and influenced by light intensity. It may generate differential gene expression under strong light and in fully dark environments. However, the regulatory and response mechanisms are unclear. With the increasing availability of sequence data in recent years, expression profiling has been used to identify genes involved in the adaptive responses to environmental factors. Recently, RNA sequencing has been used to quantify, discover and profile RNAs. This is an effective and popular approach, for high throughput sequencing, with high sensitivity. The aim of this study was to develop a better understanding of the molecular responses of *A. japonicus* when exposed to strong ambient light and dark environments and to provide a theoretical basis for the development of healthy breeding conditions for *A. japonicus*.

2 Materials and methods

2.1 *Ethics statement*

It is not applicable in this study. Human or vertebrate species or relating samples were not involved. The sea cucumber, *A. japonicus* is not endangered or protected. No special permission was needed for the collection of *A. japonicus*.

2.2 *Animals*

Thirty-six fresh and healthy *A. japonicus* (80–130 g body weight) were collected from the coast of Qingdao, China and acclimated in tanks containing aerated sand-filtered seawater (salinity 31, pH 8.1) at (15±0.5)°C for one week before being exposed to different light conditions. They were fed once a day during this period. The animals were then divided randomly into three groups (12 individuals in each group). One group of sea cucumbers was maintained as the control group with natural light ("control") with the light intensity around 100 lx; the other two groups were exposed separately to strong light exposure with the light intensity around 2 000 lx ("light"), and in a fully dark tank covered by a shade cloth ("dark") for two hours. Six individuals randomly selected from each group were then dissected promptly and the body walls were sampled to be preserved for RNA extraction and sequencing. A brief overview of the rearing conditions of the sampled sea cucumbers and summarizes the key characteristics of the project are listed in Table 1.

2.3 *RNA extraction and sequencing*

RNA samples were extracted from the body walls of sea cucumbers in three different groups ("control", "light" and "dark") with an RNeasy mini kit, including DNase treatment with a RNase-free DNase (Qiagen Inc., Germany), according to the protocols of the manufacturer. Agilent 2100 bioanalyzer was used to determine the concentration and quality of the samples. Equal amount of the RNA samples from six individuals per group was pooled to prepare the sequencing library. The preparation of Libraries from the three RNA pools was carried out by Beijing Genomics Institute (BGI, Shenzhen, China), including mRNA enrichment, fragmentation, ligation of adapters, PCR amplification, and sequencing was conducted using an IlluminaHiSeq™ 2000 (BGI, Shenzhen). The sequencing was for single end read, and its read length was 200 bp.

2.4 *Read mapping and sequence quality control*

After quality control, which is applied for raw reads from primary sequencing to determine if resequencing is needed, the filtration of raw reads was involved to get clean reads through removing reads with adaptors, more than 10% unknown bases, and

Table 1. Gene expression profiles and environmental feature

Item	Description
Investigation type	sea cucumber, *Apostichopus japonicus*
Project name	gene expression response to strong lighting and dark
Collection date	April 15, 2013
Geographic location	35.97°N, 120.28°E
Country	China (Qingdao)
Environment (biome)	marine-subtidal area
Environment (material)	sea cucumbers maintained in seawater at laboratory
Temperature	(15±0.5)°C
Salinity	31
pH	8.1
Light	100 lx (control), 2 000 lx (light), fully dark (dark)
Sequencing method	pyrosequencing
Sequencing technology	IlluminaHiSeq™2000
Mapping method	Soap(2.21)
Annotation method	Blast(2.2.23), Blast2GO(2.2.5)
Reference database	Sun et al. (2011) (NCBI accession No. SRA020994), Du et al. (2012) (NCBI accession No. SRA046386)

low quality reads. Clean reads were then mapped to the reference databases using SOAP aligner/soap2 from large scale transcriptome profiling of sea cucumber, *A. japonicus* (Sun et al., 2011; Du et al., 2012). QC of alignment was also involved, including the calculation of the distribution of reads on reference genes and mapping ratio. Quality assessment of reads, sequencing saturation analysis, and randomness assessment were involved to confirm the quality of sequencing.

2.5 *Gene expression analysis, real-time PCR validation and functional classification*

Differentially expressed genes (DEGs) were detected by the RPKM method (reads per kb million reads), based on the normalized number of clean tags mapped exclusively for each gene (Mortazavi et al., 2008). The deviation of gene expression brought about by sequencing difference and gene length preference can be removed effectively by the standardization. In this study, the false discovery rate (FDR) not greater than 0.001 and an absolute value of $\log_2$ratio not less than 1 were set to determine DEGs, as described previously by Audic and Claverie (1997).

To validate RNA-seq results, the top five up-regulated genes and top five down-regulated genes were taken to perform real-time PCR. Primers were designed for optimal performance with primer3 (Table 2). The input RNA used in the synthesis of cDNA was run in triplicate of each group. The synthesis of the first strand cDNA was in 25 μL reaction system, as described in our earlier research (Sun et al., 2013). The SYBR Green® real-time PCR assay with an Eppendorf Mastercycler®eprealplex (Eppendorf, Hamburg, Germany) was used to determine the mRNA expression levels. The amplification volume (25 μL) contained 10.5 μL of RNase-free water, 12.5 μL of SYBR GreenMasterMix (Takara), 0.5 μL (each) of forward and reverse primer, and 1 μL of diluted cDNA. Thermal cycling procedure was 95°C for 5 s, and followed by 40 cycles at 95°C for 10 s, 60°C for 20 s and 72°C for 30 s. The specificity of the amplification products was confirmed by melting curve analysis. All the data were given as mean±SD (N=3) and $P<0.05$ was set for the statistical significance. And the analysis was performed with SPSS18.0 software.

To identify functional classifications of DEGs, all DEGs were mapped to gene ontology terms with the gene ontology (GO) database (http://www.geneontology.org/) and Kyoto Encyclopedia of Genes and Genomes (KEGG) (http://www.genome.jp/kegg/). Subsequently, the significantly enriched GO terms and pathways were determined by the calculation of the gene numbers related to each term and the application of a hypergeometric test applied to the DEGs. Q value was involved to determine the threshold of P value in multiple tests by the Bonferroni method (Abdi, 2007), and $P<0.05$ was set as the threshold to determine significantly enriched GO terms and KEGG pathways.

3 Results

3.1 *Analysis of sequencing data quality*

Libraries of three different groups ("control", "dark" and "light") were constructed from sea cucumber body walls. After filtering out low quality reads (adaptor reads, 10% unknown bases, and low quality reads) (Table 3), 5 919 823, 5 921 246 and 6 227 616 clean reads corresponding to the three groups have been deposited at GEO under the accession No. GSE87803. The reference transcriptome used in this work was from a 454 sequence transcriptomic database including different tissues, different developmental stages and different physiological conditions of *A. japonicus* (NCBI accession No. SRA020994 and No. SRA046386) (Sun et al., 2011; Du et al., 2012), which is currently the most thorough sea cucumber transcriptomic database. After alignment to the reference transcriptome, a total of 2 538 654 (42.88%), 2 723 388 (45.99%) and 2 633 299 (42.28%) reads were mapped to the "control", "dark" and "light" libraries as shown in Table 3. Of these, 1 777 034, 1 915 744 and 1 842 939 reads were uniquely aligned in one of the three libraries, accounting for 30.02%, 32.35% and 29.59% of all the mapped reads. Rigid data quality control and conservative matching ensured the effectiveness and accuracy of our results (Fig. S1). Saturation analysis indicated that 5×10^6 clean reads were already nearly saturated at

Table 2. Primers designed for optimal performance

Gene	Primer F	Primer R	Product size/bp
SAPA	GTACCACTGGGCGTGAGTTT	CGTTGCCCTATCGTTGCTAT	173
DSI	GGCAGGTGTTGGAAACAAAT	TCTGTCCTTCCGTCTGTGTG	186
TRA	GTGGACGGGGAAAACTTGTA	AGCTCATCCACACCTTTTGG	203
LRCP	GAGGTCGAGTGGACAGAAGC	TGTCACGAACAGCTCCAAAG	240
ASF	GCTCTGTGCATCCATCTGAA	AGCTTTCTACGGTGCGTTGT	241
AM	GCCTGAAGTTCGACCAAGTC	AATTTGAAGGATGGCGTGTC	171
PAP	CCATCCTTTTGCTCCATTGT	CCTCCGGACAATCCTGAATA	249
LRBAP	CCCCGATGGAATGAAGAGTA	CGATGGCAAGTTGACTCAGA	188
PGT	CGTTCCAAGTCAAGCGTACA	ATCATTGCCTCCATCCTGAG	201
AAPK	GTGTGCAAGTCTGCAAGGAA	ATGGTGAATTTTCCGCTCTG	202

Note: SAPA represents serum amyloid protein A; DSI dynactin subunit 5-like isoform 1; TRA transcobalamin I-like; LRCP leucine-rich repeat-containing protein; ASF ATP synthase-coupling factor 6, mitochondrial-like; AM alpha-2-macroglobulin-like; PAP papilin-like; LRBAP lipopolysaccharide-responsive and beige-like anchor protein-like, partial; PGT procollagen galactosyltransferase 1-like; and AAPK AP2-associated protein kinase 1-like.

Table 3. Summary of mapping result (mapping to reference genes)

Sample ID	Total reads	Total base pairs	Total mapped reads	Perfect match	≤2 bp mismatch	Unique match	Multi-position match	Total unmapped reads
Control	5 919 823 (100.00%)	290 071 327 (100.00%)	2 538 654 (42.88%)	1 777 034 (30.02%)	761 620 (12.87%)	1 570 290 (26.53%)	968 364 (16.36%)	3 381 169 (57.12%)
Dark	5 921 246 (100.00%)	290 141 054 (100.00%)	2 723 388 (45.99%)	1 915 744 (32.35%)	807 644 (13.64%)	1 698 268 (28.68%)	1 025 120 (17.31%)	3 197 858 (54.01%)
Light	6 227 616 (100.00%)	305 153 184 (100.00%)	2 633 299 (42.28%)	1 842 939 (29.59%)	790 360 (12.69%)	1 644 816 (26.41%)	988 483 (15.87%)	3 594 317 (57.72%)

this platform stage (Fig. S2). Assessment of sequencing randomness indicated the distribution of the reads and, in this study, the aligned reads seemed to be evenly distributed in the three libraries (Fig. S3).

3.2 *Differential gene expression analysis*

RNA-seq provided a general overview of the gene expression profiles of the body walls of *A. japonicus* exposed to strong light, normal light and fully dark environment. As a result, 1 161, 113 and 1 705 DEGs were identified following the criteria of $|\log_2 \text{ratio}| \geqslant 1$ and FDR$\leqslant$0.001, respectively, in comparisons of "control" vs. "dark", "control" vs. "light" and "dark" vs. "light" (Fig. 1).

Specifically, 145 up-regulated DEGs (0.23%, 145/62 000) and 1 016 down-regulated DEGs (1.64%, 1 016/62 000) were produced in the "control" vs. "dark" comparison, 46 up-regulated DEGs (0.07%, 46/62, 000) and 67 down-regulated DEGs (0.11%, 67/62 000) were identified when "light" was compared with "control", but 1 468 up-regulated DEGs (2.37%, 1 468/62 000) and 237 down-regulated DEGs (0.38%, 237/62 000) were detected in the "dark" vs. "light" comparison.

The top 20 up- or down-regulated DEGs from these three comparisons are listed in Table S1, S2 and S3. We found genes with light-specific expression. Compared with "dark", some DEGs, including neurogenic locus notch homolog protein 2, 60S ribosomal protein L8, phosphoinositide-3-kinase, lysine-specific demethylase 4C isoform 1, C2 domain-containing protein 3, rho GTPase-activating protein 18 isoform 2, and kinesin light chain isoform 1, were only expressed in the "light" group. Compared with "control", some DEGs, such as angiopoietin-1 receptor, were only expressed in the "light" group. However, because of the limitation of the reference databases, many DEGs were not annotated accurately.

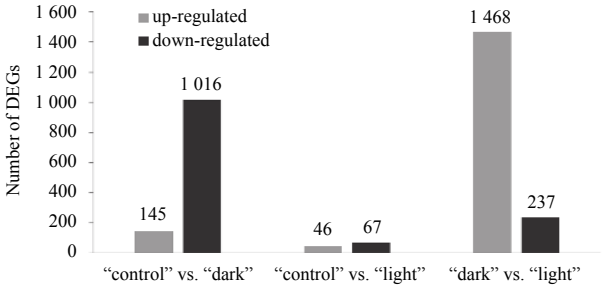

Fig. 1. Overview of differential expression (light representing strong light, dark fully dark, and control normal light).

3.3 *Classification of gene ontology (GO)*

Gene ontology analysis can provide complete functional information by assigning DEGs to three major sections ("cellular component", "molecular function" and "biological process"). In order to determine the function of the DEGs, DGEs were conducted by GO analysis. The GO term enrichment analysis detected a total of 27, 1 and 38 significantly overrepresented GO terms enriched in the comparisons of "control" vs. "dark", "control" vs. "light" and "dark" vs. "light", respectively, with corrected *P*-value less than 0.05 (Table 4). In the three comparisons, "cellular pro-

Table 4. Gene ontology (GO) terms enriched of differentially expressed genes correlated with strong light, natural light and fully dark exposure

Gene ontology term	GO No.	Reference frequency (N/M)	Cluster frequency (n/m)	Corrected *P* value
"Dark" vs. "control"				
Biological process				
Regulation of biological process	GO: 0050789	156/365 (42.7%)	1 530/5 347 (28.6%)	1.59×10^{-6}
Regulation of cellular process	GO: 0050794	138/365 (37.8%)	1 331/5 347 (24.9%)	9.76×10^{-6}
Biological regulation	GO: 0065007	167/365 (45.8%)	1 804/5 347 (33.7%)	0.000 54
Cell communication	GO: 0007154	89/365 (24.4%)	821/5 347 (15.4%)	0.001 99
Signaling	GO: 0023052	85/365 (23.3%)	775/5 347 (14.5%)	0.002 25
Single organism signaling	GO: 0044700	85/365 (23.3%)	775/5 347 (14.5%)	0.002 25
Negative regulation of cellular process	GO: 0048523	37/365 (10.1%)	251/5 347 (4.7%)	0.004 86
Signal transduction	GO: 0007165	76/365 (20.8%)	682/5 347 (12.8%)	0.004 99
Epithelial cell differentiation	GO: 0030855	10/365 (2.7%)	27/5 347 (0.5%)	0.005 68
Regulation of localization	GO: 0032879	21/365 (5.8%)	112/5 347 (2.1%)	0.016 45
Negative regulation of biological process	GO: 0048519	40/365 (11.0%)	304/5 347 (5.7%)	0.032 40
Response to stimulus	GO: 0050896	135/365 (37.0%)	1 478/5 347 (27.6%)	0.035 12
Cell surface receptor signaling pathway	GO: 0007166	41/365 (11.2%)	316/5 347 (5.9%)	0.035 85
Appendage development	GO: 0048736	13/365 (3.6%)	54/5 347 (1.0%)	0.047 49
Cellular component				
Anchoring junction	GO: 0070161	13/306 (4.2%)	48/4 541 (1.1%)	0.001 68
Cell-substrate adherens junction	GO: 0005924	10/306 (3.3%)	31/4 541 (0.7%)	0.003 39
Cell-substrate junction	GO: 0030055	10/306 (3.3%)	32/4 541 (0.7%)	0.004 64
Adherens junction	GO: 0005912	10/306 (3.3%)	36/4 541 (0.8%)	0.014 36
Cell junction	GO: 0030054	17/306 (5.6%)	91/4 541 (2.0%)	0.015 12
Neuron part	GO: 0097458	21/306 (6.9%)	137/4 541 (3.0%)	0.045 31
Molecular function				
Phosphotransferase activity, alcohol group as acceptor	GO: 0016773	45/348 (12.9%)	253/5 067 (5.0%)	2.31×10^{-7}
Protein kinase activity	GO: 0050222	41/348 (11.8%)	238/5 067 (4.7%)	3.55×10^{-6}

to be continued

Continued from Table 4

Gene ontology term	GO No.	Reference frequency (N/M)	Cluster frequency (n/m)	Corrected P value
Kinase activity	GO: 0016301	50/348 (14.4%)	348/5 067 (6.9%)	4.12×10^{-5}
Transferase activity, transferring phosphorus-containing groups	GO: 0016772	61/348 (17.5%)	492/5 067 (9.7%)	0.000 34
Enzyme binding	GO: 0019899	28/348 (8.0%)	201/5 067 (4.0%)	0.038 67
Protein binding	GO: 0005515	111/348 (31.9%)	1 209/5 067 (23.9%)	0.044 41
Protein domain specific binding	GO: 0019904	13/348 (3.7%)	63/5 067 (1.2%)	0.048 4
"Light" vs. "control"				
Biological process				
Cellular component				
Molecular function				
Hydrolase activity, acting on carbon-nitrogen (but not peptide) bonds	GO: 0016810	2 out of 10 genes, 20.0%	29 out of 5 067 genes, 0.6%	0.012 45
"Light" vs. "dark"				
Biological process				
Regulation of biological process	GO: 0050789	241/555 (43.4%)	1 530/5 347 (28.6%)	2.88×10^{-12}
Regulation of cellular process	GO: 0050794	211/555 (38.0%)	1 331/5 347 (24.9%)	3.42×10^{-10}
Biological regulation	GO: 0065007	257/555 (46.3%)	1 804/5 347 (33.7%)	7.38×10^{-8}
Intracellular signal transduction	GO: 0035556	68/555 (12.3%)	320/5 347 (6.0%)	2.98×10^{-6}
Cell communication	GO: 0007154	134/555 (24.1%)	821/5 347 (15.4%)	7.75×10^{-6}
Signal transduction	GO: 0007165	116/555 (20.9%)	682/5 347 (12.8%)	9.87×10^{-6}
Signaling	GO: 0023052	127/555 (22.9%)	775/5 347 (14.5%)	1.73×10^{-5}
Single organism signaling	GO: 0044700	127/555 (22.9%)	775/5 347 (14.5%)	1.73×10^{-5}
Negative regulation of cellular process	GO: 0048523	52/555 (9.4%)	251/5 347 (4.7%)	0.000 61
Negative regulation of biological process	GO: 0048519	59/555 (10.6%)	304/5 347 (5.7%)	0.001 05
Regulation of response to stimulus	GO: 0048583	53/555 (9.5%)	270/5 347 (5.0%)	0.002 77
Cell surface receptor signaling pathway	GO: 0007166	58/555 (10.5%)	316/5 347 (5.9%)	0.008 48
Cellular response to stimulus	GO: 0051716	137/555 (24.7%)	946/5 347 (17.7%)	0.008 66
Regulation of phosphorylation	GO: 0042325	29/555 (5.2%)	119/5 347 (2.2%)	0.009 01
Actin cytoskeleton organization	GO: 0030036	24/555 (4.3%)	90/5 347 (1.7%)	0.010 83
Cellular response to chemical stimulus	GO: 0070887	28/555 (5.0%)	114/5 347 (2.1%)	0.011 04
Gastrulation	GO: 0007369	15/555 (2.7%)	42/5 347 (0.8%)	0.012 01
Actin filament-based process	GO: 0030029	24/555 (4.3%)	91/5 347 (1.7%)	0.013 30
Regulation of protein phosphorylation	GO: 0001932	27/555 (4.9%)	109/5 347 (2.0%)	0.013 48
Small GTPase mediated signal transduction	GO: 0007264	18/555 (3.2%)	58/5 347 (1.1%)	0.015 17
Positive regulation of response to stimulus	GO: 0048584	27/555 (4.9%)	111/5 347 (2.1%)	0.019 32
Cell migration	GO: 0016477	26/555 (4.7%)	105/5 347 (2.0%)	0.019 74
Regulation of metabolic process	GO: 0019222	88/555 (15.9%)	559/5 347 (10.5%)	0.025 05
Immune response-activating cell surface receptor signaling pathway	GO: 0002429	6/555 (1.1%)	8/5 347 (0.1%)	0.034 36
Antigen receptor-mediated signaling pathway	GO: 0050851	6/555 (1.1%)	8/5 347 (0.1%)	0.034 36
Immune response-regulating cell surface receptor signaling pathway	GO: 0002768	7/555 (1.3%)	11/5 347 (0.2%)	0.034 38
Positive regulation of biological process	GO: 0048518	66/555 (11.9%)	394/5 347 (7.4%)	0.044 41
Cellular component				
Dendrite	GO: 0030425	14/461 (3.0)	38/4 541 (0.8)	0.001 68
Neuron part	GO: 0097458	30/461 (6.5)	137/4 541 (3.0)	0.005 12
A band	GO: 0031672	4/461 (0.9)	4/4 541 (0.1)	0.017 84
Neuron projection	GO: 0043005	26/461 (5.6)	124/4 541 (2.7)	0.036 97
Cell junction	GO: 0030054	21/461 (4.6)	91/4 541 (2.0)	0.037 37
Molecular function				
Phosphotransferase activity, alcohol group as acceptor	GO: 0016773	58/512 (11.3)	253/5 067 (5.0)	1.49×10^{-7}
Protein kinase activity	GO: 0050222	54/512 (10.5)	238/5 067 (4.7)	9.08×10^{-7}
Kinase activity	GO: 0016301	67/512 (13.1)	348/5 067 (6.9)	1.41×10^{-5}
Protein binding	GO: 0005515	168/512 (32.8)	1 209/5 067 (23.9)	0.000 16
Transferase activity, transferring phosphorus-containing groups	GO: 0016772	79/512 (15.4)	492/5 067 (9.7)	0.002 11
Enzyme binding	GO: 0019899	39/512 (7.6)	201/5 067 (4.0)	0.007 91

Note: N is the number of all genes with GO annotation, n the number of DEGs in N, M the number of all genes that are annotated to certain GO terms, and m the number of DEGs in M.

cess" and "binding" enriched the most DEGs in the category of "biological process" and "molecular function", while "cell" and "cell part" enriched the most DEGs in the category of "cellular component" (Fig. 2). Moreover, in the comparison of "control" vs. "light", "metabolic process" was another dominant term for "biological process", and "catalytic activity" was another dominant term for "molecular function".

3.4 *Classification according to the Kyoto Encyclopedia of Genes and Genomes (KEGG)*

The DEGs were also mapped to KEGG metabolic and regulatory pathways with a correct *P*-value cutoff of being less than 0.05. The differential gene expression in the three comparisons "dark" and "control", "light" and "control", "light" and "dark" affected a range of KEGG pathways. The top ten significantly enriched pathways for DEGs are listed in Table 5. The differentially expressed genes were mapped to 214, 41, and 229 pathways in the KEGG database, and 51, 2, and 57 pathways were significantly enriched, respectively (corrected *P*-value less than 0.05). The most representative KEGG pathways included Focal adhesion (ko04510), the ErbB signaling pathway (ko04012), and Fc gamma R-mediated phagocytosis (ko04666) in the comparison of "control" vs. "dark", ECM-receptor interaction (ko04512) and Focal adhesion (ko04510) in the comparison of "control" vs. "light", and the Chemokine signaling pathway (ko04062), ErbB signaling pathway (ko04012), and Focal adhesion (ko04510) in the comparison of "dark" vs. "light".

3.5 *Validation of DGE analysis*

Real-time PCR was carried out to confirm the expression profiles of the top DGEs identified in the RNA-seq. Top five up-regulated genes (serum amyloid protein A (SAPA); dynactin subunit 5-like isoform 1 (DSI), transcobalamin I-like (TRA), leucine-rich repeat-containing protein (LRCP), ATP synthase-coupling factor 6, mitochondrial-like (ASF)) and top five down-regulated genes (alpha-2-macroglobulin-like (AM), papilin-like (PAP), lipopoly-

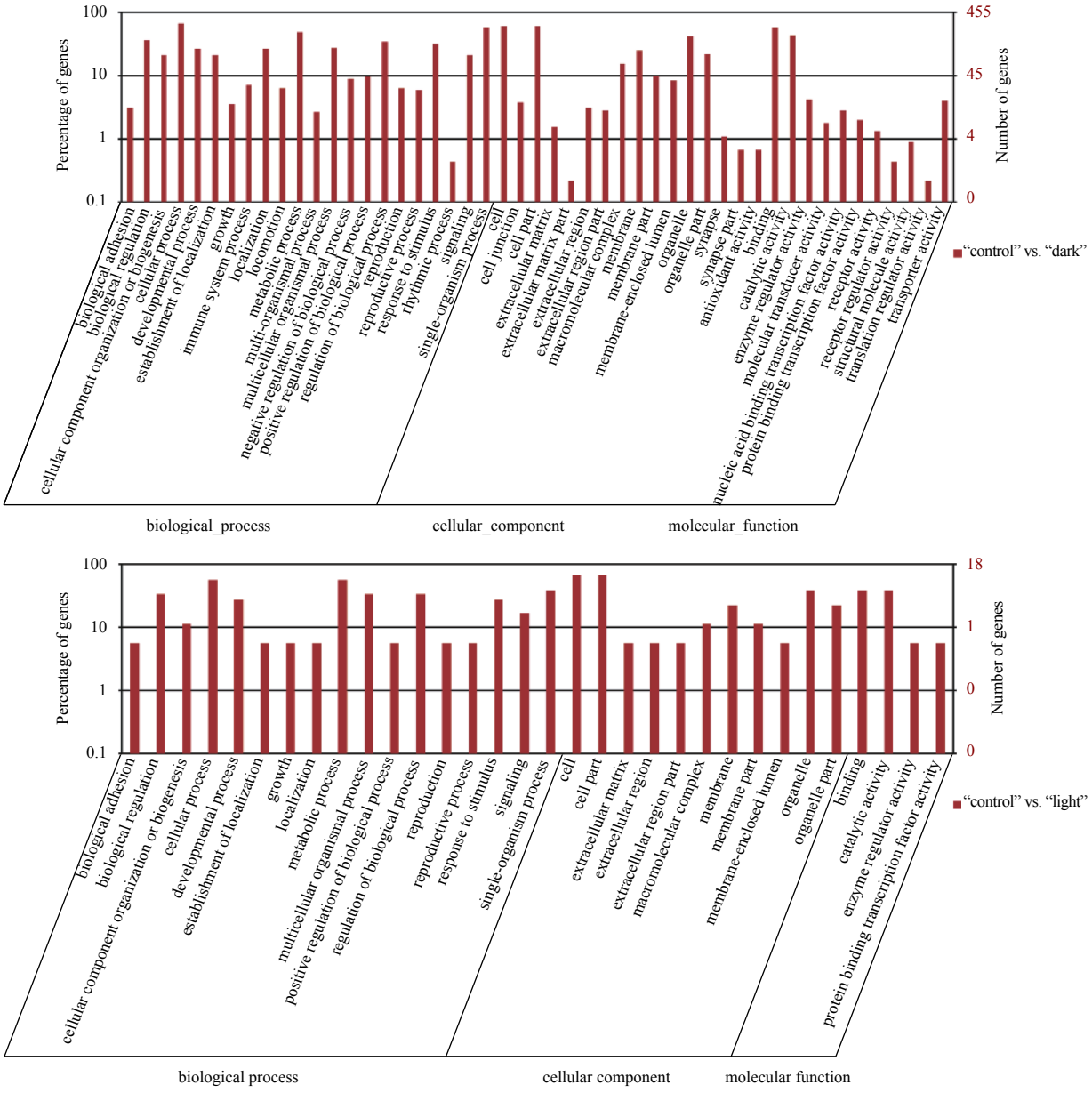

Fig. 2

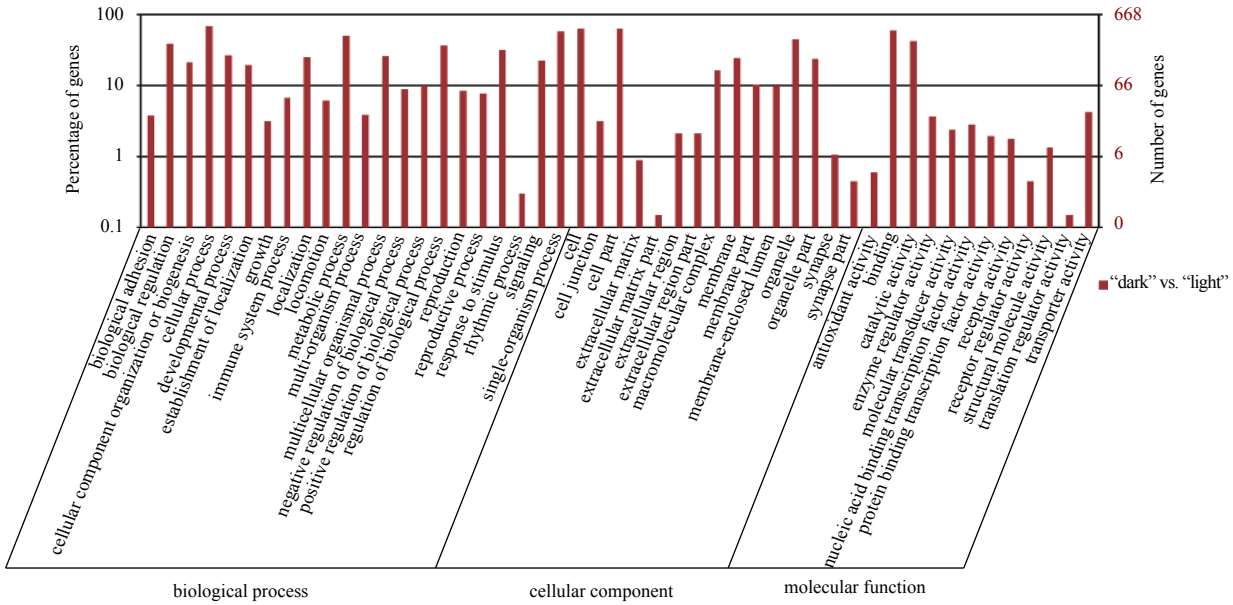

Fig. 2. Distribution of gene ontology (GO) terms of DEGs from the body wall of *A. japonicus* exposure to different light environment ("control" vs. "dark", "control" vs. "light", and "dark" vs. "light") (light representing strong light, dark representing fully dark, control representing normal light). The percentage of GO terms in the categories “cellular component”, “molecular function” and “biological process” are shown.

saccharide-responsive and beige-like anchor protein-like, partial (LRBAP), procollagen galactosyltransferase 1-like (PGT), AP2-associated protein kinase 1-like (AAPK)) were applied to real-time PCR at “dark” vs. “control” (Fig. 3). β-actin was taken as a reference gene to normalize gene expression data. Real-time PCR results showed that five up-regulated genes and four out of the five down-regulated genes showed exact correlations in their expression profiles between real-time PCR and RNA-seq, which implied our results were credible.

3.6 *Key DEGs responding to different light conditions*

Based on the primary results, genes whose functions appear to be important for understanding the response of *A. japonicus* when its body wall is exposed to different light conditions are shown in Table 6. The key DEGs associated with light density were classified into five groups. Generally speaking, when compared with “control”, the change (-fold) in gene expression varied less in “light” than in “dark”. For example, when compared with “control”, some key DEGs associated with movement of cells or subcellular components, such as dynein light chain roadblock-type 2, exhibited up-regulation in both “dark” and “light”. Some DEGs, such as dynactin subunit 1-like, showed down-regulation in “dark” but no significant change in “light”.

4 Discussion

Most organisms exhibit daily physiological and behavioral rhythms that are regulated by molecular circadian clocks. Light is the most common signal that entrains these rhythms (Reitzel et al., 2010). *Apostichopus japonicus* is nocturnal, sensitive to light and tends to keep away from light. The animals usually hide during daylight hours and feed during the dark of night (Sun et al., 2015). *Apostichopus japonicus* prefers habitats with low light intensity. Lin et al. (2013) found that *A. japonicus* moved quickly to the low light area after being placed in the center of the flume within 90 min. They prefer to spawn in the dark and have distinct rhythms, most individuals retreating to shelter during the daytime and emerging and feeding during the night (Zhang et al., 2015a; Dong et al., 2011). They usually inhabit and are attached to the shadow area of reefs when exposed to strong light (Zhang et al., 2006; Zhang et al., 2009; Chen et al., 2007). As a result, when *A. japonicus* is exposed to different light conditions, specific behavioral and physiological characteristics may be observed and molecular regulatory mechanisms may be affected.

Large scale gene expression profiling may facilitate the identification of systemic gene expression and regulatory mechanisms for the environmental tolerance of sea cucumbers. In this study, RNA-seq analysis was used to allow a comprehensive evaluation of differences in gene expression in the body wall of the sea cucumber *A. japonicus* under the influence of full darkness and strong light. The results indicated that exposure of *A. japonicus* to environments of different light intensity is associated with thousands of transcriptional variations. Numerous light-associated genes (Tables 4–6) showed different levels of expressions under the influences of full darkness and the strong light environment. These genes may be excellent candidates for future studies on the molecular mechanisms associated with the behavior of *A. japonicus* under different light conditions. In addition, based on the annotation of unigenes, the classification of DEGs was conducted by a GO process in terms of different functions, biological processes, and locations (Table 4, Fig. 2). Pathway enrichment analysis identified the most significantly affected pathways when sea cucumbers were exposed to light of different intensities (Table 5).

4.1 *Genes associated with movement of cells or subcellular components*

Molecular motors are biological machines. They are the essential agents of movement in animals. The movement of all kinds of tissues, organs, and even the whole body is ultimately attributed to the movement of molecular motors. Dynein is a molecular motor in cells which can convert the chemical energy contained in ATP into the mechanical energy of movement.

Table 5. Top ten Significant enrichment of pathways for DEGs

Number	Pathway	DEGs with pathway annotation (662)	All genes with pathway annotation (10 236)	*P* value	*Q* value	Pathway ID
"Dark" vs. "control"						
1	Focal adhesion	65 (9.82%)	463 (4.52%)	1.64×10^{-9}	2.10×10^{-7}	ko04510
2	ErbB signaling pathway	21 (3.17%)	71 (0.69%)	1.97×10^{-9}	2.10×10^{-7}	ko04012
3	Fc gamma R-mediated phagocytosis	25 (3.78%)	115 (1.12%)	5.88×10^{-8}	4.19×10^{-6}	ko04666
4	Insulin signaling pathway	26 (3.93%)	132 (1.29%)	2.60×10^{-7}	1.18×10^{-5}	ko04910
5	Bacterial invasion of epithelial cells	25 (3.78%)	124 (1.21%)	2.76×10^{-7}	1.18×10^{-5}	ko05100
6	Chemokine signaling pathway	25 (3.78%)	129 (1.26%)	6.08×10^{-7}	1.91×10^{-5}	ko04062
7	Fc epsilon RI signaling pathway	17 (2.57%)	66 (0.64%)	6.24×10^{-7}	1.91×10^{-5}	ko04664
8	Chronic myeloid leukemia	17 (2.57%)	69 (0.67%)	1.23×10^{-6}	3.29×10^{-5}	ko05220
9	Neurotrophin signaling pathway	22 (3.32%)	112 (1.09%)	2.26×10^{-6}	5.39×10^{-5}	ko04722
10	Natural killer cell mediated cytotoxicity	14 (2.11%)	53 (0.52%)	4.43×10^{-6}	9.48×10^{-5}	ko04650
"Light" vs. "control"						
1	ECM-receptor interaction	8 (20%)	245 (2.39%)	3.81×10^{-6}	0.000156	ko04512
2	Focal adhesion	8 (20%)	463 (4.52%)	0.000 353	0.007 236	ko04510
3	PPAR signaling pathway	3 (7.5%)	91 (0.89%)	0.005 295	0.064 526	ko03320
4	Rheumatoid arthritis	3 (7.5%)	101 (0.99%)	0.007 071	0.064 526	ko05323
5	Staphylococcus aureus infection	3 (7.5%)	105 (1.03%)	0.007 869	0.064 526	ko05150
6	Complement and coagulation cascades	4 (10%)	250 (2.44%)	0.015 939	0.108 916	ko04610
7	Hematopoietic cell lineage	2 (5%)	60 (0.59%)	0.022 85	0.133 834	ko04640
8	Oxidative phosphorylation	3 (7.5%)	178 (1.74%)	0.031 919	0.145 074	ko00190
9	Autoimmune thyroid disease	1 (2.5%)	9 (0.09%)	0.034 639	0.145 074	ko05320
10	Cell adhesion molecules (CAMs)	2 (5%)	76 (0.74%)	0.035 384	0.145 074	ko04514
"Light" vs. "dark"						
1	Chemokine signaling pathway	38 (3.85%)	129 (1.26%)	1.65×10^{-10}	3.77×10^{-8}	ko04062
2	ErbB signaling pathway	26 (2.63%)	71 (0.69%)	7.24×10^{-10}	8.29×10^{-8}	ko04012
3	Focal adhesion	85 (8.6%)	463 (4.52%)	2.72×10^{-9}	2.07×10^{-7}	ko04510
4	Bacterial invasion of epithelial cells	33 (3.34%)	124 (1.21%)	4.23×10^{-8}	2.42×10^{-6}	ko05100
5	Chronic myeloid leukemia	23 (2.33%)	69 (0.67%)	5.42×10^{-8}	2.48×10^{-6}	ko05220
6	Fc gamma R-mediated phagocytosis	31 (3.14%)	115 (1.12%)	7.88×10^{-8}	3.01×10^{-6}	ko04666
7	Axon guidance	40 (4.05%)	172 (1.68%)	9.57×10^{-8}	3.13×10^{-6}	ko04360
8	Neurotrophin signaling pathway	30 (3.04%)	112 (1.09%)	1.49×10^{-7}	4.25×10^{-6}	ko04722
9	Natural killer cell mediated cytotoxicity	19 (1.92%)	53 (0.52%)	2.12×10^{-7}	4.87×10^{-6}	ko04650
10	Insulin signaling pathway	33 (3.34%)	132 (1.29%)	2.13×10^{-7}	4.87×10^{-6}	ko04910

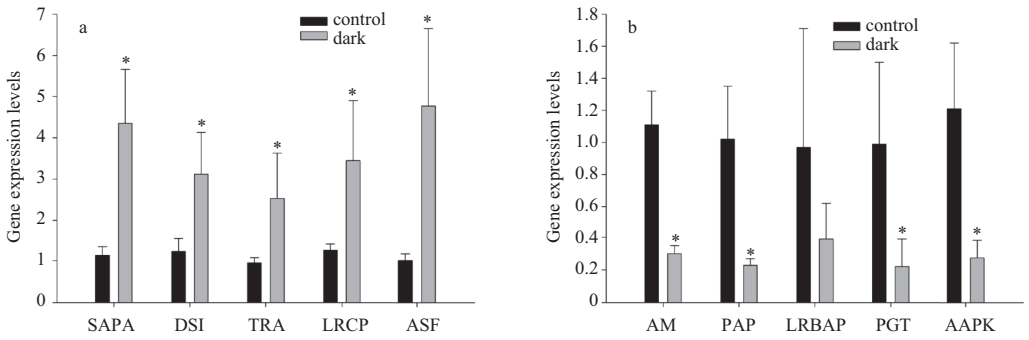

Fig. 3. Real-time PCR analysis for the top five up-regulated and five down-regulated genes in "dark" vs. "control". a. SAPA represents serum amyloid protein A; DSI dynactin subunit 5-like isoform 1; TRA transcobalamin I-like; LRCP Leucine-rich repeat-containing protein; and ASF ATP synthase-coupling factor 6, mitochondrial-like. b. AM represents alpha-2-macroglobulin-like; PAP papilin-like; LRBAP lipopolysaccharide-responsive and beige-like anchor protein-like, partial; PGT procollagen galactosyltransferase 1-like; and AAPK AP2-associated protein kinase 1-like. * indicates significant differences between dark and control groups ($P<0.05$). Values indicate the mean±SD (N=3).

Dynein works associated with another large protein complex called dynactin which is required for virtually all known functions of dynein (Haghnia et al., 2007). After binding to dynactin, dynein transports various cellular cargos, which vary from mRNAs to entire organelles, by "walking" along cytoskeletal microtubules towards the minus-end of the microtubule (Mallik and Gross, 2004). The results of this study revealed the differential expression of numerous movement-associated genes under

Table 6. Key DEGs associated with light influence

Gene	Gene ID	Normal light (RPKM)	Dark light (RPKM)	Strong light (RPKM)
DEGs associated with movement of cell or subcellular component				
Dynein light chain roadblock-type 2	isotig08721	2.01	9.91	5.44
Cytoplasmic dynein 1 heavy chain 1-like isoform 2	isotig17784	35.45	7.28	44.50
Cytoplasmic dynein 1 light intermediate chain 2-like	isotig14932	44.63	13.62	45.16
Dynactin subunit 5-like isoform 1	isotig09020	1.03	12.81	3.92
Dynactin subunit 1-like	isotig13914	52.68	21.35	56.15
Kinesin-like protein KIF1B-like	isotig13747	10.23	1.89	10.42
Kinesin heavy chain	isotig13276	70.32	31.54	83.28
Myosin VI	isotig16090	33.15	6.43	29.10
Myosin phosphatase Rho-interacting protein-like	isotig15515	18.64	4.99	17.80
Dedicator of cytokinesis protein 9	isotig15901	36.91	12.50	45.66
Unconventionnal myosin-X	isotig18746	67.90	23.13	68.92
Unconventional myosin-Id isoform 2	isotig09887	32.04	11.11	32.50
Amoeboid myosin I	isotig17115	73.39	26.92	79.33
Amoeboid myosin I	isotig18961	58.36	23.61	69.64
Myosin-IIIB	isotig13235	58.08	24.39	85.71
Unconventional myosin-XVIIIa	isotig13782	100.30	48.78	101.05
DEGs associated with metabolic process				
Pancreatic alpha-amylase-like	isotig10221	370.71	801.41	365.99
6-phosphofructo-2-kinase/fructose-2, 6-bisphosphatase	isotig13300	47.33	19.40	42.36
1-phosphatidylinositol 4, 5-bisphosphate phosphodiesterase gamma-1	isotig20602	77.37	11.79	81.98
Glucosamine-6-phosphate deaminase 1-like	isotig03620	5.00	16.57	7.16
Pancreatic alpha-amylase	isotig10221	370.71	801.41	365.99
Procollagen galactosyltransferase 1	isotig18726	31.59	1.99	28.10
60S ribosomal protein L10a	isotig10422	5.49	10.88	0.01
60S ribosomal protein L23a	isotig11170	136.53	321.65	123.20
Serum amyloid protein A	isotig08093	1.58	32.79	7.52
MICAL-3	isotig01569	5.56	0.24	3.79
ATP synthase-coupling factor 6, mitochondrial-like	isotig03824	3.4	17.29	7.03
ATP synthase subunit gamma, mitochondrial-like	isotig08835	14.37	34.42	17.24
ATP-binding cassette sub-family A member 3	isotig19240	18.77	2.08	20.79
ATP-binding cassette transporter subfamily A	isotig17944	43.16	6.75	58.96
Phospholipid-transporting ATPase ID-like	isotig28066	48.73	10.88	27.27
ATP-binding cassette transporter subfamily A	isotig14200	73.21	19.70	91.71
Potassium-transporting ATPase subunit beta-1-like isoform 1	isotig06693	44.26	14.35	43.90
DEGs associated with stimulus and Immune defense				
C-type lectin	isotig10929	32.86	99.83	45.56
Fucolectin-7	isotig03693	35.74	101.54	16.75
Fibrinogen-like protein A	isotig19241	298.89	823.54	538.43
Fibrinogen C domain-containing protein 1-like	isotig16485	16.98	45.01	2.70
Fibropellin-1	isotig05245	835.64	1 925.45	899.84
Alpha-2-macroglobulin	isotig16383	51.50	2.05	3.17
DEGs associated with signal transduction				
Translationally-controlled tumor protein	isotig09381	21.08	56.66	24.34
Translocon-associated protein subunit gamma	isotig07409	24.06	59.79	29.43
Alpha-1D adrenergic receptor	isotig10079	19.04	44.94	16.74
Thioredoxin	isotig10271	19.01	40.24	12.42
Lipopolysaccharide-responsive and beige-like anchor protein-like, partial	isotig24634	35.58	2.19	49.82
DEGs associated with photoreceptors				
CREB-regulated transcription coactivator 1	isotig21193	28.70	3.32	22.26

environments with different levels of light (Tables S1–S3). It was found that the well-known movement associated genes dynactin subunit 5-like isoform 1 and dynein light chain roadblock-type 2 were over-expressed under dark conditions compared with the normal and strong light environments. It can be inferred that some biomacromolecules involved in movement processes correspond to the active behavior in *A. japonicus* when being placed under dark conditions.

However, cytoplasmic dynein 1 heavy chain 1-like isoform 2, cytoplasmic dynein 1 light intermediate chain 2-like, and dynactin subunit 1-like were up-regulated under normal and strong light conditions when compared with dark environment (Table 6).

In addition, a large variety of myosin genes, such as myosin VI, myosin phosphatase Rho-interacting protein-like, dedicator of cytokinesis protein 9, unconventional myosin-X, unconventional myosin-Id isoform 2, amoeboid myosin I, myosin-IIIB, and unconventional myosin-XVIIIa, were shown to be up-regulated under normal and strong light conditions compared with fully dark environment in this study (Table 6). Myosins are a superfamily of motor proteins that move along actin filaments, while hydrolyzing ATP. They are import for muscular contraction and account for 40%–50% of the total proteins in muscles (Mehl, 1940). Myosin light chain phosphorylation was also found to regulate contraction in the body wall muscles of the sea cucumber *Parastichopus californicus* (Kerrick and Bolles, 1982). Interestingly, the myosin genes that were overexpressed under different light conditions in this study have also been suggested to be involved in muscle differentiation in *A. japonicus* (Sun et al., 2011) and *Holothuria glaberrima* (Ortiz-Pineda et al., 2009). In the previous study, it was found the distribution of *A. japonicus*, being placed in the flume after 1 h, became stable in comparatively dark area (Lin et al., 2013). In this study, the sea cucumbers were sampled after 2 h's stress, and it might bring about a comparative stable status in the latter for sea cucumbers under fully dark environment. The sea cucumbers under strong and normal light conditions might be still searching some area with low illumination level. Maybe it is the reason why the variety of gene homologs associated with movement were up-regulated under normal and strong light environments.

The expression of genes encoding dynein, dynactin and myosin, to which may be attributed the movement of *A. japonicus*, may be coordinated in response to light intensity. This may underlie the molecular mechanism of movement in *A. japonicus* under conditions of different light intensity.

4.2 *Genes associated with metabolism*

When active behaviors occur, energy will be consumed in *A. japonicus*, as in all other organisms. Biological processes related to metabolism of substances and energy will be activated. Among the annotated unigenes, 60S ribosomal protein L10a, belonging to the ribosomal protein L1P family, which has the function of preventing protein synthesis inhibition, mRNA–rRNA processing and signal transduction (Kim and Jang, 2002; Warner and McIntosh, 2009), was found to be down-regulated under strong light compared with fully dark conditions (Table 6). The protein is a component of the large 60S subunit of ribosome. Ribosomes, which consist of a small 40S subunit and a large 60S subunit, are the organelles functioning in catalyzing protein synthesis. It can be inferred that some protein synthesis function might be restricted in *A. japonicus* under strong light condition, and might be promoted when *A. japonicus* is active under fully dark condition.

Light is a powerful environmental factor for *A. japonicus*. The growth, behavior, and digestive physiology of the sea cucumber may be affected by light intensity and photoperiod (Dong et al., 2010a, b, 2011; Sun et al., 2015). Exposure to different color spectra may also result in different growth performance and energy budgets in *A. japonicus* (Bao et al., 2014). There is a close connection between ATP and energy metabolism (Wang et al., 2012). In this study, some of the mRNA expressions of genes related to ATP synthase, e.g., ATP synthase subunit gamma, mitochondrial-like, ATP synthase subunit gamma, mitochondrial-like, ATP-binding cassette sub-family A member 3, ATP-binding cassette transporter subfamily A were regulated differently under the fully dark and strong light conditions compared with the normal light condition (Table 6), which indicated that the differences of ATP synthesis and energy metabolism may occur when the animals are exposed to different light conditions. The mRNA expression of ATP synthase was down-regulated when *A. japonicus* was in a state of torpor, such as in the aestivation state or when challenged with thermal stress (Zhao et al., 2014a; Shao et al., 2015). It has been suggested that ATP synthase plays an important role in energy metabolism in *A. japonicus* when it responds to light and temperature.

Serum amyloid A (SAA) proteins, found in all mammals, ducks, salmonid fishes, and even echinoderms, comprise a family of highly conserved apolipoproteins (Santiago et al., 2000). They possess enough functional diversity to participate in and regulate metabolic processes. SAAs were up-regulated in the body wall of *A. japonicus* under fully dark conditions and down-regulated under the strong light condition when compared with the normal condition respectively (Table 6). However, in the previous study, SAA was significantly over-expressed in *A. japonicus* undergoing deep aestivation with hypometabolism, compared with non-aestivation (Zhao et al., 2014a, b). The different regulations of SAA at mRNA level, in the less active circumstances of *A. japonicus* under strong light conditions and in the aestivation period, may indirectly indicate the functional diversity of SAA in regulating metabolic processes.

4.3 *Genes associated with stimulus and signal transduction*

Light is a key environmental factor. In the study, when the sea cucumbers were transferred directly from tanks under normal light to tanks under fully dark or strong light environment, the sharp changes of the light condition might be stimuli to *A. japonicus*, and immune defenses could be triggered. Lectins are a group of proteins which bind to cell surface carbohydrates and play critical roles in innate immunity. Fucolectin-7, which recognizes blood group fucosylated oligosaccharides and acts as a defensive agent (Wu et al., 2004), was found to be up-regulated in "dark" compared with "control" in this study (Table 6). Lipopolysaccharide (LPS)-stimulated expression of fucolectins in the Japanese eel *Anguilla japonica* (Honda et al., 2000) suggests that they serve as powerful defense agents. Fucolectin-7 was also found in the pathogen recognition system of *A. japonicus* (Dong et al., 2014). Some genes related to fibrinogen, which is important for the immune system of both vertebrates and invertebrates (Xu and Doolittle, 1990), for example fibrinogen-like protein A and fibrinogen C domain-containing protein 1-like, were also found to be over-expressed under fully dark conditions (Table 6). The changes in immune response genes such as fucolectin-7 and fibrinogen suggest that self-defense mechanisms are activated in response to light density. The different expressions of genes related to immune defense might be the responses of *A. japonicus* to the sharp changes of light condition, which is different from the natural light.

Furthermore, some signal transduction related genes were involved. For example, alpha-1D adrenergic receptor and thioredoxin, were found to be up-regulated under dark condition compared with normal light and strong light conditions (Table 6), when *A. japonicus* is active. The alpha-1D adrenergic receptor mediates its effect through the influx of extracellular calcium, and may play an important role in the phospholipase C-activating G-protein coupled receptor signaling pathway. Wheel-running activity, exploratory rearing behavior in a novel cage environment, and hyperlocomotion are significantly reduced in mice with mutated copies of this gene. The alpha-1D adrenergic receptor signaling gene is required for stimulus-induced locomotor activity (Sadalge et al., 2003). This may be why it is up-reg-

ulated under a fully dark environment, when *A. japonicus* shows active locomotion. Thioredoxins (TRxs), known to be present in all living organisms, are a family of small evolutionarily conserved proteins. They are critical for the maintenance of cellular homeostasis. They act roles in many important biological processes, including positive regulation of protein kinase B signaling, participating in various redox reactions. In the present study, the up-regulation of TRx under dark environment might be because of its participation of some signaling pathway. And further investigation should be conducted to unveil the regulation mechanism.

Lipopolysaccharide-responsive and beige-like anchor was down-regulated under dark condition compared with strong light and normal light conditions (Table 6). This protein may be involved in coupling signal transduction and vesicle trafficking to enable polarized secretion and/or membrane deposition of immune effector molecules. Compared to dark, the up-regulation lipopolysaccharide-responsive and beige-like anchor protein-like, partial in light group might be an indication that the signal transduction associated with immune system was involved in *A. japonicus* under strong light.

4.4 *Genes associated with photoreceptors*

It is very important for animals to detect light and interact with the environment (Ullrich-Lüter et al., 2011). Optimization in all aspects of an organism's performance according to the daily light–dark cycle is essential for normal physical function (Highland et al., 2014). Photoreceptors can convert light into signals, following which several biological processes may be stimulated. CREB-regulated transcription coactivator 1 (CRTC1) is a transcriptional coactivator for CREB1, which is involved in synchronization of circadian rhythmicity. CRTC1 and salt inducible kinase 1 (SIK1) participate in the CRTC1–SIK1 pathway, which regulates the light-induced entrainment of the circadian clock (Jagannath et al., 2013). In response to a light stimulus, CREB-mediated transcription plays an important role in the photic entrainment of the circadian clock (Sakamoto et al., 2013). Compared to fully dark group, CRTC1 was found to be up-regulated significantly in the body wall of *A. japonicus* under normal and strong light conditions (Table 6). This finding indirectly proves CRTC1 is important in light-induced regulations in *A. japonicus*, and partly reveals the circadian clock of *A. japonicus* might be regulated under conditions of different light intensity (Lin et al., 2013). In addition, CRTC1 may be an important gene for future study of the mechanism underlying the behavioral rhythms of sea cucumbers.

Some species of echinoderm have photosensory organs related to light illumination. Photoreceptor cells have been found in the tube feet of the purple sea urchin, *Trongylocentrotus purpuratus*. The two genes *Sp-opsin4* and *Sp-pax6* are essential for photoreceptor function and development, respectively. Specific reactivity of the Sp-opsin4 antibody with sea star optic cushions, which regulate phototaxis, suggests a similar visual function in sea urchins (Ullrich-Lüter et al., 2011). Opsin protein gene expression has also been found in the brittle star *Amphiura filiformis* and the sea star *Asterias rubens* (Delroisse et al., 2013, 2014). However, in this study, opsin protein genes were not detected, perhaps because of the limitation of the reference genomes currently available.

A large proportion of DEGs were not annotated in this study, and they may include the light-associated genes that encode the photoreceptors, which may play key roles in adaption to different environments. The sea cucumber *A. japonicus*, which has slightly different morphological characteristics from other echinoderms, has undeveloped bones with tiny scattered ossicles inside body wall. Future behavioral and histological studies, and the use of molecular biology methods, are needed to determine whether *A. japonicus* has similar photoreceptors.

5 Conclusions

Large scale gene expression profiling of body wall of *A. japonicus*, comparing animals exposed to natural light ("control"), strong light ("light") and full darkness ("dark") identified a series of candidate genes and GO terms that indicate that proteins involved in these processes are important to regulating the biological responses to different light conditions in echinoderms. Light-specific DEGs identified in this study will be important targets for further investigation to establish the biochemical mechanisms involved in the adaption of *A. japonicus* to changes in the level of environmental light.

Acknowledgements

The authors thank Beijing Genomics Institute (Shenzhen, China) for high throughput sequencing of the mRNA library.

References

Abdi H. 2007. The bonferonni and Šidák corrections for multiple comparisons. In: Salkind N, ed. Encyclopedia of Measurement and Statistics. Thousand Oaks, CA: Sage Publications, 3: 103–107

Aizenberg J, Tkachenko A, Weiner S, et al. 2001. Calcitic microlenses as part of the photoreceptor system in brittlestars. Nature, 412(6849): 819–822

Audic S, Claverie J M. 1997. The significance of digital gene expression profiles. Genome Research, 7(10): 986–995

Bao Jie, Jiang Hongbo, Tian Xiangli, et al. 2014. Growth and energy budgets of green and red type sea cucumbers *Apostichopus japonicus* (Selenka) under different light colors. Aquaculture, 418–419: 139–143

Chen Yong, Gao Feng, Liu Guoshan, et al. 2007. The effects of temperature, salinity and light cycle on the growth and behavior of *Apostichopus japonicus*. Journal of Fisheries of China (in Chinese), 31(5): 687–691

Chen Muyan, Storey K B. 2014. Large-scale identification and comparative analysis of miRNA expression profile in the respiratory tree of the sea cucumber *Apostichopus japonicus* during aestivation. Mar Genomics, 13: 39–44

Delroisse J, Lanterbecq D, Eeckhaut I, et al. 2013. Opsin detection in the sea urchin *Paracentrotus lividus* and the sea star *Asterias rubens*. Cah Biol Mar, 54(4): 721–727

Delroisse J, Ullrich-Lüter E, Ortega-Martinez O, et al. 2014. High opsin diversity in a non-visual infaunal brittle star. BMC Genomics, 15: 1035

Dong Yunwei, Dong Shuanglin, Meng Xianliang. 2008. Effects of thermal and osmotic stress on growth, osmoregulation and Hsp70 in sea cucumber (*Apostichopus japonicus* Selenka). Aquaculture, 276(1–4): 179–186

Dong Guancang, Dong Shuanglin, Tian Xiangli, et al. 2011. Effects of photoperiod on daily activity rhythm of juvenile sea cucumber, *Apostichopus japonicus* (Selenka). Chinese Journal of Oceanology and Limnology, 29(5): 1015–1022

Dong Guancang, Dong Shuanglin, Wang Fang, et al. 2010a. Effects of light intensity on daily activity rhythm of juvenile sea cucumber, *Apostichopus japonicus* (Selenka). Aquac Res, 41(11): 1640–1647

Dong Guancang, Dong Shuanglin, Wang Fang, et al. 2010b. Effects of materials, incubation time and colors of artificial shelters on behavior of juvenile sea cucumber *Apostichopus japonicus*. Aquacultural Engineering, 43(1): 1–5

Dong Ying, Sun Hongjuan, Zhou Zunchun, et al. 2014. Expression analysis of immune related genes identified from the coelomo-

cytes of sea cucumber (*Apostichopus japonicus*) in response to LPS challenge. International Journal of Molecular Sciences, 15(11): 19472–19486

Du Huixia, Bao Zhenmin, Hou Rui, et al. 2012. Transcriptome sequencing and characterization for the sea cucumber *Apostichopus japonicus* (Selenka, 1867). PLoS One, 7(3): e33311

Fisheries Bureau of Ministry of Agriculture. 2016. 2016 China Fishery Statistical Yearbook (in Chinese). Beijing: China Agriculture Press, 184

Haghnia M, Cavalli V, Shah S B, et al. 2007. Dynactin is required for coordinated bidirectional motility, but not for dynein membrane attachment. Molecular Biology of the Cell, 18(6): 2081–2089

Highland J A, Weiser M J, Hinds L R, et al. 2014. CRTC2 activation in the suprachiasmatic nucleus, but not paraventricular nucleus, varies in a diurnal fashion and increases with nighttime light exposure. American Journal of Physiology-Cell Physiology, 307(7): C611–C621

Honda S, Kashiwagi M, Miyamoto K, et al. 2000. Multiplicity, structures, and endocrine and exocrine natures of eel fucose-binding lectins. Journal of Biological Chemistry, 275(42): 33151–33157

Jagannath A, Butler R, Godinho S I H, et al. 2013. The CRTC1-SIK1 pathway regulates entrainment of the circadian clock. Cell, 154(5): 1100–1111

Kerrick W G L, Bolles L L. 1982. Evidence that myosin light chain phosphorylation regulates contraction in the body wall muscles of the sea cucumber. Journal of Cellular Physiology, 112(3): 307–315

Kim Y K, Jang S K. 2002. Continuous heat shock enhances translational initiation directed by internal ribosomal entry site. Biochemical and Biophysical Research Communications, 297(2): 224–231

Lambert C C, Brandt C L. 1967. The effect of light on the spawning of Ciona intestinalis. The Biological Bulletin, 132(2): 222–228

Liao Yulin. 1980. The aspidochirote holothurians of China with erection of a new genus. In: Proceedings of the European Colloquium on Echinoderms. Rotterdam, the Netherlands: A A Balkema Publishers, 115–120

Lin Chenggang, Zhang Libin, Liu Shilin, et al. 2013. A comparison of the effects of light intensity on movement and growth of albino and normal sea cucumbers (*Apostichopus japonicus* Selenka). Mar Freshw Behav Physiol, 46(6): 351–366

Mallik R, Gross S P. 2004. Molecular motors: strategies to get along. Current Biology, 14(22): R971–R982

Mehl J W. 1940. Studies on the proteins of smooth muscle: II. The myosins of the octopus, snail, sea cucumber and sea anemone. The Biological Bulletin, 79(3): 488–497

Mortazavi A, Williams B A, McCue K, et al. 2008. Mapping and quantifying mammalian transcriptomes by RNA-Seq. Nature Methods, 5(7): 621–628

Naylor E. 1999. Marine animal behaviour in relation to lunar phase. Earth, Moon, and Planets, 85–86: 291–302

Ortiz-Pineda P A, Ramírez-Gómez F, Pérez-Ortiz J, et al. 2009. Gene expression profiling of intestinal regeneration in the sea cucumber. BMC Genomics, 10: 262

Pan Yang, Zhang Libin, Lin Chenggang, et al. 2015. Influence of flow velocity on motor behavior of sea cucumber *Apostichopus japonicus*. Physiol Behav, 144: 52–59

Raible F, Tessmar-Raible K, Arboleda E, et al. 2006. Opsins and clusters of sensory G-protein-coupled receptors in the sea urchin genome. Dev Biol, 300(1): 461–475

Reitzel A M, Behrendt L, Tarrant A M. 2010. Light entrained rhythmic gene expression in the sea anemone Nematostella vectensis: the evolution of the animal circadian clock. PLoS One, 5(9): e12805

Ringelberg J. 1995. Changes in light intensity and diel vertical migration: a comparison of marine and freshwater environments. Journal of the Marine Biological Association of the United Kingdom, 75(1): 15–25

Sadalge A, Coughlin L, Fu H, et al. 2003. α1d Adrenoceptor signaling is required for stimulus induced locomotor activity. Molecular Psychiatry, 8(7): 664–672

Sakamoto K, Norona F E, Alzate-Correa D, et al. 2013. Clock and light regulation of the CREB coactivator CRTC1 in the suprachiasmatic circadian clock. Journal of Neuroscience, 33(21): 9021–9027

Santiago P, Roig-López J L, Santiago C, et al. 2000. Serum amyloid A protein in an echinoderm: its primary structure and expression during intestinal regeneration in the sea cucumber *Holothuria glaberrima*. Journal of Experimental Zoology, 288(4): 335–344

Shao Yina, Li Chenghua, Chen Xiaocong, et al. 2015. Metabolomic responses of sea cucumber *Apostichopus japonicus* to thermal stresses. Aquaculture, 435: 390–397

Shao Yina, Li Chenghua, Ou Changrong, et al. 2013. Divergent metabolic responses of *Apostichopus japonicus* suffered from skin ulceration syndrome and pathogen challenge. Journal of Agricultural and Food Chemistry, 61(45): 10766–10771

Sloan N A. 1984. Echinoderm fisheries of the world: a review. Echinodermata. In: Proceedings of the 5th International Echinoderm Conference. Rotterdam, Netherlands: AA Balkema Publishers, 109–124

Sui Jiajia, Dong Shuanglin, Tian Xiangli, et al. 2010. The effect of light color on respiration and excretion of sea cucumber, *Apostichopus japonicus*. Periodical of Ocean University of China (in Chinese), 40(3): 61–64

Sun Lina, Chen Muyan, Yang Hongsheng, et al. 2011. Large scale gene expression profiling during intestine and body wall regeneration in the sea cucumber *Apostichopus japonicus*. Comparative Biochemistry and Physiology Part D: Genomics and Proteomics, 6(2): 195–205

Sun Lina, Yang Hongsheng, Chen Muyan, et al. 2013. RNA-Seq reveals dynamic changes of gene expression in key stages of intestine regeneration in the sea cucumber *Apostichopus japonicas*. PLoS One, 8(8): e69441

Sun Jiamin, Zhang Libin, Pan Yang, et al. 2015. Feeding behavior and digestive physiology in sea cucumber *Apostichopus japonicus*. Physiol Behav, 139: 336–343

Thorson G. 1964. Light as an ecological factor in the dispersal and settlement of larvae of marine bottom invertebrates. Ophelia, 1(1): 167–208

Ullrich-Lüter E M, Dupont S, Arboleda E, et al. 2011. Unique system of photoreceptors in sea urchin tube feet. Proceedings of the National Academy of Sciences of the United States of America, 108(20): 8367–8372

Volpato G L, Bovi T S, de Freitas R H A, et al. 2013. Red light stimulates feeding motivation in fish but does not improve growth. PLoS One, 8(3): e59134

Wang Xingqiang, Wang Lingling, Zhang Huan, et al. 2012. Immune response and energy metabolism of *Chlamys farreri* under Vibrio anguillarum challenge and high temperature exposure. Fish & Shellfish Immunology, 33(4): 1016–1026

Warner J R, McIntosh K B. 2009. How common are extraribosomal functions of ribosomal proteins?. Molecular Cell, 34(1): 3–11

West A B, Lambert C C. 1976. Control of spawning in the tunicate *Styela plicata* by variations in a natural light regime. Journal of Experimental Zoology, 195(2): 263–270

Wu A M, Wu J H, Singh T, et al. 2004. Lectinochemical studies on the affinity of *Anguilla anguilla* agglutinin for mammalian glycotopes. Life Sciences, 75(9): 1085–1103

Xu Xun, Doolittle R F. 1990. Presence of a vertebrate fibrinogen-like sequence in an echinoderm. Proceedings of the National Academy of Sciences of the United States of America, 87(6): 2097–2101

Xue Suyan, Fang Jianguang, Mao Yuze, et al. 2007. The influence of different light intensity on growth of juvenile sea cucumber *Apostichopus japonicus*. Marine Fisheries Research (in Chinese), 28(6): 13–18

Yang Aifu, Zhou Zunchun, Dong Ying, et al. 2010. Expression of immune-related genes in embryos and larvae of sea cucumber *Apostichopus japonicus*. Fish & Shellfish Immunology, 29(5): 839–845

Zhang Shuo, Chen Yong, Sun Manchang. 2006. Behavior characteristics of *Apostichopus japonicus* and attractive effects of artificial reef models under different light intensities. Journal of Fishery Sciences of China (in Chinese), 13(1): 20–27

Zhang Pengjuan, Li Chenghua, Zhang Peng, et al. 2014. iTRAQ-based proteomics reveals novel members involved in pathogen challenge in sea cucumber *Apostichopus japonicus*. PLoS One, 9(6): e100492

Zhang Pengjuan, Li Chenghua, Zhu Lin, et al. 2013. De novo assembly of the sea cucumber *Apostichopus japonicus* hemocytes transcriptome to identify miRNA targets associated with skin ulceration syndrome. PLoS One, 8(9): e73506

Zhang Libin, Pan Yang, Song Hao. 2015a. Environmental drivers of behavior. In: Yang Hongsheng, Hamel J F, Mercler A, eds. The Sea Cucumber *Apostichopus japonicus*: History, Biology and Aquaculture. Boston, USA: Academic Press, 133–152

Zhang Libin, Song Xiaoyue, Hamel J F, et al. 2015b. Aquaculture, stock enhancement, and restocking. In: Yang Hongsheng, Hamel J F, Mercler A, eds. The Sea Cucumber *Apostichopus japonicus*: History, Biology and Aquaculture. Boston, USA: Academic Press, 289–322

Zhang Hui, Wang Yingeng, Rong Xiaojun, et al. 2009. Behavioral responses of sea cucumber (*Apostichopus japonicus*) to different light intensity and settlement substratum color. Chinese Journal of Ecology (in Chinese), 28(3): 477–482

Zhao Ye, Yang Hongsheng, Storey K B, et al. 2014a. Differential gene expression in the respiratory tree of the sea cucumber *Apostichopus japonicus* during aestivation. Mar Genomics, 18: 173–183

Zhao Ye, Yang Hongsheng, Storey K B, et al. 2014b. RNA-seq dependent transcriptional analysis unveils gene expression profile in the intestine of sea cucumber *Apostichopus japonicus* during aestivation. Comparative Biochemistry and Physiology Part D: Genomics and Proteomics, 10: 30–43

Zhou Z C, Dong Y, Sun H J, et al. 2014. Transcriptome sequencing of sea cucumber (*Apostichopus japonicus*) and the identification of gene-associated markers. Molecular Ecology Resources, 14(1): 127–138

Zhou Xianqing, Niu Cuijuan, Li Qingfen. 2000. Effects of light on feeding behavior, growth and survival of aquatic animals. Acta Hydrobiologica Sinica (in Chinese), 24(2): 178–181

Supplementary information:

Table S1. The top 20 up- or down-regulated DEGs from "dark" vs. "control".

Table. S2. The top 20 up- or down-regulated DEGs from "light" vs. "control".

Table. S3. The top 20 up- or down-regulated DEGs from "light" vs. "dark".

Fig. S1. Quality assessment of reads (light representing strong light, dark fully dark, and control normal light).

Fig. S2. Sequencing saturation analysis (light representing strong light, dark fully dark, and control normal light).

Fig. S3. Randomness assessment (light representing strong light, dark fully dark, and control normal light).

The supplementary information is available online at www.hyxb.org.cn/aosen/ch/index.aspx. The supplementary information is published as submitted, without typesetting or editing. The responsibility for scientific accuracy and content remains entirely with the authors.

Acta Oceanol. Sin., 2018, Vol. 37, No. 5, P. 67–76
DOI: 10.1007/s13131-018-1212-6
http://www.hyxb.org.cn
E-mail: hyxbe@263.net

Impacts of changing scale on Getis-Ord Gi* hotspots of CPUE: a case study of the neon flying squid (*Ommastrephes bartramii*) in the northwest Pacific Ocean

FENG Yongjiu[1, 2, 3, 4], CHEN Xinjun[1, 3, 4*], GAO Feng[1, 3, 4], LIU Yang[1]

[1] College of Marine Sciences, Shanghai Ocean University, Shanghai 201306, China

[2] Laboratory for Marine Fisheries Science and Food Production Processes, Qingdno National Laboratory for Marine Science and Technology, Qingdao 266235, China

[3] National Distant-water Fisheries Engineering Research Center, Shanghai Ocean University, Shanghai 201306, China

[4] Key Laboratory of Sustainable Exploitation of Oceanic Fisheries Resources (Shanghai Ocean University), Ministry of Education, Shanghai 201306, China

Received 6 December 2016; accepted 5 February 2017

Abstract

We examined the scale impacts on spatial hot and cold spots of CPUE for *Ommastrephes bartramii* in the northwest Pacific Ocean. The original fishery data were tessellated to 18 spatial scales from 5′×5′ to 90′×90′ with a scale interval of 5′ to identify the local clusters. The changes in location, boundaries, and statistics regarding the Getis-Ord Gi* hot and cold spots in response to the spatial scales were analyzed in detail. Several statistics including Min, mean, Max, SD, CV, skewness, kurtosis, first quartile (Q1), median, third quartile (Q3), area and centroid were calculated for spatial hot and cold spots. Scaling impacts were examined for the selected statistics using linear, logarithmic, exponential, power law and polynomial functions. Clear scaling relations were identified for Max, SD and kurtosis for both hot and cold spots. For the remaining statistics, either a difference of scale impacts was found between the two clusters, or no clear scaling relation was identified. Spatial scales coarser than 30′ are not recommended to identify the local spatial patterns of fisheries because the boundary and locations of hot and cold spots at a coarser scale are significantly different from those at the original scale.

Key words: *Ommastrephes bartramii*, scale impacts, local clusters, Getis-Ord Gi*, spatial hotspots

Citation: Feng Yongjiu, Chen Xinjun, Gao Feng, Liu Yang. 2018. Impacts of changing scale on Getis-Ord Gi* hotspots of CPUE: a case study of the neon flying squid (*Ommastrephes bartramii*) in the northwest Pacific Ocean. Acta Oceanologica Sinica, 37(5): 67–76, doi: 10.1007/s13131-018-1212-6

1 Introduction

Spatial patterns of marine and estuarial fisheries are important geographic observations that can benefit sustainable exploration (Feng et al., 2017a; Huang et al., 2014; Jiang et al., 2016) and provide managers with the best information for responsible and responsive management (Cope and Punt, 2011). These patterns are usually in the form of a spatiotemporal distribution and its relationships with oceanic environments (Chen et al., 2014; Jennings et al., 2009; Swartz et al., 2010; Yu et al., 2015). They are commonly analyzed using integrated geographic information systems (GIS), spatial analysis, geostatistics and remote sensing (Carocci et al., 2009; Meaden and Aguilar-Manjarrez, 2013). The spatiotemporal distribution of fisheries resources has been investigated extensively for offshore and pelagic species such as *Ommastrephes bartramii*, *Dosidicus gigas*, *Lophelia pertusa*, *Chaceon notialis*, and *Thunnus albacares* (Chen and Chiu, 2003; Chen et al., 2008; Feng et al., 2017b; Fosså et al., 2002; Gilly et al., 2006; Gutiérrez et al., 2011; Nishida and Chen, 2004; Paulino et al., 2016; Yu et al., 2016a). These studies have made a substantial contribution towards understanding spatial distribution and aggregation of fisheries and resolution of spatial problems of fisheries and aquaculture worldwide.

Spatial patterns in fisheries are commonly analyzed on a specified grid where the original data have been tessellated to a regularly-defined spatial scale. In some case studies, original and un-tessellated fishery data at a very coarse scale were used to analyze the spatial patterns of pelagic species (Feng et al., 2017c; Su et al., 2008). Feng et al. (2017a) identified the spatial variability of *O. bartramii* in the northwest Pacific Ocean at original scales, while Su et al. (2008) examined the relationship between spatiotemporal patterns of blue marlin (*Makaira nigricans*) in the Pacific Ocean on a 5°×5° coarse scale. A spatial scale of 30′×30′ is the most widely used fishing grid for investigating the distribution of commercial fisheries such as *O. bartramii* and *D. gigas* (Chen et al., 2008; Yu et al., 2016b). For example, Chen et al. (2008) conducted a stock assessment at a 30′×30′ scale to spatially estimate stock size and proportional escapement of *O. bartramii* in the northwest Pacific Ocean. On the same scale, Xu et al. (2016) examined the effect of sea surface temperature increase on the potential habitat of *O. bartramii* in the Northwest

Foundation item: The National Natural Science Foundation of China under contract No. 41406146; the Open Fund from Laboratory for Marine Fisheries Science and Food Production Processes at Qingdao National Laboratory for Marine Science and Technology of China under contract No. 2017-1A02; Shanghai Universities First-class Disciplines Project-Fisheries (A).
*Corresponding author, E-mail: xjchen@shou.edu.cn

Pacific Ocean; Yu et al. (2016b) evaluated the effects of climate variability on habitat suitability of *D. gigas* over the 2006–2012 period in the sea waters offshore Peru. Finer scales have commonly been used to examine spatial patterns of fisheries in coastal waters. Saul et al. (2013) explored the spatial distribution of reef fish and estimated their spatial autocorrelation at a spatial scale of 10′×10′ on the West Florida Shelf. Using the same spatial resolution of 10′×10′, Gao et al. (2016) built a boosted regression trees-based model to forecast fishing ground of *Scomber japonicus* in the Yellow Sea and East China Sea. At a much finer 1 km×1 km spatial scale, Harford et al. (2015) simulated scenarios representing spiny lobster distribution at Glover's Reef Marine Reserve, Belize.

Spatial patterns at one scale may not be valid at a different scale (Wu, 2004) and mismatch of model spatial scale and biological stock structure may compromise management goals (Cope and Punt, 2011), because the patterns and structures differ from scale to scale (Feng and Liu, 2015). This phenomenon has been recognized as "scale impact" or "scale effect" (Turner et al., 1989; Wiens, 1989). Tian et al. (2010) noted the scale impact on catch-per-unit-effort (CPUE) standardization and conducted a case study using the commercial fishery data of *O. bartramii* and the corresponding oceanographic data in the northwest Pacific Ocean. They tessellated the fishery data into 0.5°, 1°, 2°, 3°, 4° and 5° scales and showed that spatial scale significantly affected the standardization of CPUE. Using a similar tessellation scheme, Gong et al. (2014) evaluated the effects of spatial scale on habitat suitability modeling for *O. bartramii* in the northwest Pacific Ocean. They noted that a scale such as 30′ is too large and may compromise the reliability of modelling and miss significant details of the scaling relations. Research has also showed that the changing spatial scales may substantially affect the observed spatial patterns for fisheries resources (Guinet et al., 2001; Yang et al., 2013).

We have conducted a quantitative evaluation of the scale effect on several spatial indices in analyzing the observed patterns of *O. bartramii* resources in the northwest Pacific Ocean (Feng et al., 2016). These spatial indices included global Moran's I index, Geary's C, Getis-Ord General G, the average nearest neighbor (ANN) and Ripley's K function. These indices were focused on the examination of global patterns in terms of clustering, dispersal and random distribution of fisheries. We proposed trend and extent indicators that quantify the scale impacts of the spatial indices. Based on spatial autocorrelation statistics Moran's I and Geary's C, we identified 25′×25′ as the optimum scale for August and October and 20′×20′ as the optimum scale for September in conducting spatial analyses of *O. bartramii* in the northwest Pacific Ocean. We also identified 50′×50′ as the coarsest allowable spatial scale for August and October and 50′×50′ as the coarsest allowable spatial scale for September. The optimum and coarsest allowable spatial scales changed by month since the scaling effects depend on monthly different commercial fishery data.

This paper extends early study of Feng et al. (2016) and examines the scale impact of on local spatial clusters using the same fishery dataset of *O. bartramii*. There are three major differences between the earlier study and the present paper, which are as follows: (1) the early study investigated the scale impacts of the *global* patterns while the present paper examines the scale impacts of the *local* patterns, (2) the global indices of spatial relationships were calculated in the earlier study while the summary statistics within the *local* clusters are computed in the present paper, and (3) the early study examined a vast of spatial indices while the present paper focuses on the spatial hotspots derived from Getis-Ord Gi*. Specifically, the hot and cold spots at various spatial scales were identified and changes in their locations, boundaries and statistics in relation to spatial scales were studied in more detail. In examining scale impacts, we selected a number of spatial and non-spatial indices including Min, mean, Max, SD, CV, skewness, kurtosis, first quartile (Q1), median, third quartile (Q3), area and centroid. Our study examines the relationships between hot/cold spots and spatial scale. Our results contribute to enhancing our understanding of the relationships between spatial scale and local spatial clusters of fisheries, and to the selection of an appropriate spatial scale for analysis of fisheries.

2 Materials and methods

2.1 *Commercial fishery data*

Commercial fishery data of *O. bartramii* in the northwest Pacific Ocean were collected by the Chinese Squid-jigging Technology Group (CSTG). The data include the dates of fishing, fishing locations (longitude and latitude), the number of fishing vessels operating per day, and daily catch of vessels. The commercial fishing data of *O. bartramii* were selected within the boundary of 38°–46°N and 150°–162°E. In this paper, we focused on Chinese Mainland fisheries of *O. bartramii* in August, September and October from 2004 to 2013 and examined their scale impacts on the hot and cold spots of this squid fishery.

Examination of the scale impacts on local clusters was conducted using CPUE data. The CPUE at each vessel location was calculated as the total catches divided by the number of fishing operations at the location:

$$CPUE_j = \frac{\sum_{i=1}^{10} C_{i,j,ss}}{\sum_{i=1}^{10} E_{i,j,ss}}, \tag{1}$$

where $C_{i,j,ss}$ is the catch (t) in month j year i within a fishing grid (spatial scale, SS), and $E_{i,j,ss}$ is the number of the corresponding fishing operations (efforts) in month j year i within the same fishing grid.

The spatial scale of the original data was assessed using the ANN method (Ebdon, 1985; Mitchell, 2005). The estimated spatial scales of the original datasets are 1.07′ for August, 0.94′ for September and 0.99′ for October (Feng et al., 2016). These original datasets were then tessellated to 18 spatial scales from 5′×5′ to 90′×90′, with a scale interval of 5′ between two adjacent spatial scales. We therefore used a total of 19 spatial scales for multi-scale analysis, including the original dataset. Figure 1 illustrates the original fishery data and the datasets that were tessellated at 30′×30′, 60′×60′ and 90′×90′ spatial scales.

2.2 *Hot and cold spots*

Global spatial autocorrelation methods such as Getis-Ord General G measure the overall clustering or dispersion pattern of fishing grounds (Feng et al., 2017a). In contrast, local spatial autocorrelation statistics (Getis and Ord, 1996; Ord and Getis, 1995; Peeters et al., 2015) are commonly used to investigate the specific spatial distribution and local clusters of fisheries (Feng et al., 2017a). Getis-Ord Gi* is one of the most widely used local spatial autocorrelation statistics, and is given by (Getis and Ord, 1996; Ord and Getis, 1995):

$$Gi^* = \frac{\sum_{j=1}^{n} w_{i,j}x_j - \bar{X}\sum_{j=1}^{n} w_{i,j}}{S \times \sqrt{\left(n\sum_{j=1}^{n} w_{i,j}^2 - \left(\sum_{j=1}^{n} w_{i,j}\right)^2\right)/(n-1)}}, \tag{2}$$

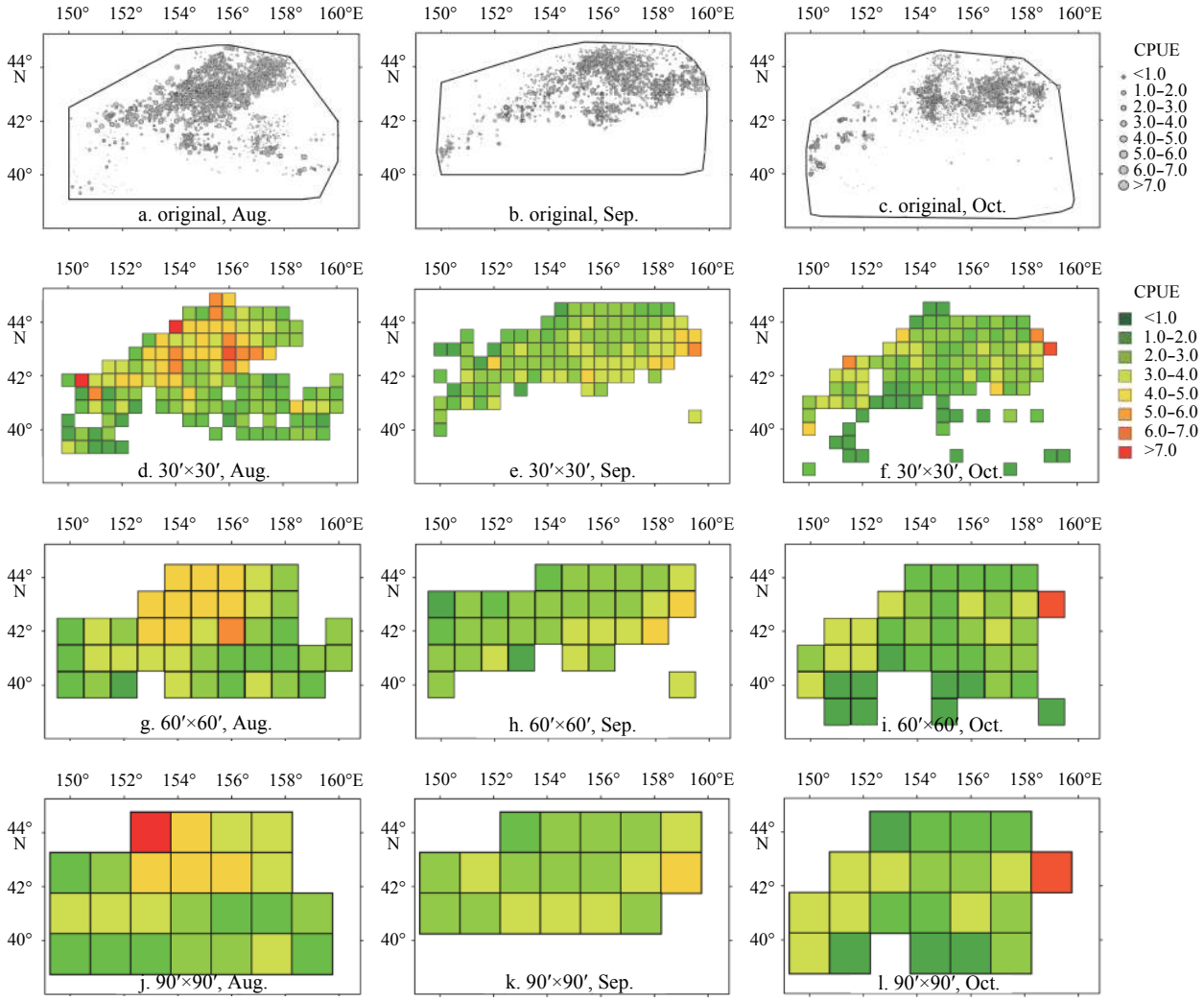

Fig. 1. Original fishery data and tessellated fishery data at 30′×30′, 60′×60′ and 90′×90′.

where S is the standard deviation of all data points, n is the number of data points, x_j is the CPUE of points j, $\bar{X}$ is the averaged value of all points, and $w_{i,j}$ is the spatial weights matrix indicating the spatial adjacency relations between the point (i) in processing and the neighboring point j. Generally, the spatial weight matrix $w_{i,j}$ is defined by using either an adjacency standard or a distance standard (Getis and Aldstadt, 2010).

In practice, Getis-Ord Gi* statistics return two values: (1) the z-score of each point, and (2) the consequent significance p-value. At 5% significance, a z-score greater than 2 indicates a hot spot while a z-score smaller than –2 indicates a cold spot. A hot spot signifies that the data points with high CPUE values are surrounded by similarly high CPUE points, whereas a cold spot signifies that points with low CPUE are surrounded by similarly low CPUE points. This indicates that both hot and cold spots are spatial clusters in the fishery. A z-score between –1 and 1 indicates that the underlying pattern probably results from random spatial processes (Feng et al., 2017a). In our study, the hot and cold spots of *O. bartramii* in the northwest Pacific Ocean were identified using Getis-Ord Gi* in ArcGIS 10.1.

2.3 *Measured indices*

Several spatial and non-spatial indices were selected to measure the spatial distribution of CPUE for *O. bartramii* and then to examine any scale impacts. We used indices such as summary statistics including Min, mean, Max, SD, CV, skewness, kurtosis, Q1, median, and Q3 as well as spatial measurements such as area and centroid. Spatial hot and cold spots in the fishery were identified by Getis-Ord Gi*, a widely used local spatial autocorrelation statistic (Getis and Aldstadt, 2010; Getis and Ord, 1996; Ord and Getis, 1995). Hot and cold spots on different spatial scales were identified and the changes in their locations, boundaries, and statistics resulting from the changes in spatial scales were studied in detail.

2.4 *Measuring the scale impacts*

The scale impacts of the indices were assessed by regression modelling using linear, power law, logarithmic, exponential, and polynomial functions (Table 1), drawing references from the literature in landscape ecology (Feng and Liu, 2015; Turner et al., 1989; Wu, 2004).

In Table 1, y is the spatial index and x is the spatial scale. For linear, logarithmic and exponential functions, positive a indicates a growing trend of an index while a negative a indicates a decaying trend as the spatial scale increases. The sign of a is a trend indicator. For power law functions, the fractal dimension d quantifies the scale extent according to earlier works (Feng and Liu, 2015), where d=–1–a (a>0) or d=1–a (a<0). Negative d (a>0) in-

Table 1. Potential scale impacts of indices in analyzing fisheries resources

Scaling relations	Equation	Meaning
Linear	$y=ax+b$	$a>0$ means that the index increases as spatial scale (fish grid) becomes coarser, i.e., a growing trend, whereas $a<0$ means that the index decreases as the spatial scale becomes coarser, i.e., a decaying trend.
Logarithmic	$y=a\ln x+b$	
Exponential	$y=a+be^{cx}$	
Power law	$y=bx^a$	
Polynomial	$y=a_nx^n+\ldots+a_1x+a_0$, $n\geqslant 2$	$n=2$ indicates a parabolic curve, while $n>2$ indicates a more complex relationship between a spatial index and the corresponding spatial scales.

dicates that the spatial index increases as the spatial scale becomes coarser (i.e., a larger grid size), whereas a positive d ($a<0$) indicates that the spatial index decreases as the spatial scale becomes coarser. The dimension $|d|$ approaching 1 means that the spatial index is not sensitive to the change of the spatial scale, whereas large $|d|$ (e.g., $|d|\geqslant 1.3$) means that the spatial index is sensitive to the change of the spatial scale (Feng and Liu, 2015; Wu, 2004).

3 Results

3.1 *The distribution of O. bartramii CPUE at 30′*

Each fishery data in this study corresponds to 19 spatial scales, leading to a total of 57 datasets for all three months. We therefore analyzed the distribution of CPUE under a widely applied spatial scale of 30′ (Fig. 2). There are 136, 101 and 107 fishing points and their mean values are 2.89, 2.69 and 2.12 for August, September and October, successively. The standard deviation ranges from 1.05 to 1.59, suggesting relatively aggregation distribution of the CPUE data. Figure 2 shows that the CPUE yield leptokurtic distribution for all three months, indicating low variations of *O. bartramii* CPUE across space. These CPUE datasets are therefore suitable for identifying the spatial hot and cold spots using local Getis-Ord Gi* statistic.

3.2 *Scale impacts on summary statistics of entire dataset*

The summary statistics for CPUE in the study area did not exhibit any clear scaling relations except Max and CV, as illustrated by scaling equations, the associated goodness-of-fit R^2s (Table 2) and the scaling curves (Fig. 3). This means that most of the summary statistics varied with a change in spatial scale. Both Max and CV showed exponential scaling relations with decaying trends for August and September, which may be due to the fact that the calculated CPUE is the averaged value of all data points within a fishing grid. The two statistics yielded double-quadratic polynomials that open upward for October. The 55′ scale defines the break point in the two quadratic polynomials for both Max and CV, and the early stages of Max and CV show decaying trends

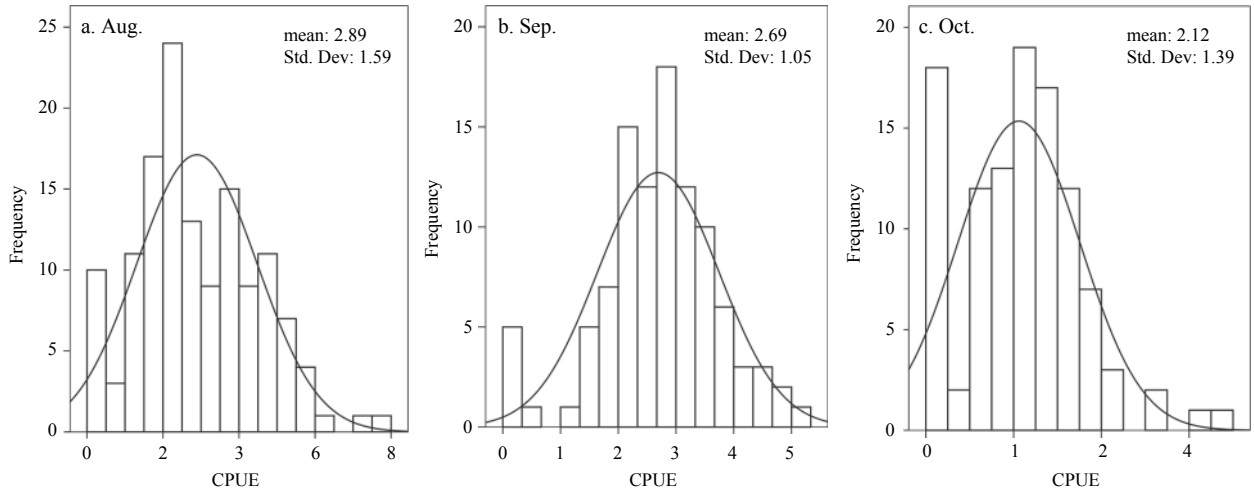

Fig. 2. The distributions of CPUE at 30′×30′ for *O. bartramii* CPUE in the northwest Pacific Ocean.

Table 2. Scaling equations and goodness-of-fit R^2s of entire fishery data of each month for *O. bartramii* in the northwest Pacific Ocean

Index	Month	Equation	R^2	Relation	Character
Max	Aug.	$y=6.120\,5+8.752\,4\exp(-0.061\,1x)$	0.861 6	exponential	decay
	Sep.	$y=5.166\,5+8.452\,7\exp(-0.062\,9x)$	0.775 4	exponential	decay
	Oct.	$y=10.582\,3-0.283\,4x+0.004\,3x^2$	0.824 3	quadratic polynomial	upward
		$y=76.356\,2-1.950\,1x+0.013\,1x^2$	0.901 7	quadratic polynomial	upward
CV	Aug.	$y=0.306\,9+0.290\,9\exp(-0.017\,7x)$	0.851 3	exponential	decay
	Sep.	$y=0.414\,5+0.125\,3\exp(-0.976\,7x)$	0.707 7	exponential	decay
	Oct.	$y=0.665\,3-0.007\,2x+0.000\,2x^2$	0.766 4	quadratic polynomial	upward
		$y=3.642\,7-0.080\,3x+0.000\,5x^2$	0.886 0	quadratic polynomial	upward

Note: y represents the summary statistics and x the spatial scale measured in minutes (hereinafter the same).

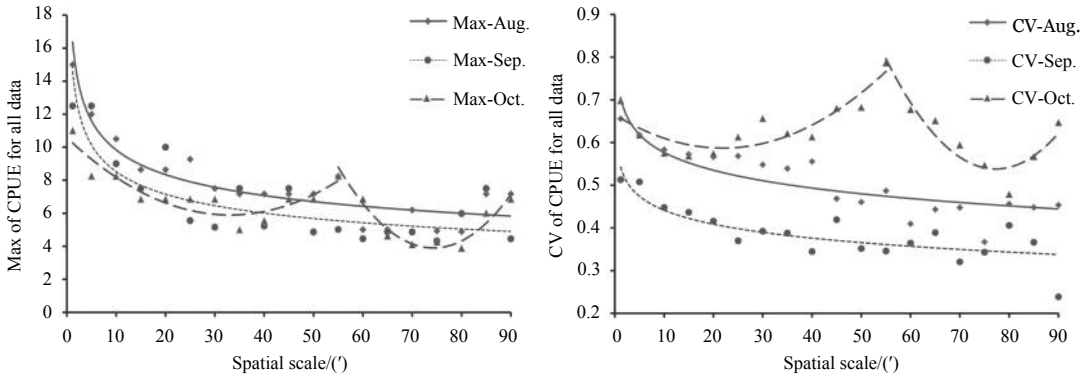

Fig. 3. Scaling relations of Max and CV of CPUE for *O. bartramii* in the northwest Pacific Ocean.

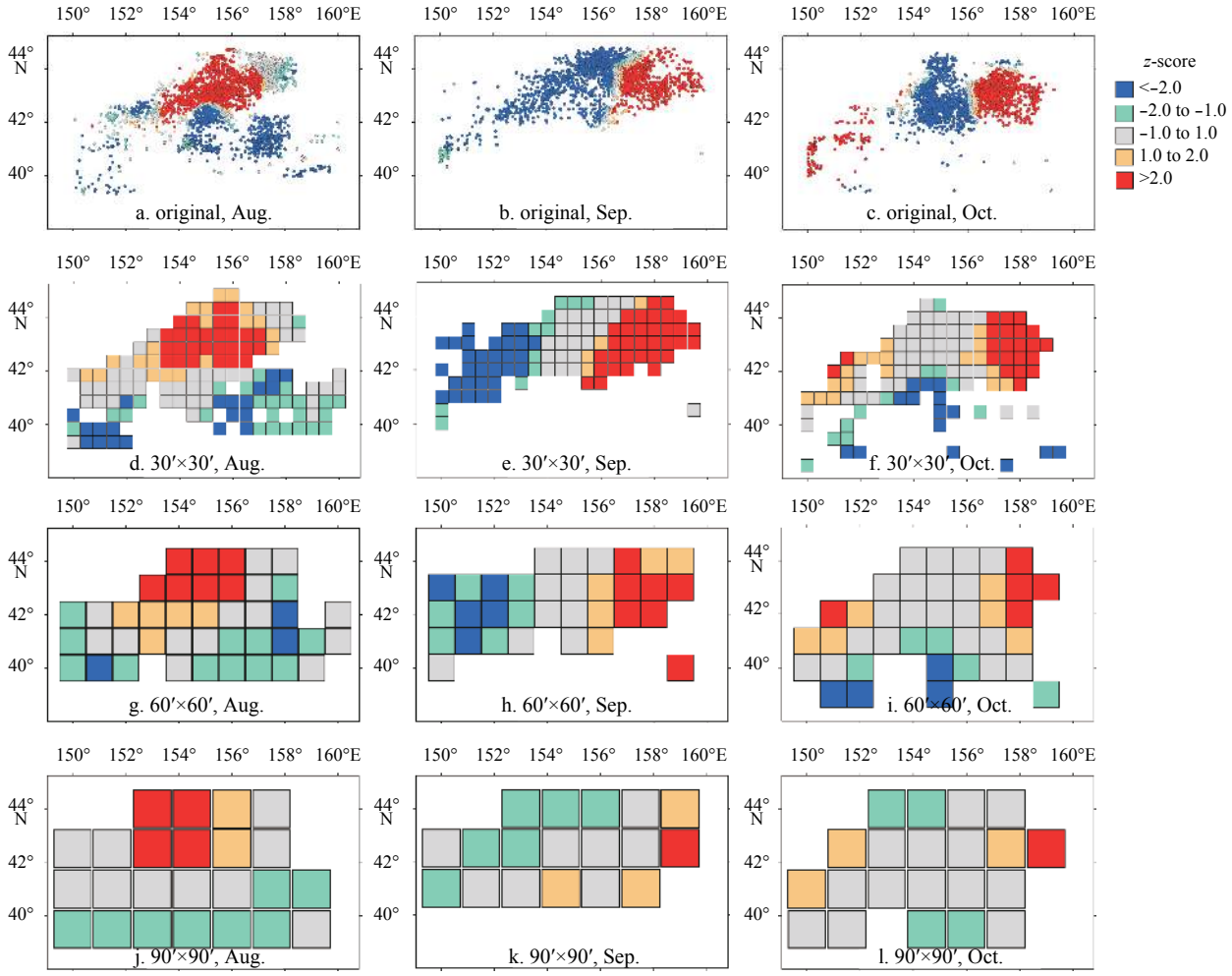

Fig. 4. The spatial hotspots of *O. bartramii* in the northwest Pacific Ocean at original, 30′×30′, 60′×60′ and 90′×90′ scales.

with changing scales. The CV for August and September showed a consistent lowering variation for *O. bartramii* CPUE as the spatial scale became coarser, while the CV for October is more complex.

3.3 *Scale impacts on summary statistics for hot/cold spots*

Spatial hot and cold spots were identified for all three months, as illustrated by the local clusters at four spatial scales including original, 30′×30′, 60′×60′, and 90′×90′ (Fig. 4). One hot and two cold spots were identified for August at the original scale, one hot and one cold spots were identified for September, and two hot and one cold spots were identified for October. The tessellations at 30′×30′ and 60′×60′ scales showed the same results, but the shapes differ between spatial scales. No cold spot was identified for any fishery data at coarse spatial scales from 80′ to 90′. The locations of both hot and cold spots moved slightly with changing scales. Points with *z*-score ranging from –1 to 1 (indicating spatial random patterns of CPUE) increased significantly as the spatial scale became coarser. In other words, the spatial patterns of CPUE were homogenized as spatial scale became coarser.

Table 3. Scaling equations and goodness-of-fit R^2s of spatial hot and cold spots for *O. bartramii* in the northwest Pacific Ocean

Cluster	Index	Month	Equation	R^2	Relation	Character
Hot spot	Max	Aug.	y=13.378–0.240 1x+0.001 9x^2	0.853 0	quadratic polynomial	upward
		Sep.	y=12.373–0.268 5x+0.002 4x^2	0.763 6	quadratic polynomial	upward
		Oct.	y=10.418–0.246x+0.003x^2	0.830 7	quadratic polynomial	upward
	SD	Aug.	y=2.234 1–0.053 8x+0.000 5x^2	0.775 8	quadratic polynomial	upward
		Sep.	y=1.516 8–0.025 1x+0.000 2x^2	0.667 0	quadratic polynomial	upward
		Oct.	y=1.601–0.415x+0.000 8x^2	0.758 1	quadratic polynomial	upward
	CV	Aug.	y=0.512–0.012 8x+0.000 1x^2	0.845 7	quadratic polynomial	upward
		Sep.	y=0.489 7–0.009 4x+8×10$^{-5}x^2$	0.801 0	quadratic polynomial	upward
		Oct.	y=0.582 4–0.018 3x+0.000 3x^2	0.919 8	quadratic polynomial	upward
	kurtosis	Aug.	y=4.170 1–0.025 4x	0.612 9	linear	decay
		Sep.	y=6.648 6exp(–0.02x)	0.783 4	exponential	decay
		Oct.	y=5.830 4exp(–0.015x)	0.718 9	exponential	decay
	Q1	Aug.	y=2.403$x^{0.143\,9}$	0.914 0	power law	growth
		Sep.	y=1.651 6$x^{0.188\,6}$	0.860 7	power law	growth
		Oct.	y=1.564 2$x^{0.161\,5}$	0.860 7	power law	growth
	median	Aug.	y=1.651 6$x^{0.188\,6}$	0.754 1	power law	growth
		Sep.	y=1.564 2$x^{0.161\,5}$	0.800 1	power law	growth
		Oct.	y=2.739 8+0.015 1x	0.755 5	linear	growth
Cold spot	mean	Aug.	y=2.725 6–0.029 8x+0.000 2x^2	0.882 9	quadratic polynomial	upward
		Sep.	y=2.717 8–0.028 6x+0.000 2x^2	0.798 1	quadratic polynomial	upward
		Oct.	y=2.223 8–0.074 5x+0.000 7x^2	0.974 4	quadratic polynomial	upward
	Max	Aug.	y=1.690 6+11.555 4exp(–0.068 7x)	0.964 5	exponential	decay
		Sep.	y=2.600 9+11.005 3exp(–0.065 3x)	0.953 7	exponential	decay
		Oct.	y=0.642 8+9.381 5exp(–0.067 9x)	0.985 8	exponential	decay
	SD	Aug.	–	–	–	–
		Sep.	y=1.6–0.020 8x+0.000 1x^2	0.749 9	quadratic polynomial	upward
		Oct.	y=1.537–0.040 6x+0.000 4x^2	0.977 6	quadratic polynomial	upward
	skewness	Aug.	y=1.729 9–0.047 2x+0.000 4x^2	0.728 7	quadratic polynomial	upward
		Sep.	y=1.130 5–0.040 8x+0.000 7x^2	0.811 4	quadratic polynomial	upward
		Oct.	y=1.285 4–0.069 4x+0.000 6x^2	0.888 2	quadratic polynomial	upward
	kurtosis	Aug.	y=8.272 6–0.252 7x+0.002 2x^2	0.820 7	quadratic polynomial	upward
		Sep.	y=7.088 4–0.213 5x+0.002 0x^2	0.879 2	quadratic polynomial	upward
		Oct.	y=4.490 3–0.115 3x+0.001 1x^2	0.780 1	quadratic polynomial	upward
	Q3	Aug.	y=2.938 9–0.055 6x+0.000 6x^2	0.766 9	quadratic polynomial	upward
		Sep.	y=3.365 1–0.02x+0.000 1x^2	0.747 6	quadratic polynomial	upward
		Oct.	y=3.098 4–0.087 8x+0.000 8x^2	0.980 4	quadratic polynomial	upward

The results show that the scaling relationships of hot spots differ from those of cold spots (Table 3, Figs 5 and 6). For hot spots, clear scaling relationships were identified for six of the summary statistics including Max, SD, CV, kurtosis, Q1 and median (Table 3 and Fig. 5) while no clear scaling relationships were identified for the remaining statistics such as Min, mean, skewness and Q3. There are only two statistics (CV for October and Q1 for August) with goodness-of-fit R^2s exceeding 0.9, two statistics (SD for September and kurtosis for August) with R^2s smaller than 0.7, while the remaining statistics have R^2s between 0.7-0.9. The scaling relationships for the hot spots define four general categories: (1) quadratic polynomial relationships that open upward for Max, SD and CV; (2) exponential relationships with a decaying trend for kurtosis in September and October; (3) linear relationships with a decaying trend for kurtosis in August and linear relationships with a growing trend for median in October; and (4) power law relationships with a growing trend for Q1 for all three months and for median in August and September. The Max value decreased before the nadirs but increased after the nadirs with changing spatial scales. The CV showed a lowering variation for *O. bartramii* CPUE before the nadirs but an increasing variation after the nadirs, as the spatial scale became coarser. CPUE kurtosis changed from leptokurtic to platykurtic with increasingly coarser spatial scales. Moreover, both Q1 and median indicate a general increase of CPUE for hot spots, as the spatial scale became coarser. This also indicates that these two statistics were highly sensitive to the change of the spatial scales.

For cold spots, clear scaling relationships were identified for six of the summary statistics including mean, Max, SD, skewness, kurtosis and Q3 (Table 3 and Fig. 6) while no clear scaling relationships were identified for the remaining statistics such as Min, CV, Q1 and median. Goodness-of-fit R^2s exceed 0.7 except SD in August; its R^2s is small and does not exhibit a clear scaling relationship (Fig. 6). The scaling relationships for the spatial cold spots come in two general categories: (1) a quadratic polynomial relationship that opens upward for mean, SD, skewness, kurtosis and Q3; and (2) an exponential relationship with a decaying trend for Max. The mean, SD, skewness, kurtosis and Q3 statistics decrease before the nadirs and increase after the nadirs. The SD for September and October showed that a decreasing trend and the CPUE values tend to be close to the mean. Skewness for September and October was positive but the left-skew was in-

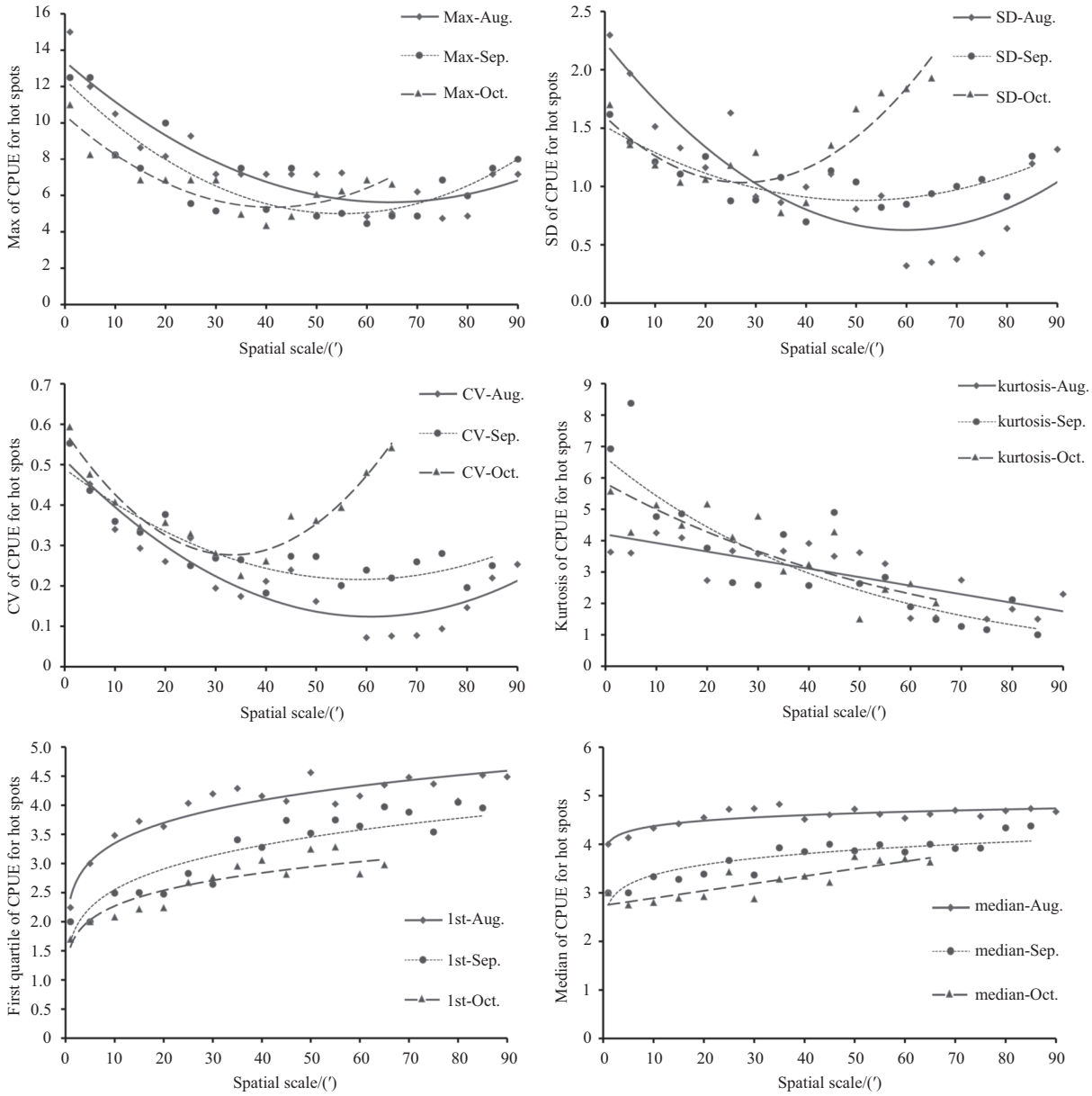

Fig. 5. Scale impacts on statistics of spatial hot spots for *O. bartramii* in the northwest Pacific Ocean.

creasingly weaker while it changed from left-skew to right-skew for August as the spatial scale became coarser. Kurtosis for August and September is larger than 3 at scales finer than 30′, indicating that the CPUE of cold spots yielded leptokurtic distributions; in contrast, the CPUE yielded platykurtic distributions at a scale coarser than 30′. For October, only scales finer than 20′ showed leptokurtic distributions. In addition, Q3 showed that CPUE decreases before the nadirs while it increases after the nadirs with the changing scales. Generally, the distribution of CPUE tends to be increasingly asymmetric and platykurtic as the spatial scale becomes coarser.

3.4 *Scale impacts on centroids of hot/cold spots*

The location of hot and cold spots as represented by their centroids is significantly affected by spatial scale (Fig. 7). For hot and cold spots, the centroids are close to each other at scales finer than 30′ while they vary in location at scales coarser than 30′. The centroid of the hot spot in August moved within a region about 2°×2° at scales finer than 60′, while it shifted over larger distances at scales coarser than 60′. For September, the centroid of the hot spot moved only about 60′ at scales finer than 30′ but fluctuated more widely at scales coarser than 30′. For October, the centroid moved along a line with a southwest-northeast direction at scales finer than 60′, but was significantly redistributed to the far west and east of the study area at scales coarser than 60′. The centroid of the cold spot in August does not move significantly at scales finer than 25′ but fluctuates more widely at coarser scales, especially above 60′. The centroid in September moved from the center (about longitude 155°E) to the west (about longitude 151°E), while the centroid in October moved from the north (latitude 41°N) to the south (latitude 39°N).

4 Discussion

Scaling issues are critical in identifying global and local spatial patterns in fisheries (Ciannelli et al., 2008). Multi-scale analysis has proven effective in addressing scaling issues in land-

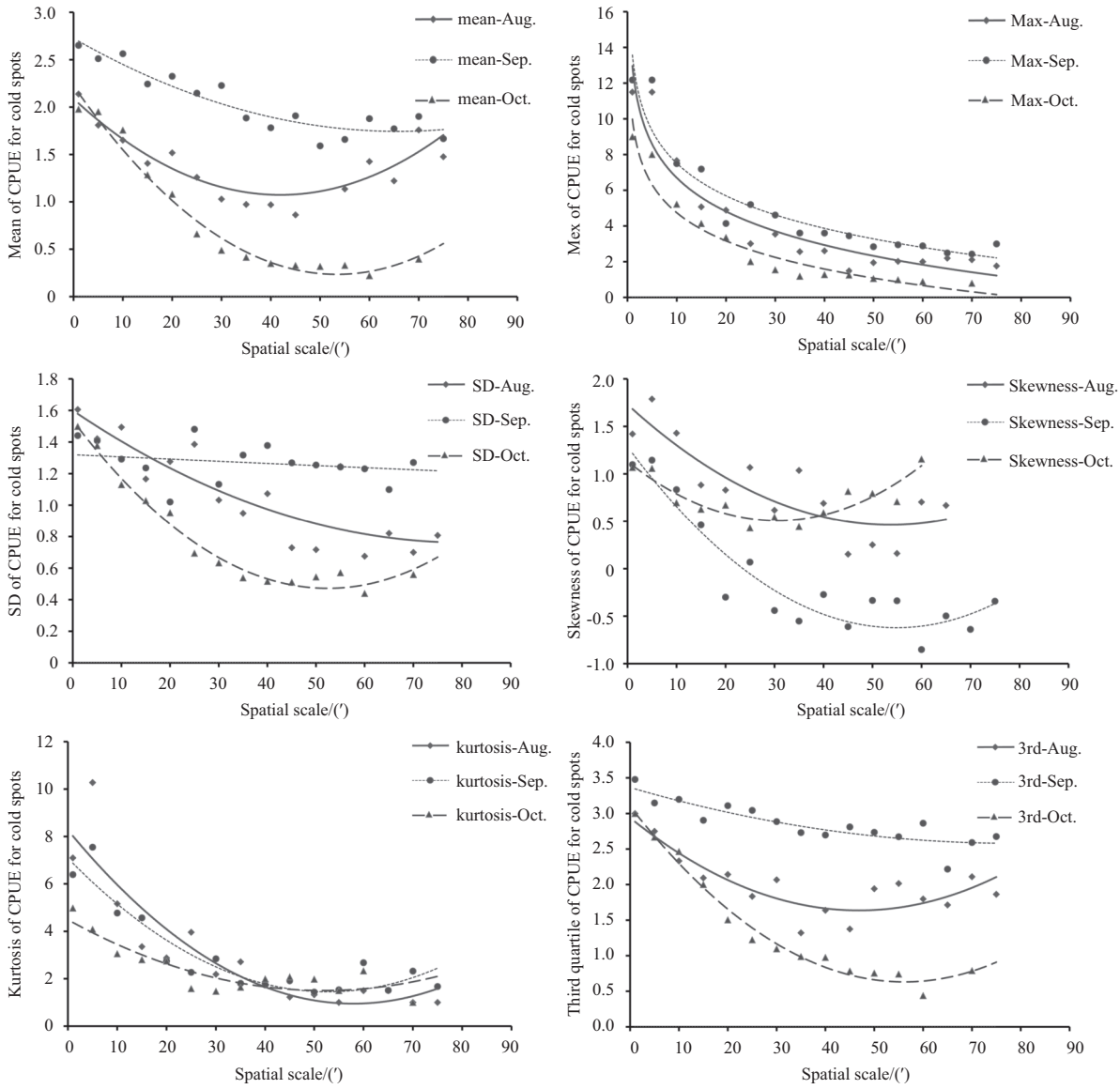

Fig. 6. Scale impacts on statistics of spatial cold spots for *O. bartramii* in the northwest Pacific Ocean.

scapes, in geography and in pelagic fisheries (Feng et al., 2016; Turner et al., 1989; Wu, 2004). We examined the scaling relations and scale effects of local spatial patterns of fisheries, using nominal CPUE data of *O. bartramii* in the northwest Pacific Ocean. As revealed in a previous study (Feng et al., 2016) and in this research, global and local spatial patterns such as clustering are significantly affected by spatial scale. We have identified scaling relationships for global spatial patterns of fisheries for *O. bartramii* in the northwest Pacific Ocean that include linear, logarithmic, exponential, power law, polynomial and descriptive functions. Logarithmic and descriptive relationships were not identified in local spatial patterns for *O. bartramii* based on the same fishery data.

For all data, the spatial indices (Feng et al., 2016) have clearer scaling relationships than do the summary statistics (c.f. Table 2 and Fig. 3). The spatial indices are therefore more appropriate as indicators of the optimum scale and coarsest allowable scale for conducting spatial analyses. The goodness-of-fit R^2s for the local spatial patterns are small when compared to the global patterns, indicating that the local patterns showed a slightly less strong regularity for scaling. In other words, the scaling relationships and scale effects of local spatial patterns are more complex. Our previous research showed that the non-zero CPUE data points (the Count index) yield power law scaling relationships and that the fractal dimensions of the scale effects were 2.224, 2.265, 2.268 for August, September and October, successively (Feng et al., 2016). We did not conduct a detailed analysis of scaling relations for Count index of hot and cold spots in this research. A brief examination of Count index change showed that the fractal dimensions are 2.487, 2.379 and 2.751 for hot spots for August, September and October, successively, and are 2.593, 2.529 and 2.539 for cold spots for the same three months. This suggests that the hot and cold spots are more sensitive to spatial scales as compared to the entire fishery data, because the former have larger fractal dimensions. The Count index is closely associated with the areas of hot and cold spots, however, the scaling relationship are more difficult to obtain when there are fewer data within the hot and cold spots of *O. bartramii*.

We identified hot and cold spots at a 0.05 significance level, but 0.01 has been used in previous research. We speculate that

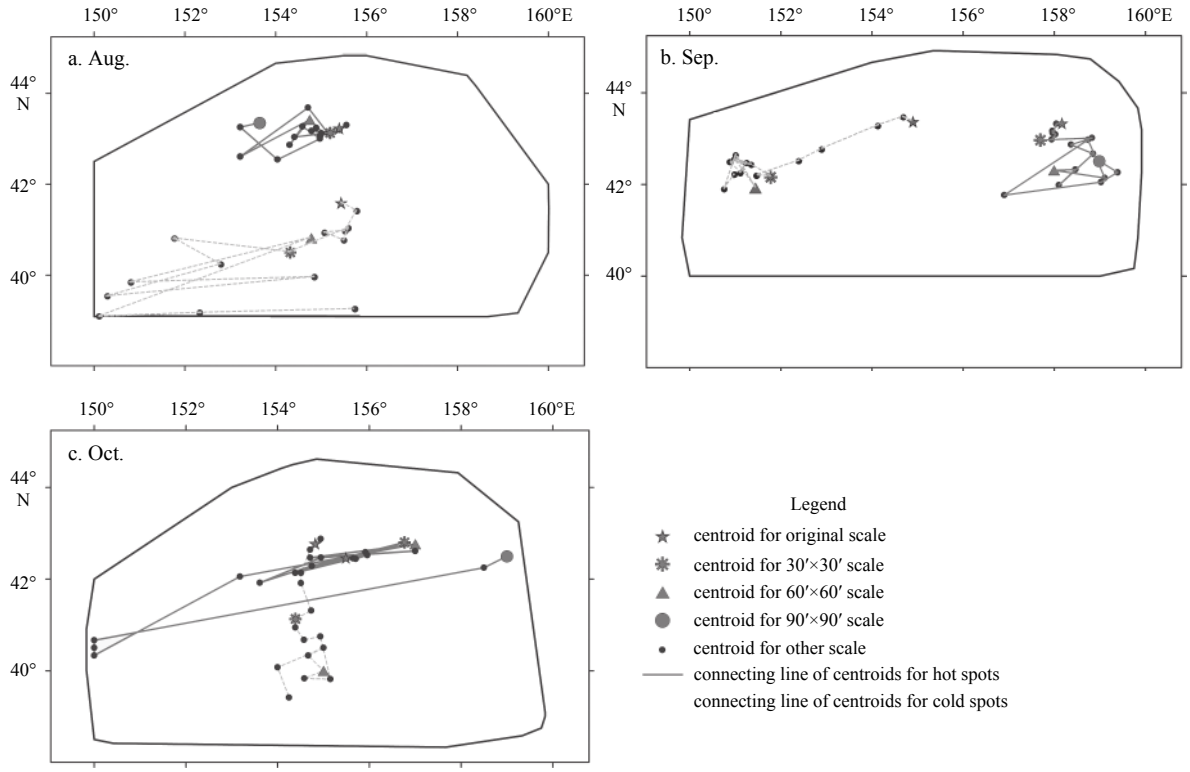

Fig. 7. Trajectories of centroids of spatial hot and cold spots across spatial scales.

the scaling relationships are similar at 0.01 significance, but the areas of the hot and cold spots would be smaller, and the cold spots would disperse on a less coarse scale. From the centroid perspective, the hot and cold spot locations at scales coarser than 30′ usually differ significantly from those at the original scale. It is therefore not advisable to identify the local spatial patterns of fisheries using this scale. Anselin Local Moran's I can be used to explore the statistically significant spatial clusters, i.e., hot and cold spots (Anselin, 1995, 2004). The impact of scale on clusters of Anselin Local Moran's I is not discussed in this paper, but the scaling relationships and scale effects are probably similar to those for the hot/cold spots derived using Getis-Ord Gi*. Spatial K-means can also identify spatial clusters of fisheries but these clusters are not necessarily associated with the hot/cold spots (Jain, 2010; Mullon et al., 2005). As such, the scale impacts on the spatial clusters derived using spatial K-means may be quite different from those based on Getis-Ord Gi* and Anselin Local Moran's I.

We speculate that in some pelagic fisheries such as *Dosidicus gigas*, *Thunnus albacares* and *Katsuwonus pelamis*, the scaling relationships are more complex because there are fewer commercial fishing records for these species as compared to *O. bartramii*. For example, commercial fishery data of *K. pelamis* are usually available at a coarse 1° spatial scale; as a consequence, multi-scale analysis may not be accurate and/or informative. The jumbo flying squid (*D. gigas*) is a fast-growing and short-lived species similar to *O. bartramii*. Its population is usually composed of individuals who have the capacity to migrate both vertically and horizontally in respond to changing environments (Arkhipkin and Murzov, 1986; Chen and Chiu, 2003; Yu et al., 2016b).

This study examined the impacts of changing spatial scales on spatial hot and cold spots for *O. bartramii* in the northwest Pacific Ocean. It extends the work of Feng et al. (2016) and describes the scale impacts on local clusters by considering several statistics including mean, SD, CV, skewness, kurtosis, Q1, median, Q3, area and centroid. The scale impacts were assessed in accordance with the linear, exponential, power law, and polynomial functions as commonly reported in landscape ecology (Turner et al., 1989; Wu, 2004) and more recently in fisheries (Feng et al., 2016).

It should be noted that the specific parameters of the scaling formula may not be applicable to other pelagic fisheries because they were affected by the selection of fishery dataset, but the scaling relations of spatial hotspots are appropriate to other fast-growing and short-lived species. Meanwhile, the methods presented in this paper are widely applicable to analyses of the spatial scale effects for any other commercial species. Our results contribute to a better understanding of the relationships between spatial scale and local spatial clusters in fisheries and in selection of the appropriate spatial scale for spatial analysis in fisheries.

References

Anselin L. 1995. Local indicators of spatial association-LISA. Geogr Anal, 27(2): 93–115

Anselin L. 2004. Exploring spatial data with GeoDa™: a workbook. Urbana, USA: University of Illinois, 61801

Arkhipkin A I, Murzov S A. 1986. Age and growth patterns of dosidicus gigas (Ommastrephidae). In: Ivanov B G, ed. Present State of Fishery for Squids and Prospects of Its Development. Moscow: VNIRO Press, 107–123

Carocci F, Bianchi G, Eastwood P, et al. 2009. Geographic Information Systems to Support the Ecosystem Approach to Fisheries: Status, Opportunities and Challenge. Rome, Italy: Food and Agriculture Organization of the United Nations

Chen Xinjun, Chen Yong, Tian Siquan, et al. 2008. An assessment of the west winter–spring cohort of neon flying squid (*Ommastre-*

phes bartramii) in the Northwest Pacific Ocean. Fish Res, 92(2–3): 221–230
Chen C S, Chiu T S. 2003. Variations of life history parameters in two geographical groups of the neon flying squid, *Ommastrephes bartramii*, from the North Pacific. Fish Res, 63(3): 349–366
Chen Xinjun, Tian Siquan, Guan Wenjian. 2014. Variations of oceanic fronts and their influence on the fishing grounds of *Ommastrephes bartramii* in the Northwest Pacific. Acta Oceanol Sin, 33(4): 45–54
Ciannelli L, Fauchald P, Chan K S, et al. 2008. Spatial fisheries ecology: Recent progress and future prospects. J Mar Syst, 71(3–4): 223–236
Cope J M, Punt A E. 2011. Reconciling stock assessment and management scales under conditions of spatially varying catch histories. Fish Res, 107(1–3): 22–38
Ebdon D. 1985. Statistics in Geography: A Practical Approach. 2nd ed. London: Wiley-Blackwell
Feng Yongjiu, Chen Xinjun, Liu Yan. 2016. The effects of changing spatial scales on spatial patterns of CPUE for *Ommastrephes bartramii* in the northwest Pacific Ocean. Fish Res, 183: 1–12
Feng Yongjiu, Chen Xinjun, Liu Yan. 2017a. Detection of spatial hot spots and variation for the neon flying squid *Ommastrephes bartramii* resources in the northwest Pacific Ocean. Chin J Oceanol Limnol, 35(4): 921–935
Feng Yongjiu, Chen Xinjun, Yang Liu. 2017b. Examining spatiotemporal distribution and CPUE-environment relationships for the jumbo flying squid *Dosidicus gigas* offshore Peru based on spatial autoregressive model. Chin J Oceanol Limnol: doi: 10.1007/s00343-018-6318-3
Feng Yongjiu, Cui Li, Chen Xinjun, et al. 2017c. A comparative study of spatially clustered distribution of jumbo flying squid (*Dosidicus gigas*) offshore Peru. J Ocean Univ China, 16(3): 490–500
Feng Yongjiu, Liu Yan. 2015. Fractal dimension as an indicator for quantifying the effects of changing spatial scales on landscape metrics. Ecol Indic, 53: 18–27
Fosså J H, Mortensen P B, Furevik D M. 2002. The deep-water coral *Lophelia pertusa* in Norwegian waters: distribution and fishery impacts. Hydrobiologia, 471(1–3): 1–12
Gao Feng, Chen Xinjun, Guan Wenjiang, et al. 2016. A new model to forecast fishing ground of *Scomber japonicus* in the Yellow Sea and East China Sea. Acta Oceanol Sin, 35(4): 74–81
Getis A, Aldstadt J. 2010. Constructing the spatial weights matrix using a local statistic. In: Anselin L, Rey S J, eds. Perspectives on Spatial Data Analysis. Berlin, Heidelberg: Springer, 147–163
Getis A, Ord J K. 1996. Spatial analysis and modeling in a GIS environment. In: McMaster R B, Lynn Usery E, eds. A Research Agenda for Geographic Information Science. Boca Raton: CRC Press, 157–196
Gilly W F, Markaida U, Baxter C H, et al. 2006. Vertical and horizontal migrations by the jumbo squid *Dosidicus gigas* revealed by electronic tagging. Mar Ecol Prog Ser, 324: 1–17
Gong Caixia, Chen Xinjun, Gao Feng, et al. 2014. Effect of spatial and temporal scales on habitat suitability modeling: A case study of *Ommastrephes bartramii* in the northwest pacific ocean. J Ocean Univ China, 13(6): 1043–1053
Guinet C, Dubroca L, Lea M A, et al. 2001. Spatial distribution of foraging in female Antarctic fur seals *Arctocephalus gazella* in relation to oceanographic variables: a scale-dependent approach using geographic information systems. Mar Ecol Prog Ser, 219: 251–264
Gutiérrez N L, Masello A, Uscudun G, et al. 2011. Spatial distribution patterns in biomass and population structure of the deep sea red crab *Chaceon notialis* in the Southwestern Atlantic Ocean. Fish Res, 110(1): 59–66
Harford W J, Ton C, Babcock E A. 2015. Simulated mark-recovery for spatial assessment of a spiny lobster (*Panulirus argus*) fishery. Fish Res, 165: 42–53
Huang Jiansheng, Sun Yao, Jia Haibo, et al. 2014. Spatial distribution and reconstruction potential of Japanese anchovy (*Engraulis japonicus*) based on scale deposition records in recent anaerobic sediment of the Yellow Sea and East China Sea. Acta Oceanol Sin, 33(12): 138–144
Jain A K. 2010. Data clustering: 50 years beyond K-means. Pattern Recogn Lett, 31(8): 651–666
Jennings S, Kaiser M, Reynolds J D. 2009. Marine Fisheries Ecology. New York: John Wiley & Sons
Jiang Tao, Chai Chai, Wang Jifang, et al. 2016. Temporal and spatial variations of abundance of phycocyanin- and phycoerythrin-rich *Synechococcus* in Pearl River Estuary and adjacent coastal area. J Ocean Univ China, 15(5): 897–904
Meaden G J, Aguilar-Manjarrez J. 2013. Advances in Geographic Information Systems and Remote Sensing for Fisheries and Aquaculture. Roma, Italy: Food and Agriculture Organization of the United Nations
Mitchell A. 2005. The ESRI Guide to GIS Analysis, Volume 2: Spatial Measurements and Statistics. Redlands, CA: Esri Press
Mullon C, Fréon P, Cury P. 2005. The dynamics of collapse in world fisheries. Fish Fish, 6(2): 111–120
Nishida T, Chen Dinggeng. 2004. Incorporating spatial autocorrelation into the general linear model with an application to the yellowfin tuna (*Thunnus albacares*) longline CPUE data. Fish Res, 70(2–3): 265–274
Ord J K, Getis A. 1995. Local spatial autocorrelation statistics: Distributional issues and an application. Geogr Anal, 27(4): 286–306
Paulino C, Segura M, Chacón G. 2016. Spatial variability of jumbo flying squid (*Dosidicus gigas*) fishery related to remotely sensed SST and chlorophyll-a concentration (2004–2012). Fish Res, 173: 122–127
Peeters A, Zude M, Käthner J, et al. 2015. Getis–Ord's hot-and cold-spot statistics as a basis for multivariate spatial clustering of orchard tree data. Comput Electron Agr, 111: 140–150
Saul S E, Walter III J F, Die D J, et al. 2013. Modeling the spatial distribution of commercially important reef fishes on the West Florida Shelf. Fish Res, 143: 12–20
Su N J, Sun C L, Punt A E, et al. 2008. Environmental and spatial effects on the distribution of blue marlin (*Makaira nigricans*) as inferred from data for longline fisheries in the Pacific Ocean. Fish Oceanogr, 17(6): 432–445
Swartz W, Sala E, Tracey S, et al. 2010. The spatial expansion and ecological footprint of fisheries (1950 to present). PLoS One, 5(12): e15143
Tian Siquan, Chen Yong, Chen Xinjun, et al. 2010. Impacts of spatial scales of fisheries and environmental data on catch per unit effort standardisation. Mar Freshwater Res, 60(12): 1273–1284
Turner M G, O'Neill R V, Gardner R H, et al. 1989. Effects of changing spatial scale on the analysis of landscape pattern. Landscape Ecol, 3(3–4): 153–162
Wiens J A. 1989. Spatial scaling in ecology. Func Ecol, 3(4): 385–397
Wu Jianguo. 2004. Effects of changing scale on landscape pattern analysis: scaling relations. Landscape Ecol, 19(2): 125–138
Xu Jie, Chen Xinjun, Chen Yong, et al. 2016. The effect of sea surface temperature increase on the potential habitat of *Ommastrephes bartramii* in the Northwest Pacific Ocean. Acta Oceanol Sin, 35(2): 109–116
Yang Mingxia, Chen Xinjun, Feng Youjiu, et al. 2013. Spatial variability of small and medium scales, resource abundance of *Ommastrephes bartramii* in Northwest Pacific. Haiyang Xuebao (in Chinese), 33(20): 6427–6435
Yu Wei, Chen Xinjun, Chen Yong, et al. 2015. Effects of environmental variations on the abundance of western winter-spring cohort of neon flying squid (*Ommastrephes bartramii*) in the Northwest Pacific Ocean. Acta Oceanol Sin, 34(8): 43–51
Yu Wei, Chen Xinjun, Yi Qian, et al. 2016a. Spatio-temporal distributions and habitat hotspots of the winter–spring cohort of neon flying squid *Ommastrephes bartramii* in relation to oceanographic conditions in the Northwest Pacific Ocean. Fish Res, 175: 103–115
Yu Wei, Yi Qian, Chen Xinjun, et al. 2016b. Modelling the effects of climate variability on habitat suitability of jumbo flying squid, *Dosidicus gigas*, in the Southeast Pacific Ocean off Peru. ICES J Mar Sci, 73(2): 239–249

Acta Oceanol. Sin., 2018, Vol. 37, No. 5, P. 77–86
DOI: 10.1007/s13131-018-1180-x
http://www.hyxb.org.cn
E-mail: hyxbe@263.net

Macrobenthic assemblage characteristics under stressed waters and ecological health assessment using AMBI and M-AMBI: a case study at the Xin'an River Estuary, Yantai, China

ZHOU Zhengquan[1, 2], LI Xiaojing[1, 2], CHEN Linlin[1], LI Baoquan[1]*, LIU Tiantian[1, 3], AI Binghua[1], YANG Lufei[1, 4], LIU Bo[1, 4], CHEN Qiao[5]

[1] Key Laboratory of Coastal Biology and Bioresource Utilization, Yantai Institute of Coastal Zone Research, Chinese Academy of Sciences, Yantai 264003, China

[2] University of Chinese Academy of Sciences, Beijing 100049, China

[3] Zhejiang Ocean University, Zhoushan 316022, China

[4] Ocean School of Yantai University, Yantai 264003, China

[5] Shandong University of Science and Technology, Qingdao 266590, China

Received 11 March 2017; accepted 30 July 2017

Abstract

To understand the ecological status and macrobenthic assemblages of the Xin'an River Estuary and its adjacent waters, a survey was conducted for environmental variables and macrobenthic assemblage structure in September 2012 (Yantai, China). Several methods are adopted in the data analysis process: dominance index, diversity indices, cluster analysis, non-metric multi-dimentional scaling ordination, AMBI and M-AMBI. The dissolved inorganic nitrogen and soluble reactive phosphorus of six out of eight sampling stations were in a good condition with low concentration. The average value of DO ((2.89±0.60) mg/L) and pH (4.28±0.43) indicated that the research area faced with the risk of ocean acidification and underlying hypoxia. A total of 62 species were identified, of which the dominant species group was polychaetes. The average abundance and biomass was 577.50 ind./m^2 and 6.01 g/m^2, respectively. Compared with historical data, the macrobenthic assemblage structure at waters around the Xin'an River Estuary was in a relatively stable status from 2009 to 2012. Contaminant indicator species *Capitella capitata* appeared at Sta. Y1, indicating the animals here suffered from hypoxia and acidification. AMBI and M-AMBI results showed that most sampling stations were slightly disturbed, which were coincided with the abiotic measurement on evaluating the health conditions. Macrobenthic communities suffered pressures from ocean acidification and hypoxia at the research waters, particularly those at Stas Y1, Y2 and Y5, which displays negative results in benthic health evaluation.

Key words: macrobenthos, Xin'an River Estuary, ocean acidification, hypoxia, AMBI, M-AMBI

Citation: Zhou Zhengquan, Li Xiaojing, Chen Linlin, Li Baoquan, Liu Tiantian, Ai Binghua, Yang Lufei, Liu Bo, Chen Qiao. 2018. Macrobenthic assemblage characteristics under stressed waters and ecological health assessment using AMBI and M-AMBI: a case study at the Xin'an River Estuary, Yantai, China. Acta Oceanologica Sinica, 37(5): 77–86, doi: 10.1007/s13131-018-1180-x

1 Introduction

Estuarine areas are one of the most productive ecosystems in nature, and have been widely concerned because of their multiple ecological function (Dolbeth et al., 2007). Massive nutrients and organics are transited by terrigenous freshwater, providing abundant nourishments and appropriate habitats for estuarine organisms (Zhang et al., 2016a, b). However, excessive nutriments aroused by anthropogenic activities and inappropriate discharge of effluents would stimulate environmental issues like water contamination and sediment deterioration leading to ocean acidification and underlying hypoxia. These deteriorated environment bring about diverse distortions on the local ecotopes (Marques et al., 2003; Lillebø et al., 2005; Zhu et al., 2014; Piló et al., 2016; Zhang et al., 2016a). Many estuary areas are encountering the same ecological problem, especially those in waters with weak circulation, which is also a balance between environmental protection and economy development (Dolbeth et al., 2007; Cai et al., 2016; Briggs et al., 2017).

The Xin'an River is about 40 km in length with a drainage area of around 315 km^2, which flows through the Muping District, Laishan District and High-tech District in Yantai City and ends up in the Yellow Sea (Ma et al., 2012). Widespread as it is, the river function and environmental conditions were not in a positive status for the past few years. Yantai government have made great efforts to bring the contamination into control since 2009, including performing afforestation, removing aquatic farms, set-

Foundation item: The Strategic Priority Research Program of the Chinese Academy of Sciences under contract Nos XDA11020403 and XDA1102702; the Key Research Program of the Chinese Academy of Sciences under contract No. KZZD-EW-14; the NSFC-NOW "Water Ways, Harbours, Estuaries and Coastal Engineering" Scheme co-supported by the National Natural Science Foundation of China under contract No. NSFC41061130543; the Netherlands Organization for Scientific Research under contract No. 843.10.003; the International Cooperation, CAS, Chinese-Foreign Cooperation in Key Projects under contract No. 133337KYSB20160002.
*Corresponding author, E-mail: bqli@yic.ac.cn

ting up sewage treatment plant and establishing 24-hour pollution monitoring systems. The research estuarine waters are located in the west of Yangma Island National AAAA Tourist Attraction. The south is the Xin'an River and Yuniao River. A sewage treatment plant is about 400 m west from the Xin'an River Estuary, of which the outlet is 3 232 m to the north of the estuary (Jia et al., 2007). The hydrodynamic water exchange in the research waters is limited due to the breakwater built to the west of Yangma Island harbor. Excessive pollutants (1 800 t per year) are produced by the surface runoff of the Xin'an River. According to Ma et al. (2012), the study areas mainly suffered perturbations from the sewage discharge plant and the rainy season runoff. Moreover, bivalve aquaculture zones scattered around the study water regions, which also impact the benthic assemblages by changing the circulation of substances, introducing physical anchoring structure and causing disturbances to benthic habitats (Dumbauld et al., 2009).

Biota indicators have been proved to be an effective method for marine ecosystem health assessment and widely applied under various water conditions (Peng et al., 2013; Rombouts et al., 2013). Macrobenthos are key components of estuarine ecosystems, playing important roles in the process of trophodynamics as well as in food chains (Herman et al., 1999). Macrobenthos facilitate the decomposition of organic materials in the process of ingestion and defaecation. Thus, the flux rates of nutrient particles could be balanced across the sediment-water interface; upper nourishment could be replenished to supply for the phytoplankton subsistence as well (Ekeroth et al., 2016). In virtue of their sedentary biotope and sensitiveness to environmental changes, macrobenthic organisms are generally adopted as biological indicators to evaluate the sediment health condition (Anderson, 2008; Borja and Tunberg, 2011; Li, 2011).

However, it could be intricate for policy makers and laymen to understand sophisticated information of scientific research data which displays the nexus of macrobenthos and environment. Various biotic indices therefore are wielded to evaluate the environment condition in a more intuitionistic way (Borja et al., 2008). Based on the commission of the water framework directive (WFD) and marine strategy framework directives (MSFD), AZTI's marine biotic index (AMBI and M-AMBI) (Muxika et al., 2007) are of two efficient indices to assess the ecological health status by macrobenthic community characteristics and confined reference conditions (Borja et al., 2008; Cai et al., 2015; Sigamani et al., 2015). Although discrepancies of the evaluation may exist due to variable environment conditions and anthropogenic perturbations, the AMBI and M-AMBI indices are still extensively accepted as well as applied in Europe, North America, South America, and East Asia (Luo et al., 2014).

Changes of certain environmental factors may induce fluctuation in both macrobenthic community structure and dominant species (Dauvin et al., 2010; Dolbeth et al., 2011; Xie et al., 2016). Sewage input is one of the disturbances in estuarine waters, which may change the macrobenthic community structure by providing appropriate conditions for tolerant or opportunistic species (Borja et al., 2000; Gusmao et al., 2016). Ma et al. (2012) found that the chemical oxygen demand (COD) and phosphates were at a high level in waters around the Xin'an River Sewage Treatment Plant. It indicated that the adjacent waters suffered from moderate eutrophication with relatively high inorganic nitrogen and restricted phosphates. COD reveals the content of the consumed oxygen when the organic matters and the inorganic substances were decomposed and oxidized (Kawai et al., 2016). In normal condition, DO values are negatively correlated with COD values in waters (Ahmed, 2014; Zhang et al., 2017). The higher the COD values, the lower the DO values (Zhang et al., 2017). Phosphorus eutrophication could be induced by marine acidification in the way that alters the form of phosphorus in aerobic sediments (Ge et al., 2017). According to aforementioned facts, high level of COD and phosphates in sea waters are closely related with marine hypoxia and acidification. Whether there are hypoxia and acidification at the Xin'an River estuarine waters remains to be discovered. To what extent the local macrobenthic communities are affected by environmental factors also need to be researched. However, so far, few studies had been reported on the macrobenthic assemblages and its relationships with environmental variables at waters around the Xin'an River Estuary.

The objectives of our study was to investigate the macrobenthic community characteristics as responding to small-scale hypoxia and acidification as well as the benthic ecological health by using AMBI and M-AMBI indices. This study also aims to ascertain whether there are divergences between biotic indices and abiotic indices on evaluating the health conditions of interfered waters. We intend to provide a dataset for the evaluation of the effects of contamination control and coastal management from the local government.

2 Materials and methods

2.1 *Sampling area and procedure*

Eight stations at the Xin'an River Estuary were investigated in September 2012, among which Y1 was located at the Xiaoyuniao River Estuary; Y2 and Y4 were located at the Xin'an River Estuary; Y3, Y5 and Y8 were around the Yangma Island; Y9 and Y10 were located at scallop aquaculture zone (Fig. 1). Sediment samples were collected by three separate replicates in each station using a 0.05 m^2 box-corer grab, then sieved through a 0.5 mm aperture mesh to obtain macrobenthos. The macrobenthic organisms were preserved in 80% ethanol and identified to the lowest possible taxonomic level in laboratory, and then counted and weighted using a 0.001 g precision electric balance. All sampling process followed with the *National Oceanography Census Regulation Methods* (State Quality and Technical Supervision Administration, 1992).

2.2 *Environmental factors*

Environmental variables, including water depth (WD), water temperature (WT), dissolved oxygen (DO), salinity (SAL), soluble reactive phosphorus (SRP, including PO_4^{3-}-P) and pH were measured *in situ* by YSI environmental monitoring system (600QS-M-O, US). Dissolved inorganic nitrogen (DIN, including NH_4^+-N, NO_2^--N and NO_3^--N), SiO_3^{2-}-Si, total nitrogen (TN) and total phosphorus (TP) were measured by the nutrient auto-analyzer using gas-segmented continuous flow analysis (AutoAnalyzer 3, Bran Luebbe, Germany).

2.3 *Statistical analysis*

2.3.1 *Environmental data processing*

Single factor evaluation was applied to classify the sea water nutrients in accordance with National Marine Industry Standards, HY/T 086–2005, China. The standard index of pollutants (P_i) was calculated by the following method:

$$P_i = M_i/S_i, \tag{1}$$

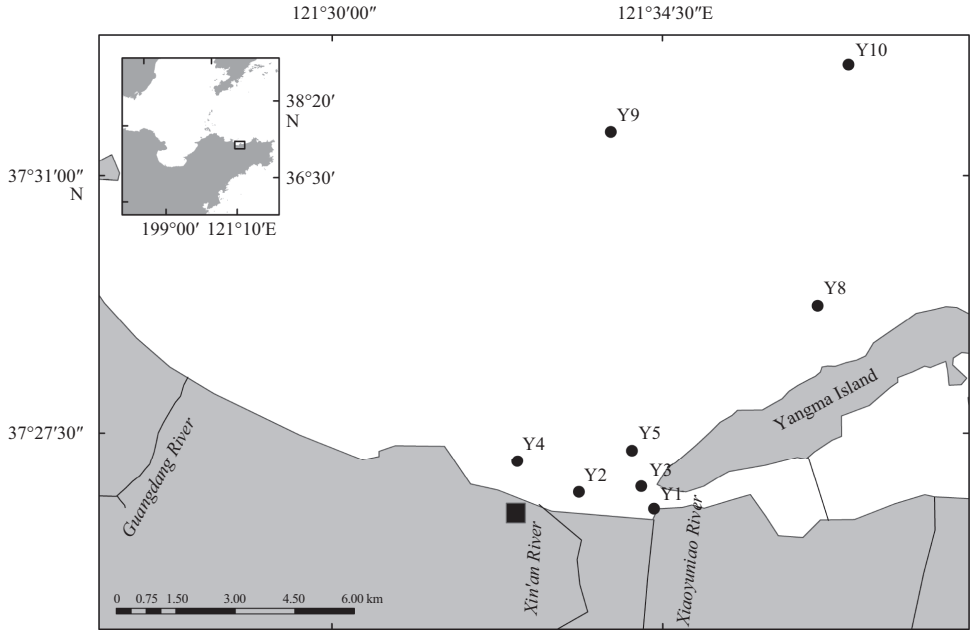

Fig. 1. Sampling stations of macrobenthos in the Xin'an River Estuary and its adjacent waters. The position of sewage treatment plant is marked with the black square.

where M_i is the average measured concentration of pollutant *i*; S_i is the standard concentration for pollutants *i*. Here, GB Class I water quality standards was used here as S_i data according to National Sea Water Quality Standard (GB 3097–1997).

The principal component analysis (PCA) was conducted based on lg (x+1) transformation of environmental data to analyze the characteristic of sampling environment data. The Pearson correlation analysis was conducted to explore the correlation between single environmental factor and benthic community structure. The bio-environment (BIOENV) analysis was performed to study the optimal combination of environmental factors to describe the community structure.

2.3.2 *Biological data processing*

The biological properties were analyzed by PRIMER software package (Version 7.0.11, PRIMER-E Ltd., 2016), including the total biomass (B), abundance (A), number of species (S), Shannon-Wiener diversity index (H_0), Margalef richness index (D), and the Pielou's evenness index (J). The dominant index (Y) (Chen et al., 1995) of species was calculated by the following formula:

$$Y = (n_i/N)f_i, \tag{2}$$

where N is the total abundance of all the stations, n_i is the abundance of the species i of all the stations, and f_i is the occurrence frequency of the species i of all the stations. Species i can be defined as the dominant species when Y>0.02.

The multivariate analysis of the macrobenthic community was also conducted by PREMER 7. Cluster and non-metric multidimensional scaling (n-MDS) plot was used to display the relationship of the species abundance of different macrobenthic communities on the basis of Bray-Curtis similarities. Analysis of similarities (ANOSIM) was used to determine if significant differences existed between samples, and similarity percentages (SIMPER) was used to calculate the contribution of the species which determined different clusters.

2.3.3 *Benthic quality assessment*

AZTI's marine biotic index (AMBI) (Borja et al., 2000) and multivariate AZTI's marine biotic index (M-AMBI) (Muxika et al., 2007) were adopted to assess the benthic quality at waters around the Xin'an River Estuary. The AMBI and M-AMBI value were calculated by the AMBI program (Version 5.0, http://ambi.azti.es). All species data were processed in accordance with the AMBI guidelines (Borja and Muxika, 2005), the non-benthic invertebrate taxa (fish and megafauna) were removed and ecological groups (EG I: disturbance-sensitive species; EG II: disturbance-indifferent species; EG III: disturbance-tolerant species; EG IV: the second-order opportunistic species; EG V: the first-order opportunistic species) were classified based on the species list made at AZTI Laboratory in November 2014. Due to the fact that the research waters suffered from different levels of anthropogenic activities, the threshold values for the M-AMBI conditions were increased by 15% on the basis of original biodiversity index and species number (Borja et al., 2008; Li et al., 2013). Under high quality status, AMBI=0, Diversity=4.24, Richness=25.30, M-AMBI=1; under bad quality status, AMBI=6, Diversity=0, Richness=0, M-AMBI=0.

3 Results

3.1 *Abiotic parameters*

According to Chinese Sea Water Quality Standard GB 3097–1997 (National Standard of the People's Republic of China GB 3097–1997 was issued by the National Environmental Protection Agency of the People's Republic of China on July 1, 1998), the GB Class I sea water quality can be used for marine fishery, natural reserve areas and natural preservation zones for rare and endangered animals; the GB Class II quality can be used for marine culture zones, bathing beaches, direct body contact marine sports and industrial water area related to marine foods; the GB Class III quality can be used for normal industrial water and coastal scenic areas; the GB Class IV quality can be used for port waters and marine development zone for specific application.

The average content of DIN and SRP of all sampling stations were (0.15±0.07) mg/L and (0.011±0.006) mg/L, respectively, which can be defined as GB Class I quality, except that Y2 and Y4 belonged to GB Class II quality, for the DIN values of which are 0.286 mg/L and 0.239 mg/L, respectively; the SRP values of which are 0.0231 mg/L and 0.0183 mg/L, respectively (Table 1). However, the average value of DO ((2.89±0.60) mg/L) and pH (4.28±0.43) were ranked as superior GB Class IV with the declining trend from open sea to the river mouth, which indicated a bad condition of DO and pH values. The pollutant standard index P_{DIN} and P_{SRP} were less than 1 at all sampling stations except for Y2 and Y4, which indicated the nutrients at most stations met with the standards for marine fishery and natural preservation zones, yet Y2 and Y4 still reached the standard for aquaculture and body contact usages (GB Class II).

3.2 *Species composition*

A total of 62 species were identified, among which Polychaeta was the most abundant taxon with 34 species (54.84%), followed by Crustacea with 12 species (19.35%), Mollusca with 10 species (16.13%), Echinodermata with 3 species (4.84%), and the others with 3 species (1 Nemertea, 1 Sipuncula and 1 Vertebrata) (4.84%). In terms of species composition at each station, Y1 (8 species) was observed with the least species, while Y10 possessed the most with 32 species. Moreover, Polychaeta took up most of the species proportions at all sampling stations (Fig. 2).

Table 1. Data and evaluation results of DIN, SRP, DO and pH in the Xin'an River Estuary waters

Station	DIN/mg·L^{-1}	DO/mg·L^{-1}	pH	SRP/mg·L^{-1}	P_{DIN}	P_{SRP}
Y1	0.143	1.60	4.03	0.0063	0.72	0.42
Y2	0.286	2.58	3.51	0.0231	1.43	1.54
Y3	0.109	3.19	4.41	0.0058	0.55	0.39
Y4	0.239	3.37	3.87	0.0183	1.20	1.22
Y5	0.118	2.88	4.5	0.0086	0.59	0.57
Y8	0.097	2.81	4.58	0.0097	0.49	0.65
Y9	0.090	3.31	4.67	0.0071	0.45	0.47
Y10	0.118	3.38	4.68	0.0088	0.59	0.59
Mean±SD	0.15±0.07	2.89±0.60	4.28±0.43	0.011±0.006	0.30±0.14	0.24±0.14

Note: DIN means dissolved inorganic nitrogen, DO dissolved oxygen, SRP soluble reactive phosphorus, P_{DIN} the pollutant standard index of dissolved inorganic nitrogen, and P_{SRP} the pollutant standard index of soluble reactive phosphorus.

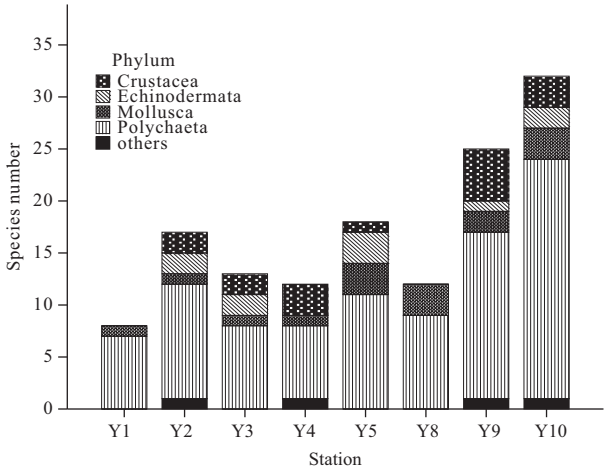

Fig. 2. Macrobenthic species composition of each station in Xin'an River Estuary and its adjacent waters.

Four Polychaeta species were identified as dominant species according to their dominant values (Y>0.02). Moreover, contaminant indicator species *Capitella capitata* (Sun and Chen, 1978; James and Gibson, 1980) was only obtained at Sta. Y1, with the abundance of 46.67 ind./m^2 (Table 2).

3.3 *Abundance and biomass*

The distribution of macrobenthic abundances showed the descending trend from the offshore to the estuary areas (Fig. 3). The average species abundance per station was 577.50 ind./m^2, among which Polychaeta contributed the most with average abundance of 470.83 ind./m^2 (81.53% of average species abundance), followed by Mollusca species 42.50 ind./m^2 (7.36%), Crustacea species 32.50 ind./m^2 (5.63%) and Echinodermata species 22.50 ind./m^2 (3.90%). Other species (1 Nemertea, 1 Sipuncula and 1 Vertebrata) contributed 1.59% with average abundance of 9.17 ind./m^2.

Table 2. Spatial distribution of dominant species in each sampling station

Station	*Lumbrineris latreilli*	*Heteromastus filiformis*	*Chaetozone setosa*	*Sigambra bassi*
Y	0.337	0.104	0.023	0.021
Y1	+	+	+	
Y2		+	+	
Y3	+	+	+	+
Y4	+	+	+	
Y5	+	+		+
Y8	+	+	+	+
Y9	+	+	+	+
Y10	+	+		+

Note: + means the dominant species were detected.

The spatial distribution of macrobenthic biomass was presented with lower value in estuary area and higher value in offshore area (Fig. 4). The average species biomass per station was 6.01 g/m^2, among which Polychaeta contributed the most with average biomass of 2.76 g/m^2 (45.90%), followed by Mollusca with 0.73 g/m^2 (12.20%), Crustacea with 0.18 g/m^2 (2.91%). Echinodermata possessed the least with 0.13 g/m^2 (2.22%). Other species (1 Nemertea, 1 Sipuncula, and 1 Vertebrata) possessed 36.74% of the total biomass with a kind of vertebrate *Chaeturichthys stigmatias* obtained at Sta. Y9, which increased the average biomass to 2.21 g/m^2.

3.4 *Biodiversity*

The Shannon-Wiener diversity index (H_0) varied from 1.57

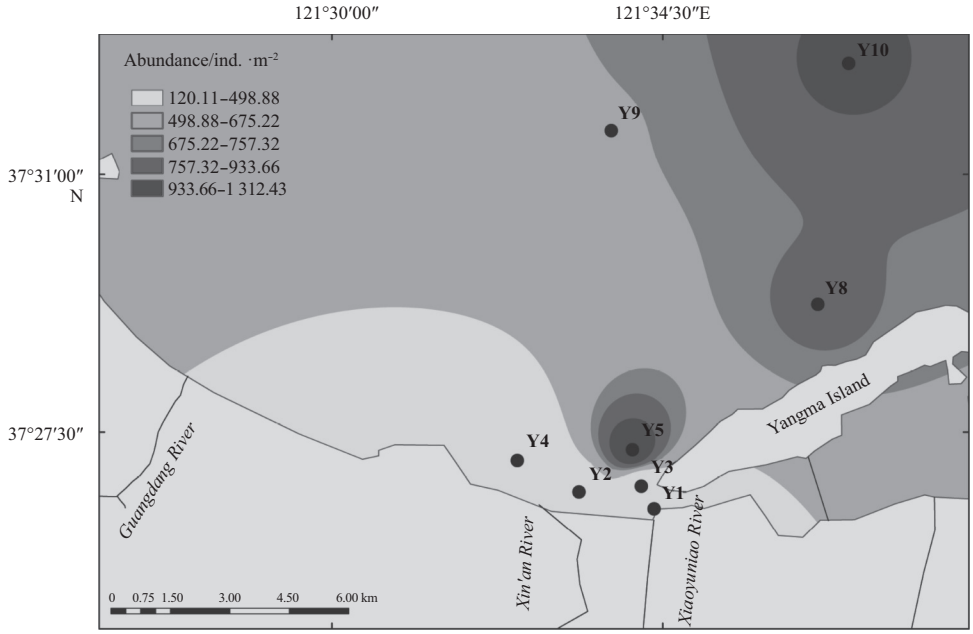

Fig. 3. Spatial distribution of macrobenthic abundance in sampling stations.

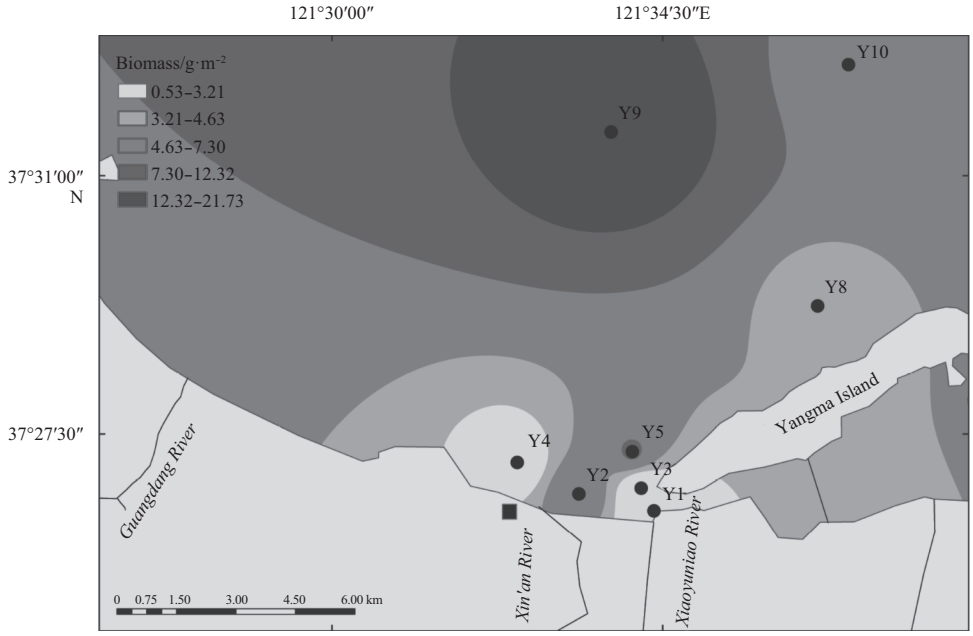

Fig. 4. Spatial distribution of macrobenthic biomass in sampling stations.

(Y5) to 4.04 (Y10), with the average value of 2.96±0.82. The Margalef richness index (*D*) varied from 1.46 (Y1) to 4.50 (Y10), with the average value of 2.60±1.04. The Pielou's evenness index (*J*) varied from 0.38 (Y5) to 0.87 (Y3), with the average value of 0.75±0.17 (Fig. 5).

3.5 *Community structure*

Cluster and n-MDS analysis showed that the similarity between macrobenthic assemblages in different stations ranged from 24.56%-55.99%. According to the similarity values, all the sampling stations were divided into four groups at an arbitrary similarity level of 36.14%. Group I included two stations, Y2 and Y4, with the similarity value of 48.95%. Group II consisted of only Sta. Y1, which was separated from Group I at similarity value of 32.25%. Group III consisted of Y3, Y5 and Y8, with the similarity value of 48.95%. Group IV included Y9 and Y10, with the similarity value of 54.95%. Group IV was separated from Group III at the similarity value of 36.14% (Fig. 6). The same results were obtained by n-MDS ordination plots, with the stress value lower than 0.1, and the four groups showed significant differences on ANOSIM global test (global R=1, significance level=0.1%<0.05, permutations=999).

The results of SIMPER analysis were as follows. Group I consisted of Y2 and Y4, and the average similarity coefficient was 48.95%. The polychaetes *Orbinia dicrochaeta* (Wu, 1962) and *Chaetozone setosa* (Malmgren, 1867) were dominant species with

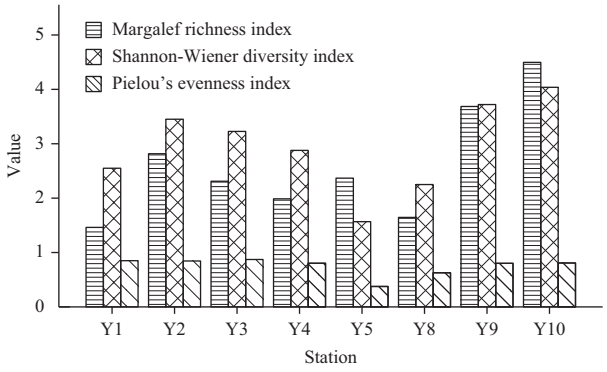

Fig. 5. Margalef richness index (D), Pielou's evenness index (J) and Shannon-Wiener diversity index (H_0) of each sampling station.

contribution rate of similarity were 22.47% and 15.36%, respectively. Other species which cumulatively contributed higher than 70% were polychaetes *Heteromastus filiformis* (Claparede) (10.8%), *Glycera rouxi* (Audouin et Milne Edwards, 1833) (10.8%) and crustacea *Paraphoxus oculatus* (10.8%). The average similarity and species contributions of Group II (only Y1, located at the estuary of Yuniao River) could not be calculated. The pollution indicator species, *Capitella capitata* (Fabricius, 1780), was only detected with a high abundance (46.67 ind./m^2, maximum in all stations) at Sta. Y1, which indicated a polluted benthic environment condition. Group III consisted of Y3, Y5 and Y8, which showed an average similarity coefficient of 51.30%. The dominant species of Group III were polychaetes *Lumbrineris latreilli* (Audouin et Edwards, 1834), *Heteromastus filiformis* (Claparede) and *Sigambra bassi* (Hartman), whose contribution rate were 33.55%, 25.42% and 11.18%, respectively. Moreover, the abundance in Sta. Y5 reached the maximal value of 1 313.33 ind./m^2. Group IV consisted of Y9 and Y10, whose average similarity coefficient was 54.95%. The species with contribution rate above 10% were *Lumbrineris latreilli* (Audouin et Edwards, 1834) (12.98%) and *Moerella iridescens* (Benson) (12.10%).

3.6 *Relationships between macrobenthic community and environmental factors*

The PCA results showed that the accumulative contribution rate of the first three principal components to total variation accounted for over 85%, maintaining most of information of the 12 environmental factors. The coefficients of eigenvectors were displayed in Table 3, among which pH, NO_3^--N and NH_4^+-N contributed most of the PC1 with coefficients of –0.364, 0.361 and 0.353, respectively; DO and NO_2^--N contributed most of the PC2 with coefficients of –0.489 and –0.385, respectively; SAL, DO and WT contributed most of the PC3 with coefficients of 0.703, –0.426 and –0.389, respectively.

Table 3. Eigenvectors of each environmental variable on the first three principal components

Environmental variable	PC1	PC2	PC3
PO_4^{3-}-P	0.314	–0.301	0.147
TP	0.236	0.337	–0.026
NH_4^+-N	0.353	–0.065	0.076
NO_2^--N	0.260	–0.385	0.259
NO_3^--N	0.361	–0.122	0.067
SiO_3^{2-}-Si	0.341	–0.230	0.144
TN	0.268	0.286	–0.175
WT	0.255	0.349	–0.389
SAL	–0.166	0.268	0.703
WD	–0.321	–0.241	0.079
DO	–0.082	–0.489	–0.426
pH	–0.364	–0.059	–0.126

Note: PO_4^{3-}-P represents phosphoric acid-phosphorus; TP total phosphorus; NH^{4+}-N ammonium salt-nitrogen; NO_2^--N nitrous acid-nitrogen; NO_3^--N nitric acid-nitrogen; SiO_3^{2-}-Si silicic acid-silicon; TN total nitrogen; WT water temperature; SAL salinity; WD water depth; DO dissolved oxygen; and PC1, PC2 and PC3 the first, second and third principal components.

The result of BIOENV analysis (Spearman) showed that the characteristics of spatial distribution of community biomass could be mainly explained by the combination of TP, NO_2^--N and pH, and the Spearman coefficient was 0.747. Pearson correlation analysis showed that only TN and TP were significantly correlative with community abundance among 12 environmental factors, and the Pearson correlation coefficient were –0.745 (sig. level=0.034) and –0.754 (sig. level=0.031), respectively.

3.7 *AMBI and M-AMBI*

Among all 62 species identified in this sea area, 29 species were found to have an abundance lower than 3, which could not be defined to any ecological group based on AMBI guidelines. Moreover, one species remained unassigned in accordance with the species list (November 2014, v 5), which was *Apseudes* sp..

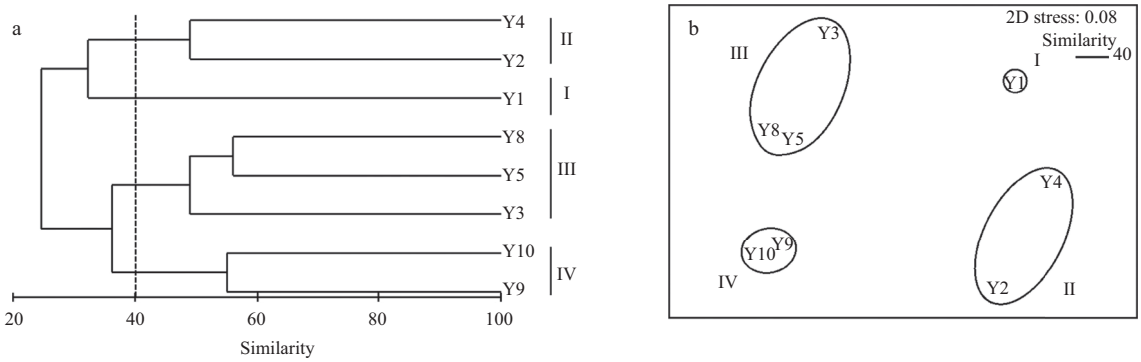

Fig. 6. Analysis of cluster (a) and MDS (b) on macrobenthos of sampling stations, September 2012. The abundance data was standardized, and then overall transformed by lg (x+1) method. The group-average linking was conducted in accordance with S17 Bray-Curtis species similarities.

Table 4. Results of AMBI and M-AMBI for each station in waters around the Xin'an River Estuary

Station	Ⅰ/%	Ⅱ/%	Ⅲ/%	Ⅳ/%	Ⅴ/%	NA/%	AMBI	DC	M-AMBI	Status
Y1	0.0	31.3	0.0	25.0	43.8	0.0	4.219	MD	0.35	poor
Y2	20.0	35.0	5.0	40.0	0.0	0.0	2.475	SD	0.63	good
Y3	8.7	39.1	8.7	43.5	0.0	0.0	2.804	SD	0.51	moderate
Y4	48.6	16.2	27.0	8.1	0.0	0.0	1.419	SD	0.62	good
Y5	2.6	82.9	0.5	14.0	0.0	0.0	1.889	SD	0.53	moderate
Y8	6.7	65.0	2.5	25.8	0.0	0.0	2.212	SD	0.55	good
Y9	16.7	56.7	13.3	13.3	0.0	2.2	1.850	SD	0.73	good
Y10	31.3	28.4	30.6	9.7	0.0	2.2	1.780	SD	0.81	high

Note: I, II, III, IV and V represent for ecological Group I, II, III, IV and V, respectively; NA not assigned; DC disturbance classification; MD moderately disturbed; and SD slightly disturbed.

The unassigned species proportion of all sampling stations was below 20%, which indicated a credible judgement on AMBI and M-AMBI results (Table 4).

The AMBI values of eight sampling stations ranged from 1.419 to 4.219, with seven slightly disturbed stations and one medium disturbed station (Y1), which indicated that the benthic environment suffered from slightly anthropogenic interference. The minimal AMBI value was captured at Sta. Y10 (1.419), where most of the species were disturbance-sensitive species (Group I: 48.6%); the maximum value was detected at Sta. Y1 (4.219), with the first-order opportunistic species as main dominant species (Group V: 43.8%).

The M-AMBI values ranged between 0.35 and 0.81, with Sta. Y10 defined as high quality status, Y1 as poor status, Y3 and Y5 as moderate status, and the rest of the stations as good status. The minimal M-AMBI value (0.35) appeared at Sta. Y1, with the least species number (six species) amongst all sampling stations; the maximum value was obtained at Sta. Y10, with the highest biodiversity index (H_0=3.69) as well as species number (20 species) among all sampling stations.

4 Discussion

The Xin'an River is located at a special geographical position with widespread drainage area. The river is under multiple anthropogenic pressures: industrial and domestic sewage discharge, aquaculture activities, and tourists impacts. Human activities could trigger prompt nutrient eutrophication, which is far more rapid than the natural process (Serrano et al., 2017). The abiotic parameters showed that the pollutant standard index (P_i) of DIN and SRP at most sampling stations belonged to GB Class I. The good condition of nutrients testified the effects that the local government had achieved on eutrophication control. However, the sampling waters still faced with the risk of hypoxia and acidification. The DO and pH values at sampling waters were at a low level with descending trend from open sea waters to the river mouth.

The results of biotic assessments including correlation analysis, AMBI and M-AMBI, which matched well with that of environmental measurements. We found that the pattern of macrobenthic abundance was closely related to the TN and TP in the research waters. Macrobenthos, together with microbes and other physical factors, continually participated in the complex nutrient circulating process across sediment-water interface (Ekeroth et al., 2016). The nutrients in turn influence the behavior of benthic organisms (Shen et al., 2016). Moreover, feeding activities of polychaetes are closely associated with TN and TP in the sediment they inhabit (Webb and Eyre, 2004; Volkenborn et al., 2007; Shen et al., 2016). Polychaetes are also identified as dominant groups in research area.

Previous research on macrobenthos had been conducted in Yantai offshores since 1985 (Wu and Zhang, 1994; Wang et al., 1995; Tang, 2011; Leng et al., 2013; Wang and Li, 2013). However, few surveys focused on the topic of biological response to environmental stressors at the Xin'an River Estuary and its adjacent waters. A precise analysis and comparison of community shift was difficult to achieve. We chose three previous surveys with same sampling methods and seasons to compare the changing of species composition in recent years (Table 5).

From 2009 to 2012, the disturbance-indifferent polychaeta species *Lumbrineris latreilli* was absolutely identified as dominant species, and Polychaeta was also the dominant taxonomic group in waters around the Xin'an River Estuary. In October 2009, 68 species were obtained in the Sishili Bay, among which *Lumbrineris latreilli*, *Musculus senhousia*, *Styela clava*, *Notomastus* sp. and *Asychis* sp. were dominant species (Tang, 2011). In September 2010, 60 species were captured in waters around the Yangma Island, among which *Lumbrinereis longiforlia*, *Mediomastus* sp. and *Sigambra* sp. were dominant species (Leng et al., 2013). In August 2010, 84 species were obtained in Yantai coastal waters, among which *Lumbrineris latreilli*, *Chaetozone setosa*, *Haploscoloplos elongatus*, and *Sternaspis scutata* were dominant species (Wang and Li, 2013). Most of the dominant species are disturbance-indifferent species in October 2009 and September 2010, while more second-order opportunistic species are defined as dominant species in November 2010 and September 2012. The macrobenthic characteristics at the research waters were in a relatively stable condition with polychaetes as the dominant species group from 2009 to 2012.

The macrobenthic communities directly or indirectly suffered from anthropogenic activities, which involve in the interactions across the sediment-water interface (Smith et al., 2000). The macrobenthic communities at waters around the Xin'an River

Table 5. Comparison of species composition with previous surveys in the Xin'an River Estuary

Sampling time	Total species	Polychaeta	Mollusca	Crustacea	Echinodermata	Others	Reference
Oct. 2009	68	54.42%	25.00%	10.29%	4.41%	5.88%	Tang (2011)
Sep. 2010	60	68.33%	10.00%	18.33%	1.67%	1.67%	Leng et al. (2013)
Aug. 2010	84	50.00%	19.05%	21.43%	3.57%	5.95%	Wang et al. (2013)
Sep. 2012	62	54.84%	16.13%	19.35%	4.84%	4.84%	this study

Estuary scattered in a geographical pattern with respective environmental stressors, which was also expressed in the CLUSTER, MDS and PCA analysis. Interfered by anthropogenic activities and environmental stress, the benthic communities in the Bohai Sea also show a trend of simplification in species composition since the 1980s, with increasing abundance of small body sized polychaete, bivalve and crustacean species but decreasing biodiversity (Zhou et al., 2007; Cai et al., 2012; Jin et al., 2015; Hu and Zhang, 2016).

AMBI and M-AMBI have proven to be operative indices on evaluating the benthic ecological conditions under various pressures of sea waters, estuaries, and coastal waters around Europe, North America, Indian and China (Muxika et al., 2005; Borja and Tunberg, 2011; Cai et al., 2013, 2015; Li et al., 2013; Liu et al., 2014; Luo et al., 2014; Sigamani et al., 2015). The establishment of reference condition for the research waters is crucial for calculating the M-AMBI value (Muxika et al., 2007). Four methods can be used to determine the reference conditions: (1) comparison with an existing undisturbed site, (2) historical data and information, (3) numerical models, and (4) best professional judgments (Borja et al., 2004; Muxika et al., 2007; Forchino et al., 2011; Borja et al., 2012). However, pristine sites as reference condition were hardly to find due to multiple disturbances at the Xin'an River Estuary. Historical data and numerical models were also unavailable. We set the reference condition with the highest richness and diversity values observed in this study and increased them by 15%, in accordance with the previous studies (Borja and Tunberg, 2011; Forchino et al., 2011; Paganelli et al., 2011). The M-AMBI value of most stations ranked as "good", which was coincided with the former research (Li et al., 2013).

Extreme conditions of pH and DO values often occurred on the same temporal and spatial scale (Wallace et al., 2014). The threshold DO value of hypoxic waters used to be below 2.0 mg/L. However, the ability of hypoxia tolerance varies with different benthic organisms. The average median sublethal DO thresholds of crustaceans, molluscs, annelids and echinoderms are (3.21±0.28) mg/L, (1.99±0.16) mg/L, (1.20±0.25) mg/L, (1.22±0.22) mg/L, respectively (Vaquer-Sunyer and Duarte, 2008). The DO value at Sta. Y1 was 1.60 mg/L, which was lower than the average median sublethal DO thresholds of crustacean and mollusc species, yet higher than that of annelid and echinoderm species. Long-term or periodic exposure to hypoxia may alter the macrobenthic community structure and thus affect the species biomass, abundance, movement and feeding activities, even the upper trophic structure (Rakocinski and Menke, 2016; Briggs et al., 2017). The species composition of Sta. Y1 indicated the macrobenthic community was exposed to hypoxia, e.g., 6 out of 7 obtained polychaete species belonged to the first and second-order opportunistic species. It is also evidenced by the minimum value of abundance (120 ind./m^2) and biomass (0.53 g/m^2) as well as the appearance of high abundance (46.67 ind./m^2) of typical pollution indicator *Capitella capitate* at Sta. Y1. Station Y5 was in moderate status, yet the macrobenthic abundance and biomass reached a quite high level. A quantity of *Lumbrineris latreilli* and *Heteromastus filiformis* was captured at Y5, whose abundance were 980 ind./m^2 and 160 ind./m^2, respectively. For this reason, the biodiversity index (H_0) at Y5 was the lowest (H_0=1.57) among sampling stations. Moreover, *Heteromastus filiformis* belongs to the second-order opportunistic species (EG IV). High abundance of *Heteromastus filiformis* resulting in a low level status of AMBI and M-AMBI at Y5, which could also be reflected by environmental factors as low DO and pH values.

Ascending level of atmospheric CO_2 result in global warming and ocean acidification, while acidic waters in coastal zones could be mainly attributed to excessive loading of nutrients and production of organisms (Fabry et al., 2008; Wallace et al., 2014). Ocean acidification would affect the growth and development process of some benthic invertebrates via meddling in the mechanisms of mineralogy and calcification, especially for crustaceans, molluscs and echinoderms (Fabry et al., 2008). Moreover, large body sized crustaceans and echinoderms species were rarely found in the research waters.

The M-AMBI results indicated the poor health status of Y1, moderate status of Y3 and Y5, which coincides well with the low DO and pH values of Y1, Y3 and Y5. The research waters suffered from hypoxia and seawater acidification due to its geographical position and aforementioned findings. These environmental and anthropogenic stressors remarkably reshaped the macrobenthic community structure.

5 Conclusions

This is the first time that AMBI and M-AMBI method were used to evaluate the benthic conditions at the Xin'an River Estuary and its adjacent waters, which is expected to be a guideline for improving monitoring measures and protective pathways. The conclusions were made as follows:

(1) The macrobenthic assemblage at waters around the Xin'an River Estuary was not shift from 2009 to 2012. Polychaetes were always presented as the dominant taxonomic group.

(2) The macrobenthic communities suffered pressures from surface runoffs and anthropogenic activities, particularly Stas Y1, Y2 and Y4 at the river mouth interfered with ocean acidification and hypoxia.

(3) AMBI and M-AMBI results showed that most sampling stations were in good to high ecological health conditions, which coincided well with the abiotic measurements.

References

Ahmed A A M. 2014. Prediction of dissolved oxygen in Surma River by biochemical oxygen demand and chemical oxygen demand using the artificial neural networks (ANNs). Journal of King Saud University—Engineering Sciences, 29(2): 151–158

Anderson M J. 2008. Animal-sediment relationships re-visited: Characterising species' distributions along an environmental gradient using canonical analysis and quantile regression splines. Journal of Experimental Marine Biology and Ecology, 366(1-2): 16–27

Borja A, Dauer D M, Díaz R, et al. 2008. Assessing estuarine benthic quality conditions in Chesapeake Bay: A comparison of three indices. Ecological Indicators, 8(4): 395–403

Borja Á, Dauer D M, Grémare A. 2012. The importance of setting targets and reference conditions in assessing marine ecosystem quality. Ecological Indicators, 12(1): 1–7

Borja A, Franco J, Perez V. 2000. A marine biotic index to establish the ecological quality of soft-bottom benthos within European estuarine and coastal environments. Marine Pollution Bulletin, 40(12): 1100–1114

Borja Á, Franco J, Valencia V, et al. 2004. Implementation of the European water framework directive from the Basque country (northern Spain): a methodological approach. Marine Pollution Bulletin, 48(3–4): 209–218

Borja A, Muxika H. 2005. Guidelines for the use of AMBI (AZTI's Marine Biotic Index) in the assessment of the benthic ecological quality. Marine Pollution Bulletin, 50(7): 787–789

Borja A, Tunberg B G. 2011. Assessing benthic health in stressed subtropical estuaries, eastern Florida, USA using AMBI and M-AMBI. Ecological Indicators, 11(2): 295–303

Briggs K B, Craig J K, Shivarudrappa S, et al. 2017. Macrobenthos and

megabenthos responses to long-term, large-scale hypoxia on the Louisiana continental shelf. Marine Environmental Research, 123: 38–52

Cai Wenqian, Borja A, Lin Kuixuan, et al. 2015. Assessing the benthic quality status of the Bohai Bay (China) with proposed modifications of M-AMBI. Acta Oceanologica Sinica, 34(10): 111–121

Cai Minggang, Liu Yan, Chen Kai, et al. 2016. Quantitative analysis of anthropogenic influences on coastal water—A new perspective. Ecological Indicators, 67: 673–683

Cai Wenqian, Liu Lusan, Qiao Fei, et al. 2012. Study on the changes of macrobenthos communities and their causes in Bohai Bay. Environmental Science (in Chinese), 33(9): 3104–3109

Cai Wenqian, Meng Wei, Liu Lusan, et al. 2013. Long-term trends of the dominant macrozoobenthos in Bohai Bay. Acta Scientiae Circumstantiae (in Chinese), 34(8): 2332–2340

Chen Yaqu, Xu Zhaoli, Wang Yunlong, et al. 1995. An ecologicl study on zooplankton in plume front zone of Changjiang (Yangtze) River estuarine area: I. Biomass distribution of dominant species. Journal of Fishery Sciences of China (in Chinese), 2(1): 49–58

Dauvin J C, Bellan G, Bellan-Santini D. 2010. Benthic indicators: From subjectivity to objectivity—Where is the line?. Marine Pollution Bulletin, 60(7): 947–953

Dolbeth M, Cardoso P G, Grilo T F, et al. 2011. Long-term changes in the production by estuarine macrobenthos affected by multiple stressors. Estuarine, Coastal and Shelf Science, 92(1): 10–18

Dolbeth M, Cardoso P G, Ferreira S M, et al. 2007. Anthropogenic and natural disturbance effects on a macrobenthic estuarine community over a 10-year period. Marine Pollution Bulletin, 54(5): 576–585

Dumbauld B R, Ruesink J L, Rumrill S S. 2009. The ecological role of bivalve shellfish aquaculture in the estuarine environment: A review with application to oyster and clam culture in West Coast (USA) estuaries. Aquaculture, 290(3–4): 196–223

Ekeroth N, Blomqvist S, Hall P O J. 2016. Nutrient fluxes from reduced Baltic Sea sediment: effects of oxygenation and macrobenthos. Marine Ecology Progress Series, 544: 77–92

Fabry J V, Seibel B A, Feely R A, et al. 2008. Impacts of ocean acidification on marine fauna and ecosystem processes. ICES Journal of Marine Science, 65(3): 414–432

Forchino A, Borja A, Brambilla F, et al. 2011. Evaluating the influence of off-shore cage aquaculture on the benthic ecosystem in Alghero Bay (Sardinia, Italy) using AMBI and M-AMBI. Ecological Indicators, 11(5): 1112–1122

Ge Changzi, Chai Yanchao, Wang Haiqing, et al. 2017. Ocean acidification: One potential driver of phosphorus eutrophication. Marine Pollution Bulletin, 115(1–2): 149–153

Gusmao J B, Brauko K M, Eriksson B K, et al. 2016. Functional diversity of macrobenthic assemblages decreases in response to sewage discharges. Ecological Indicators, 66: 65–75

Herman P M J, Middelburg J J, Van De Koppel J, et al. 1999. Ecology of estuarine macrobenthos. Advances in Ecological Research, 29: 195–240

Hu Guikun, Zhang Qingtian. 2016. Seasonal variations in macrobenthic taxonomic diversity and the application of taxonomic distinctness indices in Bohai Bay, northern China. Ecological Indicators, 71: 181–190

James C J, Gibson R. 1980. The distribution of the polychaete *Capitella capitata* (Fabricius) in dock sediments. Estuarine and Coastal Marine Science, 10(6): 671–683

Jia Yiran, Sun Yinglan, Sun Changqing. 2007. Argumentation of sewage discharge mixing zone's area of Xin'an River sewage plant of Yantai. Transactions of Oceanology and Limnology, (S1): 131–136

Jin Shaofei, Wang Yongli, Xia Jiangjiang, et al. 2015. Decline in the species richness contribution of Echinodermata to the macrobenthos in the shelf seas of China. Physics and Chemistry of the Earth, Parts A/B/C, 87-88: 43–49

Kawai M, Nagao N, Kawasaki N, et al. 2016. Improvement of COD removal by controlling the substrate degradability during the anaerobic digestion of recalcitrant wastewater. Journal of Environmental Management, 181: 838–846

Leng Yu, Liu Yiting, Zhao Sheng, et al. 2013. Analysis on the characteristics of macrobenthos community during autumn in the Yangma Island. The Administration and Technique of Environmental Monitoring (in Chinese), 25(3): 17–20

Li Xinzheng. 2011. An overview of studies on marine macrobenthic biodiversity from Chinese waters: principally from the Yellow Sea. Biodiversity Science (in Chinese), 19(6): 676–684

Li Baoquan, Wang Quanchao, Li Bingjun. 2013. Assessing the benthic ecological status in the stressed coastal waters of Yantai, Yellow Sea, using AMBI and M-AMBI. Marine Pollution Bulletin, 75(1–2): 53–61

Lillebø A I, Neto J M, Martins I, et al. 2005. Management of a shallow temperate estuary to control eutrophication: The effect of hydrodynamics on the system's nutrient loading. Estuarine, Coastal and Shelf Science, 65(4): 697–707

Liu Lusan, Li Baoquan, Lin Kuixuan, et al. 2014. Assessing benthic ecological status in coastal area near Changjiang River estuary using AMBI and M-AMBI. Chinese Journal of Oceanology and Limnology, 32(2): 290–305

Luo Xianxiang, Zhang Juan, Yang Jianqiang, et al. 2014. Assessing the benthic habitat quality in the Huanghe (Yellow River) Estuary and its adjacent areas using AMBI and M-AMBI. Acta Oceanologica Sinica, 33(9): 117–124

Ma Zhaohu, Wang Lei, Wang Dongliang, et al. 2012. Evaluation and analysis on the quality of the sea water adjacent to the Yantai Xin'an River Estuary. Ludong University Journal (Natural Science Edition) (in Chinese), 28(4): 364–369

Marques J C, Nielsen S N, Pardal M A, et al. 2003. Impact of eutrophication and river management within a framework of ecosystem theories. Ecological Modelling, 166(1–2): 147–168

Muxika I, Borja Á, Bald J. 2007. Using historical data, expert judgement and multivariate analysis in assessing reference conditions and benthic ecological status, according to the European Water Framework Directive. Marine Pollution Bulletin, 55(1–6): 16–29

Muxika I, Borja Á, Bonne W. 2005. The suitability of the marine biotic index (AMBI) to new impact sources along European coasts. Ecological Indicators, 5(1): 19–31

Paganelli D, Forni G, Marchini A, et al. 2011. Critical appraisal on the identification of reference conditions for the evaluation of ecological quality status along the Emilia-Romagna coast (Italy) using M-AMBI. Marine Pollution Bulletin, 62(8): 1725–1735

Peng Shitao, Zhou Ran, Qin Xuebo, et al. 2013. Application of macrobenthos functional groups to estimate the ecosystem health in a semi-enclosed bay. Marine Pollution Bulletin, 74(1): 302–310

Piló D, Ben-Hamadou R, Pereira F, et al. 2016. How functional traits of estuarine macrobenthic assemblages respond to metal contamination?. Ecological Indicators, 71: 645–659

Rakocinski C F, Menke D P. 2016. Seasonal hypoxia regulates macrobenthic function and structure in the Mississippi Bight. Marine Pollution Bulletin, 105(1): 299–309

Rombouts I, Beaugrand G, Artigas L F, et al. 2013. Evaluating marine ecosystem health: Case studies of indicators using direct observations and modelling methods. Ecological Indicators, 24: 353–365

Serrano L, Reina M, Quintana X D, et al. 2017. A new tool for the assessment of severe anthropogenic eutrophication in small shallow water bodies. Ecological Indicators, 76: 324–334

Shen Hui, Thrush S F, Wan Xihe, et al. 2016. Optimization of hard clams, polychaetes, physical disturbance and denitrifying bacteria of removing nutrients in marine sediment. Marine Pollution Bulletin, 110(1): 86–92

Sigamani S, Perumal M, Arumugam S, et al. 2015. AMBI indices and multivariate approach to assess the ecological health of Vellar-Coleroon estuarine system undergoing various human activities. Marine Pollution Bulletin, 100(1): 334–343

Smith C R, Austen M C, Boucher G, et al. 2000. Global change and biodiversity linkages across the sediment-water interface: hu-

man activities, modulated through global climate change, coastal-zone eutrophication, species introductions, mariculture, and bottom fishing, are expected to substantially influence biodiversity linkages across the sediment-water interface. BioScience, 50(12): 1108–1120

State Quality and Technical Supervision Administration. 1992. National Oceanography Census Regulation Methods. Beijing: Standards Press of China, 17–20

Sun Daoyuan, Chen Mu. 1978. Research on *Capitella capitata* as the biological indicator for organic pollution. Environmental Science (in Chinese), (1): 17–19

Tang Xianchun. 2011. Study on ecological functions of macrobenthos in Yantai Sishili Bay (in Chinese) [dissertation]. Beijing: Graduate School of Chinese Academy of Agricultural Sciences

Vaquer-Sunyer R, Duarte C M. 2008. Thresholds of hypoxia for marine biodiversity. Proc Natl Acad Sci USA, 105(40): 15452–15457

Volkenborn N, Hedtkamp S I C, Van Beusekom J E E, et al. 2007. Effects of bioturbation and bioirrigation by lugworms (*Arenicola marina*) on physical and chemical sediment properties and implications for intertidal habitat succession. Estuarine, Coastal and Shelf Science, 74(1–2): 331–343

Wallace R B, Baumann H, Grear J S, et al. 2014. Coastal ocean acidification: The other eutrophication problem. Estuarine, Coastal and Shelf Science, 148: 1–13

Wang Quanchao, Li Baoquan. 2013. Community structure of macrobenthos in coastal water off Yantai, East China. Oceanologia et Limnologia Sinica (in Chinese), 44(6): 1667–1680

Wang Xu'e, Xu Zongfa, Zhou Xuejia. 1995. Benthic animal survey in Yantai Inshores. Chinese Journal of Ecology (in Chinese), 14(1): 6–10

Webb A P, Eyre B D. 2004. Effect of natural populations of burrowing thalassinidean shrimp on sediment irrigation, benthic metabolism, nutrient fluxes and denitrification. Marine Ecology Progress Series, 268: 205–220

Wu Yaoquan, Zhang Bo. 1994. The characteristics of benthic environment in Zhifu Bay waters off Yantai, China. Marine Environmental Science (in Chinese), 13(3): 1–6

Xie Zhao, Zhang Jie, Cai Kun, et al. 2016. Temporal and spatial distribution of macrobenthos communities and their responses to environmental factors in Lake Taihu. Acta Ecologica Sinica, 36(1): 16–22

Zhang Wenqiang, Jin Xin, Zhu Xiaolei, et al. 2017. Do NH_3 and chemical oxygen demand induce continuous release of phosphorus from sediment in heavily polluted rivers?. Ecological Engineering, 102: 24–30

Zhang Jing, Xiao Tian, Huang Daji, et al. 2016a. Editorial: eutrophication and hypoxia and their impacts on the ecosystem of the Changjiang Estuary and adjacent coastal environment. Journal of Marine Systems, 154: 1–4

Zhang Anguo, Yuan Xiutang, Yang Xiaolong, et al. 2016b. Temporal and spatial distributions of intertidal macrobenthos in the sand flats of the Shuangtaizi Estuary, Bohai Sea in China. Acta Ecologica Sinica, 36(3): 172–179

Zhou H, Zhang Z N, Liu X S, et al. 2007. Changes in the shelf macrobenthic community over large temporal and spatial scales in the Bohai Sea, China. Journal of Marine Systems, 67(3–4): 312–321

Zhu Zhuoyi, Wu Ying, Zhang Jing, et al. 2014. Reconstruction of anthropogenic eutrophication in the region off the Changjiang Estuary and central Yellow Sea: From decades to centuries. Continental Shelf Research, 72: 152–162

Acta Oceanol. Sin., 2018, Vol. 37, No. 5, P. 87–95
DOI: 10.1007/s13131-018-1166-8
http://www.hyxb.org.cn
E-mail: hyxbe@263.net

Accelerated recruitment of copepod *Calanus hyperboreus* in pelagic slope waters of the western Arctic Ocean

XU Zhiqiang[1, 2], ZHANG Guangtao[1]*, SUN Song[1, 3]

[1] Jiaozhou Bay Marine Ecosystem Research Station, Institute of Oceanology, Chinese Academy of Sciences, Qingdao 266071, China

[2] University of Chinese Academy of Sciences, Beijing 100049, China

[3] Key Laboratory of Marine Ecology and Environmental Sciences, Institute of Oceanology, Chinese Academy of Sciences, Qingdao 266071, China

Received 29 February 2016; accepted 7 April 2016

Abstract

Shelf-basin advection is essential to subsistence of the Arctic copepod *Calanus hyperboreus* population in high basin area. Its abundance, population structure and body size in pelagic layer were investigated with samples collected over a large range in the western Arctic Ocean during summer 2003, to evaluate the geographical variation in recruitment pattern. *Calanus hyperboreus* was absent from the shallow areas of the Chukchi Sea and most abundant in the slope area between the Chukchi Sea and Chukchi Abyssal Plain (CS-slope). Total abundance varied between 1 110.0 and 5 815.0 ind./m^2 in the CS-slope area and ranged from 40.0 to 950.0 ind./m^2 in the other areas. Early stages (CI–IV) dominated in the CS-slope area, whereas CV and adult females were frequently recorded only in deep basin areas. Geographical difference of prosome length was most evident in CIII, with average ranging from 2.48 to 2.61 mm at the CS-slope stations and 2.16–2.37 mm at the others. Abundance of early developmental stages (CI–CIV) correlated positively with Chl *a* concentration, but negative correlation was observed in late stages (CV–adult). Our results indicated that *C. hyperboreus* can benefit from primary production increase through accelerated development in the first growth season and the productive CS-slope area is a potential source for slope-basin replenishment.

Key words: continental slope, prosome length, population structure, food availability, life cycle

Citation: Xu Zhiqiang, Zhang Guangtao, Sun Song. 2018. Accelerated recruitment of copepod *Calanus hyperboreus* in pelagic slope waters of the western Arctic Ocean. Acta Oceanologica Sinica, 37(5): 87–95, doi: 10.1007/s13131-018-1166-8

1 Introduction

Calanus hyperboreus is a large calanoid copepod widely distributed in the Arctic Ocean, accounting for a large proportion of the zooplankton biomass. In adaptation to the extreme polar environment, it has evolved capability of pre-bloom spawning fueled by lipid accumulation, diapausing at earlier copepodite stages and utilizing ice-algae as a food source (Smith and Schnack-Schiel, 1990; Hirche, 1997; Ji et al., 2012). However, based on evidences from population structure, grazing capacity and simulated development duration, populations of *C. hyperboreus* may still be not self-sustaining in the central Arctic Basin, but must be replenished by advection of individuals produced in the shallow and coastal regions (Rudyakov, 1983; Olli et al., 2007; Ji et al., 2012). High abundance of early copepodites (CI–CIV) had been frequently reported in shelf regions in the Atlantic sector, but it is uncertain whether shallow areas of the western Arctic Ocean can serve as possible origins, as *C. hyperboreus* was absent from some shelf waters such as the Chukchi Sea (Hopcroft et al., 2010).

Comparing to the central Arctic Basin, higher water temperature and longer growth season in shallow shelf regions lead to shorter life cycle and thus higher recruitment rate. Over its geographical distribution, *C. hyperboreus* developed flexible life history durations ranging from 1 to >4 years. In the first year, the new cohorts develop to copepodite Stage III (CIII) and accumulate energy for overwintering in deep layers (Conover, 1988). For the following years, they can overwinter further in Stages CIV, CV or CVI, depending on various development rates (Hirche, 1997). Annual life cycle was proposed only in warmer regions of the North Atlantic, such as the Gulf of Maine and Norwegian Sea (Conover, 1988). An at least 4-year life cycle was observed in the central Arctic Basin and other high latitude areas. Meanwhile, in the Greenland Sea shorter life cycle was observed in warm Westspitsbergen Current waters comparing to cold Greenland Sea Gyre waters (Hirche, 1997). Until now, there is no report on shortened life cycle duration of *C. hyperboreus* in the western part of the Arctic Ocean, as southern distribution into subarctic or shelf waters is not observed in this sector.

Furthermore, distribution and recruitment rates of *C. hyperboreus* can be influenced by food supply. Longer lifespan and higher egg production were observed in fed females than those starved in both laboratory incubations and natural environments (Conover, 1967; Hirche, 2013). In the North Water polynya and Barrow Strait area, recruitment success of early copepodites (CI–CIV) increased primarily with Chl *a* concentration for *C. hyperboreus*, and the availability of Chl *a* rather than temperature was suggested the factor triggering *Calanus* recruitment

Foundation item: The National Natural Science Foundation of China under contract No. 40406002; the Public Science and Technology Research Funds Projects of Ocean under contract No. 201105022.
*Corresponding author, E-mail: gtzhang@qdio.ac.cn

(Ringuette et al., 2002). On shelf-basin transects, elevated biomass of *C. hyperboreus* was observed in margin parts off the Laptev Sea with the recurrent polynya as a feeding hot spot for filter feeders (Kosobokova and Hirche, 2009).

In the western Arctic Ocean with significant geographical variation in primary production rate, elevated standing stocks of zooplankton had been recorded in the Chukchi Shelf areas receiving more nutrient-rich Pacific and fluvial waters (Grebmeier et al., 1995). Although the perennial northward current and shallow water depth prevent the arrival of *C. hyperboreus* into the Chukchi Sea, it can still reach the slope areas with high primary production. Thereafter, accelerated development elevated recruitment is expected. Moreover, this area has shown the largest changes in sea-ice coverage (Parkinson and Cavalieri, 2008) and massive under-ice phytoplankton bloom (Arrigo et al., 2012). Studies on the response of the predominant large calanoid copepods can favor the prediction of climate-induced effects on secondary production.

The objectives of our study include: (1) if the productive shelf region in the western Arctic Ocean can serve as a resource for advection to central basin; (2) how development of *C. hyperboreus* benefits from slope environments. Based on 43 zooplankton samples collected in pelagic layers from 37 stations in the Canada Basin, Chukchi Plateau, Chukchi Abyssal Plain and Chukchi Sea, distribution pattern of *C. hyperboreus* was defined. Its development regime was investigated with population structure and size frequency distribution of prosome length of CIII-adult. Their correlation with environment condition was statistically analyzed. Potential impact of global warming is also discussed, based on environmental preferences of this species.

2 Materials and methods

2.1 *Field observations*

The 2nd Chinese Arctic Research Expedition was carried out from 29 July to 7 September 2003 over a large area including the Chukchi Sea, Chukchi Abyssal Plain, Chukchi Plateau and Canada Basin (Fig. 1). Multi-disciplinary observation was carried out at 37 stations, with six of them (R06–14, P11) investigated twice (Table 1).

At each station, ice coverage was estimated by direct visual observation. Temperature and salinity were measured with a Mark III CTD. Water samples for Chl *a* concentration were collected with Niskin bottles at depths of 1, 10, 20, 30, 50, 75, 100, 150 and 200 m. A total of 250 mL of natural seawater was taken from each sample and filtered through Whatman GF/F filter. Each filter was extracted with 90% acetone for 24 h at 0°C and fluorescence was measured with a Model 10 Turner Designs fluorometer.

Quantitative zooplankton sampling was conducted at all stations with a conical net (mouth area 0.5 m^2; mesh size 330 μm). The net was hauled vertically from within 3 m of the bottom to the surface at 0.5 m/s at stations shallower than 200 m and from 200 m to surface at deep stations. Samples were preserved in buffered 5% formalin seawater.

2.2 *Sample counting and prosome length measurement*

In the laboratory, copepodite stage compositions were determined with the aid of a dissecting microscope according to morphological characters for *Calanus* species (Marshall and Orr, 1955; Li and Fang, 1990) and body size for *C. hyperboreus* (Hirche, 1997; Melle and Skjoldal, 1998). Integrate abundance of *C. hyperboreus* in the uppermost 200 m were here presented as individuals per m^2 (ind./m^2) taking into account the different sampling depth (Plourde et al., 2003; Ota et al., 2008; Thor et al., 2008; Broms et al., 2009). Prosome length, from the anterior end of the cephalosome to the posterior lateral edge of fifth metasome segments, was measured using a graticule in the microscope eyepiece. Prosome lengths measurement was carried out only for later stages with fully developed prosome somites and making up the vast majority of overwintering population. The

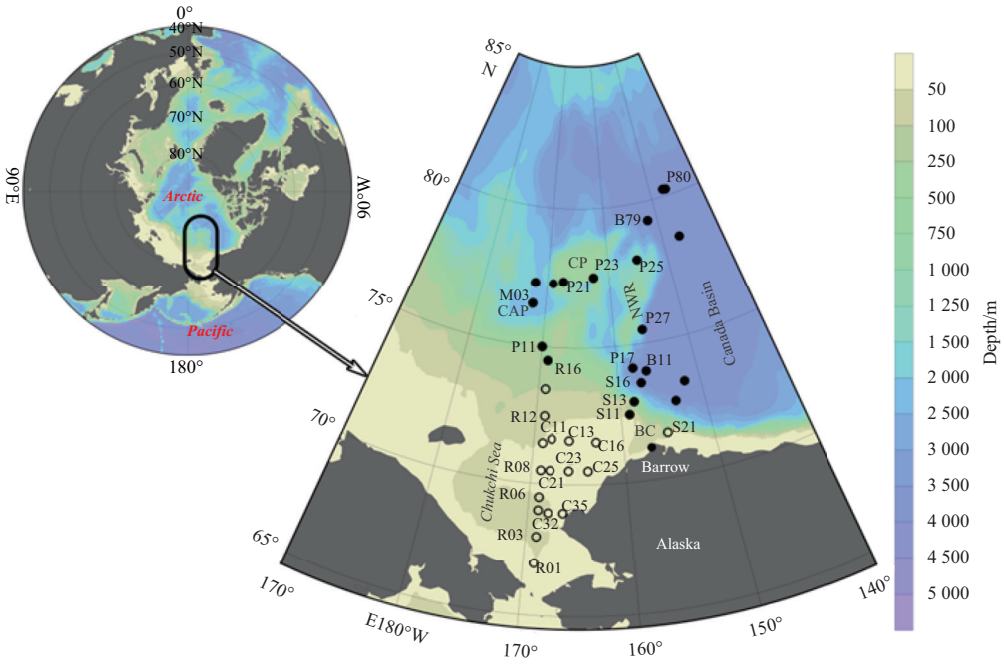

Fig. 1. Location of the study area and zooplankton sampling stations in the 2nd Chinese Arctic Research Expedition during 29 July to 7 September 2003 in the western Arctic Ocean. Black dots represent stations where *Calanus hyperboreus* was observed. Geographical locations are abbreviated as follows: BC, Barrow Canyon; CAP, Chukchi Abyssal Plain; CP, Chukchi Plateau; NWR, Northwind Ridge.

Table 1. Water depth (m), date and ice coverage (%) of all zooplankton stations in the 2nd Chinese Arctic Research Expedition during 29 July to 7 September 2003 in the western Arctic Ocean

Station	Depth/m	Date	Ice/%	Station	Depth/m	Date	Ice/%
R01	49	29 Jul.	0	R16	180	9 Aug.	50
R03	57	29 Jul.	0	P11	260	9 Aug.	60
R06	51	30 Jul.	0	P17	2 500	11 Aug.	20
R08	35	30 Jul.	0	B11	3 000	11 Aug.	20
R10	48	30 Jul.	0	B13	3 000	14 Aug.	50
R12	76	31 Jul.	5	S25	3 000	14 Aug.	20
R14	115	1 Aug.	80	S11	52	17 Aug.	20
C11	48	3 Aug.	50	S13	1 330	17 Aug.	10
C13	43	3 Aug.	10	S16	3 000	17 Aug.	5
C16	42	3 Aug.	80	P27	3 050	18 Aug.	50
S21	70	5 Aug.	20	B80	3 800	24 Aug.	95
C25	41	6 Aug.	0	P80	3 800	25 Aug.	95
C23	44	6 Aug.	0	B79	3 800	26 Aug.	20
C21	46	6 Aug.	0	B78	3 800	29 Aug.	95
C35	32	7 Aug.	0	P25	1 805	4 Sep.	80
C32	50	7 Aug.	0	P23	2 200	5 Sep.	70
R05	51	7 Aug.	0	P21	530	6 Sep.	70
R06-2	51	8 Aug.	0	M01	1 546	6 Sep.	50
R08-2	37	8 Aug.	0	M02	2 400	6 Sep.	60
R10-2	51	8 Aug.	0	M03	2 400	7 Sep.	80
R12-2	75	8 Aug.	0	P11-2	250	7 Sep.	20
R14-2	118	9 Aug.	50				

Note: Repeat samplings at same stations was marked by the suffix "-2".

original sample was divided with plankton sample splitter, and at least 10% of that was counted for population structure and abundance. For prosome length measurements, no more than 150 individuals from each stage were measured at each station.

2.3 *Data analysis*

In the present study, hydrological conditions and Chl *a* concentrations were shown in detail only at those stations with *C. hyperboreus* present. In order to check the possible overlap of cohorts with different geographical and temporal origins, normality of size frequency distribution was checked with one-sample Kolmogorov-Smirnov Test on all measured stages from each station and the entire investigation, respectively. Significance of influence from food availability and temperature was analyzed with Spearman rank correlation on abundance and proportion of each stage, as well as average prosome length of CIII-adult. As diel vertical migration was unknown, food availability was analyzed in terms of column averaged and maximum Chl *a* concentration, respectively. Their correlation with temperature was tested as both column average and surface value. All the statistics were run with software SPSS 16.0.

The relationships between abundances of each development stage and environmental variables were examined with Canonical Correspondence Analysis (CCA) on software CANOCO 4.5. After test of the length of gradients with Detrended Correspondence Analysis, CCA was performed on log transformed data. The significance of environmental variables to explain the variance of abundances in CCA was tested using forward selection of Monte Carlo simulations.

3 Results

3.1 *Environmental conditions*

This investigation covered a large area varying from ice-free shallow neritic to fast ice-cover deep basin areas. *Calanus hyperboreus* was presented at all stations deeper than 200 m, but was absent from all shallow stations except Stas R16 and S11 close to the basin (Fig. 1). Ice coverage at stations with *C. hyperboreus* occurrence varied from 10% to 95%. The highest ice coverage was observed at 80°N stations, where sampling was conducted in narrow polynias surrounded by thick sea ice. Ice coverage was lowest in the slope area near Barrow, Alaska. Sea ice retreat was observed at duplicated stations. At Sta. P11, ice coverage decreased from 65% on 9 August to 20% on 7 September (Table 1).

Temperature-salinity characteristics identified various hydrographic regimes among stations where *C. hyperboreus* was observed. Warm high-salinity water (S>34, T>–1.0°C) was observed in 150–200 m layer at stations in the north Canada Basin and Chukchi Plateau, as well as Stas P11 and R16 in the slope area between the Chukchi Sea and Chukchi Abyssal Plain (CS-slope), but absent at stations in the south Canada Basin and slope areas (Fig. 2). Salinity higher than 34.5 was observed only at 200 m depth at Sta. P11, where temperature was also as high as 0.25°C. At the adjacent Sta. R16, temperature and salinity were –0.53°C and 34.3 respectively. At all stations, surface temperature varied between –1.56 (M03) and –0.56°C (S16), and surface salinity varied between 27.56 (B13) and 29.86 (B80 and P80). High sub-surface temperature (>0°C) was detected only at Stas S25 and P27 in the south Canada Basin. Halocline was commonly observed at all stations in 30–60 m layers.

Chl *a* concentration was high and more variable above 100 m depth, and lower than 0.10 μg/L at all stations under 100 m depth (Fig. 2). At the northernmost Stas P80 and B80 with highest ice coverage, Chl *a* concentration was highest (0.21 and 0.23 μg/L) in surface layer, whereas sub-surface maximum was observed at the other stations. Extremely high concentrations of 8.60 and 39.10 μg/L were observed at 20 m and 30 m depth at Stas R16 and S11, respectively. Except these two stations, the maximum Chl *a* con-

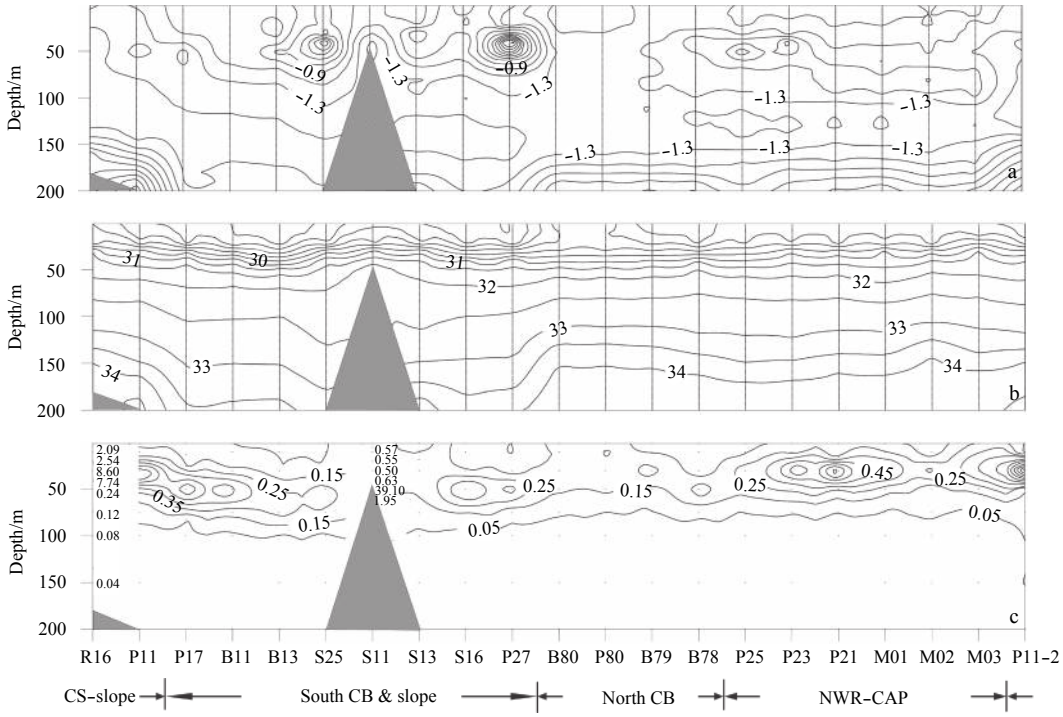

Fig. 2. Isolines of water temperature (°C, a), salinity (b) and Chl *a* concentration (μg/L, c) in the upper 200 m at stations in the western Arctic Ocean with *Calanus hyperboreus* observed. Extremely high Chl *a* concentration was shown as the exact value and not included in the contour procedure. Geographical regions were list below stations in abbreviation: CS-slope, slope between Chukchi Sea and Chukchi Abyssal Plain; South CB & slope, south Canada Basin and slope area; North CB, north Canada Basin; NWR-CAP, transect from Northwind Ridge to Chukchi Abyssal Plain. Water depth shallower than 200 m was shown by shadow triangles.

centration through the water column was highest at Sta. P11, where concentrations of 1.16 and 1.28 μg/L were recorded at 30 m depth during the duplicated observations.

3.2 *Abundance and population structure*

In our study, *C. hyperboreus* was observed in 21 samples collected from 20 stations located mainly in deep basin and adjacent slope areas (Fig. 1). *Calanus hyperboreus* is able to reach the south edge of the Chukchi Abyssal Plain and Canada Basin respectively, but its abundance in these two areas differed by 1–2 orders of magnitudes. At Sta. P11, total abundance of *C. hyperboreus* was 5 815.0 ind./m^2 in August and 5 475.0 ind./m^2 in September, and abundance of 1 110.0 ind./m^2 was observed at the nearby Sta. R16 (Fig. 3). At the other stations, their abundance was no higher than 950.0 ind./m^2. The lowest abundance of 55.0 and 40.0 ind./m^2 was observed at Stas P27 and P25, respectively. At shallow Stas S11 and S13 near the Canada Basin, total abundance was also lower than 100 ind./m^2.

Based on the population structure, late stages including CV and adult females were frequently recorded at deep high-latitude stations (B11, B13, S13, S16, S25 and P25), but populations at shallow slope stations overwhelmingly consisted of early stages (CI–CIV). In samples from Stas R16, P11 and P11-2, CV and AF (adult females) were extremely scarce, and the highest proportion was observed in CIII and CI. Meanwhile, at shallow stations in the Canada Basin, the population completely consisted of CII and CIV at Sta. S11 and CV at Sta. S13. At stations deeper than 1 000 m, the proportion of CV and females ranged from 27.6% to 86.8% and averaged at 59.8%. In the southern Canada Basin, CV and females accounted for proportions higher than 80% at central stations (S25, S16, B11 and B13) and higher than 50% at stations near the Northwind Ridge (P17 and P27). Well-proportioned population structure was observed at the four northernmost stations (B78, B79, B80 and P80), whereas dramatic change was recorded along the transect from the Northwind Ridge to the Chukchi Abyssal Plain. Population at Sta. P25 was comprised of completely CV and adult females, but CIII accounted for the highest proportion at the other four stations (P23, P21, M01 and M02). Population structure also differed between the repeated observations at Sta. P11. The proportions of CI, CII, and CIV increased from 6.0%, 12.5%, and 9.0% on 9 August to 34.9%, 24.0%, and 28.8% on 7 September, whereas that of CIII decreased from 71.4% to 12.3%.

In early stages (CI–CIV), abundance and proportion increased with Chl *a* concentration, showing significant positive correlation between abundance of CIII–IV and proportion of CIV and Chl *a* concentration (Table 2). Significant negative correlation was observed in CV and AF. Both abundance and proportion correlated more significantly with column maximum Chl *a* concentration than with column average Chl *a* concentration.

3.3 *Size distribution*

Geographical variation in prosome length differed among the four measured stages (Fig. 4). In Stage CIII, average prosome length was highest at Sta. R16 (2.61 mm), followed by 2.53 mm at Sta. P11 and 2.48 at Sta. P11-2. According to 95% confidential interval in Fig. 4, prosome length at the above three stations was significantly higher than that from any other stations. The difference of average prosome length between the maximum and minimum station was largest in CIII (1.21 mm), followed by 1.10 mm in CV. The ratios in CIV and adult female were 1.06 and 1.04 mm, respectively. Comparatively high prosome length was observed at same stations also in CIV and CV with less significant difference. Female prosome length was highest at Sta. M02. Signific-

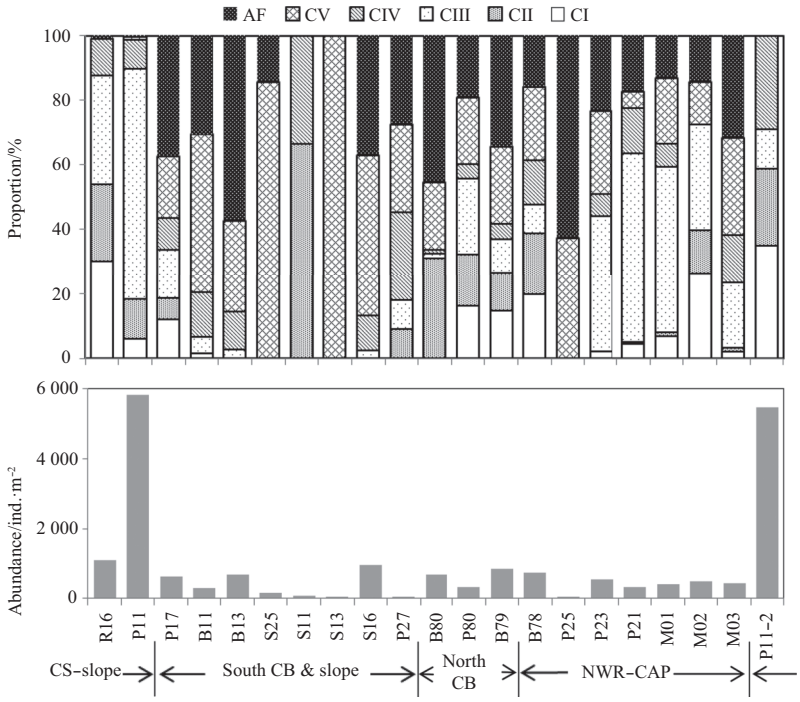

Fig. 3. Total abundance and proportion of each development stages of *Calanus hyperboreus* (AF, adult female) in the western Arctic Ocean, with geographical regions shown in same abbreviations with Fig. 2.

Table 2. Spearman's rank correlation coefficient (r_s) between column average (Ave.) and maximum (Max.) Chl *a* concentrations and abundance, proportion, and average prosome length of each development stage of *Calanus hyperboreus* from various samples (N) in the western Arctic Ocean during 29 July to 7 September

Stage	Abundance				Proportion				Prosome length			
	Ave.		Max.		Ave.		Max.		Ave.		Max.	
	r_s	N	r_s	N	r_s	N	r_s	N	r_s	N	r_s	N
CI	0.220	21	0.306	21	0.157	21	0.211	21	–	–	–	–
CII	0.171	21	0.179	21	0.193	21	0.155	21	–	–	–	–
CIII	0.463*	21	0.497*	21	0.384	21	0.390	21	0.441	18	0.534*	18
CIV	0.391	21	0.485*	21	0.414	21	0.519*	21	0.067	18	0.260	18
CV	–0.532*	21	–0.557**	21	–0.522*	21	–0.546*	21	0.414	19	0.520*	19
AF	-0.427	21	–0.441*	21	–0.537*	21	–0.442*	21	–0.051	19	–0.121	19

Note: ** Significant at the 0.01 level (2-tailed); * significant at the 0.05 level (2-tailed).

ant correlation between average prosome length at each station and Chl *a* concentration was detected only in CIII and CV (Table 2), in which average prosome length increased with maximum Chl *a* concentration.

According to one-sample Kolmogorov-Smirnov Test, normality was accepted for each developmental stage from all stations (P>0.05; Table 3), except CIV at Sta. P11-2 (P<0.05). However, normality was rejected for all the measured developmental stages as a whole, and asynchronous recruitment in various regions was accepted. The frequency distribution was positively skewed for CIII and negatively skewed for the other stages, indicating that asynchrony in newborns may be resulted from accelerated growth in some individuals and that in overwintered stages was induced by retarded development. The absolute values of skewness increased from CIV to AF, showing that individuals shorter than mode size increased in number with age.

3.4 *Canonical correspondence analysis*

The two first axes in CCA, with eigenvalues of 0.085 and 0.018, explained a total of 20.1% of cumulative variance in abundance data, and 98.2% of the correlations between environmental variables and abundance. After forward selection, four variables (in descending order, average Chl *a* concentration, surface temperature, ice coverage and surface salinity) played significant role (P<0.05) on the geographical distribution of each development stage. Based on the intersect correlations, Chl *a* and salinity were largely related to the first axis, while temperature and ice coverage were respectively positively and negatively related to the second axis.

With regard to the ordination (Fig. 5), environmental conditions were less variable at deep basal stations comparing to shelf stations. Most of the basal stations located near the ice coverage arrow, whereas scattered distribution was observed on the CS-slope stations. Abundance of each development stage was associated mainly with Chl *a* concentration, with CI and CII at higher but CV and female at lower value.

4 Discussion

Although *C. hyperboreus* is absent from shelf waters of the

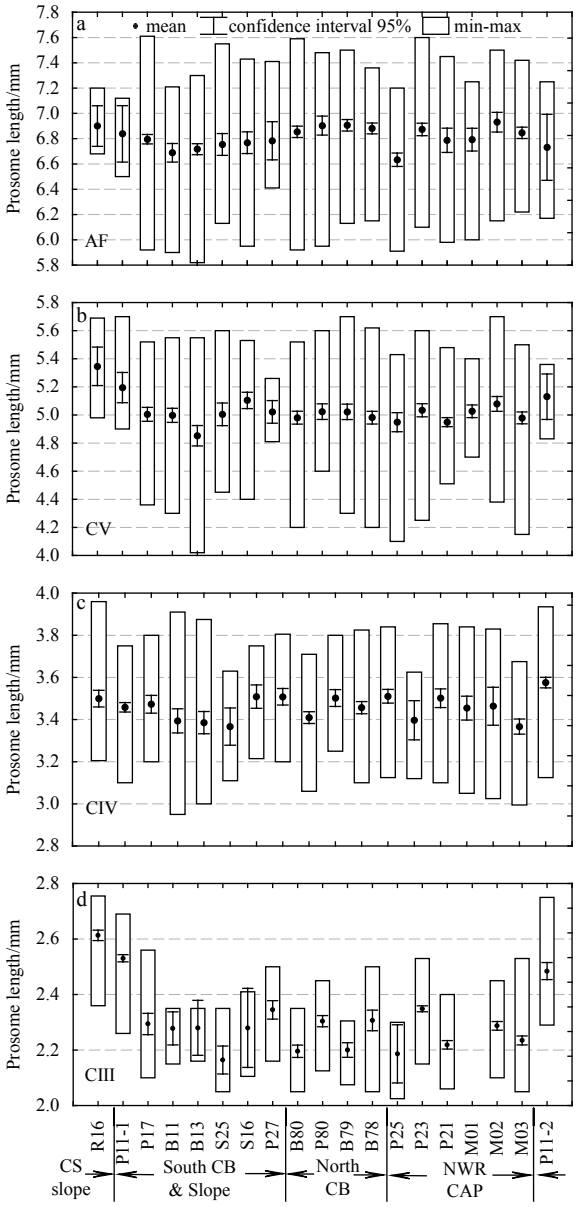

Fig. 4. Geographical variation in prosome length of *C. hyperboreus* in late Stages CIII, CIV, CV and adult female (AF), shown by average, range and 95% confidential intervals at each station. Geographical regions were shown in same abbreviations with Fig. 2.

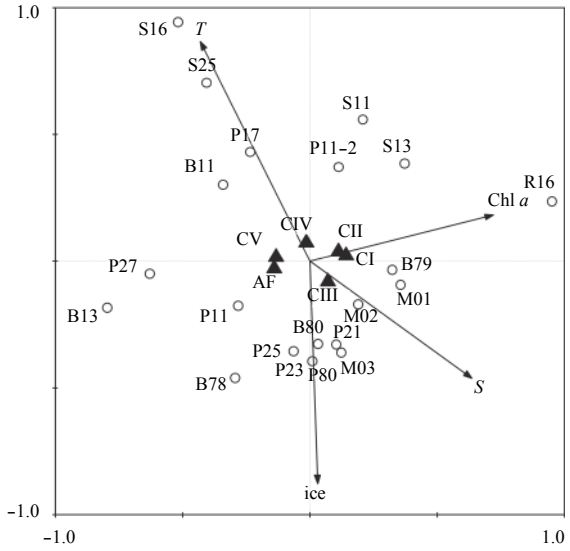

Fig. 5. Ordination diagram of canonical correspondence analysis showing abundance of each development stage (triangle) and selected environmental variables (arrows) at sampling stations (circle). Chl *a* represents average Chl *a* concentration, *S* surface salinity, *T* surface water temperature, and Ice ice coverage.

Chukchi Sea, we find that the slope area between the Chukchi Sea and Chukchi Abyssal Plain (CS-slope) was a hotspot for population development. As outlined in the introduction, shorter life cycle and high recruitment rate were expected in shelf waters with high food availability. Here we first assess variation in life cycle through geographical distribution, population structure and body size, and subsequently consider the possibility of slope-basin advection.

4.1 *Accelerated development in slope area*

The most important finding in our study is that CIV can be achieved in one growing season in the productive CS-slope area. In the multi-year life cycle of *C. hyperboreus*, it was commonly accepted that CIII is attained in the first year and descended to the deep layer as the main overwintering stage (Hirche, 1997). Most of the overwintered CIIIs molted to CIV from May to July in the next year (Dawson, 1978; Hirche, 1997). At the SHEBA station, which drifted from the Canada Basin over the Northwind Ridge and Chukchi Plateau and back over the basin, average prosome length of CIII was highest in May, the claimed molting season for overwintered individuals (Ashjian et al., 2003), but it was still lower than that in CS-slope area in our study. In our study, an overwhelming majority of CIIIs in CS-slope area were larger than the median of its size range in previous reports (Table 4). Meanwhile, at the other stations, prosome length of most CIIIs were shorter than the median of reported size range, and on average shorter than the station specific minimum at SHEBA station. We suggest that, only in CS-slope area, CIII can reach molting size in August of the first growing season.

According to temporal variation at the same sampling site from August (Sta. P11) to September (P11-2), molting from CIII to CIV was suggested during this period, as both abundance and proportion decreased in CIII but increased in CIV. Simultaneously, prosome length of CIII decreased on average, the same as the SHEBA station results. Normality was not significant for size frequency distribution of CIV at Sta. P11-2, indicating overlap of different cohorts. In the Resolute Passage (Conover, 1988) and Barrow Strait (Conover and Siferd, 1993), CIV had been recorded as the dominant overwintering stage, although its achievement in one growing season was still doubted. However, its further development to CV was suggested occurring separately in early spring and summer (Conover and Siferd, 1993), showing that the overwintered CIVs contained cohorts with different temporal origin. Thus, at least a part of the newborns of *C. hyperboreus* can develop to CIV before winter in the shelf waters of the western Arctic Ocean.

In previous studies carried out in semi-closed coastal regions, no marked temporal pattern was observed in prosome length of *C. hyperboreus* in Stages CIII–CV during the bloom period, and its somatic growth was detected mainly as an increase in dry weight or carbon content (Plourde et al., 2003; Swalethorp et al., 2011).

Table 3. Normality test on frequency distribution of *Calanus hyperboreus* prosome length, calculated with one-sample Kolmogorov-Smirnov Test

Station	CIII		CIV		CV		AF	
	N	A.S.	*N*	A.S.	*N*	A.S.	*N*	A.S.
R16	92	**0.11**	60	**0.73**	11	**0.97**	9	**0.89**
P11	129	**0.17**	124	**0.42**	20	**0.36**	6	**1**
P17	36	**0.43**	50	**0.92**	122	**0.73**	219	**0.09**
B11	8	**0.72**	42	**0.64**	106	**0.56**	80	**0.32**
B13	5	**0.92**	45	**0.61**	77	**0.85**	180	**0.23**
S25	13	**0.84**	15	**0.98**	51	**0.96**	41	**0.79**
S13	12	**0.95**	6	**0.99**	11	**1**	10	**0.67**
S16	6	**0.83**	26	**0.89**	77	**0.49**	66	**0.7**
P27	28	**0.93**	44	**0.35**	13	**0.92**	14	**0.45**
B80	40	**0.56**	122	**0.44**	92	**0.69**	164	**0.08**
P80	55	**0.82**	53	**0.59**	61	**0.77**	68	**0.96**
P79	26	**0.89**	124	**0.35**	82	**0.76**	149	**0.13**
P78	33	**0.77**	87	**0.12**	102	**0.57**	126	**0.14**
P25	7	**0.91**	14	**1**	58	**0.64**	102	**0.96**
P23	140	**0.09**	43	**0.82**	89	**0.57**	109	**0.23**
P21	106	**0.31**	33	**0.62**	119	**0.59**	50	**0.59**
M01	–	–	–	–	53	**0.79**	45	**0.35**
M02	106	**0.10**	21	**0.89**	73	**0.94**	56	**0.81**
M03	129	**0.06**	74	**0.93**	140	**0.07**	113	**0.43**
P11-2	59	**0.23**	149	0.04	7	**1**	10	**0.99**
Total	1 018	0	1 126	0.01	1 126	0	1 607	0

Note: *N* represents number of measured individuals from each developmental stages, and normal distribution was identified by A.S. (asymptotic significance) greater than 0.05 (boldface).

Table 4. Comparison of individual and station average prosome length (PL) of *Calanus hyperboreus* from previous reports and our study in the western Arctic Ocean during 29 July to 7 September 2003

Location	Data type	Time	Range of PL/mm			
			CIII	CIV	CV	AF
LSLE	individual	main and post bloom period	no data	3.0–3.8	4.0–5.2	5.0–6.5
GSG & WSC	individual	Feb.–Dec.	2.0–3.0	2.9–4.1	4.2–5.8	5.9–7.4
WAO	average	Feb.–Oct.	2.42–2.60	3.49–3.71	5.02–5.09	6.62–6.90
Our study	individual	Jul.–Sep.	2.00–2.75	2.80–3.95	4.00–5.60	5.90–7.50
	average		2.16–2.61	3.37–3.58	4.85–5.35	6.63–6.93

Note: LSLE represents the lower St. Lawrence Estuary (Plourde et al., 2003), GSG & WSC the central Greenland Sea Gyre and the West Spitsbergen Current (Hirche, 1997), and WAO the western Arctic Ocean (Ashjian et al., 2003).

However, according to our results, the prosome length achieved in various regions might increase with local food availability. Significant correlation between prosome length and Chl *a* concentration was observed in both CIII (the new-born generation) and CV (the overwintered population). Additionally, prosome length of CIV increased significantly from August to September at the same Sta. P11. Thus, its somatic growth pattern may change with various environmental conditions. In the Barrow Strait, less lipid storage was recorded in CIII and CIV, but they can still successfully overwinter along with the lipid-rich CV stages (Conover and Siferd, 1993).

The recorded abundance of early stages (CI–CIV) in CS-slope area was as high as that observed in other shallow Arctic areas (Hirche et al., 1994; Hirche, 1997; Swalethorp et al., 2011). Cross shelf abundance gradients of *C. hyperboreus* have been observed along the margins of the deep Nansen, Amundsen and Makarov Basins, and an elevated biomass was observed in the margin off the Laptev Sea (Kosobokova and Hirche, 2009). It was indicated that, though *C. hyperboreus* is absent from shallow shelf areas of the western Arctic Ocean, the CS-slope area can serve as a hotspot of population recruitment, through acceleration in both development and recruitment rates.

4.2 *Food-dependent development*

Food limitation to *C. hyperboreus* was commonly observed in natural environments. Estimated *in situ* grazing rates for the large copepod species were less than 10% of their maximum rates in a melt water influenced Greenlandic fjord (Tang et al., 2011) and *in situ* rates for *C. hyperboreus* and *C. glacialis* in the central Arctic Ocean were only about 3% and 20% of the expected food-saturated ingestion rates (Olli et al., 2007). However, *C. hyperboreus* has great potentiality to take advantage of the elevated food supply, as non-selective and non-saturated feeding was observed. It removed all types of phytoplankton in direct proportion to their abundance at Chl *a* concentrations ranging from 0.53 to 12.1 mg/m^3 (Huntley, 1981). Thus, recruitment success in early copepodites (CI–CIV) of *C. hyperboreus* increased primarily with food availability once the recruitment had started (Ringuette et al., 2002).

In the western Arctic Ocean, alleviated primary production

was induced mainly by intrusion of nutrient-rich pacific water (Nishino et al., 2008). However, in agreement with previous report (Hopcroft et al., 2010), *C. hyperboreus* cannot arrive the productive shelf waters of the Chukchi Sea. High food availability is also expected in the CS-slope area, as mesoscale eddies can bring episodic pulses of nutrients into the euphotic zone. During an investigation on a warm-core eddy in the southwestern Canada Basin, 30% higher biomass of pico-phytoplankton was sustained than in the surrounding water (Nishino et al., 2011). In another study, elevated concentrations of most zooplankton taxa were observed in eddies (Llinás et al., 2009). Though Chl *a* concentration at Sta. P11 was low on average, subsurface maximum was observed in both August and September, indicating high food availability.

Besides higher Chl *a* concentration in the CS-slope area, earlier onset of spring bloom may also contribute to the flexible life cycle. Under-ice phytoplankton blooms were observed widely in polar regions, including the Canadian Beaufort Sea and north part of Chukchi Sea (Mundy et al., 2009; Arrigo et al., 2012). Spawning of *C. hyperboreus* is fueled by lipid storage; the spring ascent was prior to or in association with the break-up of sea ice and the development of the spring phytoplankton bloom (Madsen et al., 2001). In the eastern sector of the North Water, the recruitment of the first cohort of copepodites of *C. hyperboreus* coincided with the onset of the bloom and occurred before any significant increase in temperature (Ringuette et al., 2002).

As our investigation was carried out in summer, positive correlation between abundance and Chl *a* concentration and accelerated development were observed mainly in CIII. Reproduction of *C. hyperboreus* starts before May, and most of the new generation has developed to CIII in August, so that correlation between abundance and Chl *a* concentration was not significant in CI and CII. Besides simultaneous food availability, body size and abundance of late stages (CIV-adult) can be influenced by conditions in the past growing seasons and physical advection. Well-developed individuals can be transported from productive shelf waters to barren basin areas, but we still cannot explain the significant negative correlation in CV.

4.3 *Possibility of slope-basin advection*

The mismatch between distribution centers of early (CI–IV) and late (CV–adult) stages demonstrates the importance of advection processes to population recruitment of *C. hyperboreus*. Prevalence of late stages (CV–adult) had been observed in the central Arctic Basin, the Norwegian Sea and the Chukchi Plateau (Rudyakov, 1983; Ashjian et al., 2003; Broms et al., 2009). Accordingly, different hypotheses of cross shelf-basin replenishment and insufficient sampling of individuals beneath the ice were put forward as explanations. As our investigation was carried out in August and September and significant ice melting was observed at most stations, underestimation of nauplii and early copepodites was unlikely. According to the reported reproduction season, *C. hyperboreus* spawns from January to May in the central Arctic Ocean (Brodskii and Nikitin, 1955; Johnson, 1963), and CII was commonly observed in the basin area after July (Ashjian et al., 2003). It was also suggested by numerical simulation that some of the new cohort cannot develop to CIII in one growing season (Ji et al., 2012). Considering the shorter prosome length, the early stages observed in the high latitude area in our study might be recruited locally, but the abundance of CIII was much lower than that of CIV–AF. On the other hand, net emigration was indicated by high abundance of early stages and scarcity of late ones in the CS-slope area. Thereafter, it is more likely that the *C. hyperboreus* population in the high latitude area is at least partially replenished by advection, and the CS-slope area may be an important potential source.

As early generations can be advected into deep water by the offshore current, backward supplement may also play an important role in the slope-basin interaction, as the CS-slope area tends to be an unfavorable overwintering site for *C. hyperboreus*. In previous reports, copepodite stages later than CIII were observed only at deeper than 300 m in winter, whereas both early and late stages entered upper layers in summer (Hirche, 1997; Ashjian et al., 2003). The two CS-slope stations with high early stage abundance observed in our study are shallower than 300 m. In our results, adult female were extremely scarce at Stas R16 and P11, and their prosome length showed no significant difference with basin stations.

According to previous reports on current regimes, advection between the central Arctic basin and CS-slope area is possible on both back and forth directions. Currents in deep areas in the western Arctic Ocean, such as the Barents Sea Branches of the Arctic Circumpolar Boundary Current flowing continuously along the Siberian Shelf, can reach as far as the Chukchi Plateau (Aksenov et al., 2011). Meanwhile, *C. hyperboreus* can be transported from overwintering depths in the deep basin to the Chukchi Shelf by upwelling (Lane et al., 2008; Llinás et al., 2009). Elevated abundances of Arctic-origin copepods, including *C. hyperboreus*, were recorded in a cold-core eddy in slope area between the Beaufort Sea and Chukchi Sea in summer (Llinás et al., 2009), even though most such eddies probably originated from the edges of the Chukchi and Beaufort shelves and contained water of Pacific origin (Muench et al., 2000). In our study, deep water with higher temperature and salinity reached shallower depth in the northern Chukchi Sea, indicating upwelling of deep waters. On the other hand, its absence in slope area between the Beaufort Sea and Chukchi Sea may be a reason for scarcity of *C. hyperboreus*. Shelfbreak eddies in the western Arctic Ocean last from weeks to more than a year before moving from the Chukchi Shelf into the interior Canada Basin (Manley and Hunkins, 1985), which can act as a possible pathway carrying *C. hyperboreus* from CS-slope into central basin.

Although this is the first time that early stages (CI–CIV) of *C. hyperboreus* was recorded in high abundance in the CS-slope area, its prosperity is always expected whenever overwintered cohort was transported into productive regions influenced by the Pacific waters. In previous studies, both intrusion of *C. hyperboreus* and elevated primary production had been recorded separately in slope regions in the western Arctic Ocean (Llinás et al., 2009; Nishino et al., 2011). Along the margins of the deep Nansen, Amundsen and Makarov Basins, the Arctic Ocean Boundary Current can transport the Atlantic pelagic copepod population into the Siberian shelf waters, where its abundance was further elevated by higher food availability (Kosobokova and Hirche, 2009). Furthermore, based on food-dependent development, accelerated population recruitment was expected in any other regions with elevated primary production or reduced ice coverage, supporting an increase in biomass of *C. hyperboreus* even in the Canada Basin with low phytoplankton biomass through advection (Hunt et al., 2014).

Acknowledgements

The authors thank all team members of the CHINARE-2003 for their help on field sampling, Shi Jiuxin from the Ocean University of China for CTD data, and Liu Zilin from the Second Institute of Oceanography, SOA for Chl *a* concentration data.

References

Aksenov Y, Ivanov V V, Nurser A J G, et al. 2011. The arctic circumpolar boundary current. J Geophys Res, 116(C9): C09017

Arrigo K R, Perovich D K, Pickart R S, et al. 2012. Massive phytoplankton blooms under arctic sea ice. Science, 336(6087): 1408

Ashjian C J, Campbell R G, Welch H E, et al. 2003. Annual cycle in abundance, distribution, and size in relation to hydrography of important copepod species in the western Arctic Ocean. Deep Sea Res Part I Oceanogr Res Pap, 50(10–11): 1235–1261

Brodskii K A, Nikitin M N. 1955. Hydrobiological work. In: Observational Data of the Scientific Research Drifting Station of 1950–1951. Vol 1. Massachusetts: American Meteorological Society, 404–410

Broms C, Melle W, Kaartvedt S. 2009. Oceanic distribution and life cycle of *Calanus* species in the Norwegian Sea and adjacent waters. Deep Sea Res Part II Top Stud Oceanogr, 56(21–22): 1910–1921

Conover R J. 1967. Reproductive cycle, early development, and fecundity in laboratory populations of the copepod *Calanus hyperboreus*. Crustaceana, 13(1): 61–72

Conover R J. 1988. Comparative life histories in the genera *Calanus* and *Neocalanus* in high latitudes of the northern hemisphere. In: Boxshall G A, Schminke H K, eds. Biology of Copepods. Dordrecht: Springer, 127–142

Conover R J, Siferd T D. 1993. Dark-season survival strategies of coastal zone zooplankton in the Canadian Arctic. Arctic, 46(4): 303–311

Dawson J K. 1978. Vertical distribution of Calanus hyperboreus in the central Arctic Ocean. Limnol Oceanogr, 23(5): 950–957

Grebmeier J M, Smith W O Jr, Conover R J. 1995. Biological processes on Arctic continental shelves: ice-ocean-biotic interactions. In: Smith W O, Grebmeir J M, eds. Arctic Oceanography: Marginal Ice Zones and Continental Shelves. Washington DC: American Geophysical Union, 231–262

Hirche H J. 1997. Life cycle of the copepod *Calanus hyperboreus* in the Greenland Sea. Mar Biol, 128(4): 607–618

Hirche H J. 2013. Long-term experiments on lifespan, reproductive activity and timing of reproduction in the Arctic copepod *Calanus hyperboreus*. Mar Biol, 160(9): 2469–2481

Hirche H J, Hagen W, Mumm N, et al. 1994. The northeast water polynya, Greenland Sea: III. Meso- and macrozooplankton distribution and production of dominant herbivorous copepods during spring. Polar Biol, 14(7): 491–503

Hopcroft R R, Kosobokova K N, Pinchuk A I. 2010. Zooplankton community patterns in the Chukchi Sea during summer 2004. Deep Sea Res Part II Top Stud Oceanogr, 57(1–2): 27–39

Hunt B P V, Nelson R J, Williams B, et al. 2014. Zooplankton community structure and dynamics in the Arctic Canada basin during a period of intense environmental change (2004–2009). J Geophys Res, 119(4): 2518–2538

Huntley M. 1981. Nonselective, nonsaturated feeding by three calanid copepod species in the Labrador Sea. Limnol Oceanogr, 26(5): 831–842

Ji Rubao, Ashjian C J, Campbell R G, et al. 2012. Life history and biogeography of *Calanus* copepods in the Arctic Ocean: an individual-based modeling study. Prog Oceanogr, 96(1): 40–56

Johnson M W. 1963. Zooplankton collections from the high polar basin with special reference to the Copepoda. Limnol Oceanogr, 8(1): 89–102

Kosobokova K, Hirche H J. 2009. Biomass of zooplankton in the eastern Arctic Ocean—A base line study. Prog Oceanogr, 82(4): 265–280

Lane P V Z, Llinás L, Smith S L, et al. 2008. Zooplankton distribution in the western Arctic during summer 2002: hydrographic habitats and implications for food chain dynamics. J Mar Syst, 70(1–2): 97–133

Li Song, Fang Jinchuan. 1990. Copepodites of Planktonic Copepod in China Seas (in Chinese). Bejing: China Ocean Press

Llinás L, Pickart R S, Mathis J T, et al. 2009. Zooplankton inside an Arctic Ocean cold-core eddy: probable origin and fate. Deep Sea Res II Top Stud Oceanogr, 56(17): 1290–1304

Madsen S D, Nielson T G, Hansen B W. 2001. Annual population development and production by *Calanus finmarchicus*, *C. glacialis* and *C. hyperboreus* in Disko Bay, western Greenland. Mar Biol, 139(1): 75–93

Manley T O, Hunkins K. 1985. Mesoscale eddies of the Arctic Ocean. J Geophys Res, 90(C3): 4911–4930

Marshall S M, Orr A P. 1955. The Biology of a Marine Copepod *Calanus finmarchicus* (Gunnerus). Edinburgh: Oliver and Boyd, 1–195

Melle W, Skjoldal H R. 1998. Reproduction and development of *Calanus finmarchicus*, *C. glacialis* and *C. hyperboreus* in the Barents Sea. Mar Ecol Prog Ser, 169: 211–228

Muench R D, Gunn J T, Whitledge T E, et al. 2000. An Arctic Ocean cold core eddy. J Geophys Res, 105(C10): 23997–24006

Mundy C J, Gosselin M, Ehn J, et al. 2009. Contribution of under-ice primary production to an ice-edge upwelling phytoplankton bloom in the Canadian Beaufort Sea. Geophys Res Lett, 36(17): L17601

Nishino S, Itoh M, Kawaguchi Y, et al. 2011. Impact of an unusually large warm-core eddy on distributions of nutrients and phytoplankton in the southwestern Canada Basin during late summer/early fall 2010. Geophys Res Lett, 38(16): L16602

Nishino S, Shimada K, Itoh M, et al. 2008. East-west differences in water mass, nutrient, and chlorophyll *a* distributions in the sea ice reduction region of the western Arctic Ocean. J Geophys Res, 113(C1): C00A01

Olli K, Wassmann P, Reigstad M, et al. 2007. The fate of production in the central Arctic Ocean—top-down regulation by zooplankton expatriates?. Prog Oceanogr, 72(1): 84–113

Ota Y, Hattori H, Makabe R, et al. 2008. Seasonal changes in nauplii and adults of *Calanus hyperboreus* (Copepoda) captured in sediment traps, Amundsen Gulf, Canadian Arctic. Polar Sci, 2(3): 215–222

Parkinson C L, Cavalieri D J. 2008. Arctic sea ice variability and trends, 1979–2006. J Geophys Res, 113(C7): C07003

Plourde S, Joly P, Runge J A, et al. 2003. Life cycle of *Calanus hyperboreus* in the lower St. Lawrence Estuary and its relationship to local environmental conditions. Mar Ecol Prog Ser, 255: 219–233

Ringuette M, Fortier L, Fortier M, et al. 2002. Advanced recruitment and accelerated population development in Arctic calanoid copepods of the North Water. Deep Sea Res II Top Stud Oceanogr, 49(22–23): 5081–5099

Rudyakov Y A. 1983. Vertical distribution of *Calanus hyperboreus* (Copepoda) in the Central Arctic Basin. Oceanology, 23: 249–254

Smith S L, Schnack-Schiel S B. 1990. Polar zooplankton. In: Smith W O Jr, ed. Polar Oceanography, Part B: Chemistry, Biology and Geology. New York: Academic Press, 527–598

Swalethorp R, Kjellerup S, Dünweber M, et al. 2011. Grazing, egg production, and biochemical evidence of differences in the life strategies of *Calanus finmarchicus*, *C. glacialis* and *C. hyperboreus* in Disko Bay, western Greenland. Mar Ecol Prog Ser, 429: 125–144

Tang K W, Nielsen T G, Munk P, et al. 2011. Metazooplankton community structure, feeding rate estimates, and hydrography in a meltwater-influenced Greenlandic fjord. Mar Ecol Prog Ser, 434: 77–90

Thor P, Nielsen T G, Tiselius P. 2008. Mortality rates of epipelagic copepods in the post-spring bloom period in Disko Bay, western Greenland. Mar Ecol Prog Ser, 359: 151–160

Acta Oceanol. Sin., 2018, Vol. 37, No. 5, P. 96–106
DOI: 10.1007/s13131-018-1149-9
http://www.hyxb.org.cn
E-mail: hyxbe@263.net

Influence of the northern Yellow Sea Cold Water Mass on picoplankton distribution around the Zhangzi Island, northern Yellow Sea

ZHAO Li[1, 2], ZHAO Yanchu[1, 2, 3], DONG Yi[1, 2], ZHAO Yuan[1, 2*], ZHANG Wuchang[1, 2], XU Jianhong[1], YU Ying[4], ZHANG Guangtao[5], XIAO Tian[1, 2]

[1] CAS Key Laboratory of Marine Ecology and Environmental Sciences, Institute of Oceanology, Chinese Academy of Sciences, Qingdao 266071, China

[2] Laboratory for Marine Ecology and Environmental Science, Qingdao National Laboratory for Marine Science and Technology, Qingdao 266237, China

[3] University of Chinese Academy of Sciences, Beijing 100864, China

[4] Tianjin Bohai Sea Fisheries Research Institute, Tianjin 300457, China

[5] Jiaozhou Bay Marine Ecosystem Research Station, Institute of Oceanology, Chinese Academy of Sciences, Qingdao 266071, China

Received 13 April 2017; accepted 18 July 2017

Abstract

Picoplankton distribution around the Zhangzi Island (northern Yellow Sea) was investigated by monthly observation from July 2009 to June 2010. Three picoplankton populations were discriminated by flow cytometry, namely *Synechococcus*, picoeukaryotes and heterotrophic prokaryotes. In summer (from July to September), the edge of the northern Yellow Sea Cold Water Mass (NYSCWM) resulting from water column stratification was observed. In the NYSCWM, picoplankton (including *Synechococcus*, picoeukaryotes and heterotrophic prokaryotes) distributed synchronically with extremely high abundance in the thermocline (20 m) in July and August (especially in August), whereas in the bottom zone of the NYSCWM (below 30 m), picoplankton abundance was quite low. *Synechococcus*, picoeukaryotes and heterotrophic prokaryotes showed similar response to the NYSCWM, indicating they had similar regulating mechanism under the influence of NYSCWM. Whereas in the non-NYSCWM, *Synechococcus*, picoeukaryotes and heterotrophic prokaryotes exhibited different distribution patterns, suggesting they had different controlling mechanisms. Statistical analysis indicated that temperature, nutrients (NO_3^- and PO_4^{3-}) and ciliate were important factors in regulating picoplankton distribution. The results in this study suggested that the physical event NYSCWM, had strong influence on picoplankton distribution around the Zhangzi Island in the northern Yellow Sea.

Key words: picoplankton, northern Yellow Sea Cold Water Mass, thermocline, Zhangzi Island

Citation: Zhao Li, Zhao Yanchu, Dong Yi, Zhao Yuan, Zhang Wuchang, Xu Jianhong, Yu Ying, Zhang Guangtao, Xiao Tian. 2018. Influence of the northern Yellow Sea Cold Water Mass on picoplankton distribution around the Zhangzi Island, northern Yellow Sea. Acta Oceanologica Sinica, 37(5): 96–106, doi: 10.1007/s13131-018-1149-9

1 Introduction

Since the discovery of cyanobacteria *Synechococcus* (Johnson and Sieburth, 1979; Waterbury et al., 1979) in the late 1970s, a number of studies have widely documented the ecological importance of picoplankton (⩽2 μm, including *Synechococcus*, *Prochlorococcus*, picoeukaryotes and heterotrophic prokaryotes) in various marine environments, from the eutrophic estuaries to the oligotrophic oceans (Platt et al., 1983; Agawin et al., 2003; Pan et al., 2007; Lin et al., 2010). In the coastal waters, picoplankton is generally subjected to higher pressure on environmental variability (i.e., water-mass and tidal front influences) than open oceans (Calvo-Díaz and Morán, 2006; Mitbavkar et al., 2009). For instance in the Uchiumi Bay (Japan), abundance and composition of picophytoplankton was strongly influenced by the physical events of "Kyucho" (warm surface water) and bottom intrusion (Katano et al., 2005). In the South Australian continental shelf waters, picophytoplankton distribution was affected by local physical event (downwelling and dense water outflowing) (Van Dongen-Vogels et al., 2011).

The Yellow Sea is a semi-enclosed marginal sea in the Pacific, which connects to the East China Sea in the southern part and Bohai Sea in the northern part. It is quite shallow with an average depth of about 44 m. One of the most striking hydrological phenomenon is the existence of the Yellow Sea Cold Water Mass (YSCWM) during summer period. The YSCWM forms locally during the previous winter owing to the surface cooling and strong vertical mixing. In summer, the surface water temperature increased, a cold water mass is retained in the bottom zone and

Foundation item: The National Natural Science Foundation of China under contract Nos 41306160; the NSFC-Shandong Joint Fund for Marine Science Research Centers under contract No. U1606404; the Strategic Priority Research Program of the Chinese Academy of Sciences under contract No. XDA11020103.1.
*Corresponding author, E-mail: yuanzhao@qdio.ac.cn

forms the YSCWM. It is characterized with low temperature showing a remarkable variation (5–12°C) and a rather constant salinity (31.5–32.5) (He et al., 1959; Su and Huang, 1995). The YSCWM can be recognized as northern and southern parts, with dissimilar characteristics. The northern YSCWM (NYSCWM) locates at the bottom layer within a small area of 37°–38.9°N and 121.3°–124°E, with low temperature (T<8°C) and salinity (S<32.5) in the core. The southern YSCWM (SYSCWM) locates within a larger area of 34°–37°N and 121°–126°E, with relatively higher temperature (T<9°C) and salinity (S>32.5) and more intensive thermocline in the core (Zhang et al., 2008; Bao et al., 2009; Yao et al., 2012; Xin et al., 2015).

The YSCWM has an important effect on marine ecosystems (Hur et al., 1999; Kang and Kim, 2008). The impact of the SYSCWM on picoplankton distribution has been reported by Li et al. (2006) and Zhao et al. (2011), showing low picoplankton abundance inside the SYSCWM. With dissimilar characteristics from SYSCWM, NYSCWM could have a different impact on picoplankton distribution. There has been only few reports about picoplankton variation in the northern Yellow Sea, mentioning that picoplankton abundance deceased sharply in the NYSCWM in summer (Bai et al., 2012). However, it is still unclear how the NYSCWM influenced picoplankton dynamics by changing stratification and nutrient supply. In this manuscript, we investigated the spatial and temporal dynamics of picoplankton around the Zhangzi Island in the northern Yellow Sea from July 2009 to June 2010. It is by far the first report tracking picoplankton variation during the formation to vanishment process of NYSCWM. Our objectives include: (1) clarifying the effect of NYSCWM on picoplankton distribution during summer period; (2) illustrating how NYSCWM influenced picoplankton dynamics around the Zhangzi Island in the northern Yellow Sea.

2 Materials and methods

2.1 *Study area and sampling strategy*

Thirteen stations around the Zhangzi Island in the northern Yellow Sea were investigated monthly from July 2009 to June 2010, except January and May 2010 (Fig. 1). According to previous studies (Zhang et al., 2008; Bao et al., 2009), Transect 6 (i.e., Sta. A6-B6-C6) was set as the NYSCWM influenced area. At each station, seawater was collected with a rosette multi-sampler equipped with 5 L Niskin bottles. The maximum depth was 55 m and the water samples were collected every 10 m from the surface to 2 m above the bottom, defining vertical profiles by up to five points.

2.2 *Physical, chemical and biological measurements*

Water temperature and salinity were determined with an AAQ 1183-1F CTD (conductivity, temperature, depth; Alec Electronics Co., Japan). Seawater subsamples (500 mL) for nutrient concentration analysis were filtered through Whatman GF/F filters and kept at -20°C until analysis in the laboratory. The concentrations of NO_3^- and PO_4^{3-} were determined using a QuAAtro-SFA Analyzer (Bran-Lubbe Co., Germany). The precision estimated with repeated measurements of selected samples was smaller than 3% in this study (Yin et al., 2013).

For chlorophyll *a* (Chl *a*) concentration analysis, another 500 mL subsamples were filtered on-board onto Whatman GF/F filters and kept at –20°C until analysis in the laboratory. Chl *a* was extracted with 90% acetone at –20°C in darkness for 24 h. The Chl *a* concentrations were determined using a Turner Designs Model 7200 fluorometer that was calibrated with pure Chl *a* from Sigma.

Subsamples (1 L) for ciliate enumeration were fixed with 1% acid Lugol's iodine solution and stored in a cool and dark place until analysis. Each sample was settled for at least 24 h. The supernatant was siphoned out and 150 mL sample was left. The concentrated sample (20–25 mL) was settled in an Utermöhl counting chamber for 24 h and enumerated using an inverted microscope (Olympus IX51) at 100× or 200× (Yu et al., 2013).

2.3 *Picoplankton enumeration*

Seawater subsamples (4 mL) for picoplankton enumeration were fixed on-board with paraformaldehyde (final concentration 1%) immediately, kept at room temperature for 15 min, and then freeze-trapped in liquid nitrogen until laboratory analysis within two months after the cruise.

A FACSVantage SE (Becton Dickinson, USA) flow cytometer equipped with a water-cooled Argon laser (488 nm, 1 W, Coher-

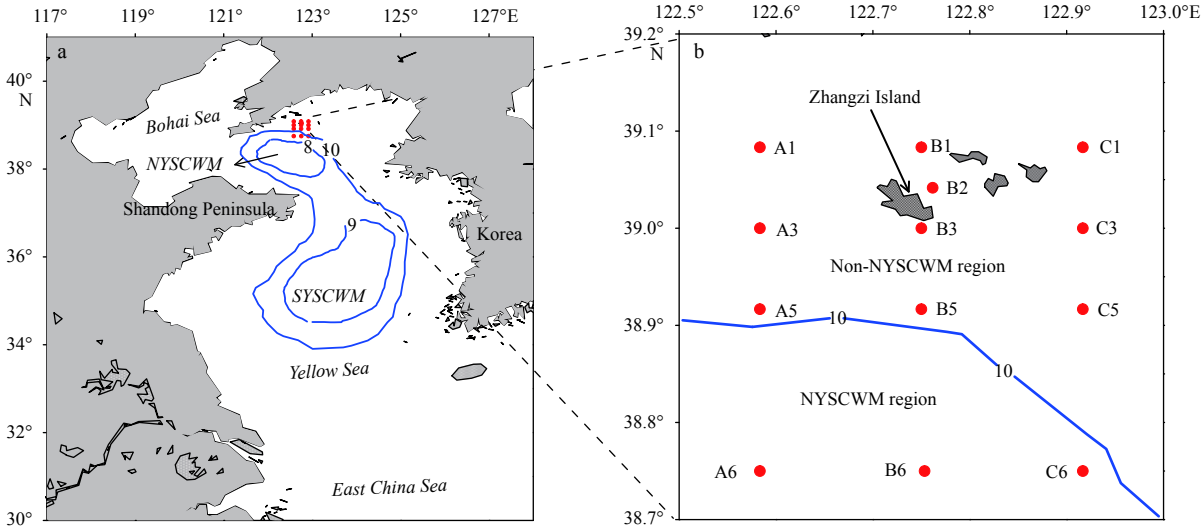

Fig. 1. Sampling stations around the Zhangzi Island in the northern Yellow Sea. The blue lines were the bottom temperature (°C) isobaths showing the range of Yellow Sea Cold Water Mass in summer (Zhang et al., 2008; Bao et al., 2009).

ent, USA) was used for picoplankton analysis at the single cell level. Five optical signals were recorded: forward scatter (FSC, related to cell size), side scatter (SSC, related to cell structure and shape), green fluorescence ((530±15) nm), orange fluorescence ((585±21) nm, related to phycoerythrin) and red fluorescence ((695±20) nm, related to Chl *a*).

Before analysis, seawater samples were thawed at room temperature in dark (about 20 min). For each sample, 2 μm fluorescent beads (Polysciences) were used as internal standard for the instrument set-up. When analyzing autotrophic picoplankton, red fluorescence was set as the trigger to eliminate signals from heterotrophic prokaryotes and inorganic particles. Two major autotrophic picoplankton groups: *Synechococcus* (SYN) and picoeukaryotes (PEUK) were resolved based on the signals of side scatter, orange and red fluorescences. *Prochlorococcus* was not detected in this study.

For the determination of heterotrophic prokaryote (HP) abundance, seawater samples were diluted five folds with TE buffer (Tris-EDTA, 100 mmol/L Tris-Cl, 10 mmol/L EDTA, pH=8.0, Sigma), and then stained with the nucleic acid dye SYBR Green I (molecular probes) (final dilution 10^{-4}, v/v). Samples were stained and kept in the dark at room temperature for 20 min, then analyzed with flow cytometry for 30 s. Heterotrophic prokaryote cell-groups were resolved on the basis of their green fluorescence ((530±15) nm) and scatter properties.

Flow cytometric data were collected and analyzed with CellQuest software (Version 3.3, Becton Dickinson). Since each 4 mL subsample for flow cytometry analysis was taken from 1 L of homogeneous seawater of a Niskin bottle, the derived cell abundance are representative of that initial volume.

2.4 *Standard of thermocline*

According to Zou et al. (2001), when water depth less than 200 m, the minimum standards for thermocline and halocline are $I_t=\Delta T/\Delta Z$ (strength of thermocline)=0.2°C/m and $I_s=\Delta S/\Delta Z$ (strength of halocline)=0.1 m^{-1}, respectively.

2.5 *Data analysis*

Seasonal variations of the data were drawn with the software Origin (Version 8.5, OriginLab Corporation). The contour plot graphs were generated using the software Surfer (Version 11, Golden Software). Statistical analysis was conducted using SPSS (Version 19, IBM SPSS Statistics). Spearman rank-order correlation analysis was used to estimate potential relationships between picoplankton abundance and environmental variables (temperature, salinity, NO_3^-, PO_4^{3-}, Chl *a* concentration and ciliate abundance). Picoplankton and ciliate abundances used for statistical analysis were log-transformed to satisfy a roughly normal distribution.

3 Results

3.1 *Physicochemical conditions*

In this study, we use the water temperature lower than 12°C in summer as definition of the NYSCWM. The bottom distribution of temperature and salinity in our study revealed the existence of NYSCWM in July, August and September, with temperature lower than 12°C (Fig. 2). The NYSCWM was most prosperous in July, covering 2/3 of the survey area, then diminished in August and September. In October, bottom temperature was higher than 12°C, indicating the vanishing of NYSCWM. Since Transect 6 was mostly covered by the NYSCWM in summer, it was considered as NYSCWM region and the rest stations as non-NYSCWM region (Fig. 1). NO_3^- and PO_4^{3-} concentrations in the bottom waters were higher in the NYSCWM than in the non-NYSCWM regions.

3.2 *Spatial-temporal variation of picoplankton abundance in the NYSCWM region*

Along Transect 6, water column stratification was observed from June to October. In July and August, pronounced thermocline was found between 10 m and 20 m depth with I_t>1°C/m. Halocline also existed in July, showing I_s>0.1 m^{-1} between 10 m and 20 m depth. In September, thermocline was less intensive (I_t>0.6°C/m) and occurred between 20 m and 30 m depth (Figs 3a and b). In June and July, Chl *a* concentrations were higher below 10 m depth whereas in August, September and October, higher concentrations of Chl *a* were observed in the upper 20 m layer. From June to October, nutrient NO_3^- increased gradually with depth and ciliate was more abundant in the upper 20 m layer (Fig. 3a).

In June, September and October, picoplankton was more abundant in the upper layer and decreased gradually with depth (Fig. 3a). In July and August, SYN, PEUK and HP abundances had same vertical pattern with maximum abundances in the thermocline (20 m) and minimum abundances in the bottom zone of the NYSCWM (below 30 m) (Figs 3a and c). Picoplankton abundance in August was much higher than that in July in the thermocline region. In July, the maximum abundances of SYN, PEUK and HP were 47.04×10^3 cells/mL (20 m, Sta. B6), 15.84×10^3 cells/mL (20 m, Sta. C6) and 6.37×10^5 cells/mL (10 m, Sta. C6), respectively. In August, the maximum abundances of SYN and PEUK (421.28×10^3 cells/mL and 30.15×10^3 cells/mL, respectively) were found in the thermocline (20 m) of Sta. A6. SYN and PEUK abundances in the thermocline was 1 or 2 order of magnitude higher than the rest of the water column. The maximum abundance of HP (18.08×10^5 cells/mL) was observed in the thermocline (20 m) of Sta. B6. HP abundance in the thermocline was one order of magnitude higher than the rest of the water column (Figs 3a and c).

From June to October, water column stratification intensified from Stas B1 to B6 (Fig. 4). The NYSCWM was observed below 30 m depth of Sta. B6 in July, August and September. In June, higher concentrations of Chl *a* and nutrient NO_3^- were both observed at the bottom of Sta. B6. Ciliate was more abundant at the surface of Stas B1 and B5. SYN was more abundant in the upper 20 m of Sta. B6. PEUK showed maximum abundance in the upper 10 m of Sta. B1. HP abundance varied less obvious than SYN and PEUK, with higher abundance in the middle layer (10–30 m) of Sta. B3. In July, the NYSCWM was observed below 30 m of Sta. B5 and 20 m of Sta. B6. Higher concentration of Chl *a* was found at 20 m of Sta. B3. Nutrient NO_3^- exhibited higher concentrations inside the NYSCWM. Ciliate was more abundant at 10 m of Stas B2 and B6. SYN was more abundant in the central part of Transect B and the maximum abundance (86.26×10^3 cells/mL) was observed at 20 m of Sta. B5. PEUK exhibited similar pattern as SYN with higher abundances in the middle layer of Transect B. HP were more abundant in the non-NYSCWM region. In August, bottom temperature was higher than 11°C, implying the less obvious NYSCWM than in July. Chl *a* exhibited much higher concentrations (>4 μg/L) at the surface of Stas B1, B2 and B3. In contrast, nutrient NO_3^- showed higher concentrations at the bottom of Stas B5 and B6. Higher abundance of ciliate was observed at the surface of Stas B1 and B5. SYN and PEUK had extremely high abund-

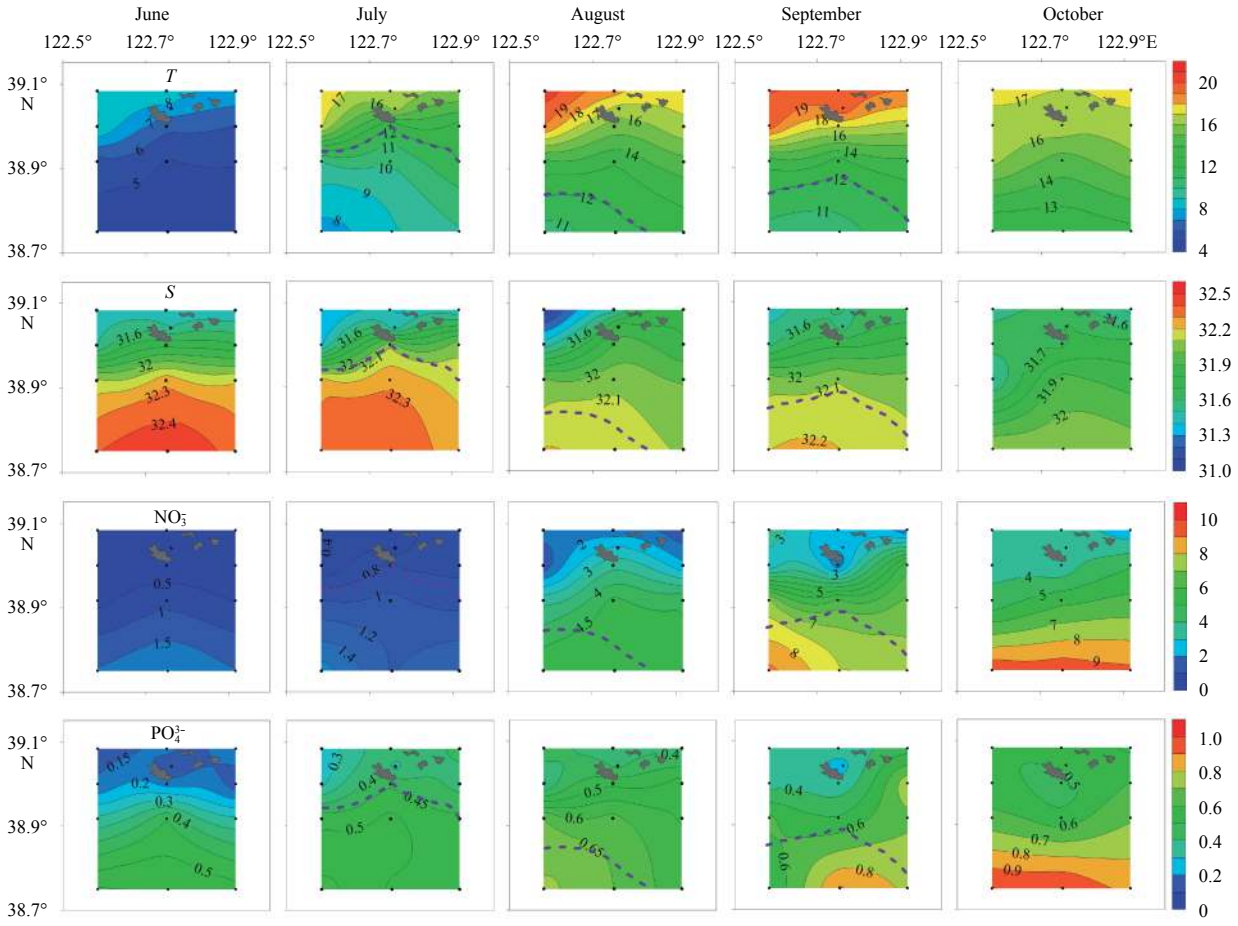

Fig. 2. Bottom distribution of temperature (T, °C), salinity (S) and nutrient concentrations (NO_3^-, PO_4^{3-}; μmol/L) from June to October, showing the existence-fading process of NYSCWM. The dashed line was T=12°C showing the boundary of the NYSCWM.

ances at Sta. B6 (20 m, 355.48×10^3 cells/mL and 28.53×10^3 cells/mL, respectively). HP were more abundant above 20 m depth. The maximum abundance (18.08×10^5 cells/mL) was also observed at 20 m of Sta. B6. In September and October, picoplankton showed similar distribution pattern as temperature and salinity, which was more abundant above 30 m depth and decreased gradually below 30 m (Fig. 4).

3.3 *Seasonal comparison of picoplankton abundance between non-NYSCWM and NYSCWM stations*

The coastal Sta. B2 was not influenced by the NYSCWM, in contrast with Sta. B6 in the open-water (Fig. 4). At Sta. B2, the vertical distributions of temperature and salinity presented well-mixed water columns almost the whole year. A weak stratification occurred in August and September. A sharp decrease in salinity was observed in the upper 20 m in June, July and August (Fig. 5). Chl *a* concentration reached its maximum value (10 m, 4.93 μg/L) in August. During the rest of the year, Chl *a* concentrations were rather low (<2 μg/L). Nutrients NO_3^- exhibited lower concentrations from March to June and higher concentrations from October to February. Ciliate exhibited higher abundances in September and October, and lower abundances in the rest of the year. The distribution pattern of SYN was synchronized with temperature. SYN abundance sustained extremely low level (<0.2×10^3 cells/mL) from March to June, and then reached the maximum abundance (63.06×10^3 cells/mL) at the surface in September when temperature was the highest. PEUK presented a different distribution pattern, exhibiting higher abundances in June and October and lower abundances in March and April. HP showed higher abundances in August, September and November and lower abundances in December, February and April.

At Sta. B6, a well-mixed water column was observed from November to April. Thereafter, water column stratification built up showing the thermocline at about 20 m depth from July to September. Due to the water column stratification in summer, the bottom NYSCWM was observed with temperature lower than 12°C (Figs 2 and 5). Chl *a* concentration reached a high value (6.53 μg/L) at the bottom in March, but remained low (<0.5 μg/L) from surface to bottom during the rest of the year, especially in the NYSCWM region (Chl *a*<0.1 μg/L). Nutrient NO_3^- showed lower concentrations (NO_3^-<0.5 μmol/L) in the upper 20 m from April to September and higher concentrations in the bottom zone of the NYSCWM. The maximum concentration of NO_3^- (9.62 μmol/L) were observed at the bottom in October. Ciliate showed higher abundances in April (10 m, 25.05×10^3 ind./L) and July (10 m, 20.52×10^3 ind./L). It was less abundant in the NYSCWM (<5×10^3 ind./L). SYN, PEUK and HP had similar distribution pattern with extremely high abundances (355.48×10^3 cells/mL, 28.53×10^3 cells/mL and 18.08×10^5 cells/mL, respectively) at 20 m depth in August where the thermocline and halocline were well established. From October to June, SYN and PEUK sustained low abundances, especially in March and April. In the bottom zone of the NYSCWM, picoplankton abundance was quite low (Fig. 5).

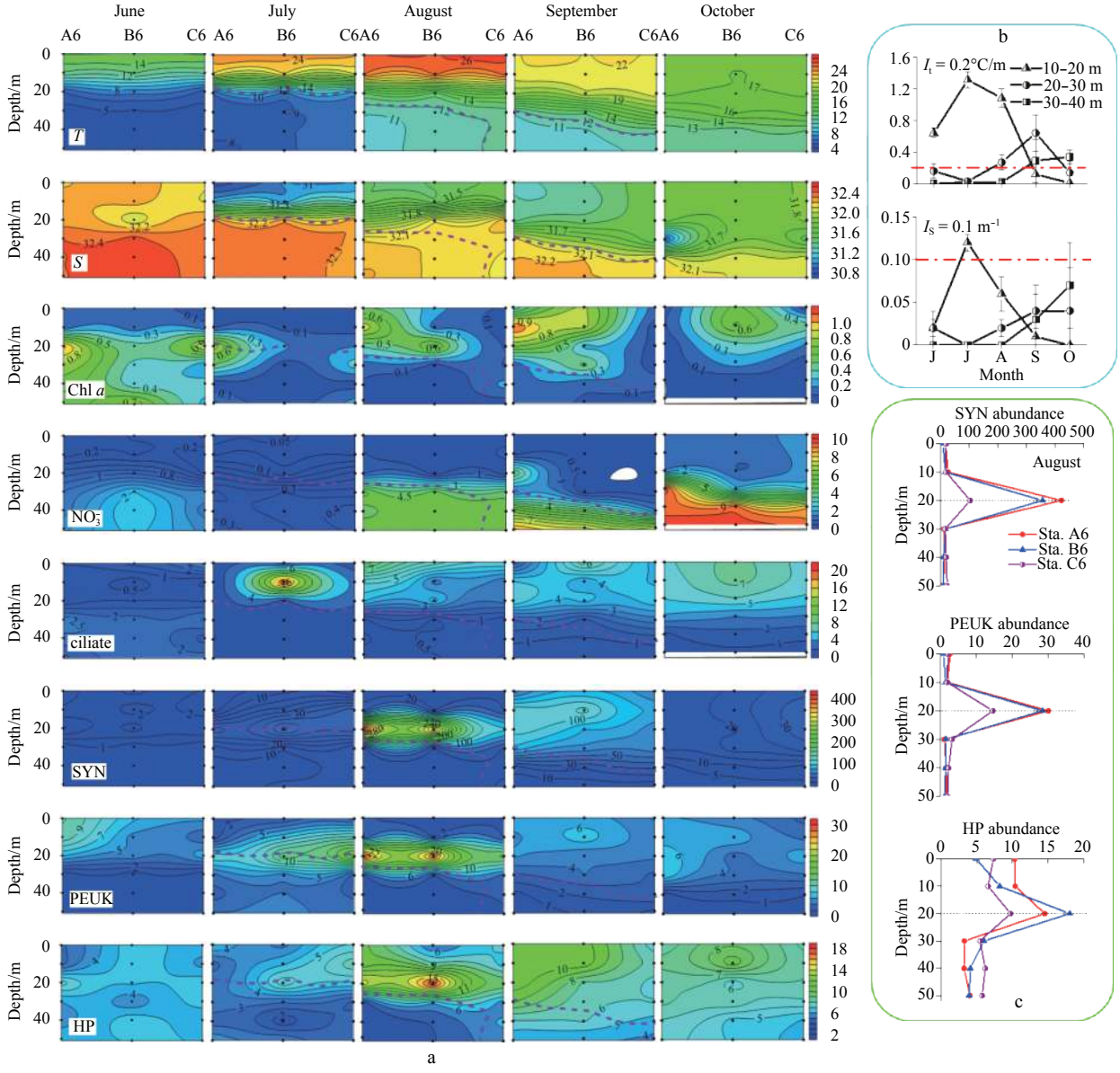

Fig. 3. Vertical distribution of temperature (T, °C), salinity (S), Chl *a* (μg/L), nutrient concentrations (NO_3^-, μmol/L), ciliate abundances (×10^3 ind./L), *Synechococcus* (SYN, ×10^3 cells/mL), picoeukaryotes (PEUK, ×10^3 cells/mL) and heterotrophic prokaryotes abundances (HP, ×10^5 cells/mL) along Transect 6 from June to October (the dashed line was T=12°C showing the boundary of the NYSCWM) (a); the strength of thermocline (I_t, °C/m) and halocline (I_s, m^{-1}) from June to October (b); and the vertical distribution of *Synechococcus* (SYN, ×10^3 cells/mL), picoeukaryotes (PEUK, ×10^3 cells/mL) and heterotrophic prokaryotes (HP, ×10^5 cells/mL) abundances at Stas A6, B6 and C6 in August (c).

3.4 *Seasonal variation of picoplankton water column integrated abundance between non-NYSCWM and NYSCWM regions*

The water column integrated abundance of SYN showed similar seasonal pattern in the non-NYSCWM (Transects 1, 3 and 5) and NYSCWM regions (Transect 6), except in summer. The maximum abundance in the NYSCWM was observed in August, one month earlier than that in the non-NYSCWM area. In August, SYN in the NYSCWM region ((3.56±1.59)×10^{12} cells/m^2) was almost three times higher than that in the non-NYSCWM region ((0.97±0.31)×10^{12} cells/m^2) (Fig. 6a).

Similar to SYN, PEUK in the NYSCWM exhibited highest water column integrated abundance ((3.15±0.06)×10^{11} cells/m^2) in August. In the non-NYSCWM, the maximum abundance ((2.71±10.7)×10^{11} cells/m^2) occurred in June, two month earlier than that in the NYSCWM. During the rest of the year, PEUK was slightly higher in the NYSCWM region than the non-NYSCWM region (Fig. 6b).

Unlike the autotrophic picoplankton, HP integrated abundance exhibited similar distribution patterns between the non-NYSCWM and NYSCWM regions, showing major peaks ((3.78±0.31)×10^{13} cells/m^2 and (3.41±0.48)×10^{13} cells/m^2, respectively) in August and minor peaks in March. HP in the NYSCWM were slightly higher than in the non-NYSCWM during the rest of the year except July (Fig. 6c).

3.5 *Relationship between picoplankton abundance and environmental variables*

Relationships between picoplankton abundance and envir-

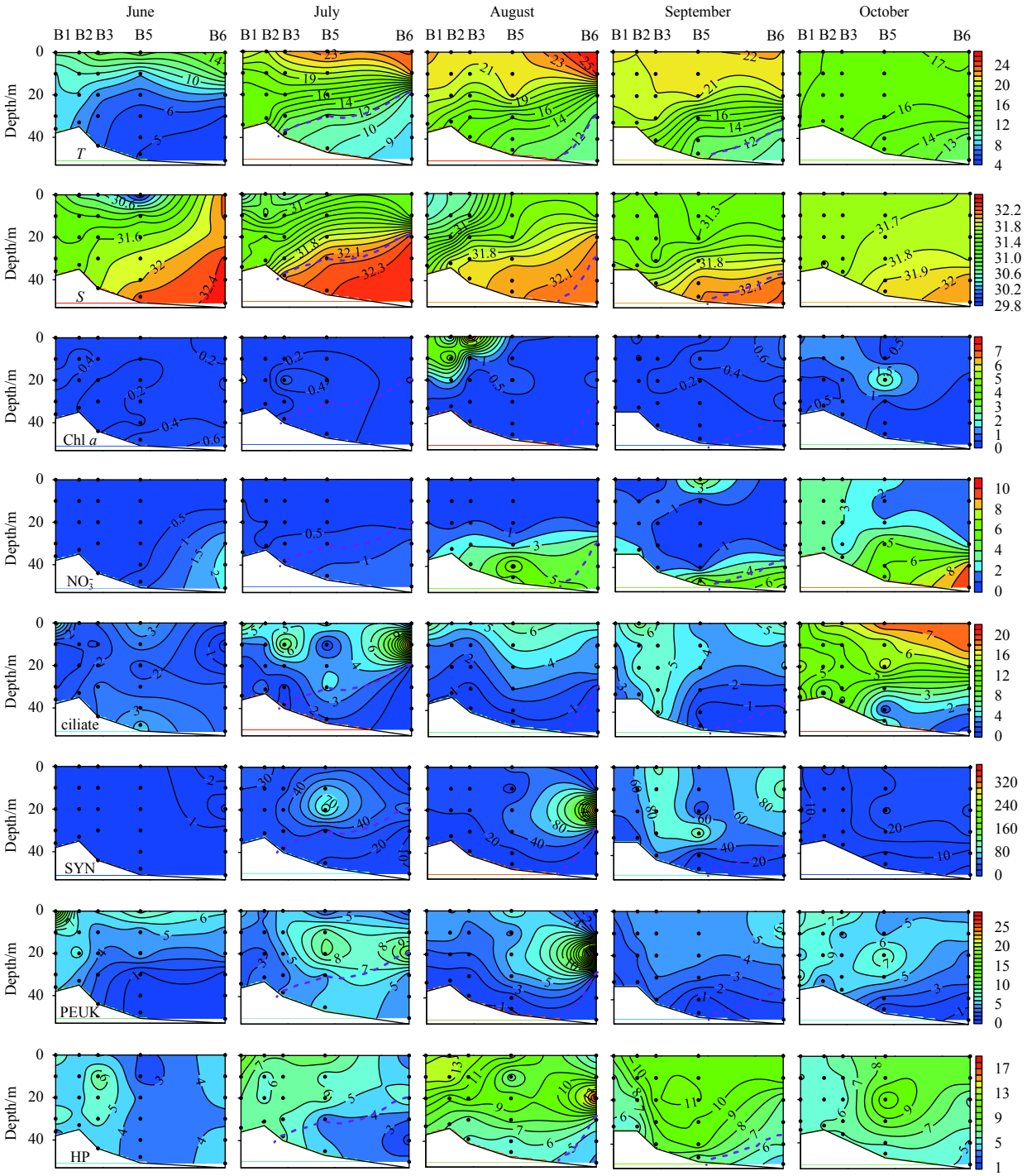

Fig. 4. Vertical distribution of temperature (*T*, °C), salinity (*S*), Chl *a* (μg/L), nutrient concentrations (NO_3^-, μmol/L), ciliate abundances (×10³ ind./L), *Synechococcus* (SYN, ×10³ cells/mL), picoeukaryotes (PEUK, ×10³ cells/mL) and heterotrophic prokaryote abundances (HP, ×10⁵ cells/mL) along Transect B from June to October. The dashed line was *T*=12°C showing the boundary of the NYSCWM.

onmental variables in the NYSCWM (Transect 6) in summer (July-September) were performed using Spearman correlation analysis (Table 1). In the NYSCWM region in summer, abundances of SYN, PEUK and HP were positively correlated with each other. They were also positively correlated with Chl *a* and ciliate, and negatively correlated with nutrients NO_3^- and PO_4^{3-}. Besides, HP abundances were also positively correlated with temperature and negatively correlated with salinity.

4 Discussion

In previous studies, the contours of 10°C were taken as the boundary of NYSCWM (Zhang et al., 2008; Xin et al., 2015). In this study, it is reasonable to use the relatively broad definition of the NYSCWM with water temperature lower than 12°C since (1) the YSCWM is characterized with low temperature showing a remarkable variation (5–12°C) (He et al., 1959; Su and Huang, 1995), (2) the temperature of NYSCWM has been reported in-

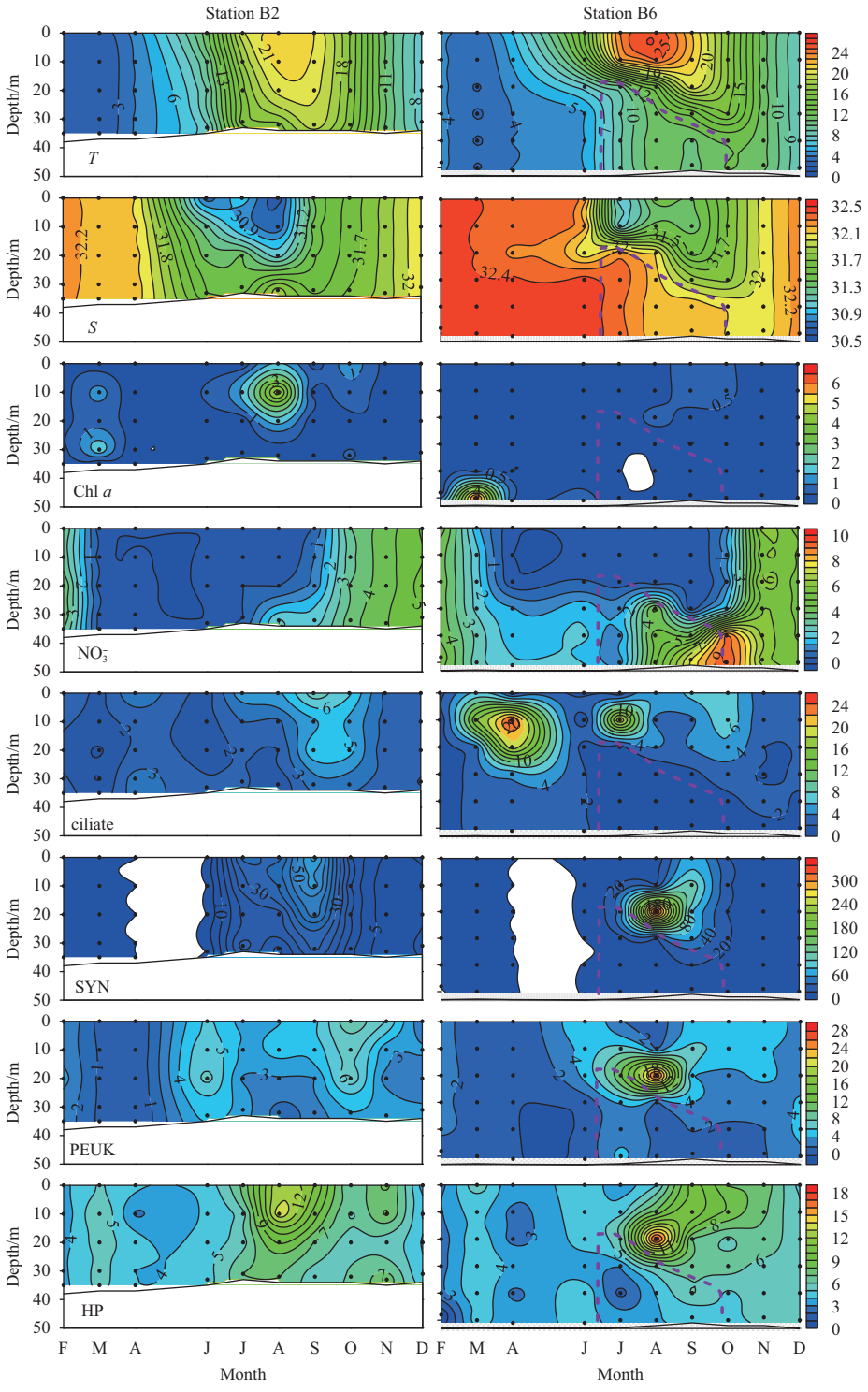

Fig. 5. Seasonal changes in the vertical distribution of temperature (*T*, °C), salinity (*S*), Chl *a* (μg/L), nutrient concentrations (NO_3^-, μmol/L), ciliate abundances (×10³ ind./L), *Synechococcus* (SYN, ×10³ cells/mL), picoeukaryotes (PEUK, ×10³ cells/mL) and heterotrophic prokaryotes (HP, ×10⁵ cells/mL) at Sta. B2 (non-NYSCWM) and Sta. B6 (NYSCWM).

creasing slightly from 1976 to 1999 (Li et al., 2015), and (3) the Zhangzi Island locates on the edge of the NYSCWM.

4.1 *Impact of NYSCWM on physical, chemical and biological conditions*

The YSCWM is a typically seasonal water mass in the Yellow Sea. It forms locally in winter owing to the surface cooling and strong vertical mixing. In spring, when surface water temperature increases, the cold water is retained in the bottom zone. In summer, this cold water mass flows southward under the thermocline. Extremely high intensity of the YSCWM occurs between July and August. In late autumn and winter, the YSCWM disappear because of the strong vertical mixing (Wang et al., 2000; Li et al., 2006).

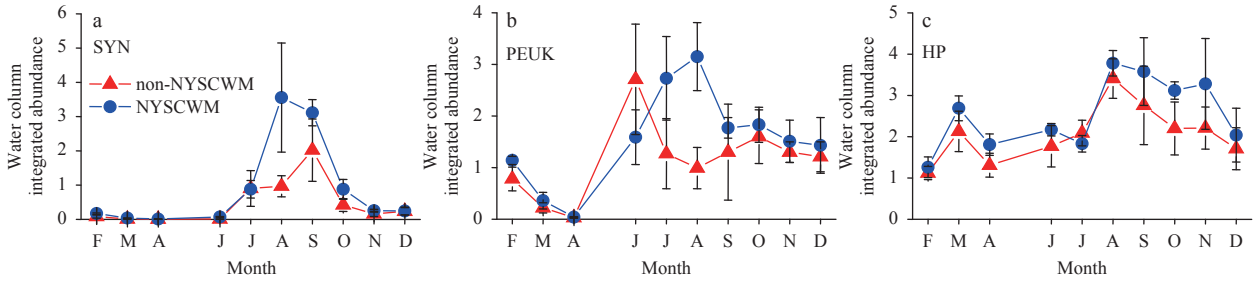

Fig. 6. Seasonal comparison of water column integrated abundances of *Synechococcus* (SYN, ×10^{12} cells/m^2) (a), picoeukaryotes (PEUK, ×10^{11} cells/m^2) (b) and heterotrophic prokaryotes (HP, ×10^{13} cells/m^2) (c) in the non-NYSCWM and NYSCWM regions around the Zhangzi Island in the northern Yellow Sea.

Table 1. Spearman's rank correlation coefficient between environmental and biological variables and picoplankton abundances along Transect 6 in July, August and September

Spearman's rho	Lg PEUK	Lg HP	*T*	*S*	NO_3^-	PO_4^{3-}	Chl *a*	Lg ciliate
Lg SYN	0.684**	0.757**			–0.411**	–0.630**	0.468**	0.664**
Lg PEUK		0.342*			–0.528**	–0.445**	0.287*	0.368**
Lg HP			0.589**	–0.532**	–0.346*	–0.664**	0.411**	0.656**

Note: ** Correlation is significant at the 0.01 level (2-tailed); * correlation is significant at the 0.05 level (2-tailed). *T* represents temperature, *S* salinity, SYN *Synechococcus*, PEUK picoeukaryotes, and HP heterotrophic prokaryotes.

In this study, the NYSCWM was observed in summer (July–September) with temperature lower than 12°C. Pronounced thermocline and halocline were observed between 10 and 30 layer, especially in July and August (Figs 2 and 3). Chlorophyll *a* showed high concentration in the upper layer and low concentration in the bottom zone. The maximum chlorophyll *a* concentration occurred above the thermocline layer (10–20 m), perhaps resulting from the coaction of thermocline and intensive photosynthesis due to subsurface chlorophyll maximum in the same layer. In the bottom zone, chlorophyll *a* was the lowest because of the low temperature (<12°C) and insufficient light (Fig. 3).

Nitrogen was considered as the proximal limiting factor for primary production (Davey et al., 2008). In the NYSCWM, nutrient NO_3^- was almost depleted (<0.5 μmol/L) by phytoplankton above the thermocline, but enriched in the bottom zone of the NYSCWM through organism decomposition. The existence of stratification prevented the exchange of nitrate from the bottom to the surface.

4.2 *Impact of NYSCWM on picoplankton distribution*

Our study is by far the first report tracking picoplankton variation during the formation to vanishment process of NYSCWM. The impact of YSCWM on picoplankton distribution has been reported by Li et al. (2006) and Zhao et al. (2011) in the southern Yellow Sea and Bai et al. (2012) in the northern Yellow Sea in summer. Li et al. (2006) reported the minimum biomass of SYN and HP in the SYSCWM. Zhao et al. (2011) observed relatively low abundance of picoplankton at the surface and bottom (in the SYSCWM). Bai et al. (2012) found low abundance of SYN and PEUK in the NYSCWM, whereas no significant variations of HP were observed between NYSCWM and non-NYSCWM waters.

In this study, pronounced thermocline was observed in July and August. Picoplankton abundance was much higher in the thermocline (20 m). Especially in August, extremely high abundances of all three picoplankton groups (SYN, PEUK and HP) were observed (Figs 3–5). Whereas in the bottom zone of the NYSCWM, minimum abundance of picoplankton was detected (Fig. 3c). Extremely high abundance in the thermocline was not common in previous studies (Li et al., 2006; Zhao et al., 2011; Bai et al., 2012). How NYSCWM influenced on picoplankton dynamics was still unclear, it is necessary to address the regulating factors on picoplankton distribution.

Temperature is considered an important factor regulating picoplankton variations (Agawin et al., 2000). In colder water (*T*<14°C), temperature was the dominant factor in SYN distribution (Li, 1998). In this study, temperature in the thermocline was higher than 14°C, indicating temperature was not the limiting factor. Whereas in the bottom zone of the NYSCWM, temperature was lower than 12°C, turning out temperature was the dominant factor on picoplankton distribution. Besides temperature, nutrient supply is another important factor influencing picoplankton distribution (Agawin et al., 2000; Moisan et al., 2010). Although the stratification prevented the exchange of nutrient from the bottom to the surface, in the thermocline layer nutrient was sufficient to supply the growth of picoplankton (Fig. 3). In the bottom zone of the NYCWM, even though nutrient was sufficient, the effect of low temperature seemed to be more important than nutrient supply. Ciliate might be another important controlling factor on picoplankton distribution. Ciliate and heterotrophic nanoflagellates have been recognized as the primary consumers of picoplankton (Tsai et al., 2008; Guo et al., 2014). In the present study, ciliate was less abundant in the thermocline, indicating lower pressure of predating on picoplankton variations. In the bottom zone of the NYSCWM, minimum abundance of ciliate was observed, suggesting ciliate was not important in controlling picoplankton distribution.

In the thermocline, with warmer temperature, sufficient nutrient supply and lower pressure of predating, the environment of thermocline was suitable for the growth of picoplankton, which explains why such high abundance of picoplankton occurring in the thermocline. In the bottom zone of the NYSCWM, in spite of sufficient nutrient supply and low predator pressure, low temperate (*T*<12°C) was the dominant factor on picoplankton distribution.

4.3 *Seasonal comparisons between non-NYSCWM and NYSCWM*

Around the Zhangzi Island, stations not influenced by the NYSCWM (namely non-NYSCWM) showed a clear seasonality in

picoplankton abundance (Fig. 5). SYN, PEUK and HP exhibited different distribution patterns, which was very common in previous studies. Seasonal dynamics of SYN abundance in this study was similar to previous reports in the coastal waters of Japan (Shimada et al., 1995; Katano et al., 2005), coastal waters of Mediterranean (Agawin et al., 1998; Bec et al., 2005; Charles et al., 2005), Bay of Biscay (Calvo-Díaz and Morán, 2006; Morán, 2007), Bedford Basin (Li, 1998), western English Channel (Tarran and Bruun, 2015) and Levantine Basin shelf waters (Uysal and Köksalan, 2006) (Table 2). A strong relationship between temperature and SYN was observed in this study, suggesting the importance of temperature in regulating SYN distribution (Fig. 7a), which has been conformed in previous studies (Agawin et al., 1998; Moisan et al., 2010). The seasonality of PEUK abundance was more complicated than SYN. PEUK reached maximum abundance in June and low abundances were observed in March and April (Fig. 7b). Our result agreed with previous observations in the southern Yellow Sea (Zhao et al., 2011) and Iwanai Bay (Miyazono et al., 1992) (Table 2). Negative relationship between PO_4^{3-} and PEUK was observed, indicating the importance of nutrient supply on PEUK distribution (Fig. 7b). HP showed major peak in August and minor peak in March (Fig. 7c). Seasonal variations of HP and Chl *a* overlapped (Fig. 7c), implying that HP relied on the released substrate by phytoplankton (Garneau et al., 2008). In the non-NYSCWM, SYN, PEUK and HP distributed diversely and they were influenced by different factors, indicating they may have different controlling mechanisms.

In the NYSCWM, the thermocline provided a suitable environment (warm water, sufficient nutrient supply and low predating pressure) for the growth of picoplankton, SYN, PEUK and HP exhibited similar distribution patterns. It seemed they had similar controlling mechanism under the influence of NYSCWM.

Table 2. Previous studies on seasonal variations of *Synechococcus* (SYN, ×10³ cells/mL), picoeukaryotes (PEUK, ×10³ cells/mL) and heterotrophic prokaryotes abundance (HP, ×10⁵ cells/mL) reported in coastal waters

Study area	Study period	SYN/10^3 cells·mL^{-1}		PEUK/10^3 cells·mL^{-1}		HP/10^5 cells·mL^{-1}		Method	Reference
		Min	Max	Min	Max	Min	Max		
Iwanai Bay (Hokkaido, Japan)	1989.4–1990.3	0.14 (Dec.–Mar.)	190 (Jun.)	0.04 (Dec.–Mar.)	4.3 (May)			EFM	Miyazono et al. (1992)
Mediterranean coastal lagoon	1999.2–2000.1	<0.3 (Nov.–Apr.)	8.2 (Jul.)	5.2 (Sep.)	90.8 (Apr.)			FCM	Bec et al. (2005)
NW Mediterranean shallow bay	2000.8–2001.7	<2 (Dec.–Apr.)	95 (Sep.)	<1 (Dec.)	21 (Jan.)			FCM	Charles et al. (2005)
Bay of Biscay	2003.1–2003.12	<1 (Apr.)	106 (Jul.)	1.6 (Aug.)	32.6 Jul.			FCM	Morán (2007)
Western English Channel	2007–2013	0.1 (May)	120 (Sep.)	0.2 (Aug.)	80 (Apr.)			FCM	Tarran and Bruun (2015)
Suruga Bay, Japan	1992.5–1993.10	<1 (Apr.)	220 (Sep.)					FCM	Shimada et al. (1995)
Bay of Blane (NW Mediterranean)	1995.1–1997.1	0.5 (Feb.)	70 (Aug.)					EFM	Agawin et al. (1998)
Bay of Biscay	2002.4–2003.4	<0.1 (Mar.–Apr.)	149 (Sep.)					FCM	Calvo-Díaz and Morán (2006)
Levantine Basin shelf waters	1998.1–1999.1	3 (Jan.)	160 (Sep.)					EFM	Uysal and Köksalan (2006)
Uchiumi Bay, Japan	2002.3–2002.10		154.9 (Aug.)	<10 (Jun., Aug., Sep.)	93.9 (May)			FCM	Katano et al. (2005)
Bay of Marseille	1997.9–1999.10		70 (Mar.)		30 (Jan.)			FCM	Grégori et al. (2001)
Bedford Basin	1991.1–1998.1	<0.01 (Jun.)	445 (Sep.)			3.2 (Feb.)	74.5 (Jun.)	EFM	Li (1998)
Northern Gulf of Bothnia	1989.3–1990.4					<2 (Feb.)	25 (July)	EFM	Wikner and Hagström (1991)
NW Mediterranean	1999.1–2000.1					1.4 (Jan.)	11 (April)	EFM	Lemée et al. (2002)
Franklin Bay	2003.11–2004.8					1 (Feb.)	17 (Jul.)	EFM	Garneau et al. (2008)
Blanes Bay (NW Mediterranean)	2005.5–2007.4					4.6 (Aug.)	16 (May)	EFM	Boras et al. (2009)
This study	2009.7–2010.6	0.08 (Mar.)	421 (Aug.)	0.25 (Mar.)	30.15 (Aug.)	1.83 Feb.	18.08 (Aug.)	FCM	

Note: SYN represents *Synechococcus*, PEUK picoeukaryotes, HP heterotrophic prokaryotes, EFM epifluorescence microscopy, and FCM flow cytometry.

5 Conclusions

Around the Zhangzi Island in the northern Yellow Sea, the bottom water mass-NYSCWM had strong influence on picoplankton distribution, showing low abundance in the bottom zone of the NYSCWM and extremely high abundance in the thermocline, which was not exactly the same as the influence of the SYSCWM on picoplankton distribution. How NYSCWM influenced picoplankton dynamics by changing thermocline layer and nutrient supply has been illustrated in this study. Since the survey region locates at the edge of the NYSCWM, it is necessary to investigate picoplankton distribution in the cores of NYSCWM and SYSCWM regions to better understand and compare the influencing strength of NYSCWM and SYSCWM on picoplankton distribution in the future.

Acknowledgements

The authors are grateful to the crew on the research vessel of Dalian Zhangzidao Fishery Group Co., Ltd for their supports on

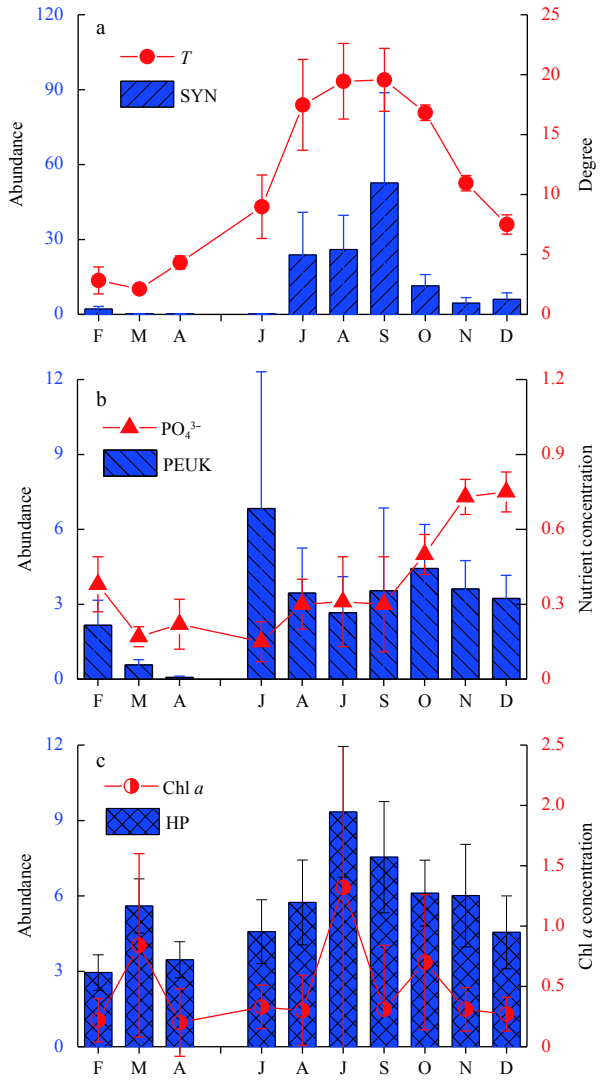

Fig. 7. Seasonal variations of average temperature (*T*, °C) vs. *Synechococcus* abundance (SYN, ×10^3 cells/mL) (a), PO_4^{3-} (μmol/L) vs. picoeukaryotes abundance (PEUK, ×10^3 cells/mL) (b), Chl *a* (μg/L) vs. heterotrophic prokaryote abundances (HP, ×10^5 cells/mL) (c) in the non-NYSCWM region around the Zhangzi Island in the northern Yellow Sea.

field sampling.

References

Agawin N S R, Duarte C M, Agustí S. 1998. Growth and abundance of *Synechococcus* sp. in a Mediterranean Bay: seasonality and relationship with temperature. Mar Ecol Prog Ser, 170: 45–53

Agawin N S R, Duarte C M, Agustí S. 2000. Nutrient and temperature control of the contribution of picoplankton to phytoplankton biomass and production. Limnol Oceanogr, 45(3): 591–600

Agawin N S R, Duarte C M, Agustí S, et al. 2003. Abundance, biomass and growth rates of *Synechococcus* sp. in a tropical coastal ecosystem (Philippines, South China Sea). Estuar Coast Shelf Sci, 56(3–4): 493–502

Bai Xiaoge, Wang Min, Liang Yantao, et al. 2012. Distribution of microbial populations and their relationship with environmental variables in the North Yellow Sea, China. J Ocean Univ China, 11(1): 75–85

Bao Xianwen, Li Na, Yao Zhigang, et al. 2009. Seasonal variation characteristics of temperature and salinity of the North Yellow Sea. Period Ocean Univ China (in Chinese), 39(4): 553–562

Bec B, Husseini-Ratrema J, Collos Y, et al. 2005. Phytoplankton seasonal dynamics in a Mediterranean coastal lagoon: emphasis on the picoeukaryote community. J Plankton Res, 27(9): 881–894

Boras J A, Sala M M, Vázquez-Domínguez E, et al. 2009. Annual changes of bacterial mortality due to viruses and protists in an oligotrophic coastal environment (NW Mediterranean). Environ Microbiol, 11(5): 1181–1193

Calvo-Díaz A, Morán X A G. 2006. Seasonal dynamics of picoplankton in shelf waters of the southern Bay of Biscay. Aquat Microb Ecol, 42(2): 159–174

Charles F, Lantoine F, Brugel S, et al. 2005. Seasonal survey of the phytoplankton biomass, composition and production in a littoral NW Mediterranean site, with special emphasis on the picoplanktonic contribution. Estuar Coast Shelf Sci, 65(1-2): 199–212

Davey M, Tarran G A, Mills M M, et al. 2008. Nutrient limitation of picophytoplankton photosynthesis and growth in the tropical North Atlantic. Limnol Oceanogr, 53(5): 1722–1733

Garneau M È, Roy S, Lovejoy C, et al. 2008. Seasonal dynamics of bacterial biomass and production in a coastal arctic ecosystem: Franklin Bay, western Canadian Arctic. J Geophys Res, 113(C7): C07S91

Grégori G, Colosimo A, Denis M. 2001. Phytoplankton group dynamics in the Bay of Marseilles during a 2-year survey based on analytical flow cytometry. Cytometry, 44(3): 247–256

Guo C, Liu H, Zheng L, et al. 2014. Seasonal and spatial patterns of picophytoplankton growth, grazing and distribution in the East China Sea. Biogeosciences, 11(7): 1847–1862

He Chongben, Wang Yuanxiang, Lei Zongyou, et al. 1959. A preliminary study of the formation of Yellow Sea Cold Mass and its properties. Oceanol Limnol Sin (in Chinese), 2(1): 11–15

Hur H B, Jacobs G A, Teague W J. 1999. Monthly variations of water masses in the Yellow and East China Seas, November 6, 1998. J Oceanogr, 55(2): 171–184

Johnson P W, Sieburth J M. 1979. Chroococcoid cyanobacteria in the sea: a ubiquitous and diverse phototrophic biomass. Limnol Oceanogr, 24(5): 928–935

Kang J H, Kim W S. 2008. Spring dominant copepods and their distribution pattern in the Yellow Sea. Ocean Sci J, 43(2): 67–79

Katano T, Kaneda A, Takeoka H, et al. 2005. Seasonal changes in the abundance and composition of picophytoplankton in relation to the occurrence of '*Kyucho*' and bottom intrusion in Uchiumi Bay, Japan. Mar Ecol Prog Ser, 298: 59–67

Lemée, R, Rochelle-Newall E, Van Wambeke F, et al. 2002. Seasonal variation of bacterial production, respiration and growth efficiency in the open NW Mediterranean Sea. Aquat Microb Ecol, 29(3): 227–237

Li W K W. 1998. Annual average abundance of heterotrophic bacteria and *Synechococcus* in surface ocean waters. Limnol Oceanogr, 43(7): 1746–1753

Li Hongbo, Xiao Tian, Ding Tao, et al. 2006. Effect of the Yellow Sea Cold Water Mass (YSCWM) on distribution of bacterioplankton. Acta Ecol Sini, 26(4): 1012–1019

Li Ang, Yu Fei, Diao Xinyuan, et al. 2015. Interannual variability of temperature of the northern Yellow Sea Cold Water Mass. Haiyang Xuebao (in Chinese), 37(1): 30–42

Lin D, Zhu A, Xu Z, et al. 2010. Dynamics of photosynthetic picoplankton in a subtropical estuary and adjacent shelf waters. J Mar Biol Assoc United Kingdom, 90(7): 1319–1329

Mitbavkar S, Saino T, Horimoto N, et al. 2009. Role of environment and hydrography in determining the picoplankton community structure of Sagami Bay, Japan. J Oceanogr, 65(2): 195–208

Miyazono A, Odate T, Maita Y. 1992. Seasonal fluctuations of cell density of cyanobacteria and other picophytoplankton in Iwanai Bay, Hokkaido, Japan. J Oceanogr, 48(3): 257–266

Moisan T A, Blattner K L, Makinen C P. 2010. Influences of temperature and nutrients on *Synechococcus* abundance and biomass in the southern Mid-Atlantic Bight. Cont Shelf Res, 30(12): 1275–1282

Morán X A G. 2007. Annual cycle of picophytoplankton photosyn-

thesis and growth rates in a temperate coastal ecosystem: a major contribution to carbon fluxes. Aquat Microb Ecol, 49(3): 267–279

Pan L A, Zhang J, Zhang L H. 2007. Picophytoplankton, nanophytoplankton, heterotrohpic bacteria and viruses in the Changjiang Estuary and adjacent coastal waters. J Plankton Res, 29(2): 187–197

Platt T, Rao D V S, Irwin B. 1983. Photosynthesis of picoplankton in the oligotrophic ocean. Nature, 301(5902): 702–704

Shimada A, Nishijima M, Maruyama T. 1995. Seasonal appearance of *Prochlorococcus* in Suruga Bay, Japan in 1992-1993. J Oceanogr, 51(3): 289–300

Su Jilan, Huang Daji. 1995. On the current field associated with the Yellow Sea Cold Water Mass. Oceanol Limnol Sin Supp, (in Chinese), 26(5): 1–7

Tarran G A, Bruun J T. 2015. Nanoplankton and picoplankton in the Western English Channel: abundance and seasonality from 2007–2013. Prog Oceanogr, 137: 446–455

Tsai A Y, Chiang K P, Chang J, et al. 2008. Seasonal variations in trophic dynamics of nanoflagellates and picoplankton in coastal waters of the western subtropical Pacific Ocean. Aquat Microb Ecol, 51(3): 263–274

Uysal Z, Köksalan I. 2006. The annual cycle of *Synechococcus* (cyanobacteria) in the northern Levantine Basin shelf waters (Eastern Mediterranean). Mar Ecol, 27(3): 187–197

Van Dongen-Vogels V, Seymour J R, Middleton J F, et al. 2011. Influence of local physical events on picophytoplankton spatial and temporal dynamics in South Australian continental shelf waters. J Plankton Res, 33(12): 1825–1841

Wang Baodong. 2000. Characteristics of variations and interrelations of biogenic elements in the Huanghai Sea Cold Water Mass. Haiyang Xuebao (in Chinese), 22(6): 47–54

Waterbury J B, Watson S W, Guillard R R L, et al. 1979. Widespread occurrence of a unicellular, marine, planktonic, cyanobacterium. Nature, 277(5694): 293–294

Wikner J, Hagström Å. 1991. Annual study of bacterioplankton community dynamics. Limnol Oceanogr, 36(7): 1313–1324

Xin Ming, Ma Deyi, Wang Baodong. 2015. Chemicohydrographic characteristics of the Yellow Sea Cold Water Mass. Acta Ecol Sin, 34(6): 5–11

Yao Zhigang, Bao Xianwen, Li Na, et al. 2012. Seasonal evolution of the Northern Yellow Sea Cold Water Mass. Period Ocean Univ China (in Chinese), 42(6): 9–15

Yin Jiehui, Zhao Zengxia, Zhang Guangtao, et al. 2013. Tempo-spatial variation of nutrient and chlorophyll-*a* concentrations from Summer to Winter in the Zhangzi Island area (Northern Yellow Sea). J Ocean Univ China, 12(3): 373–384

Yu Ying, Zhang Wuchang, Wang Shiwei, et al. 2013. Abundance and biomass of planktonic ciliates in the sea area around Zhangzi Island, Northern Yellow Sea. Acta Ecol Sin, 33(1): 45–51

Zhang S W, Wang Q Y, Lü Y, et al. 2008. Observation of the seasonal evolution of the Yellow Sea Cold Water Mass in 1996–1998. Cont Shelf Res, 28(3): 442–457

Zhao Yuan, Zhao Li, Xiao Tian, et al. 2011. Spatial and temporal variation of picoplankton distribution in the Yellow Sea, China. Chin J Oceanol Limnol, 29(1): 150–162

Zou Emei, Xiong Xuejun, Guo Binghuo, et al. 2001. Characteristics and seasonal variations of the thermocline and halocline in the Huanghai Sea and the East China Sea. J Oceanogr Huanghai Bohai Seas (in Chinese), 19(3): 8–18

Acta Oceanol. Sin., 2018, Vol. 37, No. 5, P. 107–112
DOI: 10.1007/s13131-018-1167-7
http://www.hyxb.org.cn
E-mail: hyxbe@263.net

Integration of the nuclease protection assay with sandwich hybridization (NPA-SH) for sensitive detection of *Heterocapsa triquetra*

PARK Mirye[1, 2], PARK So Yun[1], HWANG Jinik[1], JUNG Seung Won[1], LEE Juyun[3], CHANG Man[3], LEE Taek-Kyun[1]*

[1] South Sea Environment Research Department, Korea Institute of Ocean Science and Technology, Geoje 53201, Republic of Korea

[2] Bioresources Culture Collection Division, Nakdonggang National Institute of Biological Resources, Sangju 37242, Republic of Korea

[3] Research Strategy Team, Korea Marine Environment Management Corporation, Seoul 05718, Republic of Korea

Received 29 August 2017; accepted 11 December 2017

Abstract

Microalgae are photosynthetic microorganisms that function as primary producers in aquatic ecosystems. Some species of microalgae undergo rapid growth and cause harmful blooms in marine ecosystems. *Heterocapsa triquetra* is one of the most common bloom-forming species in estuarine and coastal waters worldwide. Although this species does not produce toxins, unlike some other *Heterocapsa* species, the high density of its blooms can cause significant ecological damage. We developed a *H. triquetra* species-specific nuclease protection assay sandwich hybridization (NPA-SH) probe that targets the large subunit of ribosomal RNA (LSU rRNA). We tested probe specificity and sensitivity with five other dinoflagellates that also cause red tides. Our assay detected *H. triquetra* at a concentration of 1.5×10^4 cells/mL, more sensitive than required for a red-tide guidance warning by the Korea Ministry of Oceans and Fisheries in 2015 (3.0×10^4 cells/mL). We also used the NPA-SH assay to monitor *H. triquetra* in the Tongyeong region of the southern sea area of Korea during 2014. This method could detect *H. triquetra* cells within 3 h. Our assay is useful for monitoring *H. triquetra* under field conditions.

Key words: nuclease protection assay sandwich hybridization, *Heterocapsa triquetra*, red tide, monitoring

Citation: Park Mirye, Park So Yun, Hwang Jinik, Jung Seung Won, Lee Juyun, Chang Man, Lee Taek-Kyun. 2018. Integration of the nuclease protection assay with sandwich hybridization (NPA-SH) for sensitive detection of *Heterocapsa triquetra*. Acta Oceanologica Sinica, 37(5): 107–112, doi: 10.1007/s13131-018-1167-7

1 Introduction

Microalgae, which occur as single cells or chains, are photosynthetic microorganisms and primary producers in aquatic ecosystems (Debelius et al., 2009; Ebenezer et al., 2012; Morel and Price, 2003). Microalgae can be utilized in producing commercial products, such as cosmetics, food, biofuels, and health-promoting medications (Priyadarshani and Rath, 2012; Spolaore et al., 2006). Some microalgae can grow quickly under favorable environmental conditions (Naito et al., 2005). The rapid growth of microalgae makes it possible to mass-produce commercial products, but also cause harmful algal blooms in marine ecosystems.

Heterocapsa triquetra is a common bloom-forming dinoflagellate species present in estuarine coastal waters and brackish waters worldwide (Tas, 2015; Baek et al., 2011). Although it does not release toxins, high-density blooms can lead to ecological damage (Litaker et al., 2002a, b). *Heterocapsa triquetra* blooms occur regularly in the North Sea, Atlantic Ocean, the Mediterranean Sea, and the eastern Pacific Ocean (Litaker et al., 2002a). In Korea, *H. triquetra* is a dominant species in the Masan Bay and the Jinhae Bay from autumn to winter (Baek et al., 2011; Lee and Han, 2007). *Heterocapsa triquetra* blooms can harm the commercial shellfish and fish industries (Archambault et al., 2004; Lu and Hodgkiss, 2004). Therefore the identification and monitoring of *H. triquetra* are needed for characterization of their distribution and favorite blooming conditions.

The traditional method for identification and quantitation of microalgal species is observation of morphology by microscopy, but this requires an experienced biologist and is time-consuming. Moreover, different biologists may report different results when microalgae are identified by this traditional method (Suh et al., 2016), and changes in the appearance and size of microalgae under different environmental conditions or different growth stages can make identification difficult (Xin et al., 2005). Therefore, there is increasing interest in several molecular-based detection methods, such as the polymerase chain reaction (PCR), fluorescence *in situ* hybridization (FISH), real-time PCR, restriction fragment length polymorphism (RFLP), flow cytometry and microscopy (FlowCAM), and the sandwich hybridization assay (SHA) (Godhe et al., 2001; Chen et al., 2013; Antonella and Luca, 2013; Jedlicki et al., 2012; Hyka et al., 2013; Diercks et al., 2008b).

The rRNA-targeted sandwich hybridization assay (SHA) uses

Foundation item: The Public Welfare & Safety Research Program through the National Research Foundation of Korea (NRF), funded by the Ministry of Science, ICT & Future Planning under contract No. NRF-2013M3A2A1067529.
*Corresponding author, E-mail: tklee@kiost.ac.kr

two probes, a capture probe and signal probe. The capture probe (rRNA) and signal probe are combined like a sandwich (Tyrrell et al., 2002). Previous researchers developed SHA-detection methods for several microalgae: *Heterosigma akashiwo*, *Fibrocapsa japonica*, *Alexandrium minutum*, *Gymnodinium catenatum*, *Lingulodinium polyedrum*, and *Protoceratium reticulatum* (Tyrrell et al., 2002; Ayers et al., 2005; Diercks et al., 2008a, b). Subsequently, problems with this method appeared when targeting unstable RNA with limited specificity and reproducibility. This led to development of a nuclease protection assay that is based on sandwich hybridization (NPA-SH) (Cai et al., 2006; Zhen et al., 2007). This newer method uses the same two probes as the SHA method, as well as a third NPA probe. More specifically, the NPA-SH method uses S1 nuclease after hybridization of the target RNA and NPA probe. The S1 nuclease degrades the sample to single stranded oligonucleotides, resulting in perfectly matched NPA probes. This method makes many copies of the target DNA, and the NPA probe is more stable and specific than the rRNA used for the SHA probe (Suh et al., 2016). Previous researchers have already developed NPA-SH detection methods for *Cochlodinium polykrikoides*, *Prorocentrum minimum*, *Prorocentrum micans*, *Prorocentrum donghaiense*, *Skeletonema costatum*, and *Phaeocystis globosa* (Suh et al., 2016; Cai et al., 2006; Zhen et al., 2008, 2009). However an NPA-SH method for detection of *H. triquetra* has not yet been developed. This species is currently detected by a beta-methylamino-L-alanine (BMAA) method that employs ultra-high pressure liquid chromatography coupled with mass spectroscopy (UHPLC-MS/MS).

In this study, we developed a *H. triquetra* NPA-SH species-specific probe in an effort to easily and rapidly detect this species, comparable to other NPA-SH assays for microalgae. Then we used the method for field monitoring near Tongyeong, in the southern sea area of Korea. Tongyeong is located near the Masan Bay and the Jinhae Bay, where blooms of *H. triquetra* are common (Park et al., 2013). However compared with other places near Tongyeong, such as the Masan Bay and the Jinhae Bay, data on *H. triquetra* is poor near Tongyeong. Thus, we monitored *H. triquetra* near Tongyeong using species specific probes and the NPA-SH method from January to December of 2014.

2 Materials and methods

2.1 *Microalgae cultures*

Ten species of microalgae (*Asterionellopsis glacialis*, *Chattonella marina*, *Chaetoceros curvisetus*, *Eucampia zodiacus*, *Heterosigma akashiwo*, *Leptocylindrus danicus*, *Prorocentrum minimum*, *Scrippsiella trochoidea*, *Skeletonema marinoi*, and *Thalassiosira nordenskioeldii*) were collected in Tongyeong, and cultivated at the Korea Institute of Ocean and Science Technology (KIOST) in Geoje, Korea. *Cochlodinium polykrikoides* was obtained from the Library of Marine Samples in KIOST and *H. triquetra* was from a laboratory at KIOST (Baek et al., 2011). All 12 species were cultured in f/2 medium with salinity 30 at 20°C under 12 h light-dark cycle.

2.2 *Microalgae RNA prep and sequencing*

RNA was extracted according to a modification of the method described by Venugopalan and Kapoor (Venugopalan and Kapoor, 1997), and was used to produce cDNA using the GoScript™ Reverse Transcription System (Promega, Madison, WI, USA). The LSU rDNA genes were subjected to PCR with a pair of primers (forward 5′-CGGAGGAAAAGAAACTAAC, reverse 5′-AGCTACTAGATGGTTCGAT) (Zhen et al., 2007). PCR amplification was conducted using a 20 μL reaction mixture that contained 2 μL of 10× reaction buffer, 2 μL of 2.5 mmol/L dNTPs, 2.5 units of Taq DNA polymerase (TaKaRa, Japan), 1 μL of 30 ng/μL total DNA, and 1 μL each of 10 μmol/L forward primer and reverse primer. The PCR amplification protocol was 10 min at 94°C, 35 cycles of denaturation at 94°C for 30 s, annealing at 60°C for 30 s, extension at 72°C for 30 s, and then a 5 min extension at 72°C. The PCR products were separated by 1% agarose gel electrophoresis, and then purified using the MEGA-spin™ Agarose Gel DNA Extraction Kit (Intron, Korea). Products were then cloned into the pGEM-T-Easy Vector (Promega, Madison, WI, USA) and used for transformation of *E. coli* DH5α cells. LSU rRNA genes were sequenced by Bioneer Corporation (Daejeon, South Korea), and sequences were analyzed using DNAstar and MEGA6 software.

2.3 *NPA-SH specific probes and detection*

The sequenced LSU rDNA of *H. triquetra* was confirmed by search of BLASTn (http://www.ncbi.nlm.nih.gov/Blast.cgi). Then, the sequences of all 12 species were aligned, using Clustal W in MEGA6, and the most variable regions were identified for use in making an NPA probe for *H. triquetra*. Three probes were designed: a ~60-mer NPA probe targeting LSU rRNA; a 25-mer capture probe that was labeled with biotin at the 5′ end and had a 3′ terminal region that was complementary to the NPA probe; and a 25-mer signal probe that was labeled with fluorescein at the 3′ end and was complementary to the 5′ terminal region of the NPA probe. The NPA probe for *H. triquetra* was 5′-CCACGCTTGCGCTGAAGCAGCAGGCAATCACATTAGCACGCACCAATCTTGCCAAGAAGC; the capture probe was 5′-biotin-GCTTCTTGGCAAGATTGGTGCGTGC; and the signal probe was 5′-GCCTGCTGCTTCAGCGCAAGCGTGG-fluorescein (Table 1). All probes were chemically synthesized by Bioneer Corporation (Daejeon, Korea). The NPA-SH analysis was modified from Cai et al. (2006) (Zhen et al., 2007). Cultured *H. triquetra* were collected in a 1.5 mL Eppendorf tube after centrifugation to remove growth medium. Then, 950 μL of lysis buffer (80% formamide, 450 mmol/L NaCl, 5 mmol/L Na_2EDTA, 1 mg/mL yeast tRNA, 1% SDS, pH 6.4) and 50 μL of 10 mg/mL yeast t-RNA was added, and the sample was sonicated for 10 s with 50% duty cycle and 450 W output sets. The sample was centrifuged again to precipitate cell debris. Then, 30 μL of lysate, 3 μL of NPA probe solution (500 nmol/L NPA probes in lysis buffer), and 50 μL of mineral oil were mixed in a 1.5 mL Eppendorf tube. The sample was denatured at 98°C for 5 min and then cooled to room temperature to allow hybridization of the NPA probe with the 28S rRNA. Then, 30 μL of S1 nuclease mix was added (60 units S1 nuclease in 1.4 mol/L sodium chloride, 22.5 mmol/L zinc sulfate, 250 mmol/L sodium acetate, pH 4.5) (Promega, USA), and the sample was incubated for 1 h at 42°C to restrict non-hybridized regions. The reaction was stopped by adding 150 μL of a nuclease stop solution (62.5 mmol/L sodium hydroxide, 30 mmol/L EDTA, and 1× phosphate-buffered saline (PBS), pH 7.2). The mixture was then denatured at 98°C for 5 min, and used before it had cooled. The sample was coated with biotin-labeled capture probes in a 96-well streptavidin-coated microplate (Pierce Biotechnology, Inc. Rockford, IL.), with each well containing 100 μL of S1 nuclease-treated sample. The plate was cooled to room temperature for 5 min, washed three times with PBS and 0.5% Tween-20. Each well was filled with 100 μL of 5 nmol/L signal probes in a hybridization buffer (4× SSC, 10% formamide, 0.02% SDS pH 7.2), and the plate was incubated at 50°C for 20 min with shaking (130 r/min). After washing three times with PBST (3.2 mmol/L Na_2HPO_4, 0.5

Table 1. NPA sandwich hybridization specific probes

Detection method	Probe	Sequence	Length/bp
NPA-SH	Capture probe	Biotin-GCTTCTTGGCAAGATTGGTGCGTGC	25
	NPA probe	CCACGCTTGCGCTGAAGCAGCAGGCAATCACATTAGCACGCACCAATCTTGCCAAGAAGC	60
	Signal probe	GCCTGCTGCTTCAGCGCAAGCGTGG-FAM	25

mmol/L KH_2PO_4, 1.3 mmol/L KCl, 135 mmol/L NaCl, 0.5% Tween20, pH 7.4), 100 μL of an anti-fluorescein-POD (Roche, USA, 1:6 000 dilution in PBS, 2% goat serum) was added to each well. Then, the plate was incubated at 37°C for 10 min, and washed three times with PBS. Finally, 100 μL/well of 3, 3′, 5, 5′-tetramethylbenzidine (TMB, Sigma, USA) substrate was added, and the sample was incubated at 37°C for 10 min to allow blue color development. The reaction was stopped by adding 50 μL of 2 mol/L H_2SO_4 per well, causing the color to change to yellow. Absorbance was measured at 450 nm and 620 nm using a plate reader (FLUOstar, BMG Thermo Fisher Scientific Inc, USA) and the $A_{450\,nm}/A_{620\,nm}$ ratio was calculated.

The specificity was checked with six cultured microalgae: *C. marina*, *C. polykrikoides*, *H. triquetra*, *H. akashiwo*, *P. minimum*, and *S. trochoidea*. The sensitivity was tested by counting *H. triquetra* under light microscopy using serial dilutions. Three replicates of each dilution were analyzed. The absorbance of NPA-SH and microscopic data were compared.

2.4 *Field sample collection and test*

Natural seawater was collected monthly near Tongyeong, Korea (34°45′97.58″N, 128°22′54.62″E) from January to December 2014 (Jan. 24, Feb. 14, Mar. 10, Apr. 9, May 15, Jun. 19, Jul. 22, Aug. 27, Sep. 19, Oct. 16, Nov. 18, and Dec. 11). Samples were collected in surface seawater (1 L) using a net with a pore size of 0.2 μm. At the same time, water temperature, salinity, pH, and dissolved oxygen (DO) were measured by YSI instrument. The sample was immediately placed on ice, and then carried to the laboratory. Then, the sample was centrifuged at 3 000 r/min for 10 min, the supernatant was removed, and the pellet was stored at –70°C until use. Stored samples were used for the *H. triquetra* NPA-SH assay. Only lysis buffer and yeast t-RNA were added to the frozen samples, and the samples were sonicated for lysis of microalgae, using the same parameters as for NPA-SH lysis.

2.5 *Statistical analysis*

NPA-SH assay was performed at least three times in quadruplicate for each experiment. All data were presented as means±SE. A student's *t*-test was performed to test differences between controls and each experimental group.

3 Results

3.1 *Probe specificity*

We isolated total RNA of microalgae that are responsible for red tides (*C. marina*, *C. polykrikoides*, *H. triquetra*, *H. akashiwo*, *P. minimum*, and *S. trochoidea*), and of which the most abundant species were near Tongyeong (*A. glacialis*, *C. curvisetus*, *E. zodiacus*, *L. danicus*, *S. marinoi*, and *T. nordenskioeldii*). Then, we analyzed the LSU sequences of all species to design *H. triquetra* species-specific probes for NPA-SH. The results show the signals of sixmicroalgae samples, a negative control, and a mixed sample of *C. marina*, *C. polykrikoides*, *H. triquetra*, *H. akashiwo*, *P. minimum*, and *S. trochoidea* (Fig. 1). The signal of each sample ($A_{450\,nm}/A_{620\,nm}$) expressed relatively to the negative control. *Heterocapsa triquetra* had the strongest signal (1.59), consistent with its yellow color, and all the other samples had signals less than 1.06. This result means that the *H. triquetra* NPA-SH oligonucleotide probe can distinguish *H. triquetra* from five other microalgae that are also responsible for red tides.

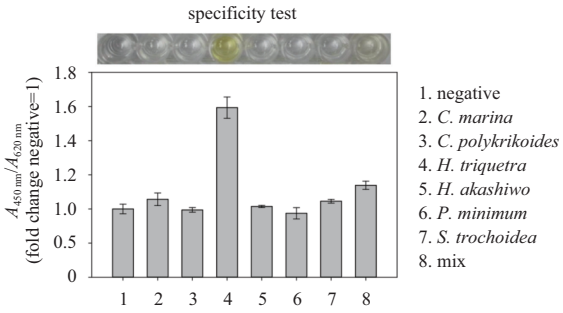

Fig. 1. Specificity of the *H. triquetra* sandwich hybridization probe. The *H. triquetra* sample and the mixed sample (which included *H. triquetra*) appeared yellow (above) and had $A_{450\,nm}/A_{620\,nm}$ values greater than all other samples.

3.2 *Probe sensitivity*

We tested probe sensitivity by measuring the signal with different numbers of cells (Fig. 2). The results show that the signal was above baseline when the cell concentration was 1.5×10^4 cells/mL (Fig. 2). This is lower than 3.0×10^4 cells/mL standard threshold for a red-tide warning issued by the Korea Ministry of Oceans and Fisheries in 2015. We also established a standard curve for the range of 3.0×10^3 to 1.5×10^5 cells/mL. The least-squares linear regression equation was $y=0.526\,4x+0.353\,5$, $r^2=0.893\,2$ (Fig. 2).

3.3 *Probes test at field sample*

Finally, we tested the NAP-SH method using field samples collected from natural seawater near Tongyeong, in the southern sea area of Korea (Fig. 3). We analyzed three samples per month from January to December of 2014. Based on the standard regression equation above, the $A_{450\,nm}/A_{620\,nm}$ value of 1.11 in September corresponds to 2 874 cells/mL, and the $A_{450\,nm}/A_{620\,nm}$ value of 1.23 in December corresponds to 3 330 cells/mL. All other months had no detectable *H. triquetra* (Fig. 4).

4 Discussion

Detection of red tide species in seawater samples is important for monitoring the occurrence of red tides. For example, identification of the onset of a harmful algal bloom may allow implementation of measures that can reduce economic and/or environmental damage. Previously, identification and detection of microalgae depended on viewing the morphological characteristics by microscopy (Suh et al., 2016; Ki and Han, 2006). Though many molecular detection methods are now available for detecting red tide species, only one chemical method is currently available for detection of *H. triquetra*. This motivated us to develop NPA-SH probes to detect *H. triquetra* in natural field samples (Jiang and Ilag, 2014).

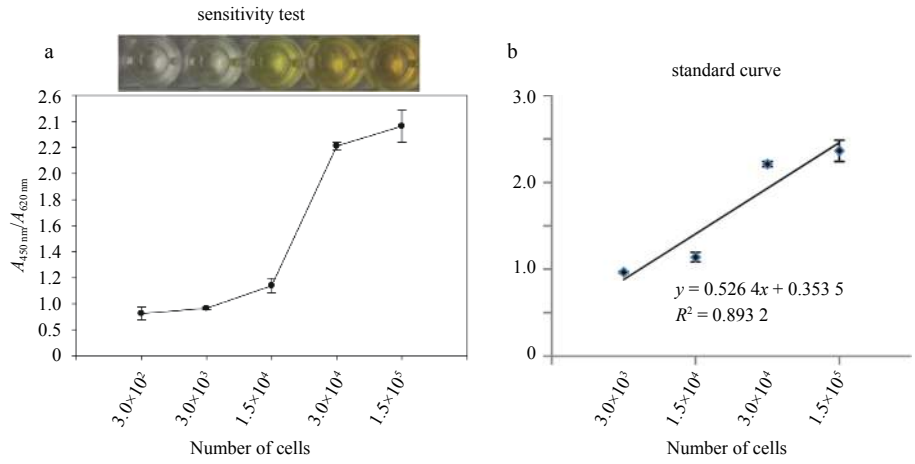

Fig. 2. Sensitivity of *H. triquetra* sandwich hybridization probe. a. Samples with fewer than 3.0×10^2 cells/mL had $A_{450\,nm}/A_{620\,nm}$ values of about 1.0, and were colorless. As cell numbers increased, they became yellow and the $A_{450\,nm}/A_{620\,nm}$ values increased. b. A standard curve for cells in the concentration range of 3.0×10^3 to 1.5×10^5 cells/mL.

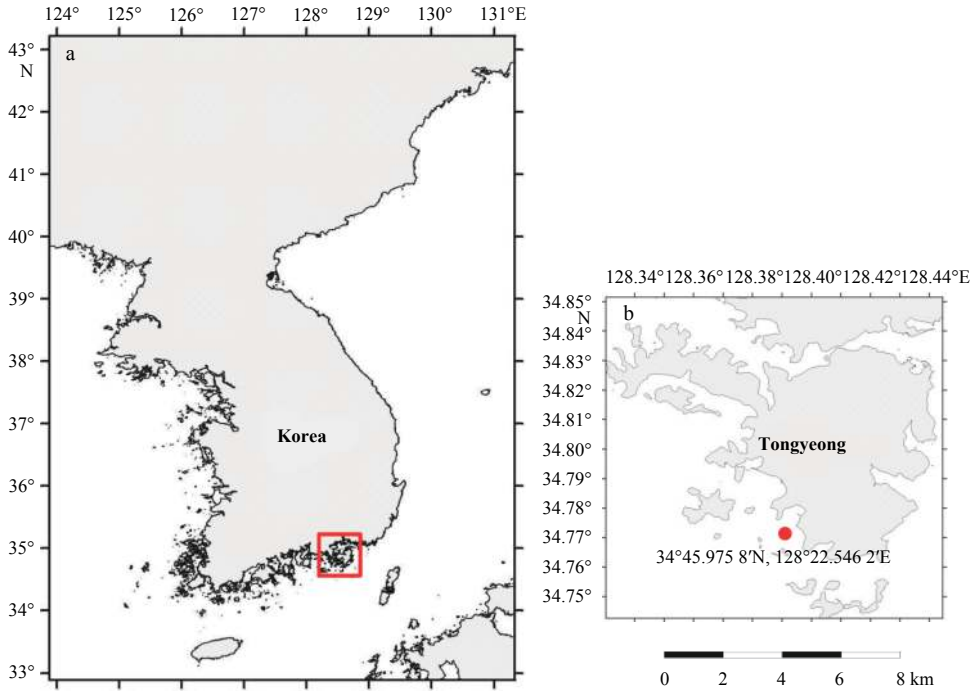

Fig. 3. Sampling locations near Tongyeong, in the southern sea area of Korea. a. The red square shows the location of Tongyeong. b. Expansion of Tongyeong region. The red circle shows the sampling location.

The NPA-SH method is an elaboration of the more simple SHA method. Researchers have used the rRNA-targeted SHA method to detect phytoplankton since 1996. In particular, researchers who used this method in New Zealand to monitor microalgae received international accreditation in 2004 (Ayers et al., 2005). However, the limitations of this method, such as use of degradative RNA, low specificity and low reproducibility, led to the development of the newer NPA-SH method (Zhen et al., 2007). Skipping the RNA extraction step also reduces the time needed for the NPA-SH method. Additionally, we also reduced hybridization times for the capture probe and NPA probe, and the NPA probe and signal probe. This reduced the total time by 4 h (Cai et al., 2006). The principle of probe hybridization is the same as the PCR annealing step. Thus, probe hybridization requires just a few seconds to a few minutes after denaturation. By reducing the hybridization time to about 5 min, we were able to detect *H. triquetra* within 3 h of sample collection. Another benefit of the NPA-SH method is that the results can be checked visually, in that the yellow color is evident on streptavidin-coated plates (Figs 1, 2 and 4). This is a major advantage of the NPS-SH method when it is in need of detecting *H. triquetra* in the field.

We developed *H. triquetra* specific-probes for NPA-SH, and monitored it over 2014 near Tongyeong. *Heterocapsa triquetra* were detected in September and December of 2014 near Tongyeong (Figs 3 and 4). Normally, *H. triquetra* is a major species from autumn to winter in the Masan Bay and the Jinhae Bay, which are located near Tongyeong (Lee and Han, 2007; Lee et al., 2005). In the Masan Bay and the Jinhae Bay, *H. triquetra*

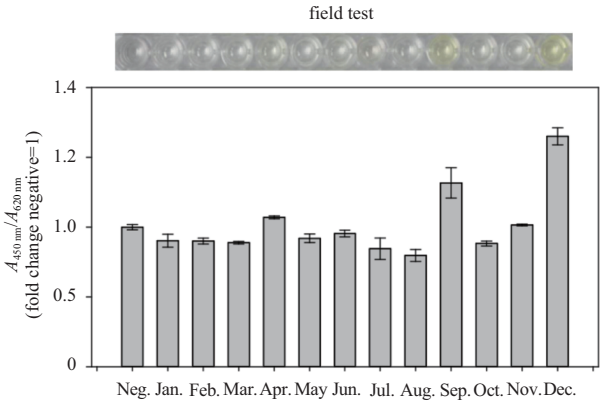

Fig. 4. *Heterocapsa triquetra* field sampling by NPA-SH during 2014. *Heterocapsa triquetra* appeared during September and December.

bloomed at extremely low salinities (below 25) after heavy rainfall (Lee and Limand, 2006). However, in the Mediterranean Sea near Turkey, this species appeared in January to April, and was undetectable in May (Tas, 2015). Normally, *H. triquetra* grows between 10°C and 25°C at salinity of 15 to 40, although it can adapt to a broad range of temperatures and salinities (Baek et al., 2011). Thus, *H. triquetra* blooms may depend on environmental conditions, such as nitrogen influx from heavy rain and the influx of freshwater.

The seawater temperature and salinity near Tongyeong were 22.5°C and 33.61 in September 2014, 13.9°C and 33.93 in December 2014. The temperatures were favorable for *H. triquetra*, but the salinity levels were a bit higher than those at the Masan Bay and the Jinhae Bay during the bloom season (Lee and Han, 2007; Lee and Limand, 2006). *Heterocapsa triquetra* is a mixotrophic dinoflagellate that does not produce toxins (Battocchi et al., 2010), but blooms can increase the pH to above 9.0, thereby disrupting ecosystem function. At the sampling times, we found no evidence of blooms based on surface observations, the seawater pH was always below 9.0, and there were no red-tide warnings. Although *H. triquetra* blooms did not appear in 2014, continuous monitoring is needed to better understand the environmental factors that influence *H. triquetra* blooming. Also, regular monitoring makes it possible to provide early warnings before the occurrence of serious red tides.

5 Conclusions

We developed species-specific probes using the NAP-SH method to detect and identify *H. triquetra* from environmental samples. This technique was effective in identification of *H. triquetra* in cultured microalgae samples and in natural seawater samples. We can detect cells at a concentration of 1.5×10^4 cells/mL, a greater sensitivity that required by the Korea Ministry of Oceans and Fisheries guidelines. We successfully used this method to monitor environmental samples for *H. triquetra* and found it could detect *H. triquetra* in the field without the use of laboratory equipment. The NPA-SH method described here can detect *H. triquetra* from field samples within 2 h without requiring expert knowledge in microalgal morphology. It is promising for the development of an easy-to-use *H. triquetra* detection kit.

References

Antonella P, Luca G. 2013. The quantitative real-time PCR applications in the monitoring of marine harmful algal bloom (HAB) species. Environ Sci Pollut Res, 20(10): 6851–6862

Archambault M C, Bricelj V M, Grant J, et al. 2004. Effects of suspended and sedimented clays on juvenile hard clams, *Mercenaria mercenaria*, within the context of harmful algal bloom mitigation. Mar Biol, 144(3): 553–565

Ayers K, Rhodes L L, Tyrrell J, et al. 2005. International accreditation of sandwich hybridisation assay format DNA probes for microalgae. New Zealand J Mar Freshw Res, 39(6): 1225–1231

Baek S H, Ki J S, Katano T, et al. 2011. Dense winter bloom of the dinoflagellate *Heterocapsa triquetra* below the thick surface ice of brackish Lake Shihwa, Korea. Phycol Res, 59(4): 273–285

Battocchi C, Totti C, Vila M, et al. 2010. Monitoring toxic microalgae *Ostreopsis* (dinoflagellate) species in coastal waters of the Mediterranean Sea using molecular PCR-based assay combined with light microscopy. Mar Pollut Bull, 60(7): 1074–1084

Cai Qingsong, Li Rongxiu, Zhen Yu, et al. 2006. Detection of two *Prorocentrum* species using sandwich hybridization integrated with nuclease protection assay. Harmful Algae, 5(3): 300–309

Chen Guofu, Liu Yang, Zhang Chunyun, et al. 2013. Development of rRNA-targeted probes for detection of *Prorocentrum micans* (Dinophyceae) using whole cell in situ hybridization. J Appl Phycol, 25(4): 1077–1089

Debelius B, Forja J M, DelValls Á, et al. 2009. Toxicity and bioaccumulation of copper and lead in five marine microalgae. Ecotoxicol Environ Saf, 72(5): 1503–1513

Diercks S, Medlin L K, Metfies K. 2008a. Colorimetric detection of the toxic dinoflagellate *Alexandrium minutum* using sandwich hybridization in a microtiter plate assay. Harmful Algae, 7(2): 137–145

Diercks S, Metfies K, Medlin L K. 2008b. Molecular probe sets for the detection of toxic algae for use in sandwich hybridization formats. J Plankton Res, 30(4): 439–448

Ebenezer V, Medlin L K, Ki J S. 2012. Molecular detection, quantification, and diversity evaluation of microalgae. Mar Biotechnol, 14(2): 129–142

Godhe A, Otta S K, Rehnstam-Holm A S, et al. 2001. Polymerase chain reaction in detection of *Gymnodinium mikimotoi* and *Alexandrium minutum* in field samples from southwest India. Mar Biotechnol, 3(2): 152–162

Hyka P, Lickova S, Přibyl P, et al. 2013. Flow cytometry for the development of biotechnological processes with microalgae. Biotechnol Adv, 31(1): 2–16

Jedlicki A, Fernández G, Astorga M, et al. 2012. Molecular detection and species identification of *Alexandrium* (Dinophyceae) causing harmful algal blooms along the Chilean coastline. AoB Plants, 2012: pls033

Jiang Liying, Ilag L L. 2014. Detection of endogenous BMAA in dinoflagellate (*Heterocapsa triquetra*) hints at evolutionary conservation and environmental concern. PubRaw Sci, 1(2): 1–8

Ki J S, Han M S. 2006. A low-density oligonucleotide array study for parallel detection of harmful algal species using hybridization of consensus PCR products of LSU rDNA D2 domain. Biosens Bioelectron, 21(9): 1812–1821

Lee J Y, Han M S. 2007. Change of blooming pattern and population dynamics of phytoplankton in Masan bay, Korea. Journal of the Korean Society of Oceanography, 12(3): 147–158

Lee C K, Lee O H, Lee S G. 2005. Impacts of temperature, salinity and irradiance on the growth of ten harmful algal bloom-forming microalgae isolated in Korean coastal waters. Journal of the Korean Society of Oceanography, 10(1): 79–91

Lee C, Limand W. 2006. Variation of harmful algal blooms in Masan-Chinhae Bay. ScienceAsia, 32(S1): 51–56

Litaker R W, Tester P A, Duke C S, et al. 2002a. Seasonal niche strategy of the bloom-forming dinoflagellate *Heterocapsa triquetra*. Mar Ecol Prog Ser, 232: 45–62

Litaker R W, Warner V E, Rhyne C, et al. 2002b. Effect of diel and interday variations in light on the cell division pattern and *in situ* growth rates of the bloom-forming dinoflagellate *Heterocapsa triquetra*. Mar Ecol Prog Ser, 232: 63–74

Lu Songhui, Hodgkiss I J. 2004. Harmful algal bloom causative collected from Hong Kong waters. Hydrobiologia, 512(1–3): 231–238

Morel F M M, Price N M. 2003. The biogeochemical cycles of trace metals in the oceans. Science, 300(5621): 944–947

Naito K, Matsui M, Imai I. 2005. Ability of marine eukaryotic red tide microalgae to utilize insoluble iron. Harmful Algae, 4(6): 1021–1032

Park J, Jeong H J, Yoo Y D, et al. 2013. Mixotrophic dinoflagellate red tides in Korean waters: distribution and ecophysiology. Harmful Algae, 30(S1): S28–S40

Priyadarshani I, Rath B. 2012. Commercial and industrial applications of micro algae-a review. J Algal Biomass Utln, 3(4): 89–100

Spolaore P, Joannis-Cassan C, Duran E, et al. 2006. Commercial applications of microalgae. J Biosci Bioeng, 101(2): 87–96

Suh S S, Park M, Hwang J, et al. 2016. Detection of the dinoflagellate, *Cochlodinium polykrikoides*, that forms algal blooms using sandwich hybridization integrated with nuclease protection assay. Biotechnol Lett, 38(1): 57–63

Tas S. 2015. A prolonged red tide of *Heterocapsa triquetra* (Ehrenberg) F. Stein (Dinophyceae) and phytoplankton succession in a eutrophic estuary in Turkey. Mediterr Mar Sci, 16(3): 621–627

Tyrrell J V, Connell L B, Scholin C A. 2002. Monitoring for *Heterosigma akashiwo* using a sandwich hybridization assay. Harmful Algae, 1(2): 205–214

Venugopalan C, Kapoor H C. 1997. Single step isolation of plant RNA. Phytochemistry, 46(8): 1303–1305

Xin Zeyu, Yu Zhigang, Wang Tanchun, et al. 2005. Identification and quantification of the toxic dinoflagellate *Gymnodinium* sp. with competitive enzyme-linked immunosorbent assay (cELISA). Harmful Algae, 4(2): 297–307

Zhen Yu, Mi Tiezhu, Yu Zhigang. 2008. Detection of *Phaeocystis globosa* using sandwich hybridization integrated with nuclease protection assay (NPA-SH). J Environ Sci, 20(12): 1481–1486

Zhen Yu, Mi Tiezhu, Yu Zhigang. 2009. Detection of several harmful algal species by sandwich hybridization integrated with a nuclease protection assay. Harmful Algae, 8(5): 651–657

Zhen Yu, Yu Zhigang, Cai Qingsong, et al. 2007. Detection of two diatoms using sandwich hybridization integrated with nuclease protection assay (NPA-SH). Hydrobiologia, 575(1): 1–11

Acta Oceanol. Sin., 2018, Vol. 37, No. 5, P. 113–116
DOI: 10.1007/s13131-018-1175-7
http://www.hyxb.org.cn
E-mail: hyxbe@263.net

Target-directed isolation and identification of a serum lectin from lamprey (*Lampetra japonica*) by chromatographys and MALDI-TOF/TOF

HAN Yinglun[1, 2†], GOU Meng[1, 2†], SONG Xiaoping[1, 2, 3†], SONG Tao[1, 2†], SHI Biyue[1, 2], PANG Yue[1, 2], LI Qingwei[1, 2*]

[1] College of Life Science, Liaoning Normal University, Dalian 116029, China

[2] Lamprey Research Center, Liaoning Normal University, Dalian 116029, China

[3] Affiliated Zhongshan Hospital of Dalian University, Dalian 116001, China

Received 13 March 2016; accepted 29 December 2017

Abstract

A 105-kDa polymer lectin was purified from lamprey (*Lampetra japonica*) serum by chromatography methods including cation ion-exchange chromatography with a SP-Sepharose^{TM} XL column and size exclusion chromatography with a Superdex 200 column. The target fractions were collected according to the direction of hemagglutinating activity. The results revealed that the active fractions could adsorb on SP-Sepharose column and showed a 280 nm UV absorbance peak corresponding to molecular weights of 105 kDa in the following size exclusion chromatography. The target fractions with hemagglutinating activity were further checked by Native-PAGE and SDS-PAGE. Two single bands at around 105 kDa and 35 kDa were displayed by two electrophoresis methods respectively, indicating that the protein exists as a trimer in solution. After Native-PAGE and SDS-PAGE, two bands were excised from the gels respectively and further identified by MALDI-TOF/TOF as serum lectin (gi: 13094239). The lectin was able to agglutinate rabbit red blood cells (RRBCs) and sheep red blood cells (SRBCs) *in vitro*. The lectin isolated from lamprey serum in the current study might be helpful for deeply understanding the innate immune molecules dependent immune defence in jawless vertebrates which have been proved recently that they possess a lymphocyte-based system of anticipatory immunity with variable lymphocyte receptors as mediators.

Key words: *Lampetra japonica*, lectin, purification, identification, MALDI-TOF/TOF

Citation: Han Yinglun, Gou Meng, Song Xiaoping, Song Tao, Shi Biyue, Pang Yue, Li Qingwei. 2018. Target-directed isolation and identification of a serum lectin from lamprey (*Lampetra japonica*) by chromatographys and MALDI-TOF/TOF. Acta Oceanologica Sinica, 37(5): 113–116, doi: 10.1007/s13131-018-1175-7

1 Introduction

Lectins are carbohydrate-binding proteins which have been investigated extensively in recent years for application in medical and immunological research (Ogawa et al., 2011). They have various biological functions from the glycoprotein synthesis to regulation of cell adhesion and the control of protein levels in the animal bloods (Rutishauser and Sachs, 1975). In addition, lectins can serve many important roles in innate immune defense by recognizing carbohydrates (Ourth et al., 2008) and agglutinating red blood cells *in vitro* (Guo et al., 2013). Agnathans, represented by lamprey and hagfish, are agreed to be the oldest vertebrates currently possessing the adaptive and innate immune defenses. The study of jawless vertebrate provides a theoretical basis for the origin of immune system. Though there are no T cell receptor (TCR) and B cell receptor (BCR) singling pathway in these jawless vertebrates, recent findings in the Agnathans have revealed that they possess an alternative adaptive immune system which could specifically recognize and respond to external pathogens (Cooper and Alder, 2006). This system undergoes germline genomic rearrangements of insertion of diverse leucine-rich repeat modules (LRRs) to generate a large number of different variable lymphatic receptors (VLRs) for the resistance to the pathogen invasion. Three types of receptors, VLRA, VLRB and VLRC have been identified in lampreys (Kasamatsu et al., 2010). Recent evidence indicates that VLRA and VLRB are expressed in different cell types that resemble T cells and B cells in jawed vertebrates, respectively. After being infected by specific a pathogen, VLRB-like lymphocytes expressing specific VLRB molecules undergo amplified expression, and begin to secrete VLRB in a manner analogous to the secretion of immunoglobulins by B cells (Guo et al., 2009). Comparing to the most advances achieved in the adaptive immune system of lamprey, little is known about the effective components that exist in lamprey blood and their roles played in innate immune system. The current study reports that a compon-

Foundation item: The National Program on Key Basic Research Project (973 Program) of China under contract No. 2013CB835304; the National Marine Public Projects under contract No. 201305016; the National Natural Science Foundation of China under contract Nos 31772884 and 31601865; the Key Projects of Scientific Research Platform of Liaoning Provincial Education Department under contract No. L201683651.

*Corresponding author, E-mail: liqw@263.net

†These authors contributed equally to this work.

ent with hemagglutinating activity was purified from lamprey (*Lampetra japonica*) serum by several chromatography steps, and it was identified as lectin by MALDI-TOF/TOF.

2 Materials and methods

2.1 *Animals and reagents*

The handling of lamprey (*Lampetra japonica*) and all experimental procedures were approved by the Animal Welfare and Research Ethics Committee of the Institute of Dalian Medical University (Permit Number: SYXK2004—0029). Adult lampreys were purchased from Tongjiang section of the Heilongjiang River (Tongjiang City, Heilongjiang Province, China) in December. Rabbit red blood cells (RRBCs) and sheep red blood cells (SRBCs) were obtained from rabbit (*Oryctolagus cuniculus*) and sheep (*Oreamnos americanus*), respectively. $NaHCO_3$, C_2H_3N, IAA, and TFA were purchased from the Sigma Company (Sigma-Aldrich, St. Louis, MO). NaCl, coomassie brilliant blue G250, CH_3COOH and the phosphate buffer were of analytical grade from Sangon Biotech (Sangon Biotech (Shanghai) Co., Ltd.). AKTA avant 25 was purchased from GE Company (GE Healthcare, Little Chalfont, Buckinghamshire, United Kingdom). Autofelx MALDI-TOF spectrometer was purchased from Bruker Corporation (Bruker Daltonics, Bremen, Germany).

2.2 *Lampreys serum*

About 100 healthy adult lampreys (200–220 g in weight) were tail-severed for collecting blood. The blood (about 530 mL) was aliquoted into 10 mL plastic centrifuge tubes and allowed to clot at 4°C overnight. Serum was separated by centrifugation (4 000 r/min) for 10 min at 4°C and kept in 1.5 mL centrifuge tube at –20°C before use.

2.3 *Cation exchange chromatography with SP-Sepharose column*

Twenty milliliters of lamprey serum were dialyzed against three changes of 6 L starting buffer consisting of 0.005 mol/L EDTA in 0.01 mol/L NaPB (pH 6.5) for 24 h. The pellets were removed by centrifugation (12 000 r/min) for 10 min at 4°C and the cleared supernatant was applied to a SP-Sepharose column (300 mm×45 mm, i.d., GE Healthcare, Little Chalfont, Buckinghamshire, United Kingdom) which was equilibrated with two column volumes of starting buffer followed by a linear salt gradient elution. The concentration of NaCl raised from 0.2 to 0.6 mol/L in 0.025 mol/L Tris-HCl buffer (pH 7.5) in one column volume. Five milliliter fractions were collected at the flow rate of 1 mL/min. The eluted protein fractions were then conducted the hemagglutinating activity examination.

2.4 *Size exclusion chromatography*

The eluted protein fractions with hemagglutinating activity were pooled together and dialyzed against three changes of 6 L elution buffer (0.005 mol/L EDTA and 0.15 mol/L NaCl in 0.01 mol/L NaPB (pH 6.5)) for 24 h. The dialyzed sample (5 mL) was applied to size exclusion chromatography on a Sephadex 200 column (700 mm×20 mm i.d., GE Healthcare, Little Chalfont, Buckinghamshire, United Kingdom) equilibrated with the elution buffer. The elution was carried out at a flow rate of 0.3 mL/min, and 1 mL-fractions were collected for hemagglutinating activity examination. Finally, the protein fractions with hemagglutinating activity were collected, dialyzed, lyophilized and stored at -20°C for future assay. The protein concentrations of the samples were determined by Bradford assay (Sigma-Aldrich, St. Louis, MO) using bovine serum albumin as standard.

2.5 *Mass spectrometry*

The protein fractions with hemagglutinating activity were electrophoresed by native polyacrylamide gel electrophoresis (Native-PAGE) and SDS polyacrylamide gelelectrophoresis (SDS-PAGE). Albumin from bovine serum 66 kDa (monomer) and 132 kDa (dimer) were used as Native-PAGE gel molecular-weight standards (Sigma-Aldrich, St. Louis, MO). The SDS–PAGE was carried out using 12% (w/v) separation gel. The molecular-weight standards (TaKaRa Biotechnology, Dalian, China) including phosphorylase b (97.2 kDa), albumin (66.4 kDa), ovalbumin (44.3 kDa), carbonic anhydrase (29.0 kDa) and trypsin inhibitor (20.1 kDa) were used for SDS–PAGE. The protein bands were visualized with Coomassie Brilliant Blue R-250. Specific protein bands were excised from the gel matrix and subjected to in-gel tryptic digestion. A total of 0.5 μL of matrix solution (10 mg of a-cyano-4-hydroxycinnamic acid dissolved in 1 mL of 30% ethanol) and 0.5 μL of the diluted analyte solution were spotted on the MALDI target plate (Bruker Daltonics). The MALDI-TOF mass spectrometry was operated in the positive ion mode and measured in reflectron modes on an Autoflex MALDI-TOF spectrometer within a mass range of 700–3 500 Da. The positive-ion mass spectra were calibrated externally using the Bruker Protein Calibration Standard I. Each spectrum corresponded to an accumulation of 3 000 laser shots (6×500 laser shots from different positions of the sample spot). The generated spectra were visualized and compared with FlexAnalysis 3.3 software (Bruker Daltonics, Bremen, Germany). All MS raw data were analyzed by biotools 3.0 (Bruker Daltonics, Bremen, Germany) and searched against all lamprey sequences available in NCBI and ensemble database using Mascot searching engine. Data were run assuming trypsin digestion with a parent ion tolerance of 0.5 Da and fragment ion mass tolerance of 0.8 Da. Oxidation was specified as global modifications and carboxymethyl as variable modifications. Database analysis was performed using the same parameters plus the possibility of up to one missed enzyme cleavages sequence coverage greater than 10%.

2.6 *Hemagglutination assay*

To assay the hemagglutinating activity, a serial two-fold dilution of the sample fractions (100 μL) was mixed with equal volume of 2% suspension of RRBCs and SRBCs in phosphate-buffered saline (PBS, pH 7.2) in a 96-well flat-bottom plate at room temperature for 1 h, respectively. After incubation, red blood cells agglutination was observed by light microscopy *in vitro*. All statistical analyses were performed with the SAS proprietary software release 8.02 and student's two-sample *t*-test.

3 Results and discussion

The target protein with hemagglutinating activity was first isolated from lamprey serum using cation exchange chromatography with a SP-Sepharose column. Twenty milliliters of the lamprey serum was applied to the column and eluted with a linear salt gradient elution as described in materials and methods. Each of the 5 mL-fractions of the effluent were collected and assayed for protein at 280 nm (Fig. 1). Forty-two fractions showed absorbance at 280 nm were assayed hemagglutinating activity and the Hemagglutinating activity was only found in Fraction 25. The dialyzed sample (Fraction 25) was applied on a Sephadex 200 column for conducting size exclusion chromatography. Under UV 280 nm, there were a major peak (Fractions 27 to 34) and a minute peak (Fractions 21 and 24) (Fig. 2). The hemagglutinating activity was only detected in Fraction 26. The elution volume of Fraction 26 was approximately 26 mL, and the molecular

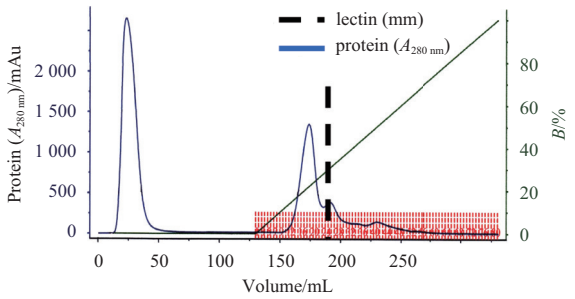

Fig. 1. Ion exchange chromatography profile of lamprey serum crude extract on SP-Sepharose column. Flow rate was 50 mL/h. Hemagglutinating activity was detected in Fraction 25. The dotted line indicates the location of hemagglutinating activity. *B* indicates concentration of elution buffer (PBS+1 mol/L NaCl).

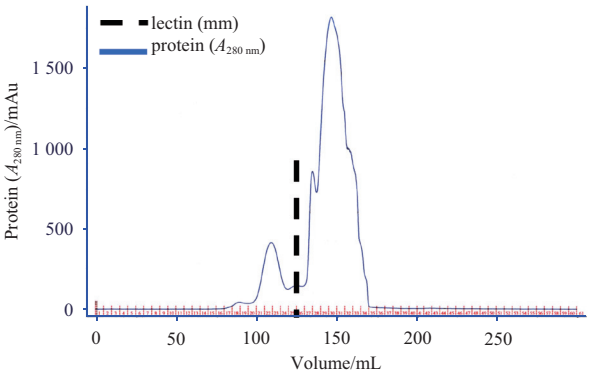

Fig. 2. A Gel filtration chromatography profile of Fraction 25 on Superdex 200 column. Flow rate was 20 mL/h. Hemagglutinating activity was detected in Fraction 26. The dotted line indicates the location of hemagglutinating activity.

weight of Fraction 26 is deduced to be approximately 105 kDa according to the calculation equation given in the manufacturer's instruction manual. The concentration of the target protein is 1.25 mg/mL in the lamprey serum by BCA assay. The result of Native PAGE analysis showed a single protein band whose molecular weight was calculated to be about 105 kDa (Fig. 3a). A single protein band was also found on the gel of SDS-PAGE analysis (Fig. 3a). It can be deduced that its molecular weight is around 35 kDa from the molecular weight calibration graph. From the results of Native PAGE and SDS-PAGE analysis, it can be concluded that the protein with hemagglutinating activity exists as a trimer. On MALDI-TOF MS/MS analysis, the peptide fragments of the protein showed significant high scores (p>0.05) from Mascot searches of peptide mass fingerprints of proteins (Fig. 3b). The complete sequence of a peptide fragment with m/z 1 671 was identified as R.WSSQLGSNP.A which showed a typical character of the product of trypsin (Fig. 3b). The identified sequence of the protein with hemagglutinating activity possesses 100% identity with the serum lectin (GenBank: BAB32787) from lamprey *Lethenteron camtschaticum*. The hemagglutinating activity of purified lamprey serum lectin was further examined by a 10-fold dilution series of sample. The high hemagglutinating ability of the lamprey serum lectin can be observed to agglutinate RRBCs and SRBCs even diluted to 100 fold (12.5 μg/mL) and 200 fold (6.25 μg/mL), respectively (Fig. 4). The ability of the lamprey serum lectin to agglutinate SRBCs was slightly stronger than RRBCs. This result suggests that the hemagglutinating activities of RRBCs and SRBCs depend on the dose of lectin.

In the current study, serum lectin was purified from lamprey *L. japonica*, a representative of jawless vertebrate. The lectin was eluted as a single peak with a molecular weight of around 105 kDa in size exclusion chromatography step. Its molecular weight was verified as 105 kDa by Native-PAGE analysis under native condition, while it was revealed a 35-kDa protein band on SDS-PAGE gel in reducing conditions. These data suggest that the lectin is a 105-kDa trimerical protein and possesses hemagglutinating activity. Agnathans, represented by lamprey and hagfish, are agreed to be the oldest vertebrates currently possessing the

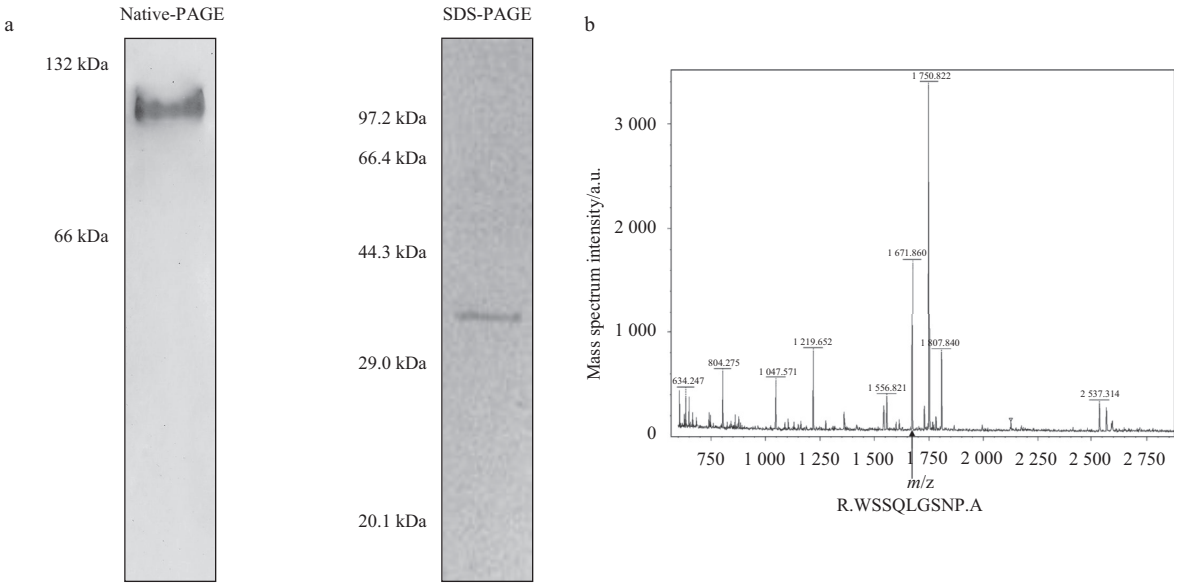

Fig. 3. Gel analyses and Peptide mass fingerprints. a. Native-PAGE and SDS–PAGE. Left lane: Native-PAGE. Right lane: SDS-PAGE. b. The peptide with m/z 1 671 corresponds to a tryptic fragment of the complete protein was identified as R.WSSQLGSNP.A, an identical homologue of serum lectin (GenBank: BAB32787), by MALDI-TOF MS/MS analysis.

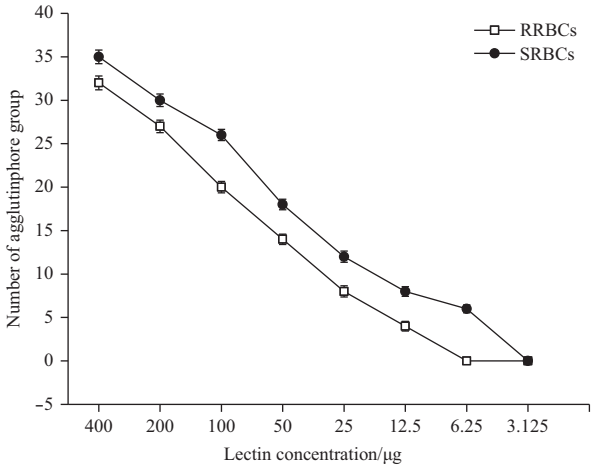

Fig. 4. Agglutination assay of lamprey lectin against erythrocytes. The antigens for agglutination assay were RRBCs and SRBCs. Data represent mean numbers±SE. Error bars, n=3.

adaptive and innate immunity. Variable lymphatic receptors are the important components for adaptive immune response in jawless vertebrates (Guo et al., 2009). In jawed vertebrates, lectin serves many important roles in the innate immunity by recognizing exogenous antigen (Guo et al., 2013). Here, we found lamprey lectin also possesses hemagglutinating activity to allogeneic red blood cells. These findings provided basic information for deeply understanding the components of innate immune system of jawless vertebrate.

References

Cooper M D, Alder M N. 2006. The evolution of adaptive immune systems. Cell, 124(4): 815–822

Guo Peng, Hirano M, Herrin B R, et al. 2009. Dual nature of the adaptive immune system in lampreys. Nature, 459(7248): 796–801

Guo Xiaonv, Jin Xingkun, Li Shuang, et al. 2013. A novel C-type lectin from *Eriocheir sinensis* functions as a pattern recognition receptor with antibacterial activity. Fish Shellfish Immunol, 35(5): 1554–1565

Kasamatsu J, Sutoh Y, Fugo K, et al. 2010. Identification of a third variable lymphocyte receptor in the lamprey. Proc Natl Acad Sci USA, 107(32): 14304–14308

Ogawa T, Watanabe M, Naganuma T, et al. 2011. Diversified carbohydrate-binding lectins from marine resources. J Amino Acids, 2011: 838914

Ourth D D, Rose W M, Siefkes M J. 2008. Isolation of mannose-binding C-type lectin from sea lamprey (*Petromyzon marinus*) plasma and binding to *Aeromonas salmonicida*. Vet Immunol Immunopathol, 126(3–4): 407–412

Rutishauser U, Sachs L. 1975. Cell-to-cell binding induced by different lectins. J Cell Biol, 65(2): 247–257